Towards microwave based ion trap quantum technology

Sebastian Weidt

Submitted for the degree of Doctor of Philosophy

University of Sussex

August 2013

Declaration

I hereby declare that this thesis has not been and will not be, submitted in whole or in part to another University for the award of any other degree.

Signature:

Sebastian Weidt

To Mum and Dad.

UNIVERSITY OF SUSSEX

Sebastian Weidt, Doctor of Philosophy

Towards microwave based ion trap quantum technology

Summary

Scalability is a challenging yet key aspect required for large scale quantum computing and simulation using ions trapped in radio-frequency (rf) Paul traps.

In this thesis $^{171}Yb^{+}$ ions are used to demonstrate a magnetic field insensitive qubit which has a measured coherence time of 1.5 s, making it an ideal candidate to use for storing quantum information. A magnetic field sensitive qubit is also characterised which can be used for the implementation of multi-qubit gates using a potentially very scalable scheme based on microwaves in conjunction with a static magnetic field gradient instead of using lasers. However, the measured coherence time is limited by magnetic field fluctuations and will prohibit high fidelity gate operations from being performed. To address this issue, the preparation of a dressed-state qubit using a microwave based stimulated rapid adiabatic passage (STIRAP) pulse sequence will be presented. This qubit is protected against the noisy environment making it less sensitive to magnetic field fluctuations. The lifetime of this qubit is measured to demonstrate its suitability for storing quantum information. A powerful method for manipulating the dressed-state qubit will be presented and is used to measure a coherence time of the qubit of 500 ms which is two orders of magnitude longer compared to the magnetic field sensitive qubit. It will also be shown that our method allows for the implementation of arbitrary rotations of the dressed-state qubit on the Bloch sphere using only a single rf field. This substantially simplifies the experimental

setup for single and multi-qubit gates.

Furthermore, this thesis will present a experimental setup capable of successfully operating microfabricated surface ion traps. This setup is then used to operate and characterise the first two-dimensional (2D) lattice of ion traps on a microchip. A unique feature of the microfabrication technique used for this device is the extremely large voltage that can be applied which allows long ion lifetimes along with large secular frequencies to be measured, demonstrating the robustness of this device. Rudimentary shuttling between neighbouring lattice sites will be shown which could be used as part of a efficient scheme to load a large lattice of ions. One of the many applications of a 2D lattice of ions lies in the field of quantum simulations where many-body systems such as quantum magnetism, high temperature superconductivity, the fractional quantum hall effect and synthetic gauge fields can be simulated. It will be shown how making only minor modifications to the microchip the ion-ion separation can be reduced sufficiently to offer an exciting platform for the successful implementation of 2D quantum simulations. A theoretical investigation on the optimal 2D ion trap lattice geometry will also be presented with the aim to maximise the ratio of ion-ion coupling strength to decoherence from motional heating of the ions and to laser induced off-resonant coupling.

Acknowledgements

General acknowledgements

I would like to thank my supervisor, Dr. Winfried Hensinger, for playing a very active role in my decision process to undertake a DPhil and for giving me the opportunity to undertake this DPhil in his very motivated and lively research group. His enthusiasm and intuition is unmatched and the vast number of lessons I have learned from him will guide me through the next stages in my career. I would also like to thank my second supervisor Dr. Barry Garraway for always being available to give advice. Special thanks also to Dr. Matthias Keller without whom I would have never even considered undertaking a DPhil.

I would like to thank Dr. James (Jim) McLoughlin, Dr. James Siverns, Dr. Robin Sterling, Dr. Altaf Nizamani, Dr. Marcus Hughes and Bjoern Lekitsch who were in the research group when I started, for being very welcoming and always happy to answer the many questions I had. Special thanks go to Jim, who I worked with a lot during the beginning of my DPhil, for taking the time to explain how the ion trap setup works and for never being too busy to give advice when the experiment stopped working. Thanks also go to the many undergraduate students I was lucky to work with especially Joe Randall who contributed a lot to my research during his many projects and it is great to see he has already become a invaluable PhD student in our group.

Kimberley (Kim) Lake joined the group half a year after I did and we ended up working together on most of the experiments presented in this thesis. Her love for physics and constant drive to investigate the unknown has been very inpiring and made me a better physicist. I would like to thank you for making the long hours in the lab so much fun and for putting up with my impatience in getting things done. Thank you also for the daily teas during my long hours of writing up:-).

Dr. Simon Webster joined the group half way through my DPhil and immediately moved our experiments forward with his incredible experience in our field. I would like to thank you for all your support and for your patience in explaining various theoretical

concepts. I am also hugely grateful for your detailed feedback on my thesis. Writing up would most certainly not have gone as smoothly without your support.

My thanks also go to the rest of the group, Darren De Motte, Dr. Gouri Giri, Eamon Standing and David Murgia for never being too busy to help out when needed and for adding to the great atmosphere in the lab. Furthermore, many parts of the experimental setup were built by our outstanding workshop managed by Peter Henderson. I would like to extend my thanks to the whole workshop for their amazing work and for always squeezing urgent work into their busy schedule. Thank you also to the whole group of Prof. Wolfgang Lange and Dr. Matthias Keller for all their help and for lending us equipment whenever ours was broken.

A huge thank you goes to my mother and father for always being there for me. None of this would have been possible without your endless love and support. A big thank you also to my brother Stephan who has been more supportive than he probably realises and always made sure I had the best IT during my DPhil. A heartfelt thank you to Eleanor Tubman who has always been there for me. Thank you also to all my friends in and out of the lab who always offered a welcomed break and also listened to all the complaining when something in the lab was not working.

Detailed Acknowledgements

The work presented in this thesis would not have been possible without the valuable input from other members of the research group. Here I wish to acknowledge their contributions.

Chapter 3 - Experimental setup and initial experiments

I joined the group shortly after they trapped the first ion. Consequently, the core experimental setup was built by previous students. The macroscopic linear trap was designed by Dr. Robin Sterling and built by himself, Dr. James McLoughlin, Dr. Marcus Hughes, Dr. Altaf Nizamani and Dr. James Siverns. The resonator presented in this chapter was built by Dr. James Siverns. The majority of the locking setup was built and designed by Dr. Robin Sterling and Kimberly Lake. The imaging system in this chapter was designed and built by Dr. James Siverns and Dr. Marcus Hughes. The vacuum system in this chapter was designed and constructed by Dr. Altaf Nizamani with assistance from Dr. James McLoughlin. The theory for the heating rate measurement was developed by Wesenberg *et al.* [1] and reproduced by Bjoern Lekitsch with help from Dr. James McLoughlin. The heating rate measurements was performed by Dr. James McLoughlin, Dr. Altaf Nizamani, Dr. James Siverns, Dr. Robin Sterling, Dr. Marcus Hughes, Bjoern Lekitsch and myself.

The wavelength measurements were taken by the same people.

Chapter 4 - Single qubit manipulation

The experiments shown in this chapter were performed, and the data analysed, by myself and Kimberley Lake with assistance from Dr. James McLoughlin during the initial stage and from Dr. Simon Webster when he joined the group later on.

Chapter 5 - Dressed-states

The experiments shown in this chapter were performed, and the data was analysed, by myself, Kimberley Lake and Dr. Simon Webster. Dr. James McLoughlin helped during the early stages of setting up the experiment. Dr. Simon Webster developed the theory behind the dressed-state manipulation method.

Chapter 6 - Two-dimensional ion trap lattice on a microchip

The microchip and the fabrication process was designed by Dr. Robin Sterling. The microchip was fabricated by Hwanjit Rattanasonti at the University of Southampton. The vacuum system was designed by Dr. Robin Sterling and James Sayers and built by Dr. Robin Sterling, myself and Kimberley Lake. The experiments were performed by Dr. Robin Sterling, myself, Kimberly Lake and Dr. Simon Webster.

Chapter 7 - Optimisation of two-dimensional ion trap arrays for quantum simulation

The electric fields from the trap geometries were calculated using a C++ program written by Dr. Bjoern Stein which was adapted by Dr. James Siverns. The optimisation was performed by Dr. James Siverns, myself, Kimberley Lake, Bjoern Lekitsch and Dr. Marcus Hughes. The resultant publication is presented in this chapter.

Publications

Two-dimensional ion trap lattice on a microchip for quantum simulation

R. C. Sterling, H. Rattanasonti, S. Weidt, K. Lake, P. Srinivasan, S. C. Webster, M. Kraft, W. K. Hensinger, *Nat. Commun.* 5:3637 (2014)

Simple Manipulation of a Microwave Dressed-State Ion Qubit

S. C. Webster, S. Weidt, K. Lake, J. J. McLoughlin and W. K. Hensinger, Phys. Rev. Lett. 111, 140501 (2013)

Optimisation of two-dimensional ion trap arrays for quantum simulation

James D. Siverns, Seb Weidt, Kim Lake, Bjoern Lekitsch, Marcus D. Hughes and Winfried K. Hensinger, New J. Phys. 14, 085009 (2012)

On the application of radio frequency voltages to ion traps via helical resonator

J.D. Siverns, L.R. Simkins, S. Weidt and W. K. Hensinger, Applied Physics B 106, 327 (2012)

Versatile ytterbium ion trap experiment for operation of scalable ion trap chips with motional heating and transition frequency measurements

James J. McLoughlin, Altaf H. Nizamani, James D. Siverns, Robin C. Sterling, Marcus D. Hughes, Bjoern Lekitsch, Björn Stein, Seb Weidt and Winfried K. Hensinger, Phys. Rev. A 83, 013406 (2011)

Contents

List of Tables

List of Figures

Chapter 1

Introduction

1.1 Quantum computing

Understanding the natural and social world we live in is a key motivator for performing research. To acquire an understanding of the ever increasing complex systems we investigate, classical computers have become of fundamental importance. The classical computer was first introduced by Alan Turing in 1936 [8] and nowadays builds on elementary physical elements called 'bits' which can have two possible states denoted 0 and 1. While extremely efficient at executing many algorithms to solve deterministic problems, the classical computer we know today has limitations. These limitations stem from current computers obeying classical physics, which makes them extremely inefficient when simulating quantum systems. It would therefore be desirable to develop a computer which obeys the laws of quantum mechanics.

It was not until the work by Richard Feynman in 1982 that it was realised that a controllable quantum system can be used to simulate a large quantum system considerably more efficiently than a classical computer ever could [9]. In his work he used the example of a photon where the direction of the polarisation represents two states, 0 and 1. Since this system obeys the laws of quantum mechanics it can be in a superposition of 0 and 1. We can refer to such a system as a quantum bit, or 'qubit'. This qubit, which is made up of the two orthogonal states $|0\rangle$ and $|1\rangle$, is described by

$$|\Psi\rangle = \alpha|0\rangle + \beta|1\rangle \tag{1.1}$$

where α and β are two complex numbers and $|\alpha|^2 + |\beta|^2 = 1$.

What this means is that the state of a quantum computer with N qubits can be in a superposition of 2^N states unlike the state of a classical computer which can only be in

one of the 2^N states at a time. A measurement of the system will cause the collapse of the superposition and result in a random output. As pointed out by Feynman, repeating the same experiment many times does however allow to extract the probability of the system being in a certain state which is very useful when simulating the evolution of a quantum system.

Taking this a step further, David Deutsch showed that it is possible for a quantum gate operation, such as an entangling gate, to work in an analogous way to logic gates in a classical computer and should therefore be capable of processing information [10]. The most significant difference is that due to the creation of entanglement the qubits of the quantum computer can no longer be described as individual entities. The result of this is that a operation on a single qubit will influence all the other qubits and can lead to parallel quantum computing which can significantly increase the speed of a quantum computer.

To make use of this computational power, impressive quantum computing algorithms have been developed. One example is Shor's factoring algorithm which can factor large numbers [11]. Factoring large numbers is an essential part of current encryption schemes since this is a inherently difficult task for classical computers. This algorithm has therefore seen increasing interest from national security agencies. Another well known algorithm is called Grover's search algorithm [12]. As the name suggests it is an algorithm designed to search through large unsorted databases. Due to the quantum mechanical behaviour of a quantum computer the required search iterations are reduced to $\sqrt{N}$. In contrast, a classical computer requires N/2 iterations.

A major limitation at the time was the requirement of every operation on the qubits needing to be perfect in order for any algorithm to be successfully implemented. It was therefore no surprise that with the introduction of error correction schemes [13] and fault tolerant quantum computing [14] the interest in the field of quantum information grew significantly. Following the proposal of these schemes, allowing quantum computing to be performed despite non-optimal qubit operations, the focus shifted towards what physical system could be used as a quantum computer. It was David DiVincenzo in 2000 who listed 5 physical requirements to be met by any system being used which are [15]:

1. A scalable physical system with well characterised qubits - This means that the system should allow for a large number of qubits to be used. It also means that the qubit should be well understood including the Hamiltonian describing its internal energy, the coupling between multiple qubits and the interaction between the qubit

and external fields used for quantum operations.

2. The ability to initialise the state of the qubits - This means that it needs to be possible to prepare the qubit in any arbitrary state with a high fidelity.

3. Long relevant decoherence times - The decoherence time of the qubit needs to exceed the time it takes for gate operations to be performed which means that the qubit needs to be well protected from the environment. The minimum the decoherence time needs to exceed the gate time by is set by the error correction scheme used.

4. A universal set of quantum gates - To implement a universal set of gates the required operations can be simplified to single qubit gates and one two-qubit gate operation known as the controlled NOT (CNOT) gate.

5. A qubit-specific measurement capability - It must be possible to read-out the state of single qubits without affecting other qubits which are part of the computation.

Keeping the above requirements in mind, there are several systems that are currently being used with the aim to perform quantum computing. Examples of such systems include optical systems such as photons [16], solid-state systems such as quantum dots [17], atomic systems such as neutral atoms [18] and trapped ions [19]. Optical systems have been used to perform exciting experiments and it can easily be seen how photons could be the ideal carrier for transferring quantum information over large distances. Due to the difficulty of confining a photon, storing of information is extremely difficult and requires a second system. Solid-state systems have the advantage of being very scalable and offering a platform for fast quantum gate operations however a challenge lies in the short coherence times which limits the achievable gate fidelities. The internal states of atomic systems on the other hand can be well protected from the environment and easily manipulated using lasers or microwaves. While neutral atoms tend to suffer from a short lifetime, trapped ions have been shown to have long coherence times and lifetimes and impressive progress towards scaling to a large number of qubits has been made. This makes the quantum computer based on trapped ions one of the most promising candidates for the implementation of quantum computing.

1.1.1 Quantum computing using ions

Ions can be trapped in a Penning trap using a homogeneous static magnetic field and a spatially inhomogeneous static electric field and many of the requirements for quantum

computing have been implemented in such a trap [20]. The problem is that the ions in a Penning trap are not stationary; instead they form a rotating crystal which makes individual ion addressing and readout very challenging. A more common approach is to trap ions in a radio-frequency (rf) Paul trap which uses oscillating and static electric fields. The information can be encoded in two internal states of the ion which are either separated by a optical frequency (optical qubit) or by a microwave/rf-frequency (hyperfine/zeeman qubit).

Using ions as a quantum computer was first proposed by Cirac and Zoller in 1995 [19]. In their proposal single and multi-qubit gate operations are performed using well-controlled laser beams which are tightly focused to individually address each ion. As a prerequisite to performing the CNOT gate a collective mode of motion of the ions is cooled to the ground state. To perform the CNOT gate the same mode is then used as an auxiliary 'bus' qubit which is used to transfer knowledge of the state of the 'control' qubit to the 'target' qubit. A simplified version of this gate was first implemented by Monroe *et al.* [21] in 1995 using a single ion while the full scheme was first implemented by Schmidt-Kaler *et al.* [22] in 2003 using a string of ions.

The Cirac and Zoller CNOT gate comes with two major experimental challenges. The first is the requirement of having to ground state cool the mode that is being used as the auxiliary qubit. The second challenge is the requirement of individual ion addressing which is very difficult using lasers. While both challenges can be overcome they add to the complexity of the experiment and can limit the achievable gate fidelity.

The above challenges were removed by the proposals and implementations of new gates where ions do not have to be in the motional ground state and individual addressing is not required either [23–30]. The gates are usually implemented by using a pair of bichromatic Raman laser fields (in the case of a hyperfine qubit) where the frequencies are tuned such that the upper (blue) and lower (red) motional sideband of the ions are near resonantly addressed. Having removed some of the stringent requirements that come with the Cirac and Zoller gate has lead to very impressive experimental demonstrations of multi-qubit hot gates. This includes the entanglement of up to 14 ions [31] and the demonstration of a entangling gate fidelity of 99.3% [32], both of which have been implemented using the Mølmer-Sørensen scheme [23, 25].

Nevertheless, there are problems with the above implementations when trying to scale them up to many more ions and when trying to improve the gate fidelity. Technical problems include fluctuations of the laser output which can be separated into frequency,

phase and intensity fluctuations as well as the limited absolute intensity that can be obtained. Furthermore, beam pointing instability and non-perfect beam quality can cause infidelities even if it was possible to perfectly stabilise the laser output. While these technical challenges could in principle be overcome with great effort, a more fundamental problem is off-resonant coupling to states outside of the qubit subspace caused by the Raman beams. This puts a limit on the maximum achievable gate fidelity [33]. On the economic side, lasers can be very expensive to purchase and a lot of time and money has to be spent on maintaining these systems.

A very promising solution to the stability and scalability issues that come with using lasers to implement multi-qubit gate operations was proposed by Mintert and Wunderlich [34] in 2001. Due to the long wavelength of microwaves (on the order of centimetres) it is not possible to achieve a sufficiently strong coupling between the internal state of the ion and its motion. However, as pointed out by Mintert and Wunderlich, by adding a static magnetic field gradient and using a qubit made up of two states with different magnetic moments a sufficient coupling, similar to that achieved using lasers, can be achieved. The scheme is suitable for current multi-qubit gates that have so far been experimentally realised using lasers and remove most of the laser specific limitations. A important advantage of using microwaves is the non-existent spontaneous emission to unwanted states which puts a fundamental limit on the achievable laser gate fidelity. Another important advantage is the possibility of individually addressing ions in frequency space due to the position dependant qubit energy splitting resulting from a magnetic field gradient along a string of ions. On the technical side, microwave engineering is a very mature field allowing extremely stable microwave fields to be generated at comparably low costs. Microwaves also naturally address a large volume of space making them potentially very useful when scaling any operation to many more ions.

The ability to individually address ions and resolve motional sidebands using this scheme was first demonstrated by Johanning *et al.* [35]. This was followed by the implementation of a two-ion gate by Khromova *et al.* three years later [36]. A different scheme using a oscillating magnetic field gradient has also been proposed [37] and implemented [38]. This scheme itself does not allow individual ion addressing however this can be solved by using microwave near-field gradients [39].

Currently, the limiting factor in achieving very high gate fidelities using microwaves in conjunction with a static magnetic field gradient stems from the difficulty of achieving high magnetic field gradients and from magnetic field noise causing uncontrollable fluctuations

of the energy of the magnetic field sensitive qubit state(s) [36]. To address this issue microwave dressed-states can be used to significantly suppress the effect of magnetic field noise [40]. In this scheme, microwaves are used to create a dressed-state which, while being insensitive to magnetic field noise, is still sensitive to a magnetic field gradient. Combining this dressed-state with a magnetic field insensitive bare state then results in a qubit which is protected against noisy magnetic fields. Radio-frequency (rf) fields can then be used to implement single and multi-qubit gate operations and should significantly improve the currently achievable gate fidelities.

1.1.2 Scalable architectures for quantum computing and quantum simulation

While one of the main challenges lies in performing multi-qubit gate operations with a fidelity high enough to be part of a large scale quantum computer, another challenge lies in developing scalable architectures that allow thousands of ions to be stored, shuttled and manipulated [41]. A core, successful ingredient in developing such architectures is the use of state-of-the-art microfabrication techniques [42]. Microfabricated ion traps have already been used to shuttle ions [43, 44] and perform two-qubit gate operations [38] which mark important milestones towards the implementation of large scale quantum computing with ions. Indeed, the realisation of such a computer still requires many challenges such as limited two-qubit gate fidelities to be overcome however as pointed out by Feynman, a collection of two-level systems could form part of a 'quantum simulator' to simulate large quantum systems and outperform a classical computer [9]. Since a quantum simulation is not based on multi-qubit gate operations, as is the case for a quantum computer, the requirements for the successful implementation are less stringent. Following the exciting proposal to use ions as effective spins to simulate many-body systems such as quantum magnetism by Porras and Cirac in 2004 [45], many impressive small-scale quantum simulations have been implemented using a linear string of ions [46–52]. A focus now lies on developing microfabricated architectures that allow trapping of a tightly spaced two-dimensional (2D) lattice of ions which could be achieved using a lattice of individual rf ion traps [53–55]. The experimental realisation of a quantum simulator based on such an architecture has the potential to outperform a classical computer for the first time.

1.2 Thesis outline

This thesis is structured in the following way. The first part of the thesis presents the first coherent manipulation experiments using $^{171}Yb^{+}$ in our laboratory. It presents the implementation and novel manipulation of a dressed-state qubit which is resilient to magnetic field fluctuations and will now be used for the implementation of high fidelity multi-qubit gates based on microwave and radio-frequency (rf) fields in conjunction with a static magnetic field gradient. The second part presents work towards two-dimensional (2D) ion lattices for the implementation of quantum simulations.

In more detail, chapter 2 outlines how an ion trap works and describes how specific isotopes of ytterbium can be used as an ion in quantum information experiments. Chapter 3 reviews the main experimental setup and presents a heating rate measurement for the trap used for some of the experiments shown in this thesis.

Chapter 4 describes how single qubit gate operations can be implemented. It also describes how microwaves in conjunction with a static magnetic field gradient can be used to individually address ions in frequency space and to couple the spin state to the motion of the ion. This is followed by the implementation of single qubit gate operations where the qubit is made up of two states which are part of the $^{2}S_{1/2}$ hyperfine manifold of $^{171}Yb^{+}$. Two possible qubits are investigated, one of which is a magnetic field insensitive qubit for which a coherence time of 1.5 s is measured. The second qubit consists of one magnetic field insensitive and one magnetic field sensitive state. The coherence time of this qubit is found to be approximately 500 μs which limits its usefulness for high fidelity multi-qubit gate operations. To address this issue chapter 5 presents the experimental demonstration of microwave dressed-states to form a qubit which is insensitive to magnetic field noise but still suitable for multi-qubit gate operations. We measure a coherence time of this qubit in the excess of 500 ms, a two orders of magnitude increase compared to the magnetic field sensitive bare state qubit. We also present a novel method of manipulating the dressed-state qubit using only a single rf field which allows arbitrary qubit rotations to be performed and significantly simplifies the experimental setup required for the implementation of multi-qubit gate operations.

Chapter 6 presents the operation of a 2D ion trap lattice on a microchip. This includes a brief description of the specialised fabrication method used which allows very large voltages to be applied to the microchip. Trapping of the first 2D lattice of ions on a microchip will be shown along with shuttling between lattice sites which could be used as part of a scheme to load larger ion lattices. Chapter 7 addresses the question of the optimal 2D lat-

tice geometry which maximises the effective spin-spin coupling rate between neighbouring ions while minimising sources of decoherence such as motional heating and spontaneous emission. It will also be shown how simple modifications to the microchip design could offer a platform for the successful implementation of 2D quantum simulations.

Chapter 2

The rf Paul trap and the Yb ion

The experiments presented in this work rely on the radiofrequency (rf) ion trap which is used to strongly confine ions for a long period of time. The rf ion trap was invented by Wolfgang Paul in the late 1950's following which Wineland *et al.* [56] and Neuhauser *et al.* [57] independently demonstrated laser-cooling of trapped Mg^+ and Ba^+ ions respectively in 1978. Since then the rf (Paul) ion trap has been used in fields such as cavity quantum electrodynamics [58], atomic clocks [59–61] and quantum information [41, 53, 62, 63]. Due to the major impact of the rf ion trap on a variety of scientific research fields Wolfgang Paul shared the 1989 Nobel prize in Physics [64].

Focusing on the field of quantum computing using trapped ions, a variety of different ion species have been used in experiments including Mg^+ [65], Ca^+ [66], Cd^+ [67], Ba^+ [68], Be^+ [21], Sr^+ [69] and Yb^+ [70, 71]. No consensus has yet been reached as to which species is most suitable for quantum information processing and it is likely that it will depend on the specific experimental requirements. The experiments presented in this work use Yb^+ and it will be the focus of this chapter to present this ion in more detail along with an explanation of the underlying principle of the rf Paul trap.

2.1 The ion trap

When first thinking about how to design a device to confine a charged particle one might think that this can simply be achieved by using a number of static electric fields. However, the well known Earnshaw's theorem states that it is not possible to confine a charged particle in three dimensions using static electric fields. This is a consequence of Laplace's equation which, for the case of working in free space, is given by

$$\nabla^2 \phi(x, y, z) = 0 \tag{2.1}$$

where $\phi(x, y, z)$ is a three-dimensional electric potential. Fortunately, it is possible to solve this problem and confine charged particles by replacing the static electric fields with a oscillating electric field. Such a field produces a time dependant potential $\phi(x, y, z, t)$ which can be described by

$$\phi(x, y, z, t) = U\frac{1}{2}(\alpha_1 x^2 + \beta_1 y^2 + \gamma_1 z^2) + V\cos(\Omega_T t)\frac{1}{2}(\alpha_2 x^2 + \beta_2 y^2 + \gamma_2) \tag{2.2}$$

where U and V are the voltages of the applied static and time dependant fields respectively and Ω_T is the frequency of the time dependant voltage. In order to satisfy Laplace's equation and confine charged particles it is a good starting point to get as close as possible to ensuring that

$$-(\alpha_1 + \beta_1) = \gamma_1 > 0 \qquad \text{and} \qquad \alpha_2 = -\beta_2, \gamma_2 = 0. \tag{2.3}$$

or

$$\alpha_1 = \beta_1 = \gamma_1 = 0 \qquad \text{and} \qquad \alpha_2 + \beta_2 = -\gamma_2 \tag{2.4}$$

By satisfying the above conditions it is possible to design trapping structures which allow confining of charged particles. Examples of such structures will now be given.

2.1.1 Two-dimensional quadrupole trap

An example of a geometry which produces a potential that satisfies the conditions shown in equation 2.3 is shown in figure 2.1. This trap structure is often referred to as a two-dimensional quadrupole trap or a linear Paul trap. Applying a static, as well as oscillating field, to two opposite electrodes and the same field but out of phase by π to the remaining two electrodes results in a total quadrupole potential given by [72]

$$\phi_p(x, y, t) = (U - V\cos(\Omega_T t))\left(\frac{x^2 - y^2}{2r_0^2}\right). \tag{2.5}$$

This provides radial confinement along the x and y-axis and results in a uniform potential along the z-axis near the centre of the trap. While this does not provide confinement in the z-axis, this can be achieved by positioning electrodes at either end of the trap which are often referred to as end cap electrodes. An alternative method involves only applying a oscillating field to two of the hyperbolic electrodes and applying a static voltage to the other two electrodes which can be segmented to provide confinement along the z-axis. A trap similar to this is shown in chapter 3.

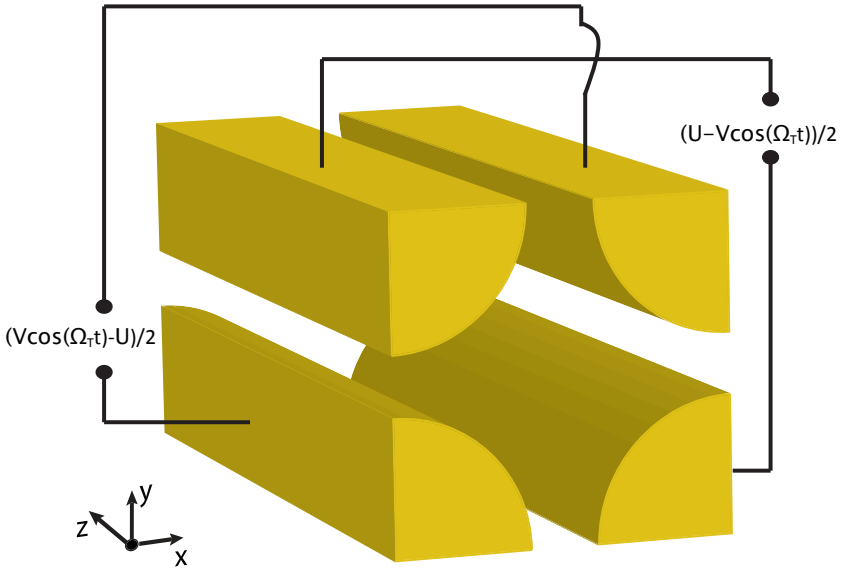

Figure 2.1: Illustration of a linear Paul trap consisting of four hyperbolic electrodes.

Ion motion

The motion of an ion in a potential created by a linear Paul trap is an important experimental parameter that needs to be considered and has been studied in great detail. A very brief summary will be given here following [42].

The motion of an ion can be described in two ways. One way gives a good approximation of the motion and will be considered first. The second way allows us to get a more complete understanding of the motion and will be considered later.

When considering the motion of an ion in a harmonic potential we find that the frequency of this motion has to be small compared to the frequency used to create the trapping potential. This allows us to time average the force an ion experiences in a inhomogeneous field over an oscillation to get a pseudopotential. This is known as the pseudopotential approximation [73]. The pseudopotential for a voltage of the form $V \cos \Omega_T t$ applied to the linear Paul trap shown in figure 2.1 is given by [74]

$$\psi = \frac{e^2}{4m\Omega_T^2} |\nabla V(x, y, z)|^2 \tag{2.6}$$

for a single ion where $|\nabla V(x, y, z)^2|$ is the gradient of the potential and m is the mass of the ion. The ion motion inside this pseudopotential can now be approximated as secular harmonic motion which greatly simplifies the ion dynamics. The secular frequency is given by [74]

$$\nu_i^2 = \frac{e^2}{4m^2\Omega_T^2} \frac{\partial^2}{\partial i^2} \left(|V(x, y, z)|^2 \right) \tag{2.7}$$

where i corresponds to the x, y or z-axis of motion and the derivative is taken at the minimum of $|V(x,y,z)|^2$.

The pseudopotential approximation is very useful for simulating a trap and obtaining a good approximation of the ion motion as it only requires a electrostatics problem to be solved. However, a more complete understanding of the ion motion is sometimes required. In this case the time dependant nature of the potential given in equation 2.5 needs to be taken into account as this can superimpose an oscillation with frequency Ω_T to the secular motion of the ion. The equations of motion for an ion trapped in a potential given by equation 2.5 can be written as [72]

$$\frac{\partial^2 x}{\partial t^2} = -\left(\frac{e}{m}\right)\frac{\partial \phi_p(x,y,t)}{\partial x} = -\frac{e}{mr_0^2}\left(U - V\cos(\Omega_T t)\right)x \tag{2.8}$$

$$\frac{\partial^2 y}{\partial t^2} = -\left(\frac{e}{m}\right)\frac{\partial \phi_p(x,y,t)}{\partial y} = \frac{e}{mr_0^2}\left(U - V\cos(\Omega_T t)\right)y \tag{2.9}$$

$$\frac{\partial^2 z}{\partial t^2} = -\left(\frac{e}{m}\right)\frac{\partial \phi_p(x,y,t)}{\delta z} = 0. \tag{2.10}$$

where, again, we can see that the potential from the rf field does not provide any confinement along the z-axis.

By using the chain rule and making the following substitutions

$$a = \frac{4eU}{mr_0^2\Omega_T^2}. \qquad q = \frac{2eV}{mr_0^2\Omega_T^2}, \qquad \zeta = \frac{\Omega_T t}{2} \tag{2.11}$$

the equations of motion can be written in the form of the Mathieu equations given by [72]

$$\frac{\partial^2 x}{\partial \zeta^2} = -\left(a - 2q\cos(2\zeta)\right)x = 0 \tag{2.12}$$

$$\frac{\partial^2 y}{\partial \zeta^2} = \left(a - 2q\cos(2\zeta)\right)y = 0. \tag{2.13}$$

The Mathieu equations can be solved using the Floquet theorem [75]. By solving the Mathieu equations of motion we find that there exist various combinations of a and q which result in stable ion motion. Figure 2.2 (a) shows a stability diagram with the green and red regions illustrating stable motion in the x and y direction respectively. Stable regions for trapping ions can be found by ensuring that a and q parameters are chosen which provide stable motion in both of these directions. An example of such a region can be found when focusing on small a and q parameters as illustrated by the orange region in figure 2.2 (b). This is the most commonly used region for trapping ions.

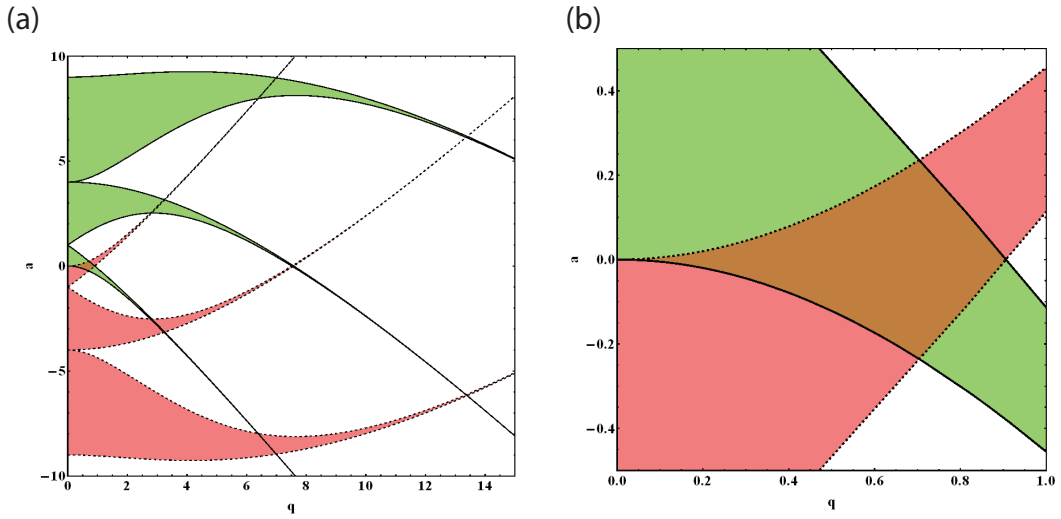

Figure 2.2: (a) Stability diagram illustrating stable regions of motion along the x-axis (green) and y-axis (red) of motion. (b) An example of a stable region along the x as well as the y-axis (orange) which can be used to trap ions.

2.1.2 Micromotion

The Floquet theorem can be used to solve the Mathieu equations for the case where $a = 0$ and $q \ll 1$. The resultant ion trajectory along the x-axis is then given by [6]

$$x(t) = \kappa \cos(\nu_x t) \left(1 + \frac{q_x}{2} \cos(\Omega_T t)\right) \tag{2.14}$$

where κ is a constant which depends on the initial conditions. We can see that the ion trajectory is made up of the secular motion, with frequency ν_x as well as a fast oscillatory motion at the frequency of the trapping field, Ω_T. This fast oscillatory motion is known as micromotion. While the so called intrinsic micromotion caused by the ion being driven away from the rf nul due to the extent of the wave packet can not be compensated for, it is indeed possible to compensate for extrinsic micromotion. Extrinsic micromotion is often caused by static offset fields which cause a constant shift of the ion away from the rf nil. This can be compensated for by incorporating static voltage electrodes into the trap structure.

Figure 2.3 illustrates the motion of an ion with a secular frequency of $\nu_x/2\pi = 1\,\text{MHz}$ trapped in a potential characterised by $\Omega_T/2\pi = 35\,\text{MHz}$ and $q = 0.1$. We can see the low frequency but large amplitude secular motion as well as a high frequency but small amplitude micromotion where the amplitude of the micromotion is proportional to the distance of the ion from the rf nil position. While recent experiments have made use of micromotion [39, 76], it often is an undesirable effect and generally needs to be minimised

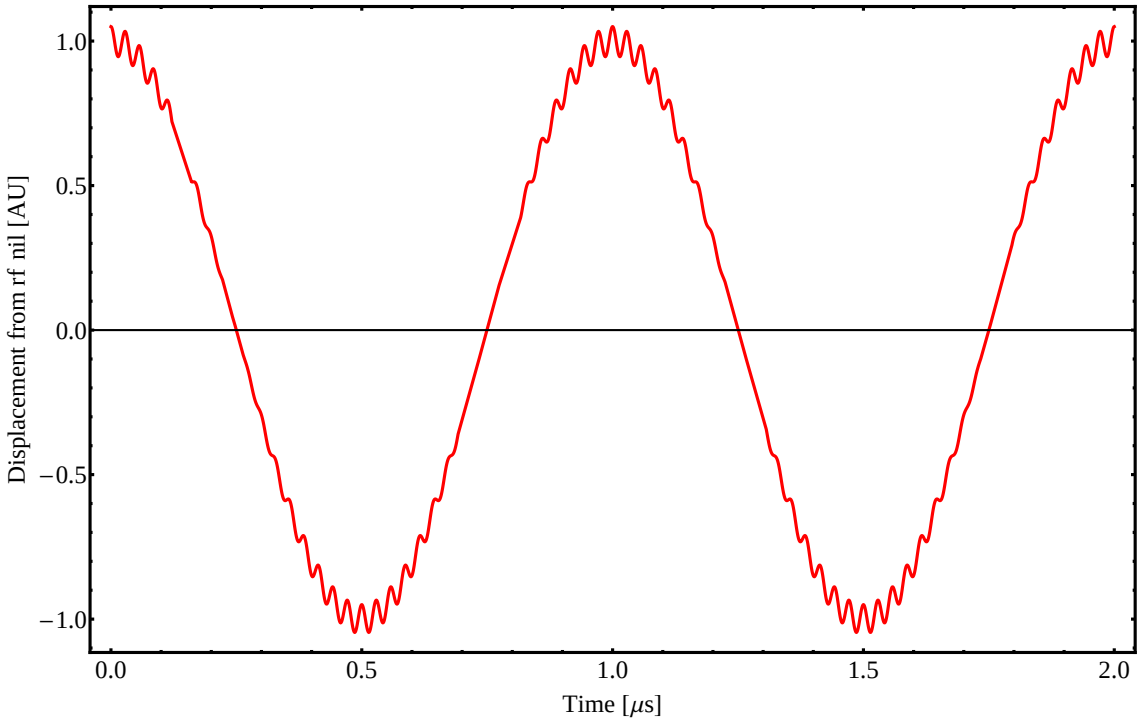

Figure 2.3: Motion of an ion trapped in a quadrupole field described using equation 2.14. The motion consists of large amplitude secular motion with a frequency of $\nu_x/2\pi = 1\,\mathrm{MHz}$ and small amplitude micromotion with a frequency of $\Omega_T/2\pi = 35\,\mathrm{MHz}$. The stability parameters are $a = 0$ and $q = 0.1$. Clearly visible is the position dependant amplitude of the micromotion which is proportional to the distance of the ion from the rf nil.

as much as possible.

We can therefore see that strings of ions trapped in a linear Paul trap will exhibit little micromotion in the uniform potential along the z-axis. This makes this type of trap an ideal tool for scalable quantum computing experiments. Such experiments can involve shuttling of ions [74] as well as the coherent interaction between many ions in a single potential well [31,52]. A linear Paul trap was therefore chosen to be used for the coherent manipulation experiments shown in this thesis.

2.1.3 Three-dimensional quadrupole trap

The conditions for the second case shown in equation 2.4, which consists only of oscillating components, can be met by using a three-dimensional (3D) quadrupole trap as pointed out by Wolfgang Paul [64]. An example of such a trap can be seen in figure 2.4. The

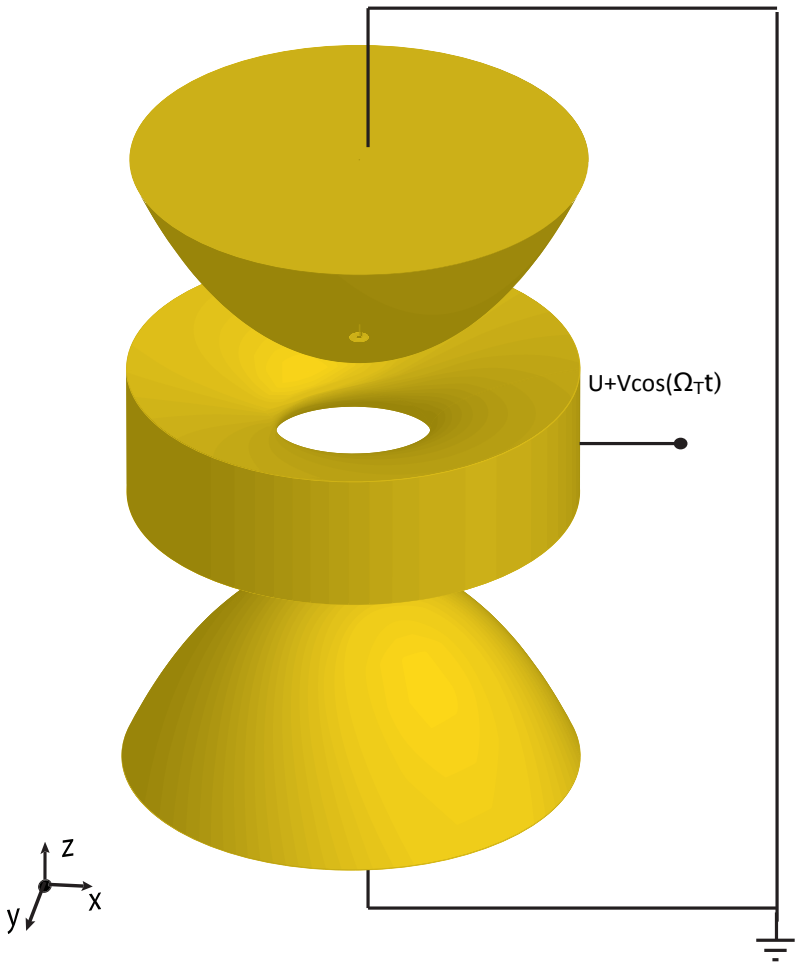

Figure 2.4: Schematic of a 3D quadrupole trap with one hyperbolic ring electrode and two hyperbolic endcap electrodes. The potential is created by applying a oscillating voltage on the ring while keeping the two endcaps at ground or vice versa.

trap consists of a hyperbolic ring electrode and two hyperbolic endcap electrodes. The oscillating voltage is either applied to the ring electrode with the endcaps held at ground or vice versa. If required, a static voltage can be applied along with the oscillating voltage. The total potential at any point in such a trap is given by [77]

$$\phi_c(x,y,z) = (U + V\cos(\Omega_T t))\left(\frac{x^2+y^2-2z^2}{r_0^2}\right) \tag{2.15}$$

where r_0 is the distance between the ion and the nearest electrode. The motion of an ion in this type of trap can be described using the same method used for the linear Paul trap. We then find that such a trap only provides one point where the potential from the oscillating voltage is minimum, making it ideal for experiments with one ion. A trap analogous to the trap shown here is used in the experiments shown in chapter 6.

2.2 Doppler cooling

Ions are generally formed and cooled using lasers. The common choice of laser cooling is Doppler cooling. In order to understand the principle of Doppler cooling we first consider an ion which, for simplicity, we approximate as a closed two-level system where the photon scattering rate from the excited level is given by [78]

$$\frac{dN}{dt} = \frac{s_0\gamma/2}{1+s_0+\left(\frac{2\Delta}{\gamma}\right)^2} \tag{2.16}$$

where γ is the natural linewidth of the transition, Δ is the detuning from resonance, and s_0 is the saturation parameter. The saturation parameter is given by [78]

$$s_0 \equiv \frac{2|\Omega|^2}{\gamma^2} = \frac{I}{I_s} \tag{2.17}$$

where Ω is the Rabi frequency and I is the intensity of the laser beam. I_s is the saturation intensity and is given by [78]

$$I_s \equiv \frac{\pi\gamma hc}{3\lambda^3} \tag{2.18}$$

where h is the Planck constant, c is the speed of light in vacuum and λ is the transition wavelength.

We now consider the motion of an ion in a potential. Due to the motion the applied laser beam will appear Doppler shifted to the ion. This instantaneous Doppler shift is given by $\Delta_D = \boldsymbol{k}\cdot\boldsymbol{\nu}$ where $\boldsymbol{k}$ is the wavevector of the beam and $\boldsymbol{\nu}$ is the velocity of the

ion. If in equation 2.16 we define $\Delta = \Delta_L + \Delta_D$ we can see that the scattering rate not only depends on the detuning of the laser field but also on the velocity of the ion. The consequence of this is that for a red detuned ($-\Delta_L$) laser beam, the highest probability of the ion absorbing one photon and obtaining a momentum kick of $-\hbar k$[1] corresponds to when the ion travels in the opposite direction to the laser beam (Δ_D is positive). The following emission event will impart a momentum kick of equal size to the ion, however, due to the isotropic nature of the spontaneous emission, the process of absorption and emission will impart a net force on the ion which is in the opposite direction to the laser beam. The trapping potential will provide a restoring force and ensure the ion remains trapped despite the net force on the ion. The overall cooling results from the red detuned laser beam which ensures that many more photons will be absorbed and scattered when the ion travels with high velocity in opposite direction to the propagation of the laser beam compared to when the ion travels with low velocity or in the same direction as the beam propagation. Ensuring that the red detuned laser beam has a component along all three axes of motion then allows the efficient cooling of the ion motion along all axes. However, Doppler cooling does not allow to cool to the absolute zero temperature. Instead, the momentum imparted onto the ion during each photon emission event limits the minimum achievable temperature using Doppler cooling and is given by [79]

$$k_B T = \frac{\hbar\gamma}{2} \tag{2.19}$$

where k_B is the Boltzmann constant.

For many experiments a lower temperature is required. A common method for further reducing the temperature of the ion as far as to the motional ground state is resolved sideband cooling which has been implemented using lasers [80,81] and microwave radiation [38].

2.3 The Ytterbium ion

Ytterbium (Yb) has seven naturally occurring stable isotopes which are shown in table 2.1 along with their nuclear spin and natural abundance and has been used in numerous different research fields. Many experiments, including most experiments shown here, only require the use of a single isotope. For this case an enriched sample can be obtained. The abundance of readily available enriched samples are also shown in table 2.1 for each stable

[1] Here, the minus sign indicates that the momentum kick is in the opposite direction to the motion of the ion.

Isotope	Nuclear Spin	Natural Abundance %	Enriched Abundance %
^{168}Yb	0	0.135	13-24
^{170}Yb	0	3.03	> 78
^{171}Yb	1/2	14.31	> 95
^{172}Yb	0	21.82	> 97
^{173}Yb	5/2	16.13	> 92
^{174}Yb	0	31.84	> 98
^{176}Yb	0	12.73	> 96

Table 2.1: Table showing naturally occurring stable Yb isotopes along with their nuclear spin and natural abundance. For experiments which require only one particular isotope a enriched Yb sample can be obtained. The commonly available abundance of such a sample for the different Yb isotopes is also shown [2].

isotope [2]. Of particular importance is $^{171}Yb^+$ due to its spin 1/2 nature for which a sample with a enriched abundance of $> 95\%$ can be obtained.

The use of Yb in the field of ion trap quantum computing has seen a rapid growth in recent years. This is in part due to the energy levels being easily addressable using commercially available lasers and the spin 1/2 nucleus of $^{171}Yb^+$ resulting in a hyperfine structure that can be used to define qubit states with a very long lifetime which are simple to prepare, manipulate and detect. Furthermore, Yb has been used in some very impressive experiments such as the creation of entanglement using lasers [82,83] as well as microwave radiation [36] demonstrating its high potential for future quantum computing experiments. Also, the main $^2S_{1/2} \leftrightarrow {}^2P_{1/2}$ cooling transition is driven by light near 369.5 nm for which optical fibres are readily available which is important for experiments that, for example, involve the transfer of quantum states between spatially separated systems [82]. For these reasons Yb was chosen for the experiments presented in this work.

2.3.1 Ionisation

Yb can be ionised to form Yb^+ ions by several different methods. The two most common are electron impact ionisation and photoionisation. While electron impact ionisation is the experimentally simpler method, it results in large amounts of charge build up on electrode surfaces, perturbing the trapping fields and leading to uncontrolled micromotion [84]. One of the most critical advantages of using photoionisation however is the possibility of performing isotope selective ionisation. Photoionisation is therefore chosen for ionising Yb in the experiments presented in this work.

Ionising Yb using photoionisation is possible using a combination of different lasers.

Isotope	$^1S_0 \leftrightarrow {}^1P_1$ wavelength [nm]
$^{170}Yb^+$	398.91051(6)
$^{171}Yb^+$	398.91070(6)
$^{172}Yb^+$	398.91083(6)
$^{174}Yb^+$	398.91114(6)
$^{176}Yb^+$	398.91144(6)

Table 2.2: Table showing the resonant wavelengths for the $^1S_0 \leftrightarrow {}^1P_1$ transition used to ionise various Yb isotopes [3].

The partial energy level diagram of neutral Yb in figure 2.5 illustrates some different possibilities. The first simply involves using one laser near 199 nm. Light at this wavelength however is extremely expensive to obtain and since the transition goes directly to the continuum it does not allow for isotope selective ionisation. The second method involves a two-stage ionisation process where laser light near 398.9 nm, resonant with the $^1S_0 \leftrightarrow {}^1P_1$ transition, is used in combination with laser light near 394 nm. While this does allow for isotope selective ionisation this process can be made more cost efficient by using the 398.9 nm light in combination with the already present 369.5 nm laser light required for Doppler cooling. The isotope selective 398.9 nm wavelengths used in the experiments are shown in table 2.2 and were taken from [3].

2.3.2 'Even' Yb isotopes

Following ionisation, Yb^+ ions are laser cooled using light resonant with the transitions shown in the gross energy level diagram in figure 2.6. The gross energy level diagram is universal for all stable Yb isotopes, the only difference being the isotope dependant transition wavelengths and the presence of the hyperfine structure for the isotopes with a non-zero nuclear spin. The strong $^2S_{1/2} \leftrightarrow {}^2P_{1/2}$ dipole transition with a linewidth of $\gamma/2\pi = 19.6$ MHz is used for Doppler cooling and fluorescence detection. This is not a closed cycle as the ion will decay to the $^2D_{3/2}$ state rather than the $^2S_{1/2}$ state with a probability of 0.5%. To depopulate this state, light near 935 nm resonant with the $^2D_{3/2} \leftrightarrow {}^3[3/2]_{1/2}$ dipole transition is used. From the $^3[3/2]_{1/2}$ state the population can then decay back to the $^2S_{1/2}$ state forming a closed cooling cycle. It is also possible for the ion to reach the $^2F_{7/2}$ state as a result of inelastic collisions with background gas when the ion is in $^2D_{3/2}$ causing a transition to $^2D_{5/2}$, followed by decay to the $^2F_{7/2}$ state. For our vacuum pressure of $\approx 10^{-12}$ Torr this process occurs once every few hours. In order

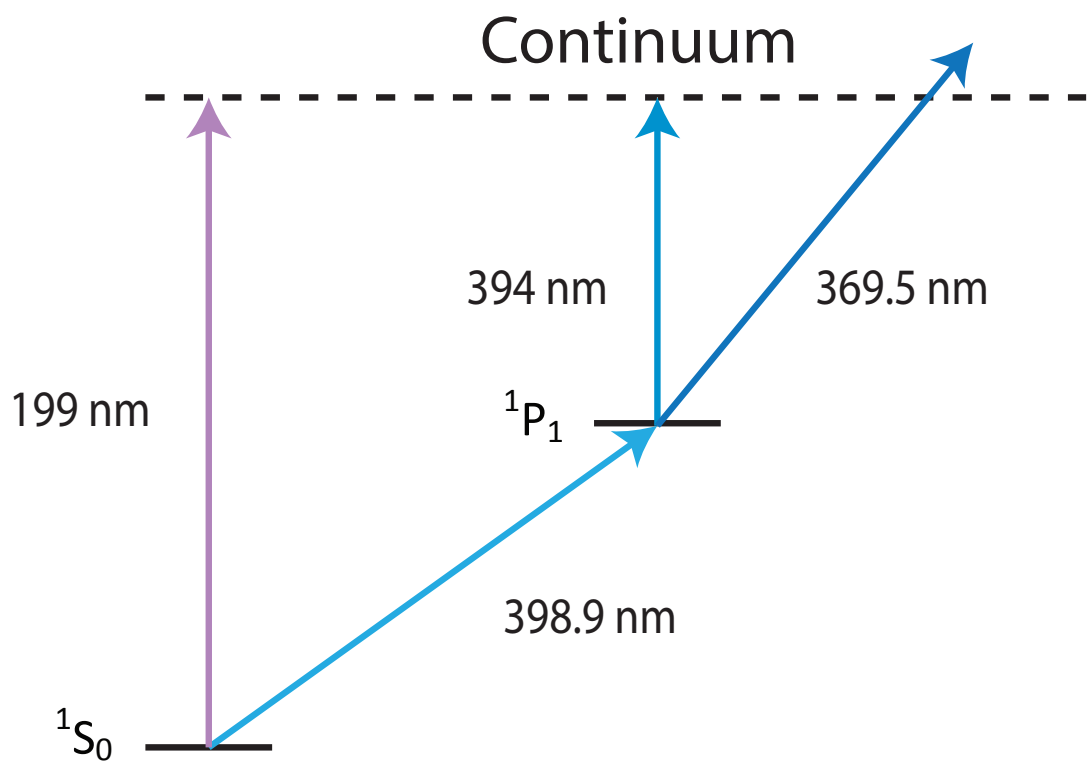

Figure 2.5: Partial energy level diagram of neutral Yb illustrating three methods of photoionisation.

to depopulate the F-state light near 638 nm resonant with the $^2F_{7/2} \leftrightarrow {}^1[5/2]_{5/2}$ dipole transition is used. From the $^1[5/2]_{5/2}$ state the population then decays to the $^2D_{3/2}$ state and thereby returning population back into the cooling cycle.

2.3.3 $^{171}Yb^+$

$^{171}Yb^+$ possesses a nuclear spin of one-half which results in a hyperfine doublet structure shown in figure 2.7. The hyperfine structure of the $^2S_{1/2}$ level is ideal for the use as a qubit in quantum computing experiments where the qubit is formed of the $^2S_{1/2}|F=0\rangle$ state and one of the $^2S_{1/2}|F=1\rangle$ Zeeman states. This is due to the extremely long lifetimes and the possibility of efficiently preparing and detecting each qubit state.

While light near 369 nm and 935 nm can be used to drive the $^2S_{1/2}|F=1\rangle \leftrightarrow {}^2P_{1/2}|F=0\rangle$ and $^2D_{3/2}|F=1\rangle \leftrightarrow {}^3[3/2]_{1/2}|F=0\rangle$ transition respectively the hyperfine structure requires additional transitions to be driven. Due to off-resonant coupling between the $^2P_{1/2}|F=0\rangle$ and $^2P_{1/2}|F=1\rangle$ states population can decay into the $^2S_{1/2}|F=0\rangle$ state. Light which is 14.7 GHz detuned can be used to drive the $^2S_{1/2}|F=0\rangle \leftrightarrow {}^2P_{1/2}|F=1\rangle$ transition. An alternative method is using microwave radiation near 12.6 GHz to couple

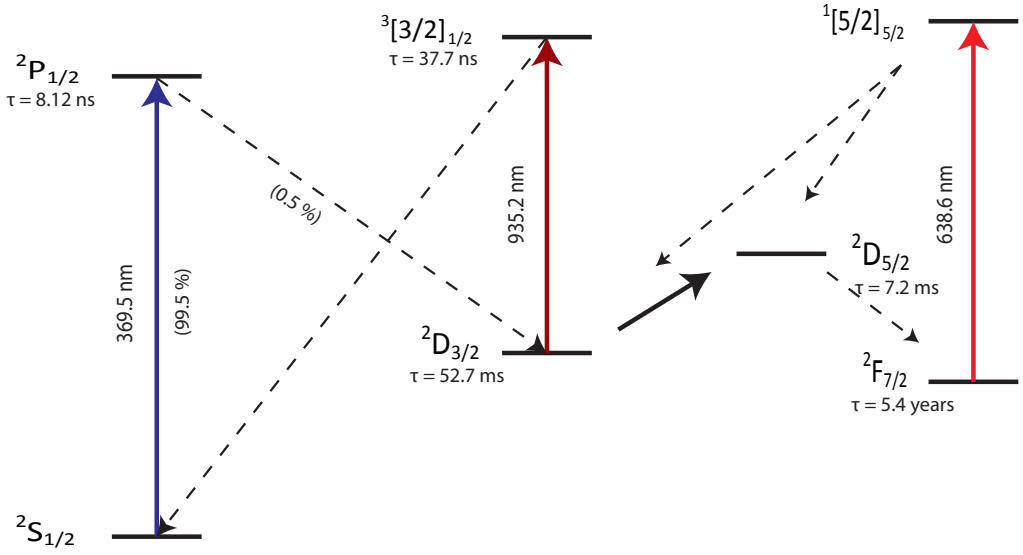

Figure 2.6: Gross energy level diagram of Yb^+ ions showing the required transitions to be driven for Doppler cooling and repumping (solid lines). Also shown are the decay channels (dashed lines). The transition near 369 nm which has a natural linewidth of $\gamma/2\pi = 19.6$ MHz is used for Doppler cooling. Population decayed into the $^2D_{3/2}$ state is transferred back to the $^2S_{1/2}$ ground state via the $^3[3/2]_{1/2}$ state using light near 935 nm. Population trapped in the $^2F_{7/2}$ state due to inelastic background collisions is transferred back to the main cooling cycle via the $^1[5/2]_{5/2}$ state using light near 638 nm. The lifetimes and branching ratios are from [6].

$^2S_{1/2}|F=0\rangle \leftrightarrow {}^2S_{1/2}|F=1\rangle$. From the $^2P_{1/2}|F=1\rangle$ state, population can also decay to the $^2D_{3/2}|F=2\rangle$ state. This requires additional light near 935 nm to be used to drive the $^2D_{3/2}|F=2\rangle \leftrightarrow {}^3[3/2]_{1/2}|F=1\rangle$ transition. To depopulate the $^2F_{7/2}$ hyperfine manifold light at 638.610 nm and 638.616 nm is used. A description of how light at the required transition wavelengths are created in our laboratory can be found in chapter 3. The pro-

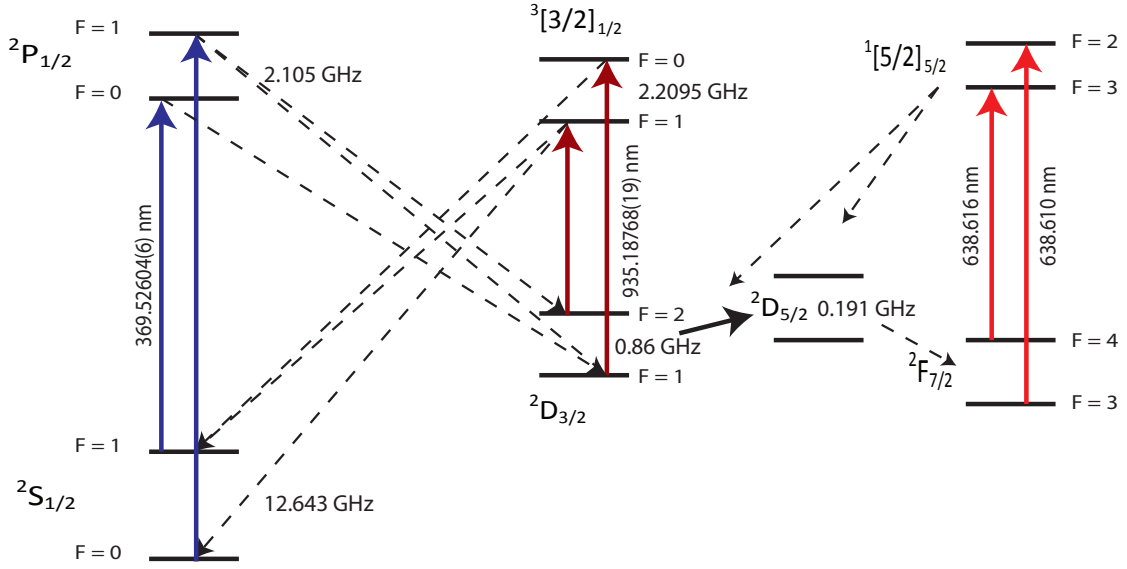

Figure 2.7: Energy level diagram of $^{171}Yb^+$. The nuclear spin of one-half results in a doublet hyperfine structure which requires additional transitions to be driven. Transitions required to be driven by lasers (solid lines) as well as the decay channels (dashed lines) are shown.

cess of state preparation and detection is described in chapter 4. Furthermore, the qubit can be formed of magnetic field insensitive as well as magnetic field sensitive states depending on the experimental requirements which allows various different methods to be used for the implementation of gate operations. This will also be discussed in more detail in chapter 4.

Chapter 3

Experimental setup and initial experiments

Performing experiments with ions is a challenging yet exciting task and requires a sophisticated experimental setup. This includes an ion trap to confine the ion(s) in space, placed inside a ultra-high vacuum (UHV) system to prevent collisions between the ions and residual gas. It also includes many optical components in conjunction with laser systems and frequency stabilisation setups to cool and manipulate the ions. Furthermore, a setup to provide stable and clean trapping fields and a very sensitive imaging setup to detect photons being scattered from the ions is required. This chapter will briefly outline the core experimental setup used for a large proportion of the work presented in this thesis followed by a characterisation of the ion trap which includes a heating rate measurement. The extension to the setup described here which is required for a new vacuum system is described in chapter 6 where that particular experiment is described in more detail. The work presented in this chapter builds on the fantastic work of previous PhD students and references to their theses will be made when more detailed information about the setup is required and available in their work.

3.1 Optical setup

The ionisation, cooling and manipulation of Yb^+ ions requires laser light of several different wavelengths to be generated and manipulated before being directed into the ion trap. For the work presented in this thesis laser light is required for ionisation and cooling as well as for state preparation and detection of ions. As shown in chapter 2 laser light near 369 nm, 399 nm, 638 nm and 935 nm is required for trapping and cooling of the various different

Yb isotopes. The optical setup used to achieve this is shown in figure 3.1.

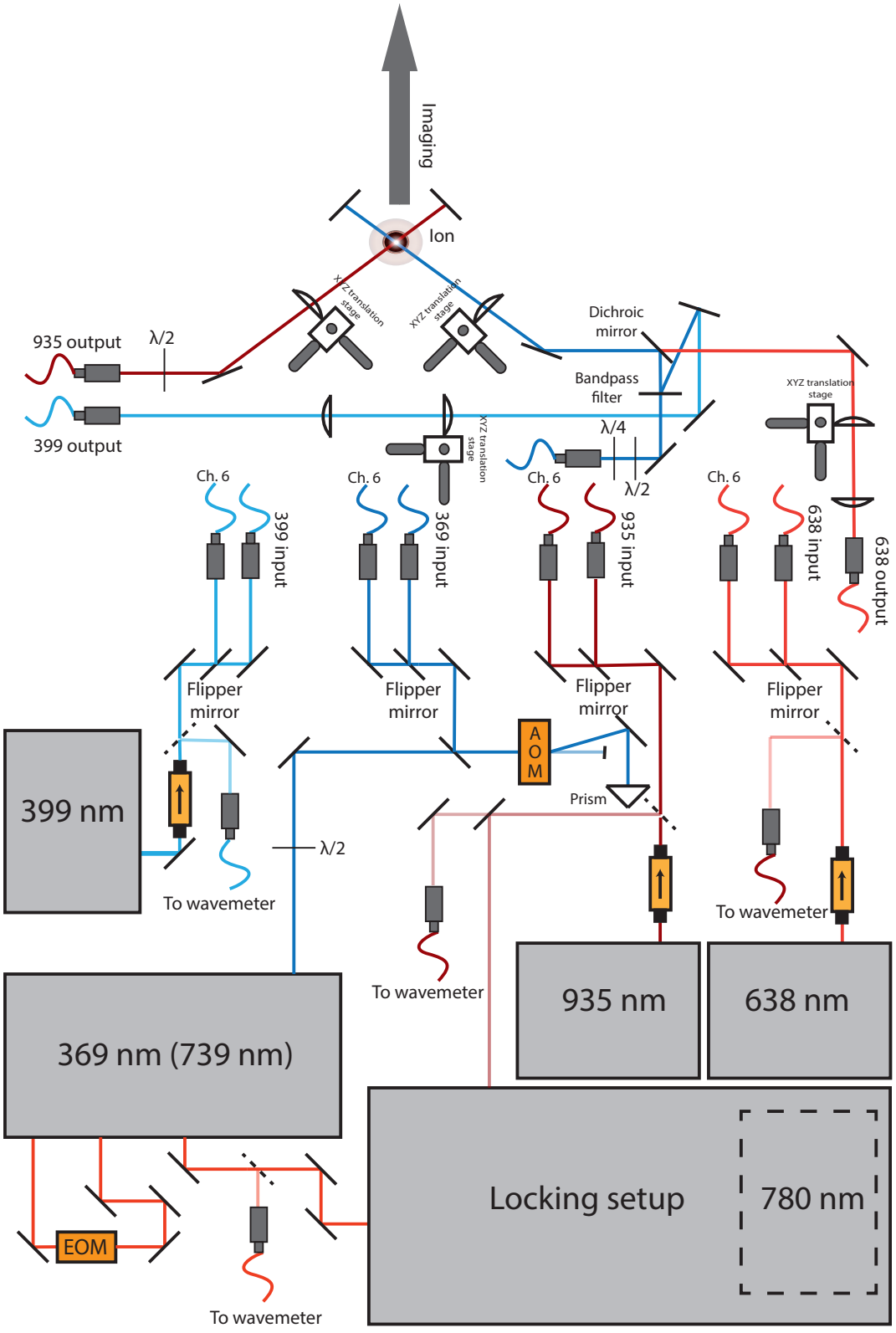

Figure 3.1: Diagram of the optical setup used to cool as well as state prepare and detect Yb^+ ions. Flipper mirrors are used to direct the laser light into fibres which either guide the light to the optical setup used for the trap shown in this chapter or to a different optical setup used for a trap which will be discussed in chapter 6.

3.1.1 Lasers

All lasers shown in figure 3.1, apart from the 369 nm system, are homebuilt external cavity diode laser (ECDL) systems. The 369 nm system is a commercially obtained frequency doubled system. All lasers can be locked to a stable reference laser at 780 nm via transfer cavities which itself is locked to an atomic transition within Rubidium (Rb).

The ECDLs use the Littrow configuration for their feedback grating [85, 86]. In this configuration the first order diffracted narrow linewidth beam from the grating is reflected back into the laser diode to stimulate emission. The zeroth-order beam is then used in the experiment. Since the diffraction grating splits the laser light up into its different spectral components, simply changing the angle of the diffraction grating will change the wavelength of the light reflected back into the diode and therefore change the wavelength the laser outputs at. Changing the angle of the diffraction grating also changes the angle of the zeroth-order and hence the output angle of the laser beam for the experiments. Given the small tuning ranges that are required, this was not found to be a problem during our experiments. If this was found to be a problem, a Littman-Metcalf configuration [87] for the ECDLs should be chosen. Larger changes in wavelength can be obtained by changing the band gap energy within the diode. This can be achieved by changing the temperature of the diode as well as by changing the current. A picture of a typical ECDL used in our setup can be seen in figure 3.2. A detailed description with all design parameters of the homebuilt laser systems used in our experiments can be found in the thesis of Dr. James McLoughlin [77].

399 nm photoionisation laser

For ionisation of Yb isotopes, light near 399 nm is required and is obtained using a homebuilt ECDL system. The Sanyo laser diode[1] output is collimated with a Thorlabs aspheric lens[2]. The diffraction grating used to form the external cavity is also a Thorlabs part[3]. The laser has an output power of $\approx 4\,\mathrm{mW}$.

369 nm Doppler cooling Laser

Laser light near 369 nm required for Doppler cooling on the $^2S_{1/2} \leftrightarrow {}^2P_{1/2}$ transition in Yb is obtained by using a frequency doubled system[4]. Here, light at 739 nm is first amplified

[1] Part number: DL-4146-301S
[2] Thorlabs. Part number: C330TM-B
[3] Thorlbas. Part number: GH13-1210
[4] Toptica Photonics. Part number: TA-SHG 36

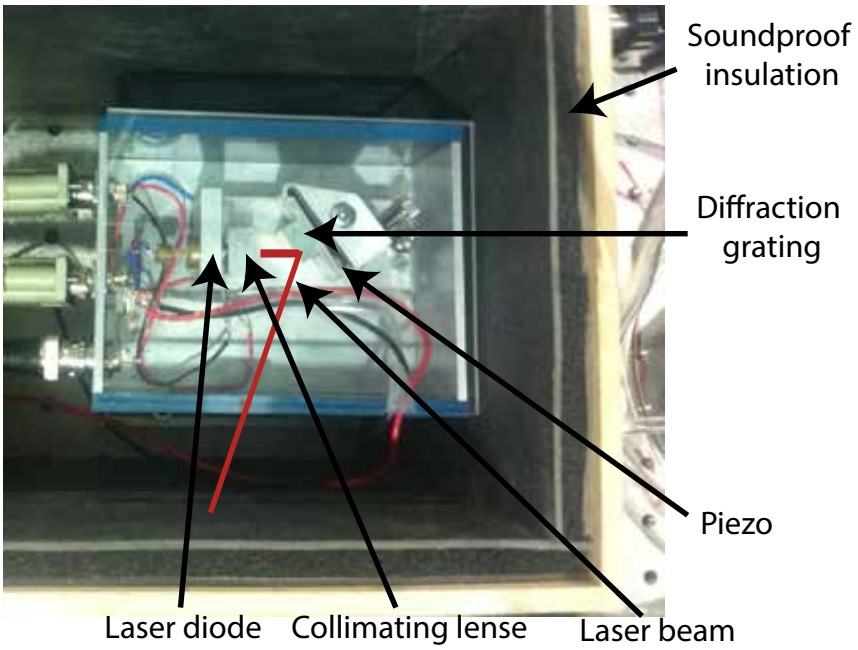

Figure 3.2: Picture of a typical ECDL setup used in the experiment.

to a power of ≈ 350 mW using a tapered amplifier before a bow-tie cavity with a Lithium Triborate (LBO) crystal is used for second-harmonic generation to obtain a wavelength of 369 nm with an output power of up to 60 mW. When $^{171}Yb^{+}$ is used, the laser is tuned to the $^2S_{1/2}|F=1\rangle \leftrightarrow {}^2P_{1/2}|F=0\rangle$ transition, as that particular transition is the main one used for laser cooling. Due to off-resonant coupling, population can get trapped in $^2S_{1/2}|F=0\rangle$. To depopulate this state the 739 nm light can be modulated at 7.35 GHz using a bulk phase electro optic modulator (EOM)[5]. Once frequency doubled, the resultant positive sideband at 14.7 GHz can then be used to drive the $^2S_{1/2}|F=0\rangle \leftrightarrow {}^2P_{1/2}|F=1\rangle$ transition. In order to drive $^2S_{1/2}|F=1\rangle \leftrightarrow {}^2P_{1/2}|F=1\rangle$ for state preparation the current of the 739 nm diode is modulated at a frequency of 1.05 GHz. This results in sidebands at 2.1 GHz after frequency doubling.

935 nm repump laser

To repump any population trapped in the $^2D_{3/2}$ manifold back to the main 369 nm cooling cycle, light near 935 nm is required. This is achieved using another homebuilt ECDL system comprising of a 935 nm diode from Roithner[6] and a aspheric lens[7] and diffraction grating[8] from Thorlabs. This setup results in a maximum output power of ≈ 20 mW. While the available power can be used to power broaden the transition enough to bridge

[5] New Focus. Part number: 4851
[6] Part number: RLT940-100GS
[7] Thorlabs. Part number: C330TM-B
[8] Thorlabs. Part number: GH13-1210

the hyperfine splitting of the $^2D_{3/2}$ and $^3[3/2]_{1/2}$ manifold which is useful for trapping and cooling the ion, state preparation and detection requires the possibility of driving $^2D_{3/2}|F=2\rangle \leftrightarrow {}^3[3/2]_{1/2}|F=1\rangle$ or $^2D_{3/2}|F=1\rangle \leftrightarrow {}^3[3/2]_{1/2}|F=0\rangle$ respectively. The laser power is therefore reduced and the wavelength is tuned on resonance with $^2D_{3/2}|F=1\rangle \leftrightarrow {}^3[3/2]_{1/2}|F=0\rangle$. For state preparation the laser current is modulated at a frequency of 3.1 GHz using a bias-tee and the resultant negative first-order sideband is used to drive $^2D_{3/2}|F=2\rangle \leftrightarrow {}^3[3/2]_{1/2}|F=1\rangle$.

638 nm repump laser

Following a background collision, population can get trapped in the $^2F_{7/2}$ manifold which we have observed to occur no more than once every couple of hours. To depopulate this state by coupling $^2F_{7/2} \leftrightarrow {}^1[5/2]_{5/2}$ we use a homebuilt ECDL system comprising of a 638 nm diode from Sanyo[9] and a aspheric lens[10] and diffraction grating[11] from Thorlabs. This setup produces a stable output power of ≈15 mW. In order to bridge the hyperfine splitting in $^{171}Yb^+$ the laser wavelength is scanned using a 10 Hz modulation which is applied to the current and piezo control box.

3.1.2 Laser stabilisation

Cooling as well as state preparation and detection requires lasers with a narrow linewidth which are stable in wavelength over the course of an experiment which can take several hours. Using the ECDL design described above already significantly stabilises the linewidth of the laser to ≤ 1 MHz [85]. However, the output wavelength from a laser is very sensitive to drifts in temperature and current and is also affected by acoustic noise. Effects from acoustic noise are minimised by placing the homebuilt laser systems inside a wooden box which is heavily insulated with soundproof material[12].

Further frequency stabilising the 369 nm and 935 nm lasers used for cooling as well as state preparation and detection requires a very stable reference such as an atomic transition. Unfortunately there are no suitable elements which have a frequency splitting corresponding to the laser frequencies used to cool Yb^+ ions. The element with a transition closest to the 739 nm light used to obtain 369 nm light is rubidium (Rb). In our experimental setup we therefore use a separate 780 nm laser which is locked to the D_2 transition line of ^{87}Rb and then use cavities to transfer the stability of the 780 nm laser to

[9] Part Number: DL-6148-030
[10] Thorlabs. Part number: A390TM-B
[11] Thorlabs. Part Number: GH13-24v
[12] Noise Stop Systems Ltd. Part number: NSSF7 Floor system 1 mm

the other lasers. An overview of the locking setup will be given here however more details can be found in the thesis of Dr. Robin Sterling [88]

The 780 nm laser is set up in a ECDL configuration and consists of a Sharp 784 nm diode[13] with an output power of 120 mW and a diffraction grating[14] and collimating lens[15] from Thorlabs. The wavelength can be pulled down to 780 nm using appropriate current and temperature settings. In this configuration the typical output power is ≈ 80 mW.

The 780 nm laser is locked to the D_2 transition line of ^{87}Rb. Since the Doppler-broadened transition has a linewidth of ≈ 500 MHz, a Doppler-free method is used. The 780 nm beam is separated into two beams called the pump and the probe beam. The two beams are passed into a Rb vapour cell so that they are counter-propagating and overlapped. The intensity of each beam after having passed through the vapour cell is monitored on a photodiode. Due to the counter-propagating nature of the beams, they will each saturate Rb atoms with opposite velocity. When on resonance, the zero-velocity atoms will be saturated however this will be dominated by the pump beam which has a higher power of ≈ 1.4 mW. This results in the probe beam with a power of 0.15 mW to saturate less atoms compared to the off-resonance case. Subtracting these two signals results in a Doppler-free background and allows individual hyperfine transitions to be resolved. The laser diode is current modulated at 100 kHz and a lock-in amplifier is then used to obtain an error signal. The lock-in amplifier multiplies the signal from the photodiode with the same 100 kHz signal used for the modulation which acts as a bandpass filter. It then differentiates the resultant signal as to provide a means of determining which side of the resonant peak the signal corresponds to. This differentiated output is then sent to a proportional integration (PI) controller which provides the feedback signal to the 780 nm piezo control box.

The stability of the 780 nm laser is transferred to the cooling and repumper lasers using transfer cavities. The cavities are Fabry-Pérot confocal cavities which each consist of two mirrors. A high reflectivity coating has been applied to the mirrors corresponding to the wavelengths used. The 935 nm laser is stabilised using a scanning cavity arrangement. The beam is overlapped with the 780 nm beam using a polarising beam splitter (PBS) and sent into the cavity. A second PBS is used to separate the two beams coming out of the cavity which are then sent to individual photodiodes. The two photodiode signals are captured by a Data Aquisition (DAQ) card and analysed using a LabVIEW program[16]. By applying

[13] Thorlabs. Part number:GH0781JA2C
[14] Thorlabs. Part number: GH13-18V
[15] Thorlabs. Part number: C150TM-B
[16] The LabVIEW program is explained in the thesis of Dr. James Siverns [89]

a 70 Hz oscillating voltage to a ring piezo attached to one of the cavity mirrors the length of the cavity is varied; transmission peaks corresponding to the 780 nm and 935 nm laser beams are then obtained. A LabVIEW program monitors the separation between the 780 nm and 935 nm peaks and keeps it constant using a proportional, integration and differential (PID) code to produce a feedback signal which is sent to the 935 nm piezo control box.

Locking the 935 nm laser via a transfer cavity which is controlled through LabVIEW is inherently slow and only has an update rate of around 10 Hz. This is sufficient for the repumper, however a faster lock is desirable for the main cooling laser and can be achieved by using a dual-resonance lock.

For the dual-resonance lock, the 780 nm and 739 nm laser beams are both passed through a second Fabry-P*é*rot confocal cavity and the output is aligned onto individual photodiodes using the same method as described above. Instead of scanning the cavity, simultaneous resonant transmission of both laser beams through the cavity is achieved by first aligning the 780 nm beam through a AOM in double-pass configuration. The AOM shifts the frequency of the laser beam corresponding to the applied frequency and the double-pass configuration removes the frequency dependence of the spatial beam output. The frequency used to drive the AOM is then used to tune the frequency of the 780 nm laser beam into resonance with the cavity. The cavity length is then locked to the 780 nm beam using a homebuilt PID controller. A side-of-fringe lock is used to lock the 739 nm beam to the cavity using another homebuilt PID controller. A side-of-fringe lock was chosen as applying a modulation with sufficient depth to the 739 nm diode would have been unnecessarily challenging. Since this setup does not require any slow scanning of the cavity and time consuming computation through LabVIEW, the update rate of the locking feedback signal is increased to ≈ 1 kHz which is sufficient for the upcoming experiments.

3.2 Imaging the ion

Photons near 369 nm from the main cooling transition are collected from the ion using a imaging system. In order to achieve high state detection fidelities it is important for the imaging system to have a high collection efficiency, while minimising collection of ambient light and 369 nm light scattered from the electrodes. There are two possible destinations for the collected light. The first is a electron multiplication charge coupled device (EMCCD) which we currently use during beam alignment and initial trapping of the ion but will also be used for multi-ion state detection in future experiments. The second destination

is a photon multiplier tube (PMT). We currently use this device for all experiments that require analysis of the number of photons collected such as state detection. A simple way of switching between these two detection devices is therefore needed.

The imaging system was designed with the possibility of having a second vacuum system sharing the same EMCCD and PMT in mind. This second vacuum system was indeed installed a couple of years later for experiments described in chapter 6. The imaging setup for those experiments is therefore presented there to make it easier for the reader to get an overview of the setup used to perform these experiments. The imaging system presented here was used for all other experiments presented in this work.

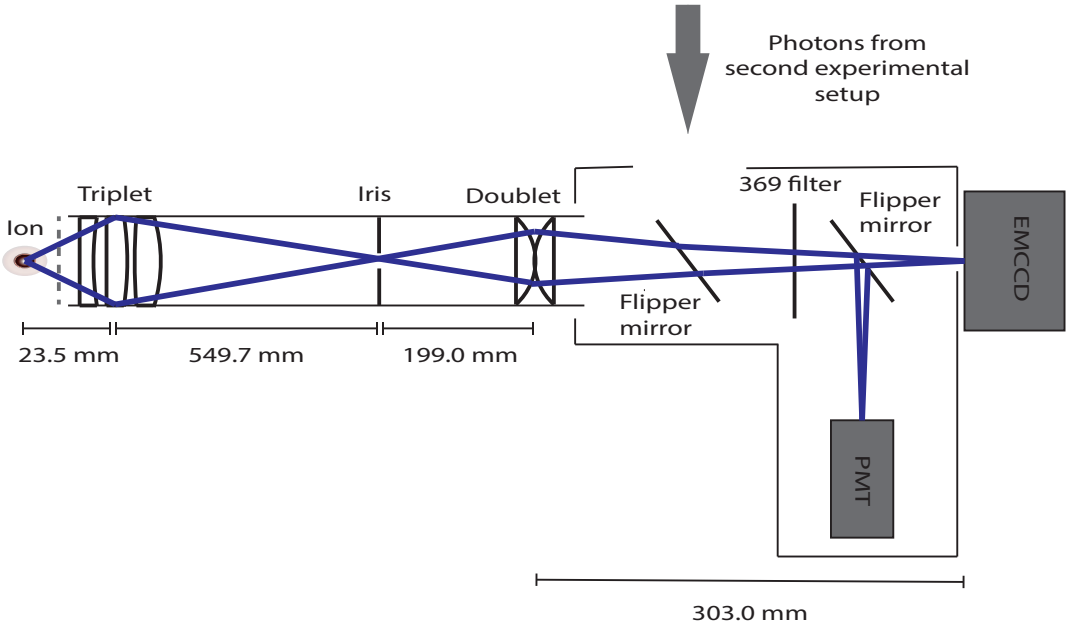

Figure 3.3: Not to scale illustration of the imaging setup used to collect photons near 369 nm from the ion. A triplet is used to initially collect the photons followed by a doublet defining the final magnification. Motorised flipper mirrors are used to switch between two experiments as well as between the EMCCD and PMT.

A schematic of the imaging system designed by Dr. James Siverns[17] can be seen in figure 3.3. The majority of the magnification is provided by a triplet lens positioned 23.5 mm from the ion. The triplet has a magnification of $M_T = -23.4$ and produces an image 549.7 mm behind the triplet. A iris can be used at the image position to block any unwanted scatter from the electrodes. A doublet consisting of a $f_1 = 200$ mm lens and a $f_2 = 300$ mm lens which when positioned at a distance of 199 mm and 303 mm from the image and object position respectively results in a doublet magnification of $M_D = -1.5$. The total magnification given by $M_{TOT} = M_T M_D$ is then 35.1. This results in an area

[17] A detailed description can be found in his thesis [89]

of 300 μm by 300 μm to be imaged using the EMCCD array. After the doublet, a filter ensures only 369 nm light makes it to the detection device. A motorised flipper mirror is then used to either direct the photons to the EMCCD array[18] or the PMT[19]. The collection efficiency of this setup is measured by comparing the expected scatter rate of the ion to the number of photons detected on the PMT. For this setup the collection efficiency is $\approx 0.1\%$.

3.3 Vacuum system

For ions to be trapped with a sufficiently long lifetime it is required to place the ion trap in a ultra-high vacuum (UHV) environment where pressures are on the order of 10^{-12} Torr. Such pressures can be achieved using a sophisticated vacuum system.

To be useful for the experiments performed in our research group the vacuum system has to fulfil some important design criteria. It is important the vacuum system is able to house symmetric as well as asymmetric traps. With this comes the requirement of allowing laser access from various angles and also ensuring that the beams are able to exit the chamber to minimise unwanted photon scattering. Furthermore, some of the traps used have many static voltage electrodes. The vacuum system therefore needs to allow at least 90 dc connections to be made between the trap and the outside environment.

The first generation vacuum system designed to address the above criteria was used in the experiments shown in chapter 4 and 5 and will be described here[20]. A different vacuum system was used for the experiments shown in chapter 6 and will be described as part of that chapter. The completely assembled first generation vacuum system can be seen in figure 3.4. To provide sufficient space and optical axis for symmetric and asymmetric traps the main chamber consists of a hemisphere[21] and a octagon[22]. The chamber is connected to the rest of the vacuum system positioned at the correct height above the optical table using a custom T-piece. The achievable laser access is shown in figure 3.5. The four 1.33" viewports used for optical access are made of UV-grade fused quartz silica and have a anti-reflection (AI) coating for the wavelengths used (369 nm, 399 nm, 638 nm and 935 nm). A custom recessed UV-grade fused quartz silica viewport used for photon collection from the ion has a AI coating for 369 nm only. The ion trap is mounted inside the chamber using

[18] Andor. Part number: iXon 885
[19] Hamamatsu. Part number: H8259-01
[20] For a more detailed description including all design parameters the thesis from Dr. Altaf Nizamani should be referred to [90]
[21] Kimball Physics. Part Number: MCF450-MH10204/8-A
[22] Kimball Physics. Part Number: MCF450-SO20008-C

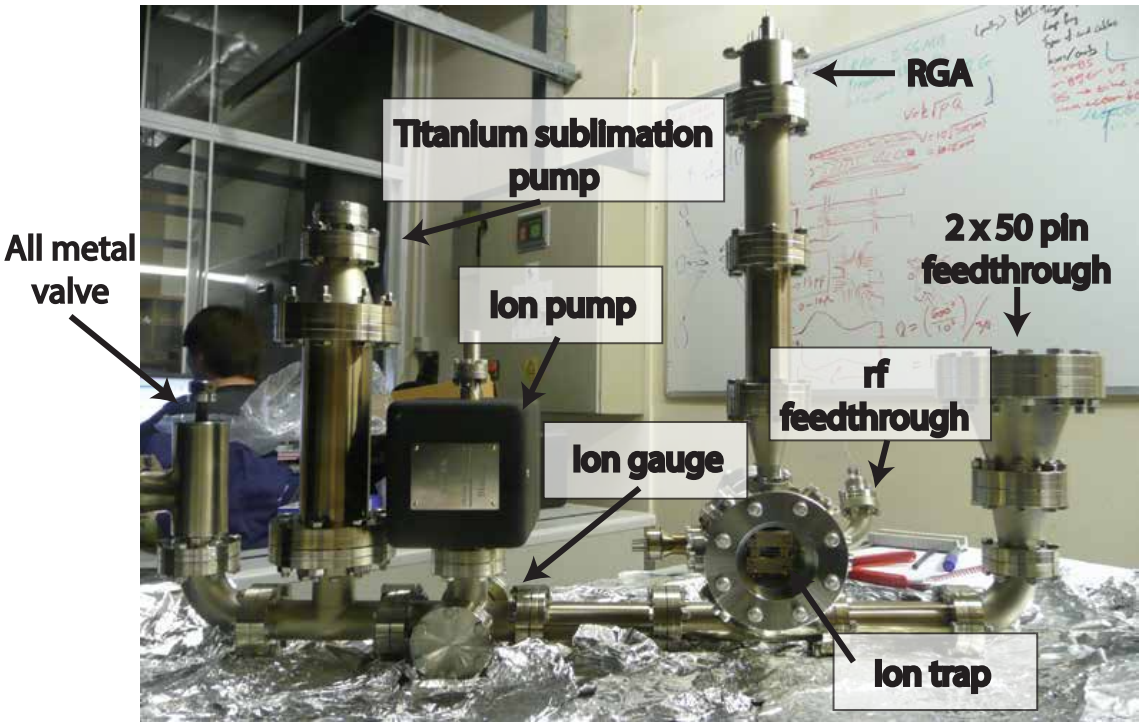

Figure 3.4: Picture of the vacuum system used to trap Yb ions.

a mounting bracket shown in figure 3.5. This bracket is attached to the chamber using special groove grabbers[23] and consists of 90 gold-plated receptacles held in place between two PEEK plates. The arrangement of the receptacles has been designed to hold a 101-pin CPGA chip carrier[24]. Electrical connection between the receptacles and the outside is made via kapton wires which connect to two 50 pin D-sub feedthrough connectors.

The atomic ovens which provide a flux of neutral Yb to the trapping centre are also part of the mounting bracket. This ensures good alignment with the trapping centre. The ovens are made of a stainless steel tube which is spot welded to copper wire using constantan (copper-nickel alloy) foil. The spot weld provides sufficient resistance to resistively heat the ovens when a current is applied. The oven setup consists of two ovens for symmetric and two ovens for asymmetric traps. Each pair of ovens consists of one filled with natural Yb and one filled with 95% enriched ^{171}Yb. The reason for having natural and enriched ovens has to do with the experimental overhead involved in trapping $^{171}Yb^{+}$. For initial trapping and calibration it is advantages to choose the natural oven to trap $^{174}Yb^{+}$. If an experiment requires $^{171}Yb^{+}$ ions then the enriched ovens can be used to reduce the probability of trapping unwanted isotopes.

To obtain and maintain a low pressure, an ion pump[25] and a titanium sublimation

[23] Kimball Physics. Part number: MCF450-GG-CT02-A
[24] Global Chip Material. Part Number: PGA10047002
[25] Varian StarCell. Part Number: 9191145

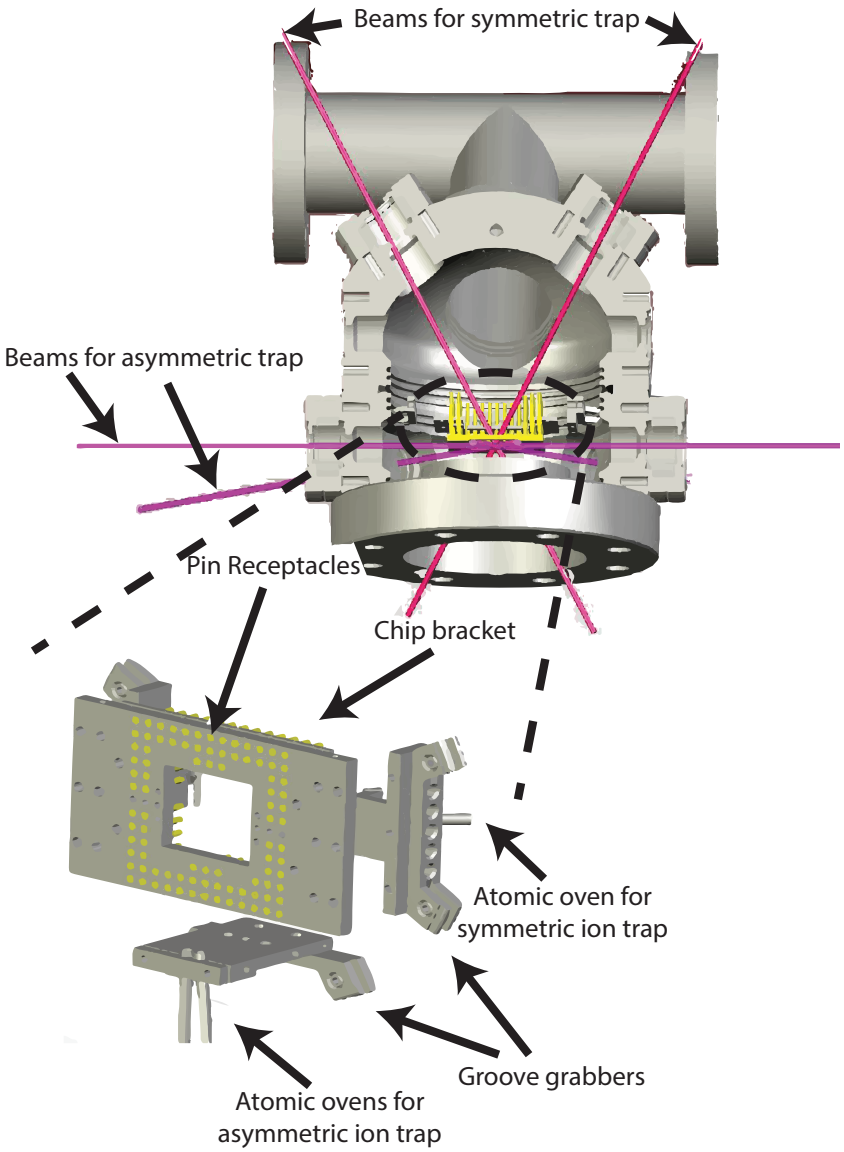

Figure 3.5: Drawing of the chamber which holds the ion trap. Laser access for symmetric as well as asymmetric traps is shown. Also shown is the chip bracket which sits inside the chamber. The chip bracket holds the ion trap in place and provides electrical connection to kapton wires via pin receptacles. Neutral Yb is supplied to the trapping region using atomic ovens.

pump[26] (TSP) is used. The ion pump is continuously running however the TSP is only used for a couple of days after baking the system to obtain a operating pressure of $\approx 10^{-12}$ Torr. The pressure is measured using a ion gauge[27]. A residual gas analyser[28] (RGA) is also part of the system and is a useful tool to obtain information about contaminants in the system during leak testing.

Using this setup a pressure of 10^{-12} Torr has been reached and maintained for several years.

3.4 Macroscopic linear Paul trap

The linear Paul trap outlined in this section was designed by Dr. Robin Sterling [88] and was the first ion trap to be used in the group. It was therefore designed with the aim to make the challenging initial trapping process as simple as possible. This includes ensuring a sufficiently large ion-electrode distance to minimise 369 nm scatter off the electrodes, minimise heating of the ion and ensure a trap depth of $\geq$1 eV. An illustration of the two layer symmetric trap is shown in figure 3.6. The trap electrodes are made out of stainless steel and have a 5 μm thick gold coating to improve the surface smoothness. The static voltage electrodes are segmented, with the four outer electrodes providing confinement along the axial direction. The two centre electrodes allow for rotation of the principal axis and cover a length of $\approx$ 1 mm along the z-axis however in the experiment they are generally used for micromotion compensation. Radial confinement is provided by the two rf electrodes. In order to be able to fully compensate for stray electric fields, which cause excess micromotion, three cylindrical gold coated compensation rods are used. Two of these rods are connected together. The static voltage electrodes are isolated from each other via PEEK spacers which also help align each electrode during the assembling process. Electrical isolation from the vacuum system is achieved by using a PEEK base which the trap is mounted onto. The assembled trap is shown in figure 3.7. Assembling this trap was not easy and resulted in non-optimal electrode positions and electrode 1 shorting to ground. Using the imaging system the position of each electrode was measured after the assembly and the potentially disruptive process of baking the vacuum system. The rf and static voltage electrodes were found to be separated by 554$\pm$14 μm in the y-direction and 343$\pm$14 μm in the x-direction. This results in a ion-electrode distance of 325$\pm$10 μm.

[26] Varian. Part number: 9160050
[27] Varian. Part number: 9715015
[28] ExTorr. Part number: XT200M

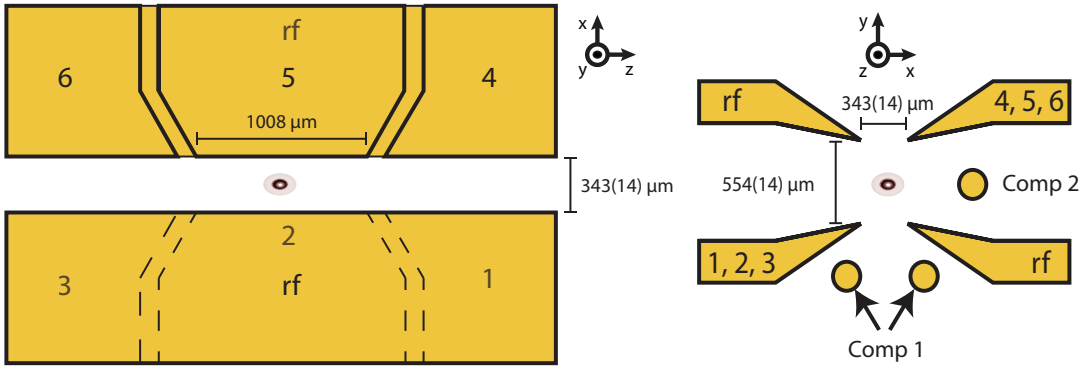

Figure 3.6: Schematic of the two layer symmetric linear Paul trap. Each layer comprises of three segmented static voltage electrodes and one rf voltage electrode. Static voltage electrodes 1, 3, 4 and 6 provide confinement in the axial direction. Static voltage electrodes 2 and 5 allow for rotation of the principal axis. Confinement in the radial direction is provided by the two rf electrodes. Three compensation rods of which two are connected together provide further flexibility when compensating for stray fields.

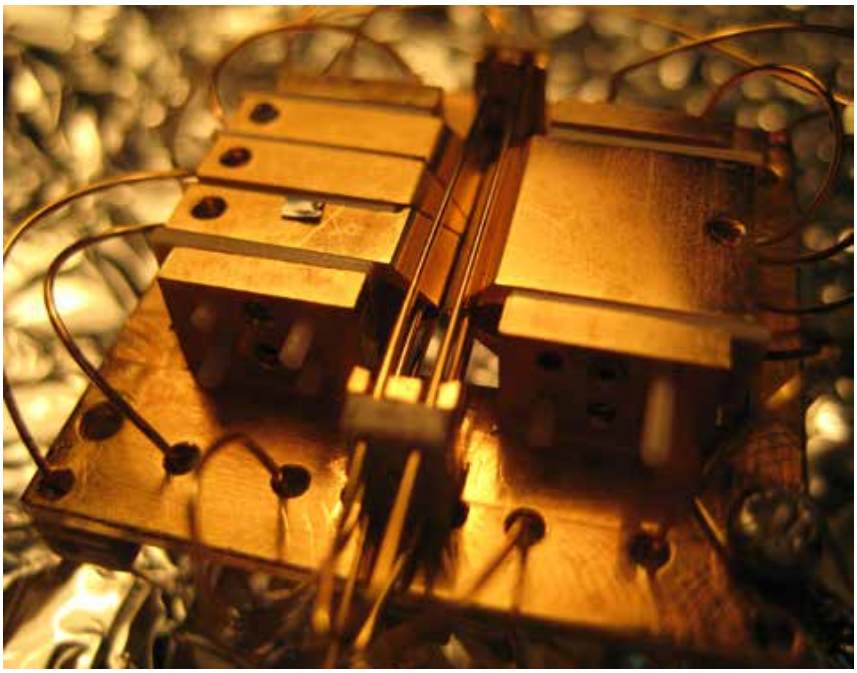

Figure 3.7: Picture of the macroscopic linear Paul trap before it was placed inside the vacuum chamber.

Electrode	Voltage (V)
rf	680(10)
1	GND
2	0
3	167.76(1)
4	148.88(1)
5	7.36(1)
6	25.03(1)
Comp 1	169.22(1)
Comp 2	-2.70(1)

Table 3.1: Table showing voltages used to trap ions which also correspond to the voltages used to obtain the pseudopotential shown in figure 3.8. Electrode 1 is shorting to ground due to the imperfect trap assembly process and the rf drive frequency $\Omega_T/2\pi = 21.34\,\mathrm{MHz}$.

Using the measured electrode positions the trapping potential is simulated using CPO[29] which uses a boundary element method (BEM) solver. With the obtained basis functions it is possible to simulate the pseudopotential for given rf and static voltages. The parameters used in the simulation are summarised in table 3.1. The pseudopotential for these parameters is shown in figure 3.8 from which the trap depth is determined to be 4.9±0.2 eV. From the same simulation the secular frequencies are determined to be $(\nu_x, \nu_y, \nu_z)/2\pi = (2.146, 2.094, 1.019)\,\mathrm{MHz}$.

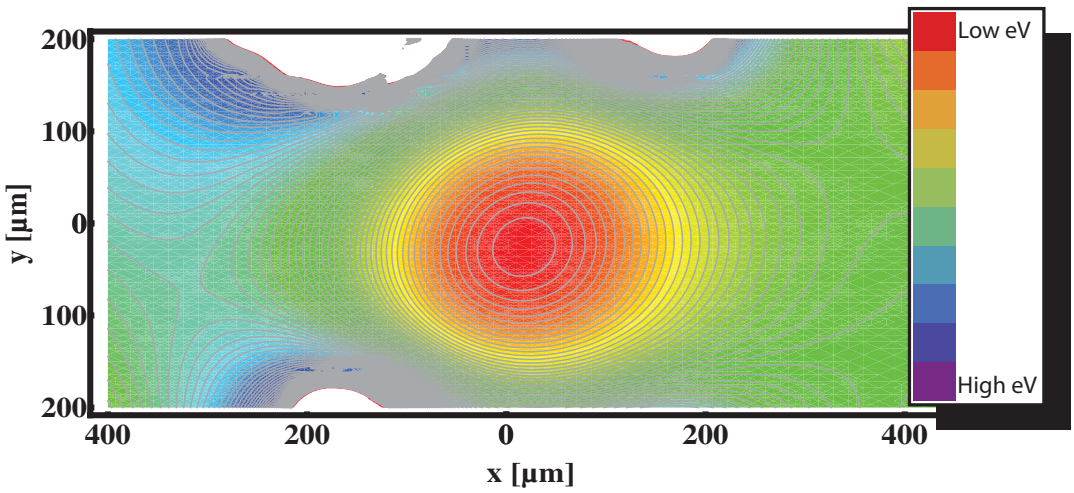

Figure 3.8: Pseudopotential of the ion trap for the parameters given in table 3.1 with a trap depth of 4.9±0.2 eV.

The trap characterised by the above numbers has been used for the relevant experiments shown in this thesis. It should be noted that the trap in operation at the time of

[29] Charged particle optics. From www.electronoptics.com

writing this thesis now includes magnets which provide a static magnetic field gradient at the trap centre. Due to the disruptive work that was required to place the magnets close to the trap the relative positions of the electrodes have changed. As a consequence the rf and static voltage electrodes are now separated by 317±14 μm in the x-direction and 533±14 μm in the y-direction with a ion-electrode distance of 310±10 μm.

3.5 High Q helical resonator

Creating a stable, high voltage and low noise rf trapping potential is critical to achieve a large trap depth and to minimise heating of the ion [91]. One way of achieving this is through the use of a high quality factor (Q) helical resonator. Figure 3.9 shows a typical

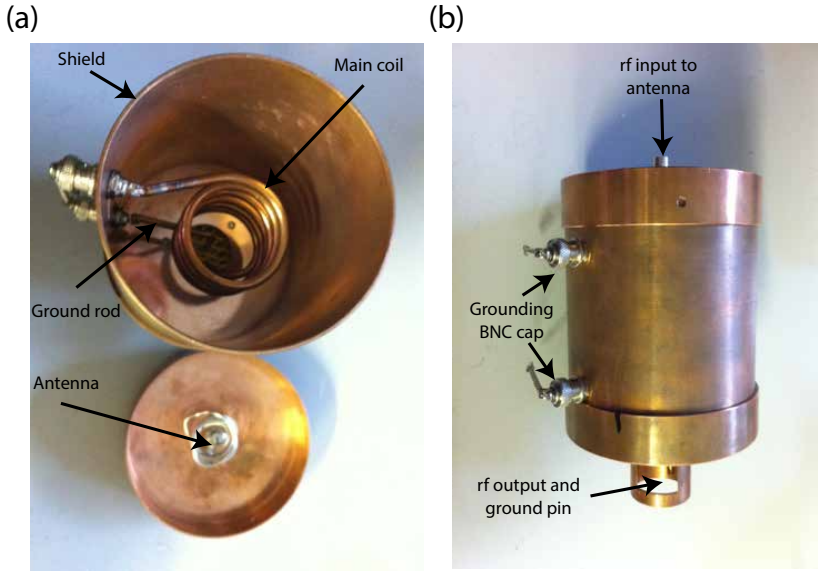

Figure 3.9: (a) shows the inside of a resonator where the shield, main coil, antenna and ground rod are clearly labelled. (b) shows the closed up resonator as used in experiments where the rf input to the antenna, the rf output and the grounding rods are labelled.

helical resonator used in our experiments where the main helical coil, the antenna and the shield is clearly labelled. Using a helical resonator provides impedance matching of the rf source to the ion trap setup and allows high voltages to be applied. It also provides very good filtering of noise if a high Q can be achieved and thereby reduces the power at unwanted frequencies. This provides higher voltages per input power, resulting in deeper trapping potentials and larger achievable secular frequencies. The Q of the resonator is therefore a very important parameter to maximise. The ion trap resonator system can be represented as a series LCR circuit where the Q and resonant frequency f_0 are given

Resonator design parameters	
Shield diameter (mm)	76±1
Shield height (mm)	105±1
Coil diameter (mm)	52±2
Coil wire diameter (mm)	4.0±0.1
Winding pitch (mm)	7±3
Number of turns	$7\frac{3}{4}$

Table 3.2: Table showing the design parameters of the resonator.

by [92]

$$Q = \frac{1}{R}\sqrt{\frac{L}{C}} \tag{3.1}$$

and

$$f_0 = \frac{1}{\sqrt{LC}} \tag{3.2}$$

respectively where R is the resistance, C the capacitance and L the inductance of the ion trap-resonator system. It is important to not exceed the maximum voltage that can be applied to the particular ion trap in use which is often given by the breakdown voltage [93]. The peak voltage over the ion trap is given by [92]

$$V_{peak} = \kappa\sqrt{2PQ} \tag{3.3}$$

where $\kappa = (L/C)^{1/4}$ and P is the rf input power.

Designing a resonator with the desirable resonant frequency capable of achieving a high Q is a challenging task. To make this task simpler we have therefore put together a design guide with detailed explanations of the ion-resonator system [92].

Using the design guide, a resonator with parameters shown in table 3.2 was built for a trap with a resistance of $R \approx 0.1\Omega$ and a capacitance of $C = 17\pm2\,\text{pF}$. The resonator was found to have an unloaded Q of 574±46 and a resonant frequency f_0 of 87.46±0.30 MHz. Upon connecting the resonator to the ion trap, the Q was found to be 200±20 while f_0 was found to be 21.49±0.30 MHz.

Once an ion has been trapped it is possible to determine κ. This is done by measuring the secular frequency of the ion for a given rf input power and Q. Simulating the trapping potential required to achieve these secular frequencies then allows us to determine the rf voltage which is used to calculate κ using equation 3.3. For the resonator and trap shown here a κ of 12.9±1.4 was calculated which matches the theoretical prediction for the ion trap-resonator system [92]. Knowing κ allows us to determine the rf voltage at the ion for

Isotope	$^1S_0 \leftrightarrow {}^1P_1$ wavelength [nm]	$^2S_{1/2} \leftrightarrow {}^2P_{1/2}$ wavelength [nm]	$^2[3/2]_{1/2} \leftrightarrow {}^2D_{3/2}$ wavelength [nm]
$^{170}Yb^+$	399.91051(6)	369.52364(6)	935.19751(19)
$^{171}Yb^+$	399.91070(6)	369.52604(6)	935.18768(19)
$^{172}Yb^+$	399.91083(6)	369.52435(6)	935.18736(19)
$^{174}Yb^+$	399.91114(6)	369.52494(6)	935.17976(19)
$^{176}Yb^+$	399.91144(6)	369.52550(6)	935.17252(19)

Table 3.3: Table showing resonant wavelengths used for different Yb isotopes. For efficient cooling a red detuned wavelength for the $^1S_0 \leftrightarrow {}^1P_1$ transition is used. For $^{171}Yb^+$ the wavelengths correspond to the $^2S_{1/2}|F=1\rangle \leftrightarrow {}^2P_{1/2}|F=0\rangle$ and $^2[3/2]_{1/2}|F=1\rangle \leftrightarrow {}^2D_{3/2}|F=1\rangle$ transition.

any input rf power.

3.6 Initial trapping experiments

The setup described so far in this chapter can be used to successfully trap Yb^+ ions. To bring the laser light to the centre of the ion trap the output from each of the relevant laser systems passes through various optical components and is then coupled into single mode fibres as shown in figure 3.1. The output from the 369 nm and 399 nm fibres are overlapped using a narrow bandpass filter[30]. The overlapped beams are then overlapped with the output from the 638 nm fibre using a dichroic mirror. The combined beams are then aligned to the trapping centre via xyz translation stages, using the trap electrodes as reference points. The output from the 935 nm fibre is aligned to the trapping centre in orthogonal direction to the other beams.

The wavelengths used for trapping various isotopes are shown in table 3.3. The resonant wavelengths for the $^1S_0 \leftrightarrow {}^1P_1$ transition was determined using a fluorescence spot technique [3]. The values for this transition, which are given in table 3.3, correspond to an angle of 63° between the atomic beam and the ionisation laser beams. The resonant wavelength for the $^2S_{1/2}|F=1\rangle \leftrightarrow {}^2P_{1/2}|F=0\rangle$ and $^2[3/2]_{1/2}|F=1\rangle \leftrightarrow {}^2D_{3/2}|F=1\rangle$ transitions were determined in our laboratory using the experimental setup described in this chapter [7].

Neutral Yb is produced by applying a current of ≈ 7 A to the atomic oven for ≈ 4 minutes. To ionise and trap ions the appropriate wavelengths for the required Yb isotope are set, the parameters shown in table 3.1 are applied and the beam intensities are set to

[30] Semrock. Part number: FF01-370136

approximately 0.4 $W/\,\mathrm{cm}^2$, 0.6 $W/\,\mathrm{cm}^2$, 8.0 $W/\,\mathrm{m}^2$ and 7.0 $W/\,\mathrm{m}^2$ for the 369 nm, 399 nm, 638 nm and 935 nm beams respectively. Images of ions taken with the EMCCD array are shown in figure 3.10. The secular frequencies of a single $^{174}\mathrm{Yb}^+$ ion were measured

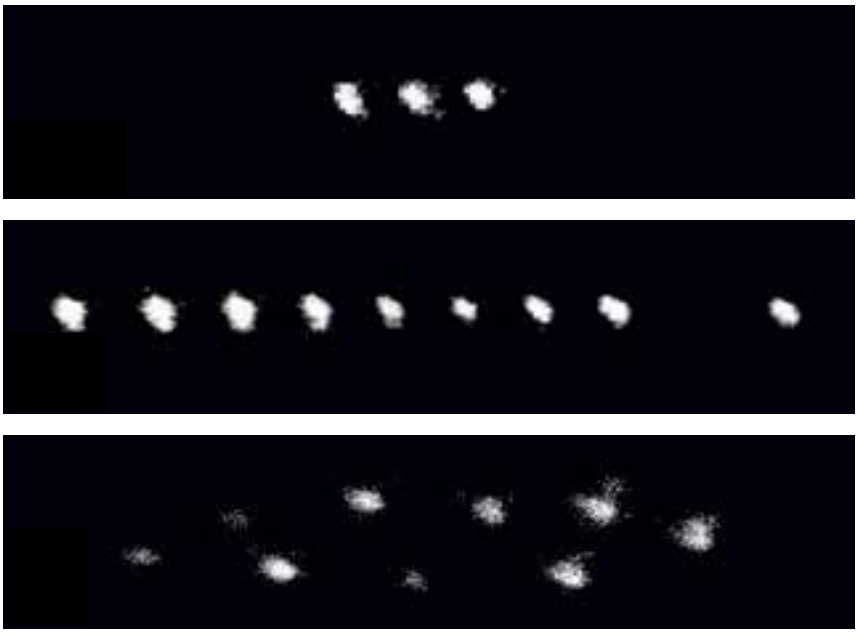

Figure 3.10: Pictures of trapped ions with fluorescence indicating the position of individual $^{174}\mathrm{Yb}^+$ ions. The picture in the middle illustrates the possibility of trapping multiple isotopes which is shown by a dark ion as part of the ion string. Lowering the radial confinement by reducing the rf voltage causes the ions to undergo a second order phase transition and form a zig-zag structure.

by applying an ac voltage to one of the static voltage electrodes. When the frequency of the ac voltage corresponds to the secular frequency along one of the axis of motion the ion will be excited and destabilise. This manifests itself in a drop in the measured fluorescence. Performing this measurement for all three axis of motion resulted in secular frequencies of $\nu_z/2\pi = (1.030 \pm 0.001)\,\mathrm{MHz}$, $\nu_x/2\pi = (2.069 \pm 0.001)\,\mathrm{MHz}$ and $\nu_y/2\pi = (2.110 \pm 0.001)\,\mathrm{MHz}$ to be measured.

Trapping $^{171}\mathrm{Yb}^+$ requires additional experimental overhead due to its hyperfine structure. As discussed in section 3.1.1, various sidebands are applied to the lasers to address this. Furthermore, a static magnetic field to lift the degeneracy of the $^2S_{1/2}|F = 1\rangle$ Zeeman states is required to prevent coherent population trapping which significantly reduces the scattering rate [94]. The static magnetic field is created using three pairs of Helmholtz coils positioned around the vacuum chamber. Each coil has a diameter of 18 cm and consists of 80 turns. Applying a current of ≈ 3 A to one pair of the coils results in a B-field of ≈ 10 Gauss at the position of the ion. Using three pairs of coils, one for each axis, allows to accurately change the direction of the B-field (quantisation axis) with respect to the

trap axis and is an important flexibility to have for experiments where the angle between the quantisation axis and the field used to manipulate the ions is critical.

3.6.1 Heating rate measurement

A very important property of an ion trap is the heating rate trapped ions experience when no laser cooling is present. One method of measuring heating rates is to perform resolved sideband spectroscopy [95] however the required Raman beams were not available at the time. An alternative method allows a heating rate to be extracted from the fluorescence profile of a initially hot ion which is being laser cooled using the Doppler cooling laser beam [1].

To extract a heating rate of the ion the cooling laser is blocked for a sufficiently long time. The laser is then unblocked and the fluorescence measured on a PMT. Using the fluorescence signal, the energy of the ion at the time the cooling beam was applied can be determined. The experiment is then repeated for an increasing time the cooling beam is blocked for and a heating rate is extracted. The method uses a 1D model so it is important that heating is dominant along one axis only. To satisfy this requirement it is important to note that noise which is near resonant with the secular motion of the ion causes heating and scales as $1/f$ where f is the frequency of the noise. Treating heating as being dominant along one axis only is therefore a good approximation if one ensures that the secular frequency of the two radial modes of motion are much larger compared to that of the axial mode of motion. In the experimental setup presented here this can be achieved by lowering the voltage on the outer static voltage trap electrodes. We can now consider the motion of the ion along the axial direction only. The motion along this axis will increase when the temperature of the ion increases and affect the instantaneous Doppler shift given by $\Delta_D = -k_z \nu_z$, where k_z is the wave vector of the Doppler cooling laser beam in the z-direction, ν_z is the velocity of the ion along the same direction and the negative sign indicates that a photon will only be absorbed when the ion travels in the opposite direction to the propagation of the cooling beam.

The scattering rate of an ion depends on the probability of the laser light being resonant with the atomic transition and is therefore a function of the instantaneous Doppler shift and the transition linewidth L. Considering many ion oscillations we can say that the scattering rate depends on the overlap of the instantaneous Doppler shift probability function $P_D(\Delta_D)$ with the line shape of the transition L. This is illustrated in figure 3.11 where two cases are considered. Figure 3.11 (a) shows the overlap for a hot ion where

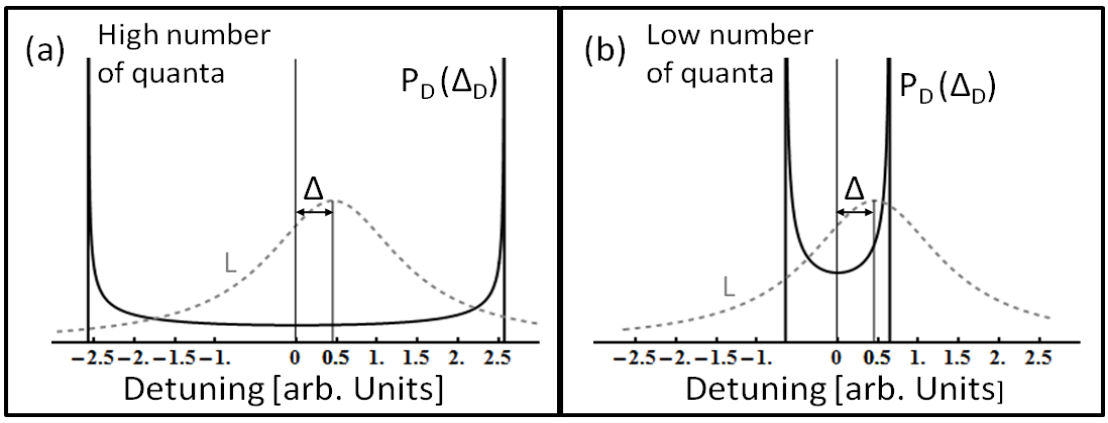

Figure 3.11: The overlap between the probability density of the Doppler shift $P_D(\Delta_D)$ (solid line) and the transition linewidth L (dashed line) [7]. (a) shows the case for a hot ion where the maximum Doppler shift is greater than the linewidth resulting in a small overlap. This reduces the scatter rate. (b) shows the case for a Doppler cooled ion which results in a bigger overlap and increases the scatter rate.

the maximum instantaneous Doppler shift Δ_{max} from a laser with a small detuning from resonance, Δ, is greater than L. It can be seen that the overlap between $P_D(\Delta_D)$ and L is poor which means there is only a small amount of time when the Doppler cooling light is on resonance with the atomic transition and results in a low scattering rate. Figure 3.11 (b) on the other hand shows the case for a cold ion and we can see that the overlap is significantly better and results in a higher scattering rate. This therefore allows us to determine the initial temperature of the ion by simply observing the scattering from the ion.

A full mathematical description of how the scattering rate from the ion relates to the initial temperature of the ion is given in [1] and only a very brief summary will be given here.

Recooling the ion after a initial time of heating from the environment is a process over many ion oscillations. The energy change during one oscillation compared to the total cooling process is therefore small, allowing us to average the scattering rate over one oscillation. This average scattering rate $\frac{dN}{dt}$ during one oscillation of the ion is given by [1, 7]

$$\left\langle \frac{dN}{dt} \right\rangle = \int \frac{dN}{dt} P_D(\Delta_D) d\Delta_D \tag{3.4}$$

where $\frac{dN}{dt}$ is the instantaneous scattering rate. Looking at figure 3.11 (a) we can see that $P_D(\Delta_D)$ is effectively constant over the linewidth of the cooling transition. This allows us to factor out $P_D(\Delta_D)$ and write $\left\langle \frac{dN}{dt} \right\rangle$ in terms of the energy of the ion at time t, the initial energy E_0 which corresponds to the energy of the ion just before the cooling laser

beam is applied, the mass of the ion m and the saturation parameter s to give [1, 7]

$$\left\langle \frac{dN}{dt} \right\rangle (E(E_0,t)) = \frac{1}{\sqrt{E(E_0,t)}} \frac{sL^2}{2\sqrt{\frac{2}{m}} k_z (1+s)^{3/2}}. \tag{3.5}$$

The thermal distribution of the ion energy just before recooling can be described using a 1D-Maxwell-Boltzmann distribution $P_B(E_0)$ which allows the average scattering rate of the ion at time t to be written as [1, 7]

$$\left\langle \frac{dN}{dt} \right\rangle_{E_0} = \int_0^\infty P_B(E_0) \left\langle \frac{dN}{dt} \right\rangle (E(E_0,t)) dE_0. \tag{3.6}$$

We can now use equation 3.6 and fit it to the observed scattering from a initially hot ion which is being Doppler cooled to determine the energy of the ion just before the cooling beam is applied. Repeating this experiment for different delay times during which the cooling laser is blocked and the ion is heated then allows us to determine the heating rate.

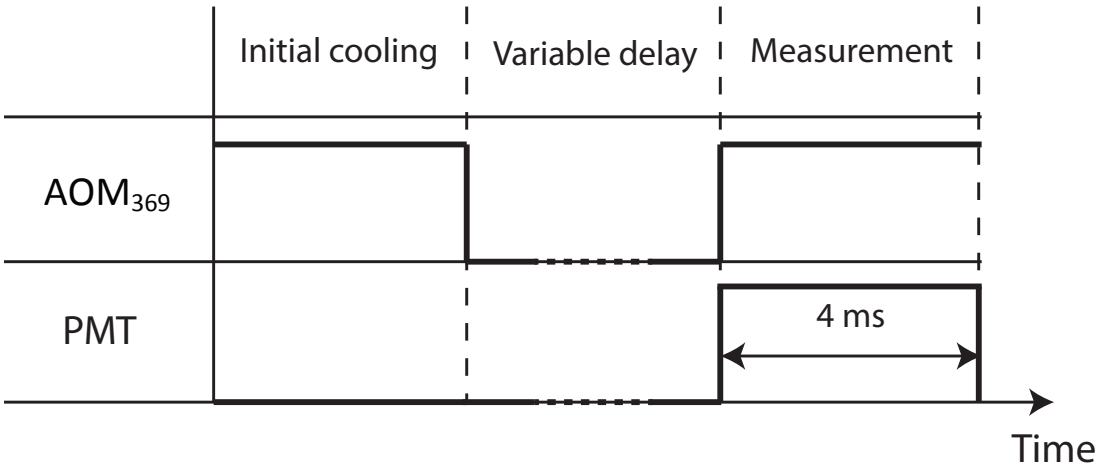

Figure 3.12: Illustration of the experimental sequence used to determine the heating rate. The sequence starts by a period of initial cooling of the ion before the cooling beam is blocked using a AOM to heat the ion for a variable length of time. The cooling beam is then unblocked and a PMT is used to measure the fluorescence for 4 ms divided into 50 μs bins.

In order to determine the heating rate of our trap a single $^{174}Yb^+$ ion is used. To ensure that heating is dominant along the axial direction the trapping voltages are altered to give secular frequencies of $(\nu_z, \nu_x, \nu_y)/2\pi = (0.178, 2.069, 2.110) \pm 0.001$ MHz. Setting $\Delta = 6 \pm 2$ MHz, $s = 1.0 \pm 0.2$ and $L = 40 \pm 5$ MHz we then use an AOM to block the cooling beam to heat the ion. When the cooling beam is unblocked a PMT is used to measure the fluorescence from the ion. The fluorescence measurement is 4 ms long and is split

into 50 μs long bins. The experimental sequence is shown in figure 3.12. The sequence is repeated 500 times and the data is averaged. This data, showing the measured fluorescence during initial cooling after a 5 second delay, is shown in figure 3.13 and is used to determine the initial energy of the ion. Repeating this experiment and plotting the determined initial energy against delay times of 1, 3, 5 and 7 seconds, as shown in figure 3.7, then allows us to determine the heating rate $\dot{n}$. Here the initial ion energy has been converted to motional quanta using $n = E_0/\hbar\nu_z$.

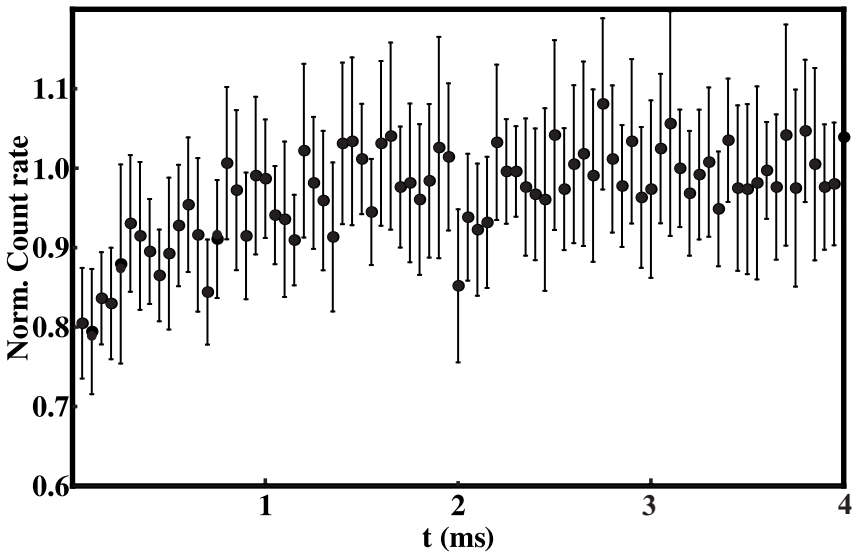

Figure 3.13: The fluorescence measured during a 4 ms detection window after the ion has been left uncooled for 5 s.

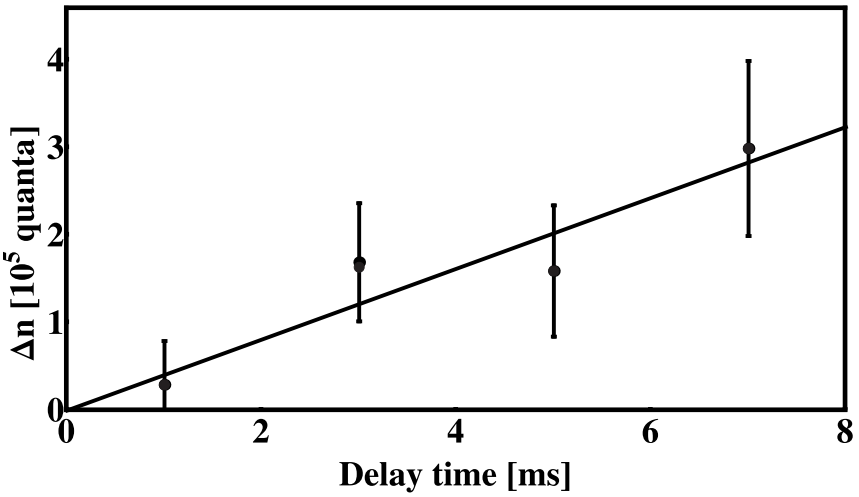

Figure 3.14: A plot showing the change in initial energy of the ion which has been converted to motional quanta n for different delay times.

To determine the relationship between the heating rate and the secular frequency the above measurements are repeated for axial secular frequencies of $\nu_z/2\pi = (287, 355)\pm 1$ kHz. The result of this can be seen in figure 3.15 and confirms the expected $\dot{n} \propto 1/\nu_z^2$ relation-

ship.

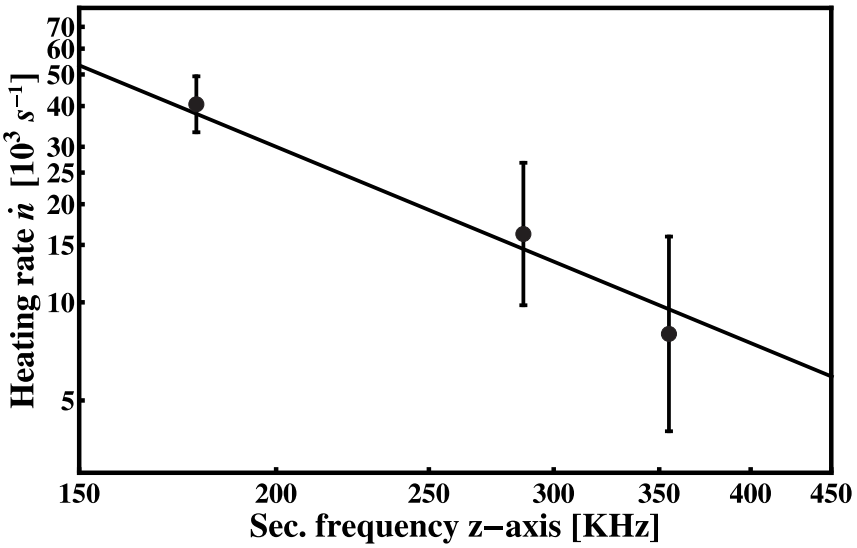

Figure 3.15: A plot showing the heating rate $\dot{n}$ for different axial secular frequencies illustrating a $1/\nu_z^2$ dependency.

The heating of an ion has been shown to be a function of the electric field noise density $S_E(\nu_z)$ [91]. The heating rate can therefore be given by

$$\dot{n} = \frac{q^2}{4m\hbar\nu_z} S_E(\nu_z) \tag{3.7}$$

where q is the charge of the ion. For a $1/\nu^2$ dependency of $\dot{n}$ we can scale out the secular frequency and calculate $S_E(1\,\mathrm{MHz}) = 3.6 \pm 0.9 \times 10^{-11} V^2 m^{-2} Hz^{-1}$. This is consistent with previous measurements for similar ion traps at room temperature [42].

Chapter 4

Single qubit manipulation

In order for a quantum computer to be used successfully we require the implementation of single qubit gates as well as two qubit gates [96]. Any two-level quantum system can be used as a qubit however the focus in this work will lie on trapped ions which each are treated as a spin-1/2 system and the qubit, in this chapter, is formed by two of the hyperfine states in the $^2S_{1/2}$ ground state of $^{171}Yb^+$. While a two qubit gate such as the CNOT gate is implemented by entangling two separate ions, a single qubit gate such as the NOT gate is implemented using qubit rotations. These single qubit rotations allow an arbitrary state of the form $\alpha|0\rangle + \beta|1\rangle$ to be prepared and will be the main focus of this chapter.

Before any qubit rotations can be performed we require the capability of efficiently preparing the qubit in a known state. We also need to be able to detect the state of the qubit after any operation has been performed. A typical experimental sequence to implement a single qubit gate is shown in figure 4.1. The experimental sequence starts with the ion being Doppler cooled. The ion is then prepared in a well defined state using optical pumping before microwave radiation is used to perform any single qubit gates. The qubit is then read out using optical radiation and a PMT is used to detect the photons from the ion. The photons are also counted during Doppler cooling to monitor the fluorescence rate of the ion. This allows to ensure that no ions are lost and the beam intensities are stable over the course of an experiment.

4.1 State preparation and detection

To implement state preparation and detection, light near 369 nm resonant with one of the $^2S_{1/2} \leftrightarrow {}^2P_{1/2}$ transitions is used. In addition, to depopulate the $^2D_{3/2}$ states, light near

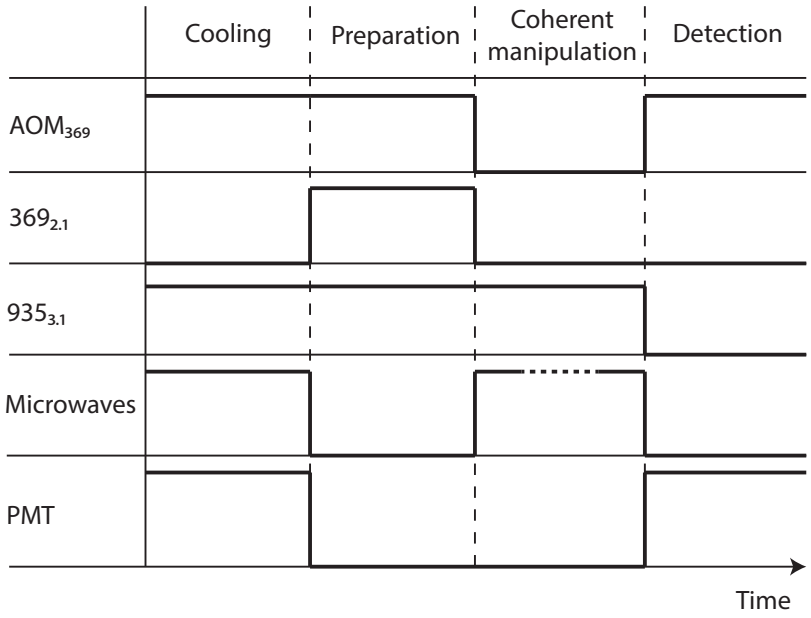

Figure 4.1: An illustration of a typical experimental sequence. The sequence starts by Doppler cooling the ion. 2.1 GHz sidebands are then applied to the 369 nm light which is then sent to the ion for state preparation. This is followed by a sequence of coherent manipulation using microwave radiation. 369 nm light is then used for state detection and the photons are collected using a PMT. Photons are also collected during cooling to monitor the fluorescence rate of the ion.

935 nm resonant with one of the $^2D_{3/2} \leftrightarrow {}^3[3/2]_{3/2}$ transitions is used. This is shown in figure 4.2 (a) and (b).

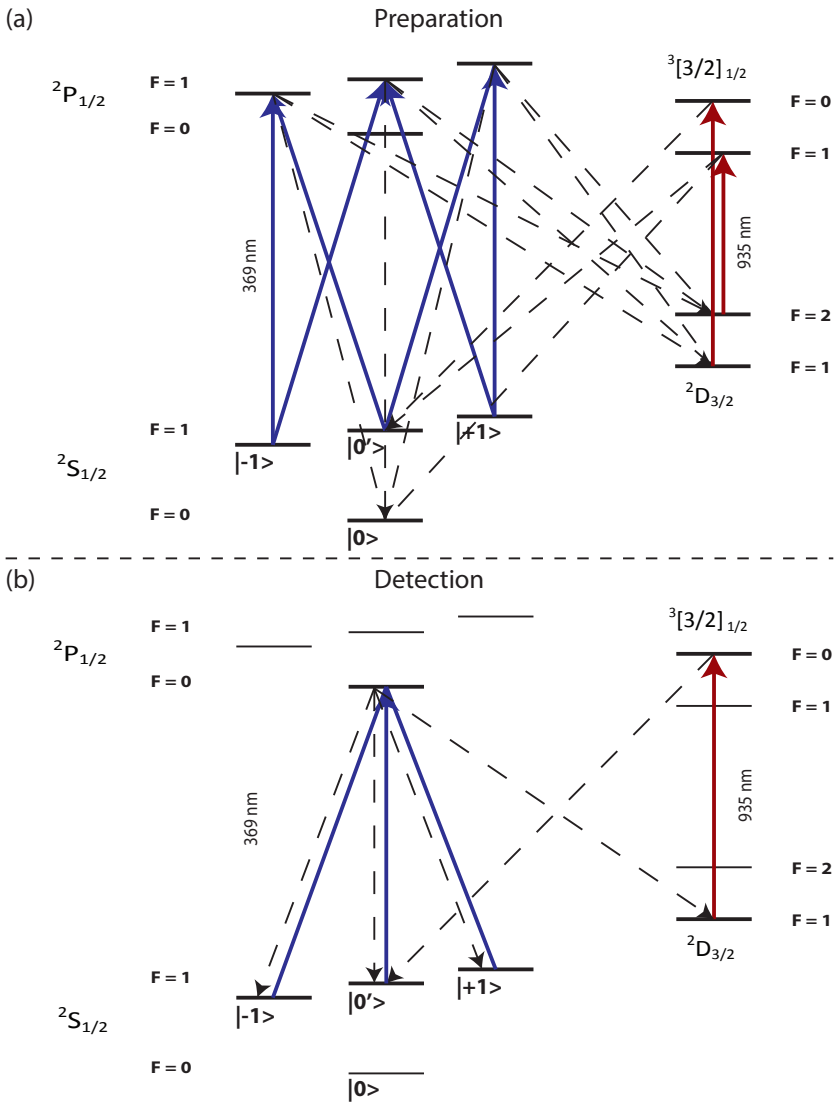

Figure 4.2: Not to scale partial $^{171}Yb^+$ energy level diagram. (a) transitions used for state preparation in the $^2S_{1/2}|F = 0\rangle$ state. (b) transitions used for state detection. If the ion is in $^2S_{1/2}|F = 0\rangle$ only a few photons will be scattered and we define this to be the dark state ($|0\rangle$). If the ion is in one of the three $^2S_{1/2}|F = 1\rangle$ states many photons will be scattered and we define this to be the bright state ($|-1\rangle$, $|0'\rangle$, $|+1\rangle$).

4.1.1 State preparation

Figure 4.2 (a) shows the preparation sequence used to optically pump the ion into the $^2S_{1/2}|F = 0\rangle = |0\rangle$ state. This is achieved using light near 369 nm with the positive first-order 2.1 GHz sideband resonant with the $^2S_{1/2}|F = 1\rangle \leftrightarrow {}^2P_{1/2}|F = 1\rangle$ transition. From $^2P_{1/2}|F = 1\rangle$ the ion can then decay to $|0\rangle$. Since the ion can also decay into the $^2D_{3/2}$ man-

ifold, the carrier and the positive first-order 3 GHz sideband of light near 935 nm is used to drive the $^2\mathrm{D}_{3/2}|F=1\rangle \leftrightarrow {}^3[3/2]_{1/2}|F=0\rangle$ and the $^2\mathrm{D}_{3/2}|F=2\rangle \leftrightarrow {}^3[3/2]_{1/2}|F=1\rangle$ transition respectively. From here the ion will decay back into the $^2\mathrm{S}_{1/2}$ manifold.

Using 8 μW of 369 nm light focused to a beam waist of 20 μm (intensity of 0.4 W/m^2) and 1 mW of 935 nm light focused to a beam waist of 150 μm (intensity of 6.67 W/m^2) the ion is optically pumped to the $|0\rangle$ state after ≈ 1 ms. The preparation time is limited by the maximum 2.1 GHz sideband strength of 0.02% with respect to the carrier that can be achieved while maintaining the stability of the 369 laser during switching. The sideband strength can be significantly improved by using a EOM[1] with which we expect to achieve a sideband strength of 20%. This is expected to reduce the preparation time to $\approx 1\,\mu$s, similar to the preparation time achieved by other ion trapping groups using $^{171}\mathrm{Yb}^+$ [6].

4.1.2 State detection

After coherent manipulation of the ion we use a fluorescence technique to determine if the ion was in $|0\rangle$ or one of the $^2S_{1/2}|F=1\rangle$ states. This is achieved using 369 nm light resonant with the $^2S_{1/2}|F=1\rangle \leftrightarrow {}^2P_{1/2}|F=0\rangle$ transition. If the ion is in $^2S_{1/2}|F=1\rangle$, this is a cycling transition provided that 935 nm light resonant with the $^2D_{3/2}|F=1\rangle \leftrightarrow {}^3[3/2]_{1/2}|F=0\rangle$ transition is applied. The fluorescence from the ion decaying from the $^2P_{1/2}|F=0\rangle$ to the $^2S_{1/2}|F=1\rangle$ state can then be collected. This is called the bright state. If the ion is in $|0\rangle$ the light field is off-resonant from $^2P_{1/2}|F=1\rangle$ by 14.7 GHz since $^2S_{1/2}|F=0\rangle \leftrightarrow {}^2P_{1/2}|F=0\rangle$ is a forbidden transition. This results in no photons being scattered by the ion and is called the dark state although unwanted counts can arise from scattered light and dark counts from the photon measuring device. A simple threshold can then be used to distinguish between the two states. The threshold is set so that if zero, one or two photons are detected during the detection sequence the ion is said to be in the dark state and if more than two photons are detected the ion is said to be in the bright state.

Theoretical limitations of the achievable detection fidelity are discussed in detail in reference [97] and arise from off-resonant coupling to the 2.1 GHz detuned $^2P_{1/2}|F=1\rangle$ state which can cause the ion to transition from the bright to the dark state. Another process that can limit the fidelity is off-resonant excitation from $^2D_{3/2}|F=1\rangle$ to $^3[3/2]_{1/2}|F=1\rangle$ which also transfers the bright to the dark state. These processes, as well as background light and dark-counts in the photon detection device, serve to limit the ability to distinguish the two states.

[1] Newport. Model: 4441

Using a detection window of 800 μs, histograms for the bright and dark state can be produced and are shown in figure 4.3. The fidelity of state detection is determined by how well we can distinguish between the bright and the dark state for a given threshold. Since the histogram for the bright state (red histogram) overlaps with the histogram for the dark state (blue histogram) the two states cannot be perfectly distinguished from each other resulting in photons being associated with the incorrect state. For the above parameters a detection fidelity of 0.93 is measured. More sophisticated techniques exist to improve the detection fidelity by looking at the arrival times of the photons [98] and will be implemented in the future.

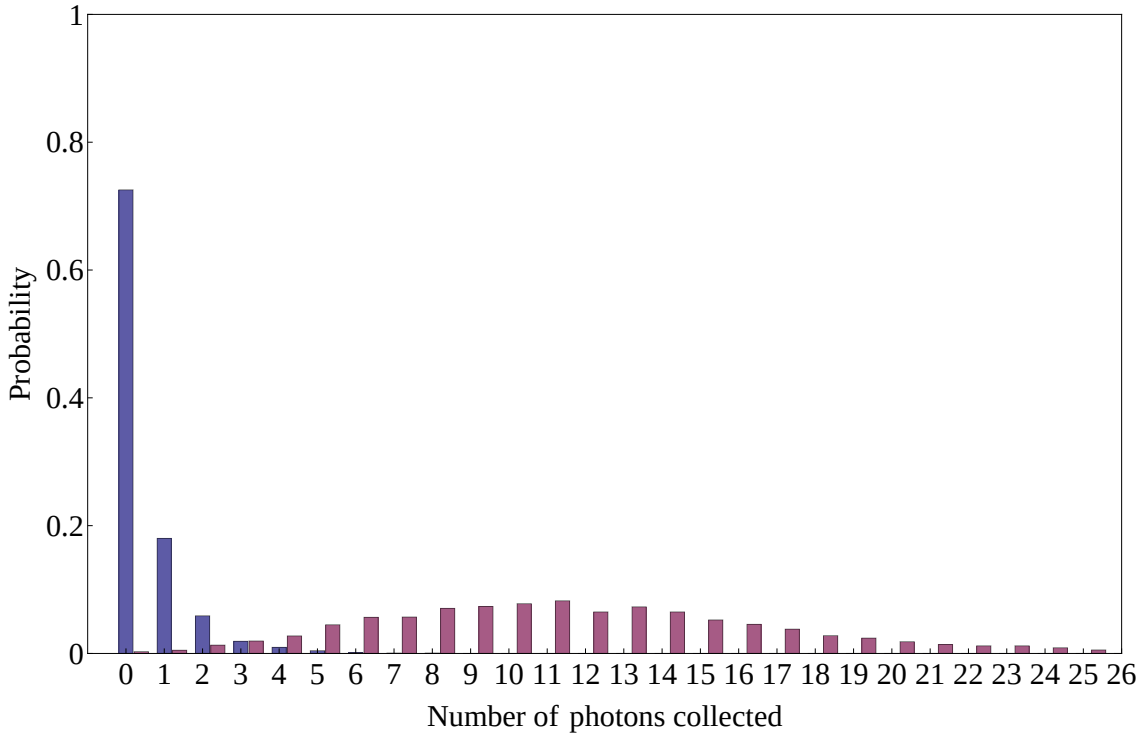

Figure 4.3: Histogram of the number of photons detected during a 800 μs detection sequence after initial preparation in either $^2S_{1/2}|F=0\rangle$ (blue) or $^2S_{1/2}|F=1\rangle$ (red). For detection we apply 8 μW of 369 nm light focused to a beam waist of 20 μm resonant with $^2S_{1/2}|F=1\rangle \leftrightarrow {}^2P_{1/2}|F=0\rangle$. If the ion is prepared in $^2S_{1/2}|F=0\rangle$ the incident light is 14.7 GHz off-resonant resulting in only a few photons being scattered. If the preparation sequence includes an additional microwave π-pulse resonant with $^2S_{1/2}|F=0\rangle \leftrightarrow {}^2S_{1/2}|F=1\rangle$ to prepare the ion in $^2S_{1/2}|F=1\rangle$ the light is on resonance and many photons are scattered. The histogram for each state is the result of 1000 measurements.

4.2 Single qubit operations

As discussed above, the qubit is formed of two long lived hyperfine states which can for example be labelled as $|0\rangle$ and $|1\rangle$ and are separated by an energy gap $\hbar\omega_0$. Later on $|1\rangle$

will often be replaced by $|-1\rangle$, $|0'\rangle$ or $|+1\rangle$ depending on the atomic state that is being used as part of the qubit. The qubit is well confined in a harmonic potential in which the motion of the ion can be described by the harmonic oscillator eigenstates $|n\rangle$ separated by $\hbar\nu_i$ where ν_i is the secular frequency of the chosen axis of motion. The Hamiltonian of this system is given by (the following mathematical derivation closely follows [77,99,100])

$$\hat{H}_0 = \frac{\hbar\omega_0}{2}\hat{\sigma}_z + \hbar\nu_i\left(\hat{a}_i^\dagger\hat{a}_i + \frac{1}{2}\right) \tag{4.1}$$

where, $\hat{\sigma}_z = \begin{pmatrix} 1 & 0 \\ 0 & -1 \end{pmatrix} = (|0\rangle\langle 0| - |1\rangle\langle 1|)$ is a Pauli spin operator and $\hat{a}_i^\dagger$ and $\hat{a}_i$ are the phonon creation and annihilation operators respectively. In the following discussion the weakly confined z-axis of motion will be considered.

The qubit can be manipulated using a resonant electromagnetic field. With a qubit splitting of $\omega_0 = 2\pi \times 12.6$ GHz the interaction with the qubit is dominated by a magnetic dipole coupling and the Hamiltonian is therefore given by

$$\hat{H}_{EM} = -\vec{\mu}\cdot\vec{B} \tag{4.2}$$

where, $\vec{\mu}$ is the magnetic dipole moment and $\vec{B}$ is the time-varying applied magnetic field. For a field with frequency ω propagating parallel to the z-axis we can expand the Hamiltonian in equation 4.2 to read

$$\hat{H}_{EM} = -\vec{\mu}\cdot\hat{z}\frac{B_z}{2}\left[e^{i(kz-\omega t+\phi)} + e^{-i(kz-\omega t+\phi)}\right] \tag{4.3}$$

where $k = 2\pi/\lambda$ is the wavenumber.

Applying the identity operator $\hat{I} = (|0\rangle\langle 0| + |1\rangle\langle 1|)$ twice we can write the scalar product as

$$\vec{\mu}\cdot\hat{z} = (|0\rangle\langle 0| + |1\rangle\langle 1|)\vec{\mu}\cdot\hat{z}(|0\rangle\langle 0| + |1\rangle\langle 1|). \tag{4.4}$$

Noting that $\langle 0|\vec{\mu}\cdot\hat{z}|0\rangle = 0$, $\langle 1|\vec{\mu}\cdot\hat{z}|1\rangle = 0$ and $\langle 0|\vec{\mu}\cdot\hat{z}|1\rangle = \langle 1|\vec{\mu}\cdot\hat{z}|0\rangle$ this can be written as

$$\vec{\mu}\cdot\hat{z} = \langle 0|\vec{\mu}\cdot\hat{z}|1\rangle(|0\rangle\langle 1| + |1\rangle\langle 0|) \tag{4.5}$$

which can be simplified to

$$\vec{\mu}\cdot\hat{z} = \langle 0|\vec{\mu}\cdot\hat{z}|1\rangle(\hat{\sigma}_+ + \hat{\sigma}_-) \tag{4.6}$$

where $\hat{\sigma}_+ = \begin{pmatrix} 0 & 1 \\ 0 & 0 \end{pmatrix} = |0\rangle\langle 1|$ and $\hat{\sigma}_- = \begin{pmatrix} 0 & 0 \\ 1 & 0 \end{pmatrix} = |1\rangle\langle 0|$ are the raising and lowering operators respectively. Defining the Rabi frequency Ω as [78]

$$\Omega = -\frac{B_z}{\hbar}(\langle 1|\vec{\mu}\cdot\hat{z}|0\rangle), \tag{4.7}$$

the Hamiltonian in equation 4.3 can be written as

$$\hat{H}_{EM} = \frac{\hbar\Omega}{2}\left(\hat{\sigma}_+ + \hat{\sigma}_-\right)\left[e^{i(kz-\omega t+\phi)} + e^{-i(kz-\omega t+\phi)}\right]. \tag{4.8}$$

We can now transform to the interaction picture with respect to H_0 given by $\hat{H}_I = e^{i\hat{H}_0 t/\hbar}\hat{H}_{EM}e^{-i\hat{H}_0 t/\hbar}$ and perform the rotating wave approximation (RWA) resulting in an interaction Hamiltonian

$$\hat{H}_I = \frac{\hbar\Omega}{2}\left[\hat{\sigma}_+ e^{i\left(\eta\left(\hat{a}^\dagger e^{i\nu t}+\hat{a}e^{-i\nu t}\right)+\Delta+\phi\right)} + h.c.\right] \tag{4.9}$$

where Δ is the detuning from resonance and the position operator has been expanded in terms of the creation and annihilation operators where $z = \sqrt{\hbar/2m\nu}\left(\hat{a}+\hat{a}^\dagger\right)$. This allows us to write $kz = \eta\left(\hat{a}+\hat{a}^\dagger\right)$ where η is the Lamb-Dicke parameter given by [99]

$$\eta = k\sqrt{\frac{\hbar}{2m\nu}} \tag{4.10}$$

which is the ratio of the position spread of the ground state wavefunction of the ion to the wavelength of the field used to manipulate the qubit.

Due to the Doppler effect, the ion will see a large spectrum of the field applied. By satisfying the Lamb-Dicke criterion given by [99]

$$\eta^2\left(2n+1\right) \ll 1 \tag{4.11}$$

we ensure that the ion will only couple to the carrier or the first red or blue motional sideband. To first order in η, we can therefore rewrite the interaction Hamiltonian in equation 4.9 as

$$\hat{H}_I = \frac{\hbar\Omega}{2}\left[\hat{\sigma}_+\left(1+i\eta\left(\hat{a}^\dagger e^{i\nu t}+\hat{a}e^{-i\nu t}\right)\right)e^{i(\phi-\Delta t)} + h.c.\right]. \tag{4.12}$$

By appropriately setting the detuning from resonance, Δ, it is possible to drive carrier ($|0,n\rangle \leftrightarrow |1,n\rangle$), blue sideband ($|0,n\rangle \leftrightarrow |1,n+1\rangle$) or red sideband ($|0,n\rangle \leftrightarrow |1,n-1\rangle$)

transitions. To see this, we set $\Delta = 0$ (carrier transition) which simplifies the Hamiltonian in equation 4.12 and gives

$$\hat{H}_I^c = \frac{\hbar\Omega}{2}\left(\hat{\sigma}_+ e^{i\phi} + \hat{\sigma}_- e^{-i\phi}\right). \tag{4.13}$$

General qubit gates, corresponding to rotating the state vector to any point on the Bloch sphere, can now be implemented by simply setting the phase ϕ of the field (and recalling that $\hat{\sigma}_z = -i\hat{\sigma}_x\hat{\sigma}_y$). For instance, by setting $\phi = 0$ we get

$$\hat{H}_I^c = \frac{\hbar\Omega}{2}\left(\hat{\sigma}_+ + \hat{\sigma}_-\right) = \frac{\hbar\Omega}{2}\hat{\sigma_x}. \tag{4.14}$$

This corresponds to rotations around the x-axis. If instead we set $\phi = \pi/2$ we get

$$\hat{H}_I^c = \frac{\hbar\Omega}{2} i\left(\hat{\sigma}_+ - \hat{\sigma}_-\right) = \frac{\hbar\Omega}{2}\hat{\sigma_y} \tag{4.15}$$

which corresponds to rotations around the y-axis.

A coupling to the first blue or red sideband of motion is achieved by setting an appropriate detuning Δ and ensuring that the resolved-sideband limit given by $\Omega \ll \nu$ is satisfied. In order to couple to a red sideband of motion we set $\Delta = -\nu$ and $\phi = 0$ and perform another RWA with respect to ν. This results in an interaction Hamiltonian, to first order, which is of the form of the Jaynes-Cummings Hamiltonian [101] and is given by

$$\hat{H}_I^{rs} = \frac{\hbar\Omega}{2} i\eta\left(\hat{a}\hat{\sigma}_+ + \hat{a}^\dagger\hat{\sigma}_-\right) \tag{4.16}$$

which removes one phonon of motional energy while exciting the internal state of the ion and therefore results in a coupling between the internal state and the motional state.

In order to couple to the blue sideband of motion we set $\Delta = \nu$ and again $\phi = 0$. In the same manner as before we now obtain a Hamiltonian of the form of the anti-Jaynes-Cummings Hamiltonian [101] given by

$$\hat{H}_I^{bs} = \frac{\hbar\Omega}{2} i\eta\left(\hat{a}^\dagger\hat{\sigma}_+ + \hat{a}\hat{\sigma}_-\right). \tag{4.17}$$

This Hamiltonian adds one phonon of motional energy when the internal state is excited, where the extra energy comes from the applied field used to implement the coupling. These couplings between the internal state of the ion and its motion can then be used in multi-ion entangling operations via the Coulomb interaction [19, 23, 26, 28].

It is important to note the η dependence in equation 4.16 and 4.17 which affects the

Rabi frequency of the coupling to the motional sidebands. In the regime where a motional coupling to the nearest red or blue motional sideband is dominant ($\Omega \ll \nu$ and the Lamb-Dicke criterion in equation 4.11 is satisfied), the Rabi frequency for the red sideband coupling ($|0,n\rangle \leftrightarrow |1,n-1\rangle$), Ω_{rs}, and the blue sideband coupling ($|0,n\rangle \leftrightarrow |1,n+1\rangle$), Ω_{bs}, can be expressed as [99]

$$\Omega_{rs} = \Omega\eta\sqrt{n} \tag{4.18}$$

and

$$\Omega_{bs} = \Omega\eta\sqrt{n+1} \tag{4.19}$$

respectively. We can therefore see that in order to produce a significant motional sideband coupling rate, a sufficiently large η is required.

The qubit states considered in this work are separated by $\omega_0 = 2\pi \times 12.6\,\text{GHz}$. For a secular frequency of $\nu = 2\pi \times 200\,\text{kHz}$ and a field propagating parallel to the axis of motion of a $^{171}\text{Yb}^+$ ion we find $\eta = 3.6 \times 10^{-6}$. In other words, the coupling strength is approximately 6 orders of magnitude smaller compared to the carrier which in practice means sidebands can not be seen using just microwave radiation.

To overcome this problem a common approach is to use a two-photon stimulated Raman process. This process involves using two non co-propagating fields in the optical wavelength regime, with a frequency difference corresponding to the energy splitting of the two qubit states, which couple the qubit states to an excited state. The two fields are detuned far from resonance allowing the excited state to be adiabatically eliminated [102], leaving an effective two-level system of the form described above. By choice of the frequency difference between the two fields it is possible to drive a motional sideband with a typical Lamb-Dicke parameter on the order of $\eta \approx 0.1$, a significantly stronger coupling. There are however drawbacks to using optical light fields. While it is possible to approximate the three-level system as an effective two-level system, decoherence in the form of off-resonant coupling to the excited state, light intensity fluctuations and phase fluctuations between the two fields can limit the fidelity of the gate operation [102]. Furthermore, laser systems are generally expensive, require a lot of maintenance and it is not immediately obvious how gate operations using such complex laser systems can be scaled to 100s of ions in an economical fashion.

By contrast, the field of microwave engineering is very mature and offers very stable, comparably cheap, and easy to maintain frequency sources. Microwaves can also easily be amplified and transmitted to the ions using a microwave horn which covers a large

volume of space. Furthermore, microwaves directly couple the two qubit states without the use of a third excited state which removes one of the main limitations of using lasers. The problem with using microwaves is the negligibly small Lamb-Dicke parameter as well as not being able to individually address ions since the wavelength of microwaves is on the order of several centimetres and ion-ion separations are usually on the order of a few micrometers (this results in the microwaves being distributed across the whole trapping region(s)). A solution to these problems is the use of microwaves in conjunction with a static magnetic field gradient as proposed by F. Mintert and C. Wunderlich [34].

Individual addressing

For a $^{171}Yb^{+}$ ion in a static magnetic field, the Zeeman states of the ground state $^{2}S_{1/2}$ manifold shift in frequency which is proportional to the magnetic field strength. To first order, the shift in frequency is given by

$$\omega_0 = \frac{\Delta E}{\hbar} = g_F m_F \mu_B B \tag{4.20}$$

where g_F is the Landé factor ($g_F = 1$ for the $^{2}S_{1/2}|F = 1\rangle$ states), m_F is the magnetic quantum number ($m_F = 0, \pm 1$ correspond to the three m_F states in the $F = 1$ manifold), μ_B is the Bohr magneton and B is the magnitude of the magnetic field at the ion. Using a inhomogeneous magnetic field along the z-axis of the form $B = B_0 + z\partial_z B$ where $\partial_z B$ is the magnetic field gradient along the z-axis and B_0 is an offset magnetic field, the position dependant Zeeman shift is given by

$$\omega_0(z) = \frac{g_F m_F \mu_B (B_0 + z\partial_z B)}{\hbar}. \tag{4.21}$$

We can therefore see that the Zeeman shift is position dependant if a magnetic field gradient is present. For multiple ions the separation of resonance frequency between ion i and ion j can be expressed as

$$\Delta\omega_0(z_i, z_j) = \frac{g_F m_F \mu_B \delta z \partial_z B}{\hbar} \tag{4.22}$$

where $\delta z = z_i - z_j$ is the separation between ion i and ion j located at position z_i and z_j respectively.

We can see that for this scheme to work it is important for the qubit to be made up of at least one non-zero m_F state which in $^{171}Yb^{+}$ corresponds to either one of the $^{2}S_{1/2}|F = 1, m_F = \pm 1\rangle$ states. Choosing the $m_F = +1$ state as one of the two qubit states

in ion 1 and 2, which are subjected to a magnetic field gradient of 10 T/m and are separated by 10 μm, we can calculate the individual resonances between the two qubits to be separated by $\Delta\omega_0(1,2)/2\pi = 1.39\,\text{MHz}$. This illustrates that by using a moderately strong static magnetic field gradient it is possible to individually address single ions in frequency space by simply tuning the microwave field to the appropriate resonant transition [35]. A visual representation of this can be seen in figure 4.4.

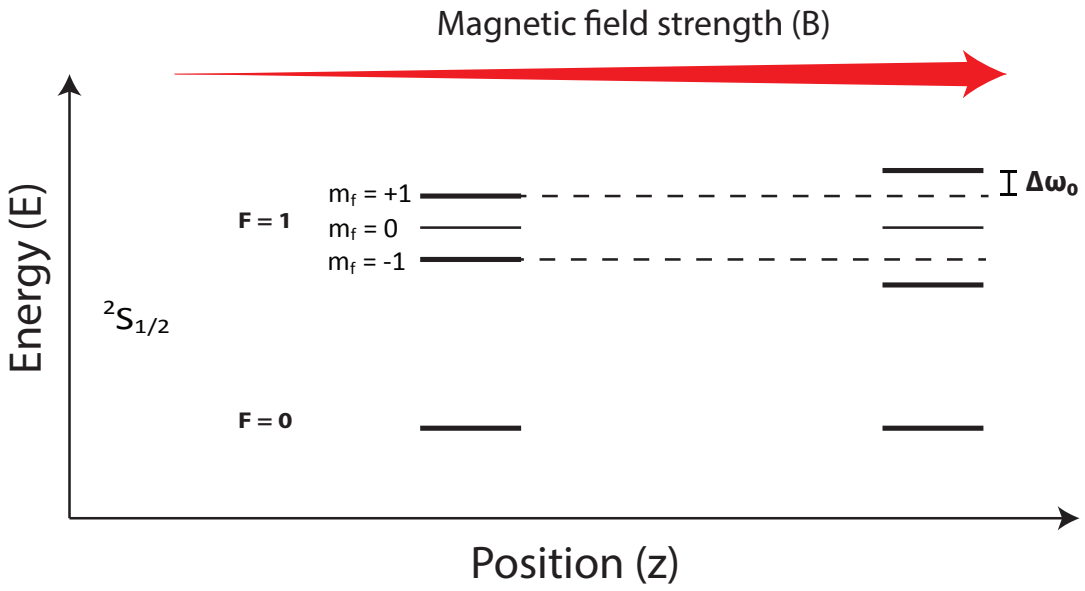

Figure 4.4: A schematic of two ions separated in space and subjected to a inhomogeneous magnetic field. The first-order magnetic field sensitive Zeeman states $m_F = \pm 1$ have a position dependant energy. This allows qubits to be individually addressed in frequency space by simply tuning the applied frequency to the appropriate transition.

Coupling between internal and motional states

The main problem with using microwaves, however is that the Lamb-Dicke parameter is negligibly small and it will be the focus of this section to demonstrate how a effective Lamb-Dicke parameter can be derived which results in a non-negligible coupling between the internal and motional states.

We have seen that a magnetic field gradient results in a position dependant Zeeman energy. This produces a state-dependant force that when added to the harmonic trapping potential gives an equilibrium position of the ion that depends on its internal state. A simple spin-flip with microwave radiation can therefore come with an extra state-dependant momentum kick and it is the aim of the following derivation to illustrate how this modifies the Hamiltonian. The derivation closely follows [34, 100, 103].

In the following, the qubit is made up of the ${}^2S_{1/2}|F=0\rangle$ and $|F=1, m_F=+1\rangle$ states

which are subjected to a static magnetic field gradient along the z-axis, the same axis along which the motion of the ion will be considered. The Hamiltonian given in equation 4.1 now has a position dependant level splitting. We can expand $\omega_0(z)$ around the position z_0 of the harmonic trapping potential as a Taylor series which to first order gives

$$\omega_0(z) = \omega_0(z_0) + \delta_z\omega_0(z)(\mid z - z_0 \mid). \tag{4.23}$$

For a single ion ($z_0 = 0$) and recalling that $z = \sqrt{\hbar/2m\nu}\left(\hat{a} + \hat{a}^\dagger\right)$, we can now re-express equation 4.1 as

$$\hat{H}_0 = \frac{\hbar\omega_0(0)}{2}\hat{\sigma}_z + \frac{\hbar\nu\epsilon_c}{2}\left(\hat{a} + \hat{a}^\dagger\right)\hat{\sigma}_z + \hbar\nu\left(\hat{a}^\dagger\hat{a} + \frac{1}{2}\right) \tag{4.24}$$

where,

$$\epsilon_c = \frac{\delta_z\omega_0(z)}{\nu}\sqrt{\frac{\hbar}{2m\nu}}. \tag{4.25}$$

This can be simplified by performing a Polaron transformation given by $\hat{H}_0' = \hat{U}\hat{H}_0\hat{U}^\dagger$ and $\hat{H}_{EM}' = \hat{U}\hat{H}_{EM}\hat{U}^\dagger$ where $\hat{U} = e^{\epsilon_c\left(a^\dagger - a\right)\hat{\sigma}_z/2}$ to give

$$\hat{H}_0' = \frac{\hbar\omega_0(0)}{2}\hat{\sigma}_z + \hbar\nu\hat{a}^\dagger\hat{a} \tag{4.26}$$

and

$$\hat{H}_{EM}' = \frac{\hbar\Omega}{2}\left(\hat{\sigma}_+ e^{\epsilon_c\left(\hat{a}^\dagger - a\right)} + \hat{\sigma}_- e^{-\epsilon_c\left(\hat{a}^\dagger - a\right)}\right)\left(e^{i\eta\left(a^\dagger + a - \epsilon_c\hat{\sigma}_z\right) - i(\omega t + \phi)} + e^{-i\eta\left(a^\dagger + a - \epsilon_c\hat{\sigma}_z\right) + i(\omega t + \phi)}\right) \tag{4.27}$$

respectively.

As for the case with no magnetic field gradient we can now transform into the interaction picture ($\hat{H}_I' = e^{i\hat{H}_0' t/\hbar}\hat{H}_{EM}' e^{-i\hat{H}_0' t/\hbar}$) and perform the RWA to get [34, 84, 100]

$$\hat{H}_I' = \frac{\hbar\Omega}{2}\left[\hat{\sigma}_+ e^{i\left(\eta_{\text{eff}}\left(\hat{a}^\dagger e^{i\nu t} + \hat{a}e^{-i\nu t}\right) + \Delta + \phi\right)} + h.c.\right]. \tag{4.28}$$

This Hamiltonian is equivalent to the Hamiltonian shown in equation 4.9 apart from η being replaced by an effective Lamb-Dicke parameter η_{eff} given by [100]

$$\eta_{\text{eff}} = \sqrt{\eta^2 + \epsilon_c^2}. \tag{4.29}$$

We have already shown that η is negligibly small when using microwave radiation allowing

us to write

$$\eta_{\text{eff}} \approx \epsilon_c = \frac{\delta_z \omega_0(z)}{\nu} \sqrt{\frac{\hbar}{2m\nu}} \tag{4.30}$$

where η_{eff} is proportional to the magnetic field gradient. For a static magnetic field gradient of $\delta_z B(z) = 50$ T/m and a secular frequency of $\nu = 2\pi \times 200$ kHz, η_{eff} is calculated to be 0.085 which is of comparable size to Lamb-Dicke parameters obtained for optical wavelengths. Microwaves in conjunction with a static magnetic field gradient are therefore a possible alternative for the implementation of coupling internal and motional states and for the realisation of multi-qubit gates [34, 40, 104].

4.2.1 Characterisation of the bare state qubits

The qubit considered in this work is formed of two long lived hyperfine states in $^{171}\text{Yb}^+$. Depending on the choice of states the qubit can be made to be magnetic field insensitive or magnetic field sensitive. The magnetic field insensitive qubit is formed of the $^2S_{1/2}|F = 0, m_f = 0\rangle = |0\rangle$ and $^2S_{1/2}|F = 1, m_f = 0\rangle = |0'\rangle$ states where both states are first-order magnetic field insensitive. If a magnetic field sensitive qubit is required then the magnetic field insensitive state $|0\rangle$ can be combined with either $^2S_{1/2}|F = 0, m_f = +1\rangle = |+1\rangle$ or $^2S_{1/2}|F = 0, m_f = -1\rangle = |-1\rangle$ which are both magnetic field sensitive.

The qubit can simply be manipulated by the use of microwave radiation at 12.6 GHz and changing the frequency allows selecting between the magnetic field sensitive and insensitive qubit. The microwaves are generated using a 12.6 GHz synthesised frequency generator[2] which pass through a switch before being amplified[3] (gain of 30 dB). The amplified signal is then applied to the ions via a microwave horn positioned 4 cm from the ion's position, making a 45° angle with the quantisation axis which is defined by a 9.8 G field. The quantisation axis is making a 90° angle with the weak trap axis. A picture of the microwave horn setup can be seen in figure 4.5.

Decoherence

An important property of a qubit is how long it retains its coherence, where the loss of coherence is known as decoherence. Any decoherence results in a loss of information of the quantum system and therefore needs to be minimised as much as possible. One source of decoherence is the limited lifetime of the state, also known as the T_1 time. Since the lifetime of the hyperfine states is on the order of years [105] it is disregarded in this work.

[2] HP 83712B
[3] Microwave amps AM25-12-13-30-33

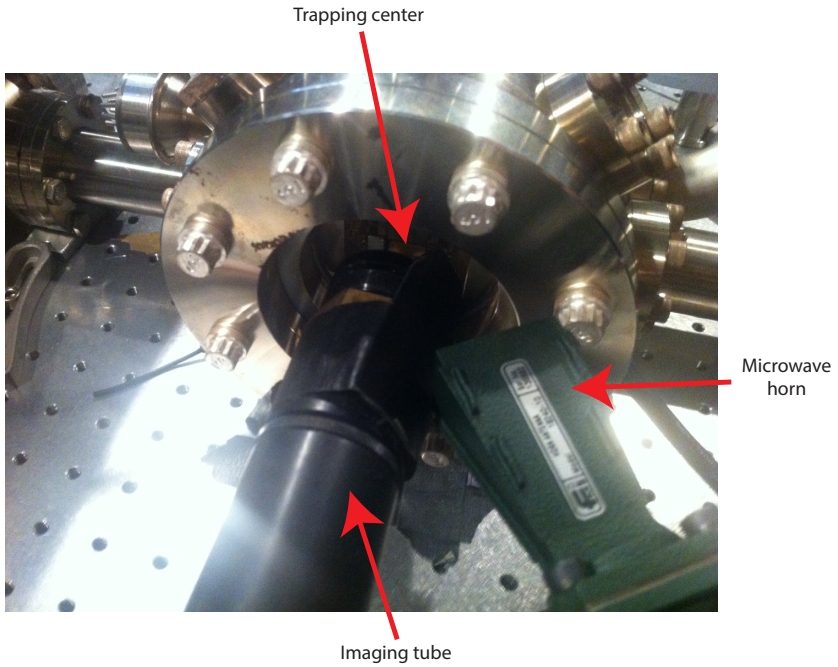

Figure 4.5: Picture showing the setup of the microwave horn with respect to the ion trap. The microwave horn is making a 45° angle with the quantisation axis. The quantisation axis is making a 90° angle with the weak trap axis and is parallel with the imaging tube. The coils used for defining the quantisation axis are not shown here.

Decoherence can also result from non-optimal coherent manipulations which will affect any subsequent gate operations. Other sources of decoherence include the instability of the microwave oscillator and often limits the achievable coherence time of magnetic field insensitive qubits [6].

When working with a magnetic field sensitive qubit the main source of decoherence stems from ambient magnetic field fluctuations. These fluctuations cause the energy of the Zeeman states and therefore the phase relationship between the two qubit states to fluctuate. This dephases a qubit superposition of the form $\alpha|0\rangle + e^{i\phi}\beta|+1\rangle$, where ϕ is the acquired phase of one of the qubit states with respect to the other qubit state. Therefore, after some free evolution time the superposition will decay into a mixed state which will eventually result in the probability of detecting one of the qubit states to approach 0.5. The decoherence due to this dephasing can be determined by measuring the free evolution time required for this to happen. This is known as the phase coherence time, also referred to as the T_2 time.

The magnetic field fluctuations in our setup are partly caused by the 50 Hz ac mains noise. The experimental sequence used in this work is therefore triggered off a fixed point on the 50 Hz cycle to minimise this source of decoherence. Nevertheless, magnetic field fluctuations are still a major source of decoherence which is shown later on.

Magnetic field insensitive qubit

In order to characterise the magnetic field insensitive qubit ($|0\rangle$ and $|0'\rangle$), coherent manipulations are performed by implementing the experimental sequence shown in figure 4.1. During the coherent manipulation window, microwaves with a frequency of $\omega = 12.642848\,\text{GHz}$ and a power of ≈ 1 W resonant with the $|0\rangle \leftrightarrow |0'\rangle$ transition are applied for an increasing period of time t which results in Rabi oscillations with a Rabi frequency of $\Omega = 2\pi \times 342\,\text{kHz}$, as shown in figure 4.6.

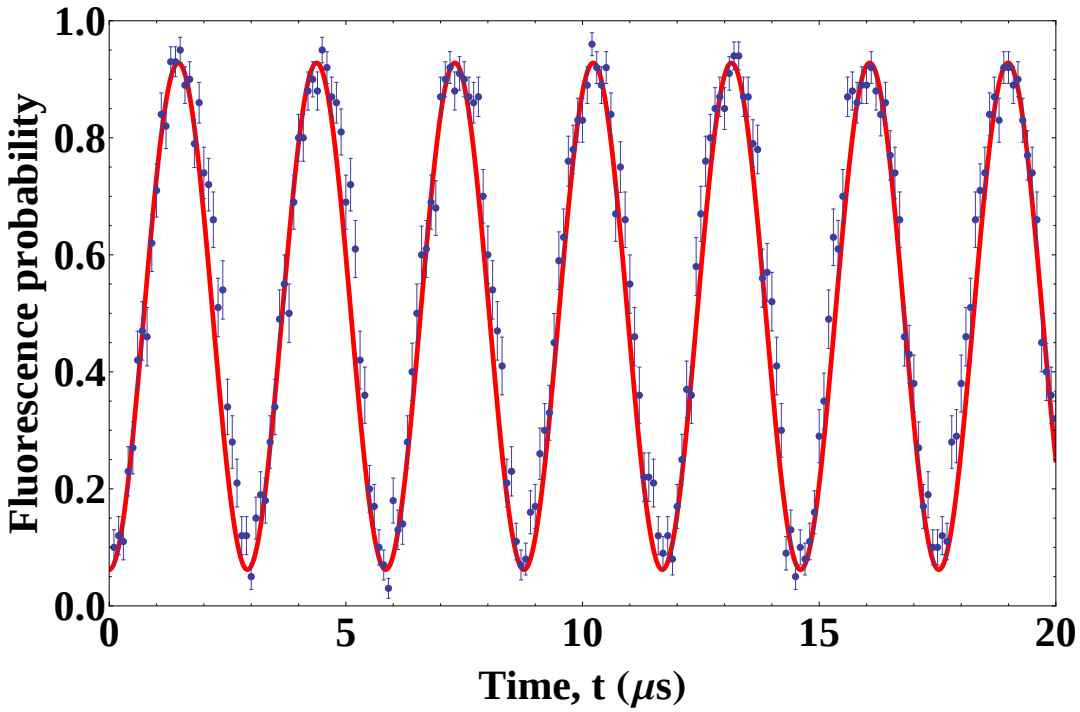

Figure 4.6: Rabi oscillations between the first-order magnetic field insensitive $|0\rangle$ and $|0'\rangle$ states. The transition is driven by applying one watt of microwave radiation at 12.642848 GHz to a microwave horn positioned 4 cm from the ion, producing oscillations with a Rabi frequency of $\Omega = 2\pi \times 342\,\text{kHz}$. Each point corresponds to 100 measurements.

To determine the T_2 coherence time of this qubit we perform a Ramsey-interference experiment [106]. One way of obtaining Ramsey fringes is by applying two $\pi/2$ microwave pulses with a fixed phase and a small detuning from resonance. The two pulses are separated by a precession time t giving the state vector time to precess. Varying this precession time then results in Ramsey fringes and are shown in figure 4.7. Here, the Ramsey fringes have a period of $1/(281\,\text{kHz})$ indicating that the two $\pi/2$ pulses are off-resonant by 281 kHz. In order to obtain an understanding of the level of coherence after a specific precession time the experiment can be modified. In this experiment we first apply a on-resonant microwave $\pi/2$ pulse with fixed phase, creating an equal superposition between $|0\rangle$ and $|0'\rangle$. After a fixed precession time t a second $\pi/2$ pulse with a variable

phase ϕ is applied before the state of the ion is detected.

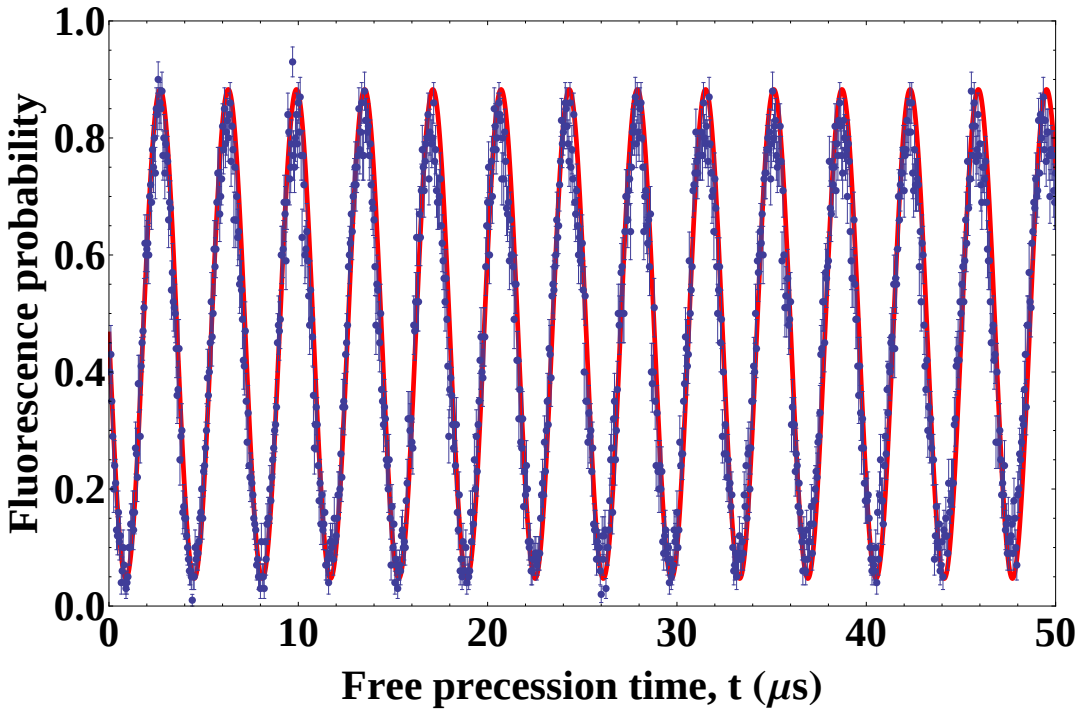

Figure 4.7: Ramsey fringes between $|0\rangle$ and $|0'\rangle$. Following preparation in $|0\rangle$ a detuned $\pi/2$ microwave pulse is applied followed by a second $\pi/2$ pulse after a variable precession time t which results in Ramsey fringes with a period of $1/(281\,\text{kHz})$ indicating that the $\pi/2$ pulses were 281 kHz off-resonant. Each point corresponds to 100 measurements.

To implement this experiment the microwave setup is required to be changed to allow for the two $\pi/2$ pulses to be of different phase. This is achieved by using a two-channel frequency source[4]. A switch is used to choose between the two rf signals (0.1-30 MHz), each of same frequency but different phase, before being mixed with the 12.6 GHz signal from the microwave oscillator using a mixer[5]. As before, the resultant signal is then sent to the microwave horn via a switch and an amplifier. This setup is shown in figure 4.8. Using this setup and Ramsey pulse sequence, a Ramsey fringe as shown in figure 4.9 (a) was obtained for a precession time $t = 15\,\text{ms}$. As discussed above, any dephasing between the two qubit states will eventually lead to a mixed state. We therefore repeat the experiment for an increasing precession time t and plot this versus the contrast of the Ramsey fringe. This can be seen in figure 4.9 (b). Using an exponential fit, we calculate a coherence time of 1.5 s. This is likely limited by magnetic field fluctuations through the second-order Zeeman shift of the qubit states [71].

While this demonstrates that this qubit is suitable for the implementation of single

[4] Agilent 33522A
[5] Mini-Circuit ZX05-153LH-S+

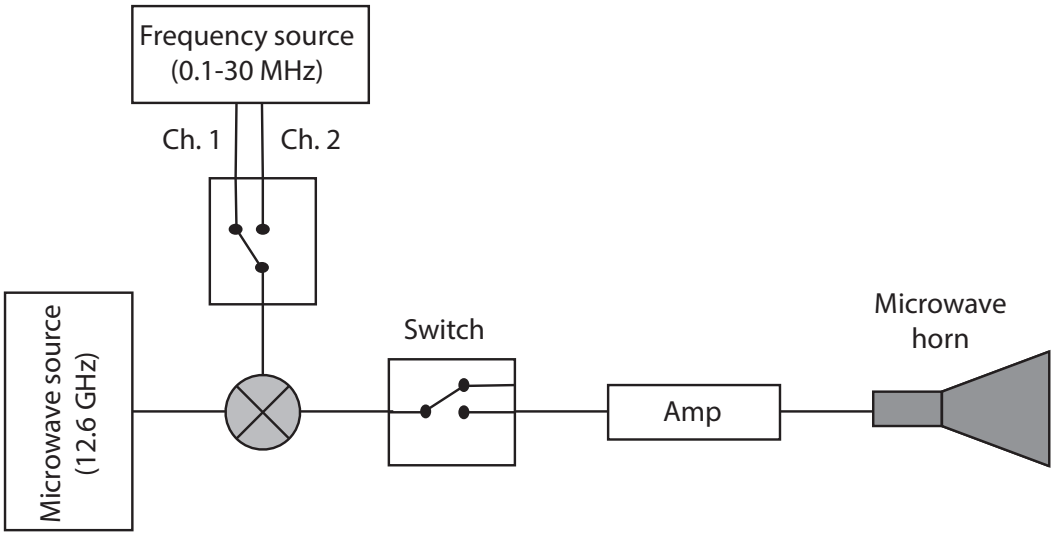

Figure 4.8: A schematic of the microwave setup used to implement Ramsey fringes. A two-channel frequency source is used to generate two rf signals of the same frequency but different phase. Fast switching between the two signals is achieved via a switch. The signal is then mixed with a microwave signal with a frequency near 12.6 GHz after which it is being sent to a microwave horn via another switch and a amplifier.

qubit gates and for storing quantum information, it is not suitable for the coupling between internal and motional states using the approach described above due to the very weak coupling of the qubit states to an external magnetic field. We therefore require a qubit which uses at least one magnetic field sensitive state which is described below.

Magnetic field sensitive qubit

A magnetic field sensitive qubit in the $^2S_{1/2}$ ground state of $^{171}\mathrm{Yb}^+$ can be formed using the $|0\rangle$ and $|-1\rangle$ state. Here, $|-1\rangle$ is a first-order magnetic field sensitive state.

Rabi oscillations between $|0\rangle$ and $|-1\rangle$ are induced using the same method as described above however this time using a microwave frequency of $\omega = 12.627648\,\mathrm{GHz}$. As can be seen in figure 4.10 (a), the contrast of the Rabi fringes is fast decaying and the coherence time does not exceed $500\,\mu\mathrm{s}$. This is due to the aforementioned ambient magnetic field fluctuations which cause a dephasing of the qubit. In contrast, figure 4.10 (b) shows Rabi oscillations between the magnetic field insensitive states $|0\rangle$ and $|0'\rangle$ extending over a period of 4 ms during which no decay of the contrast is observed. This reflects the coherence time of this qubit measured in the previous section.

We can see that while single qubit operations can be implemented using the magnetic field sensitive qubit and coupling the internal and motional states for multi-ion gate operations using the scheme described in section 4.2 should be possible, the short coherence time

(*a*)

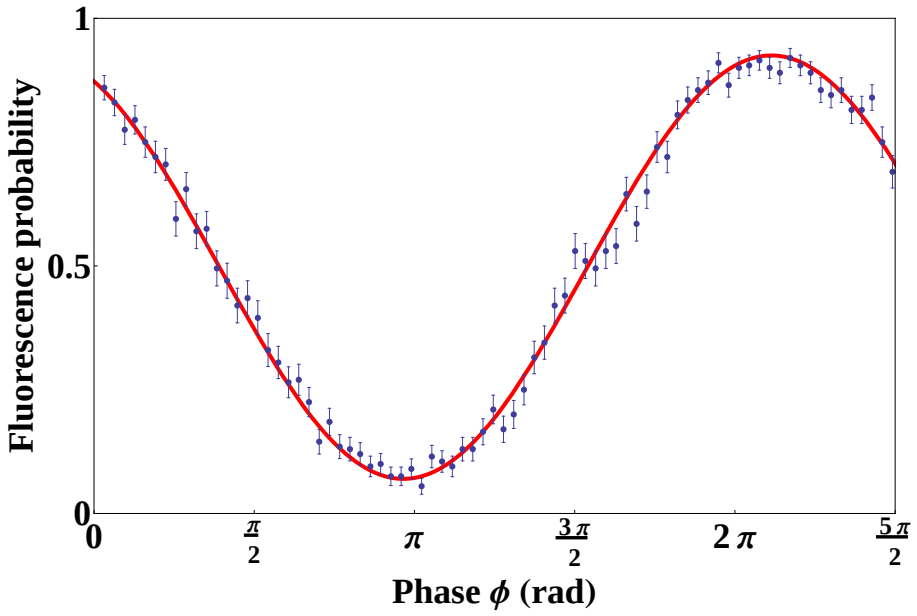

(*b*)

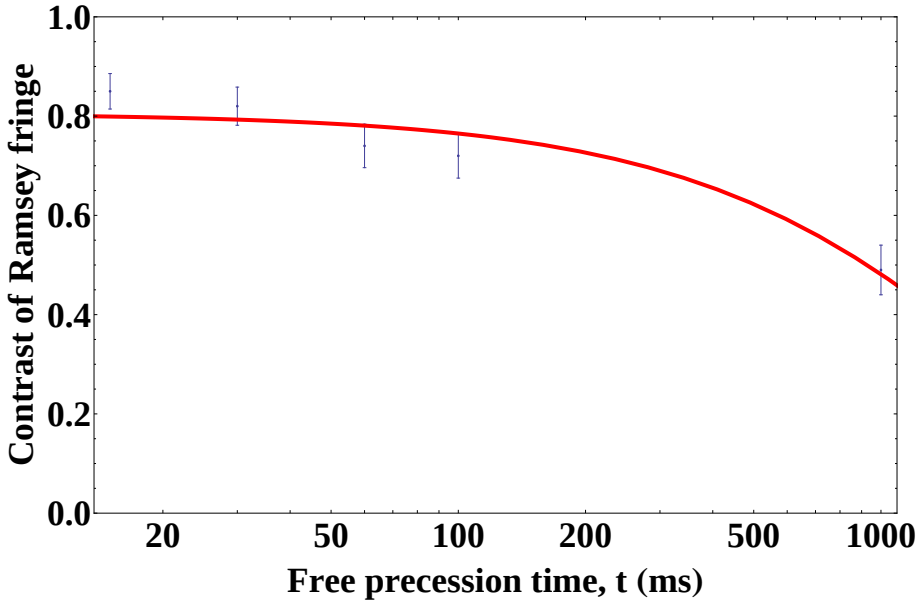

Figure 4.9: (a) Following preparation in $|0\rangle$ a resonant $\pi/2$ microwave pulse with fixed phase transfers the qubit into an equal superposition of $|0\rangle$ and $|0'\rangle$. After a fixed precession time t a second $\pi/2$ pulse with variable phase is applied resulting in Ramsey fringes. In this case $t = 15\,\text{ms}$. Each point consists to 100 measurements. (b) Coherence measurement of a qubit made up of the magnetic field insensitive $|0\rangle$ and $|0'\rangle$ states. Ramsey fringes as shown in (a) are taken for different delay times t between the two microwave $\pi/2$ pulses. A exponential fit to the decaying contrast of the Ramsey fringes over time results in a coherence time of 1.5 s.

(*a*)

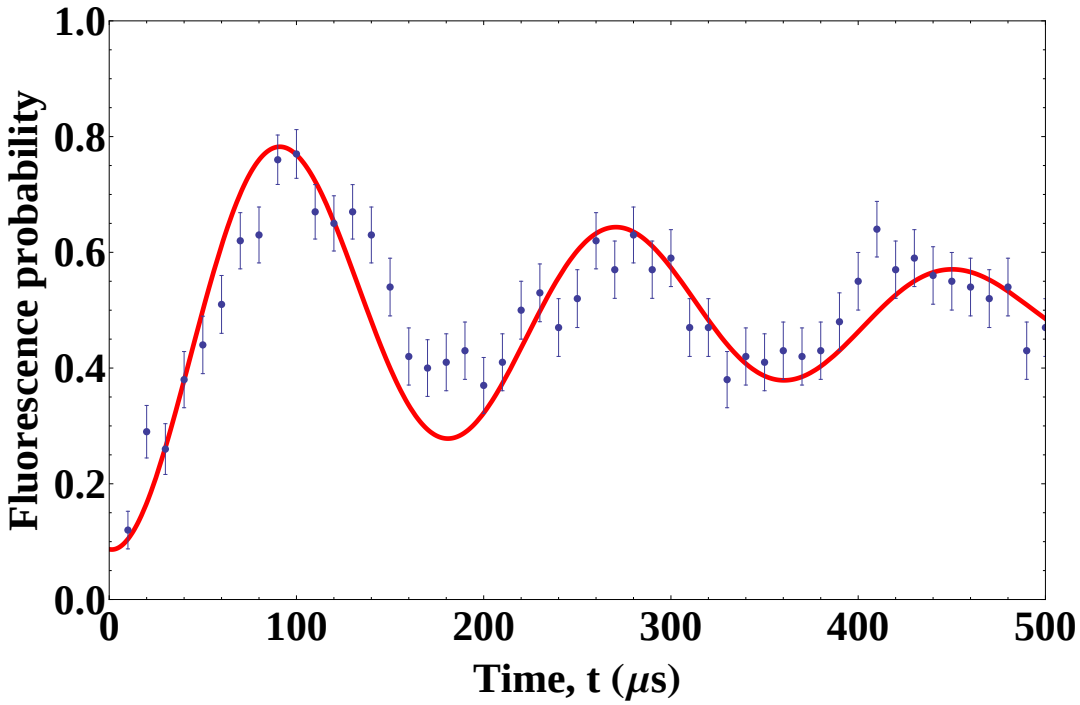

(*b*)

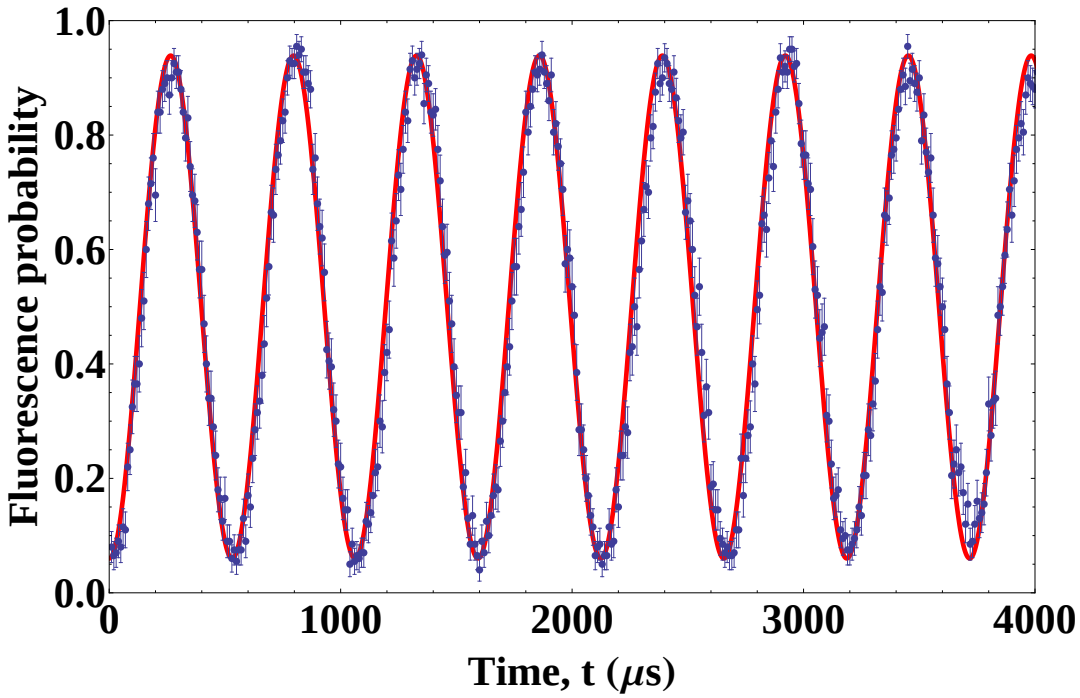

Figure 4.10: (a) Rabi oscillations between the first-order magnetic field insensitive state $|0\rangle$ and the magnetic field sensitive state $|-1\rangle$. The transition is driven by applying on-resonant microwaves at 12.627648 GHz. The fast decay of coherence is due to ambient magnetic field fluctuations which the $|-1\rangle$ state is very sensitive to. Each point corresponds of 100 measurements. In contrast, (b) shows Rabi oscillations between the first-order magnetic field insensitive states $|0\rangle$ and $|0'\rangle$ over a period of 4 ms during which no decay in contrast is visible. Each point corresponds of 200 measurements.

is a significant drawback for achieving high fidelities. A scheme to extend the coherence time of this qubit has been experimentally implemented [107] and used to demonstrate two-ion gate operations [103]. Nevertheless, while the work is very impressive, the achievable gate fidelity was low compared to those achieved in the optical regime. To address this issue and, for the first time, allow multi-qubit gate operations to be performed in the fault-tolerant regime, a step-changing approach which decouples this qubit from the noisy environment while still being sensitive to a static magnetic field gradient is required. This is the focus of the next chapter.

Chapter 5

Dressed-states

We have seen in chapter 4 that in order to implement multi-qubit gate operations using microwave radiation the energy separation of the two qubit states should have a large dependency on the magnetic field. While manipulation of such qubit is possible this dependence means that the coherence time is low, putting a limit on the achievable gate fidelity. The main source of decoherence stems from ambient magnetic field fluctuations making it desirable to implement a scheme that decouples the qubit from the environment. Such decoupling can be achieved using a series of pulses that each flip the state of the system and is often called bang-bang control [108]. It can also be achieved using a continuous driving of the qubit [109]. More recently these processes have been optimised theoretically [110] leading to impressive experimental demonstrations of a significantly decoupled qubit from the environment [111, 112].

Timoney *et al.* [40] introduced a scheme in which the qubit is formed by microwave-dressing two magnetic field sensitive states. The resultant dressed-state is magnetic field insensitive and is combined with a magnetic field insensitive bare state to form a new 'clock-state like' dressed-qubit. Manipulation of the qubit is possible using rf fields and allows the implementation of rotations around a specific axis in the x-y plane on the Bloch sphere only. The coherence time of their qubit was found to be more than two orders of magnitude longer compared to the magnetic field sensitive qubit, making it a very attractive qubit for the implementation of multi-qubit gates. We have implemented this scheme to obtain a dressed-state qubit and developed a experimentally simpler to implement method which allows direct manipulation of the dressed-state qubit around any axis in the x-y plane using a single rf field [113].

This chapter is structured in the following way. First, the scheme proposed by Timoney *et al.* will be summarised. Our scheme is then presented, highlighting the differences

as well as advantages and disadvantages. As part of the experimental section the preparation of the dressed-state is demonstrated and we investigate the effects on the preparation fidelity when varying experimental parameters. This is followed by a lifetime measurement of the dressed-state. Our modified scheme is then used to implement single qubit rotations and we show that Rabi oscillations can be maintained for more than two orders of magnitude longer compared to the magnetic field sensitive bare states.

5.1 Theory

A dressed-state is an eigenstate of the Hamiltonian which describes an atomic system being driven by near resonant electromagnetic fields. Microwave-dressed states can be implemented in the $^2S_{1/2}$ ground state hyperfine manifold of $^{171}Yb^+$ as demonstrated by Timoney *et al.* [40]. In their scheme the $|+1\rangle = {}^2S_{1/2}|F = 1, m_F = +1\rangle$, $|0\rangle = {}^2S_{1/2}|F = 0\rangle$, $|0'\rangle = {}^2S_{1/2}|F = 1, m_F = 0\rangle$ and the $|-1\rangle = {}^2S_{1/2}|F = 1, m_F = -1\rangle$ states are used, as shown in figure 5.1, where only the first-order Zeeman effect has been taken into account.

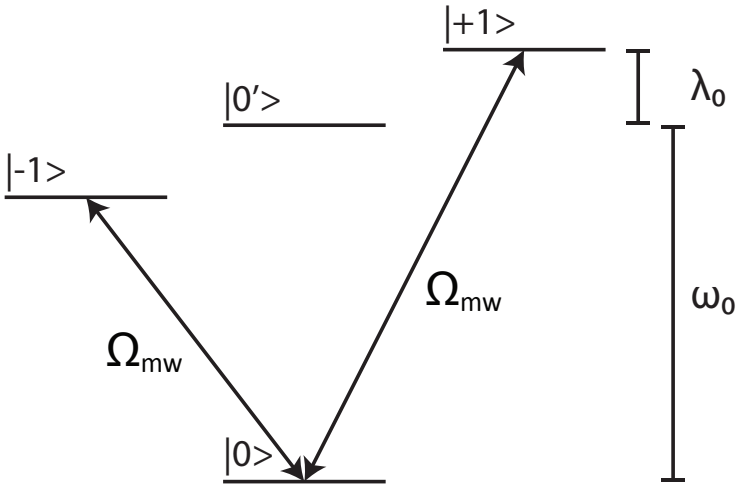

Figure 5.1: Not to scale energy level diagram of the $^2S_{1/2}$ ground state hyperfine manifold of $^{171}Yb^+$ where the degeneracy of the Zeeman states has been lifted by a magnetic field. Here $|0\rangle \leftrightarrow |+1\rangle$ and $|0\rangle \leftrightarrow |-1\rangle$ are coupled with resonant microwave radiation inducing Rabi oscillations with angular frequency of Ω_{mw}.

The Hamiltonian describing the unperturbed system is given by

$$\hat{H}_0 = -\hbar\omega_0|0\rangle\langle 0| + \hbar\lambda_0\left(|+1\rangle\langle +1| - |-1\rangle\langle -1|\right) \tag{5.1}$$

where ω_0 is the hyperfine splitting between the two clock states and λ_0 is the frequency

splitting between $|0'\rangle$ and the two magnetic field sensitive states $|+1\rangle$ and $|-1\rangle$, corresponding to the first-order Zeeman shift. The $|+1\rangle$, $|0\rangle$ and $|-1\rangle$ states are coupled using resonant microwave radiation giving an additional term in the Hamiltonian of

$$\hat{H}_{mw} = \frac{\hbar\Omega_{mw}}{2}\left(e^{i\omega_{+1}}|+1\rangle\langle 0| + e^{i\omega_{-1}}|-1\rangle\langle 0| + h.c.\right) \tag{5.2}$$

where Ω_{mw} is the Rabi frequency of the two dressing fields, $\omega_{\pm 1} = \omega_0 \pm \lambda_0$ and the phase of the driving fields has been set to zero. Moving into the interaction picture $\hat{H}^I_{mw} = e^{i\hat{H}_0 t/\hbar}\hat{H}_{mw}e^{-i\hat{H}_0 t/\hbar}$ and performing the RWA, we can write the interaction Hamiltonian as

$$\hat{H}^I_{mw} = \frac{\hbar\Omega_{mw}}{2}\left(|+1\rangle\langle 0| + |-1\rangle\langle 0| + h.c.\right). \tag{5.3}$$

The eigenstates of this Hamiltonian are

$$|D\rangle = \frac{1}{\sqrt{2}}\left(|+1\rangle - |-1\rangle\right) \tag{5.4}$$

$$|u\rangle = \frac{1}{2}|+1\rangle + \frac{1}{2}|-1\rangle + \frac{1}{\sqrt{2}}|0\rangle \tag{5.5}$$

$$|d\rangle = \frac{1}{2}|+1\rangle + \frac{1}{2}|-1\rangle - \frac{1}{\sqrt{2}}|0\rangle. \tag{5.6}$$

The interaction Hamiltonian in equation 5.3 can now be written in terms of these dressed-states as

$$\hat{H}^I_{mw} = \frac{\hbar\Omega_{mw}}{\sqrt{2}}\left(|u\rangle\langle u| - |d\rangle\langle d|\right). \tag{5.7}$$

$|D\rangle$ is a equal superposition of the magnetic field sensitive states $|+1\rangle$ and $|-1\rangle$ making it useful for experiments that require motional coupling using magnetic field gradients as described in chapter 4.

While the bare states $|+1\rangle$ and $|-1\rangle$ quickly dephase as a result of magnetic field fluctuations, dephasing of $|D\rangle$ is suppressed. This can be seen by treating the magnetic field fluctuations as a perturbation of the form

$$\hat{H}_p = \hbar\lambda_0(t)\left(|+1\rangle\langle +1| - |-1\rangle\langle -1|\right) \tag{5.8}$$

which is added to the total Hamiltonian $\hat{H}_0 + \hat{H}_{mw}$. The perturbation remains unchanged when moving into the interaction picture as it commutes with $\hat{H}_0$ given in equation 5.1.

Writing the perturbation in the dressed-state basis gives

$$\hat{H}_p^I = \frac{\hbar\lambda_0(t)}{\sqrt{2}}\left(|D\rangle\langle u| + |D\rangle\langle d| + h.c.\right) \tag{5.9}$$

from which we can see that magnetic field fluctuations will drive population from $|D\rangle$ to $|u\rangle$ and $|d\rangle$. It becomes obvious from equation 5.7 that these states are separated by an energy gap corresponding to $\hbar\Omega_{mw}/\sqrt{2}$ which is also illustrated in figure 5.2. Only magnetic field fluctuations with a frequency at or near $\Omega_{mw}/\sqrt{2}$ will therefore lead to dephasing of $|D\rangle$.

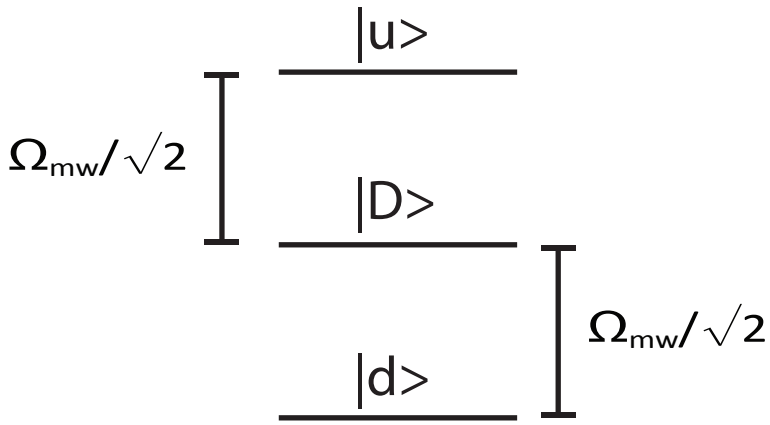

Figure 5.2: Energy level diagram of the dressed states $|D\rangle$, $|u\rangle$ and $|d\rangle$ when $|0\rangle \leftrightarrow |+1\rangle$ and $|0\rangle \leftrightarrow |-1\rangle$ are coupled with strength Ω_{mw}. It can be seen that there is an energy gap between $|D\rangle$ and the unwanted states $|u\rangle$ and $|d\rangle$ of $\Omega_{mw}/\sqrt{2}$. Only magnetic field fluctuations near $\Omega_{mw}/\sqrt{2}$ will therefore cause decoherence of $|D\rangle$.

In the work by Timoney *et al.* manipulation of the dressed-state is achieved by coupling $|+1\rangle$, $|0'\rangle$ and $|-1\rangle$ using rf radiation as shown in figure 5.3. The Hamiltonian describing the rf part of the system is given by

$$\hat{H}_{rf} = \frac{\hbar\Omega_{rf}}{2}\left(e^{i(\lambda_0 t+\phi_{rf})}|+1\rangle\langle 0'| + e^{i(\lambda_0 t-\phi_{rf})}|-1\rangle\langle 0'| + h.c.\right) \tag{5.10}$$

where Ω_{rf} is the Rabi frequency induced by the rf field and λ_0 and ϕ_{rf} is the frequency and phase of the rf field respectively.

As was done for the Hamiltonian describing the interaction with the microwave fields we can transform $\hat{H}_{rf}$ into the interaction picture ($\hat{H}_{rf}^I = e^{i\hat{H}_0 t/\hbar}\hat{H}_{rf}e^{-i\hat{H}_0 t/\hbar}$) and perform the RWA to get

$$\hat{H}_{rf}^I = \frac{\hbar\Omega_{rf}}{2}\left(e^{\phi_{rf}}|-1\rangle\langle 0'| + e^{-\phi_{rf}}|+1\rangle\langle 0'| + h.c.\right). \tag{5.11}$$

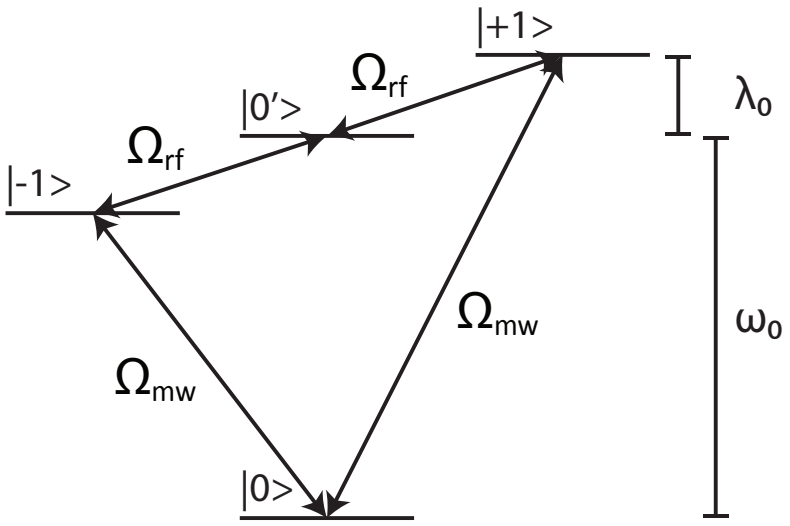

Figure 5.3: Not to scale energy level diagram of the $^2S_{1/2}$ ground state hyperfine manifold of $^{171}Yb^+$ where the degeneracy of the Zeeman states has been lifted by a magnetic field. While $|0\rangle \leftrightarrow |+1\rangle$ and $|0\rangle \leftrightarrow |-1\rangle$ are coupled with resonant microwave radiation with Rabi frequency Ω_{mw}, the dressed state qubit consisting of $|D\rangle$ and $|0'\rangle$ can be manipulated using an rf field to couple $|0'\rangle$ to $|+1\rangle$ and $|-1\rangle$ with Rabi frequency Ω_{rf}.

We can then re-write this Hamiltonian in the dressed-state basis to give

$$\hat{H}^I_{rf} = \frac{\hbar\Omega_{rf}}{2}\left(\cos\phi_{rf}\left(|u\rangle + |d\rangle\right)\langle 0'| - \sqrt{2}i\sin\phi_{rf}|D\rangle\langle 0'| + h.c.\right). \tag{5.12}$$

The total Hamiltonian in the interaction picture ($\hat{H}^I_t = \hat{H}^I_{mw} + \hat{H}^I_{rf}$) can now be written as

$$\hat{H}^I_t = \frac{\hbar\Omega_{mw}}{2}\left(|u\rangle\langle u| - |d\rangle\langle d|\right) + \frac{\hbar\Omega_{rf}}{2}\left(\cos\phi_{rf}\left(|u\rangle + |d\rangle\right)\langle 0'| - \sqrt{2}i\sin\phi_{rf}|D\rangle\langle 0'| + h.c.\right). \tag{5.13}$$

We see that by setting the phase ϕ_{rf} to $\pi/2$ the rf part of the total Hamiltonian becomes

$$\hat{H}^I_{rf} = \frac{\hbar\Omega_{rf}}{\sqrt{2}}i\left(|0'\rangle\langle D| - |D\rangle\langle 0'|\right) \tag{5.14}$$

which corresponds to a σ_y rotation on the Bloch sphere (equivalent to that shown in equation 4.15) where the qubit consists of the dressed-state $|D\rangle$ and clock-state $|0'\rangle$. We can see from equation 5.18 that while $\phi_{rf} = \pi/2$ maximises the coupling between the two qubit states, varying this phase not only changes the coupling but also leads to coupling between $|0'\rangle$ and $|u\rangle$ and $|d\rangle$. This coupling therefore drives population out of the qubit subspace causing decoherence. Simply varying the phase to change the axis in the x-y plane about which a given rotation is being performed, as is the case for a standard

two-level system, is not possible using this scheme and therefore limits its usefulness.

5.1.1 Alternative dressed-state manipulation scheme

So far we have only considered the first-order Zeeman shift resulting in the energy of $|0\rangle$ and $|0'\rangle$ being unaffected by the applied magnetic field. We therefore have that the frequency splitting, λ_0, between $|0'\rangle$ and $|+1\rangle$ and between $|0'\rangle$ and $|-1\rangle$ is the same. For typical magnetic field strengths used in ion trap experiments (on the order of 10 Gauss) only considering the first-order Zeeman shift is not sufficient and it is possible to develop a new method to manipulate the dressed-state qubit which takes advantage of the second-order Zeeman shift.

To determine the second-order Zeeman shift we consider the $|0'\rangle$ state for which the Breit-Rabi formula simplifies to [114]

$$\Delta E = \frac{\hbar\omega_0}{4}\left(-1 + 2\sqrt{1+\left(\frac{2\mu_B B}{\hbar\omega_0}\right)^2}\right). \tag{5.15}$$

From this the relative angular frequency shift of $|0'\rangle$ due to the second-order Zeeman effect can be expressed as

$$\delta\omega = \frac{\omega_0}{2}\left(-1 + \sqrt{1+\left(\frac{2\mu_B B}{\hbar\omega_0}\right)^2}\right). \tag{5.16}$$

For the case of a applied B-field strength of 10 Gauss the frequency difference between the two rf transitions is $2\delta\omega/2\pi = 15.5\,\text{kHz}$. If $\Omega_{rf} \ll 2\delta\omega$ then we can selectively couple either $|0'\rangle \leftrightarrow |+1\rangle$ or $|0'\rangle \leftrightarrow |-1\rangle$ using a single rf field. This is illustrated in figure 5.4. While the microwave part in equation 5.7 remains unchanged, the rf part in equation 5.11 becomes

$$\hat{H}^I_{rf} = \frac{\hbar\Omega_{rf}}{2}\left(e^{-i\phi_{rf}}|+1\rangle\langle 0'| + h.c.\right) \tag{5.17}$$

when using a single rf field to couple $|0'\rangle \leftrightarrow |+1\rangle$, ignoring the far from resonant $|0'\rangle \leftrightarrow |-1\rangle$ transition. When writing this in the dressed-state basis the Hamiltonian becomes

$$\hat{H}^I_{rf} = \frac{\hbar\Omega'_{rf}}{2}\left(e^{-i\phi_{rf}}|D\rangle\langle 0'| + h.c.\right) + \frac{\hbar\Omega'_{rf}}{2\sqrt{2}}\left(e^{-i\phi_{rf}}\left(|u\rangle + |d\rangle\right)\langle 0'| + h.c.\right) \tag{5.18}$$

where $\Omega'_{rf} = \Omega_{rf}/\sqrt{2}$. We know that $|0'\rangle$ is separated from $|u\rangle$ and $|d\rangle$ by an energy gap corresponding to $\Omega_{mw}/\sqrt{2}$. Satisfying $\Omega'_{rf} \ll \Omega_{mw}$ therefore allows us to ignore the second

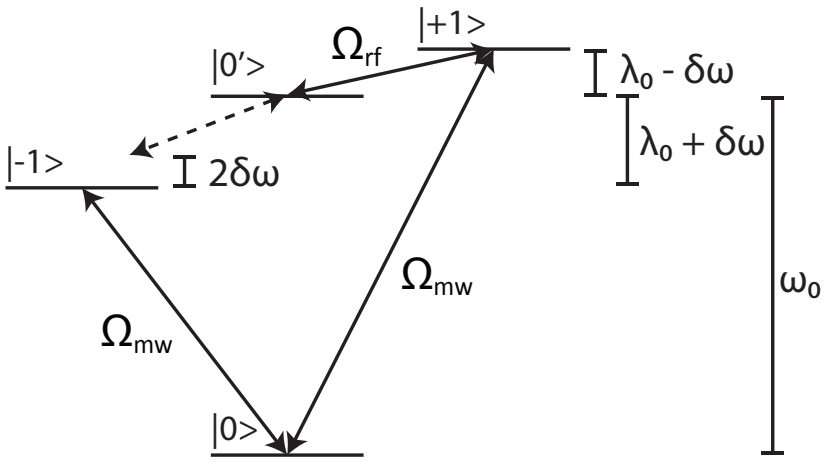

Figure 5.4: Not to scale energy level diagram of the $^2S_{1/2}$ ground state hyperfine manifold of $^{171}Yb^+$ where the degeneracy of the Zeeman states has been lifted by a sufficiently strong magnetic field to cause $|0'\rangle$ to obtain a relative energy shift $\delta\omega$ due to the second-order Zeeman effect. This causes $|0'\rangle \leftrightarrow |+1\rangle$ and $|0'\rangle \leftrightarrow |-1\rangle$ to have non-equal transition frequencies. A single rf field can therefore be used to manipulate the dressed-state qubit by selectively coupling $|0'\rangle$ to $|+1\rangle$ (shown here) or to $|-1\rangle$ with Rabi frequency Ω_{rf}. $|0\rangle \leftrightarrow |+1\rangle$ and $|0\rangle \leftrightarrow |-1\rangle$ are coupled with resonant microwave radiation with Rabi frequency Ω_{mw} to create the dressed-state qubit.

part in equation 5.18 and we have

$$\hat{H}^I_{rf} = \frac{\hbar\Omega'_{rf}}{2}\left(e^{-i\phi_{rf}}|D\rangle\langle 0'| + h.c.\right). \tag{5.19}$$

Arbitrary single qubit operations can now be implemented and only requires a single rf field as long as $\Omega_{rf} \ll \delta\omega$ and $\Omega'_{rf} \ll \Omega_{mw}$. Furthermore, this scheme halves the number of rf fields required to implement a Mølmer and Sørensen type multi-qubit gate operation. A drawback of this scheme compared to the previously proposed and implemented scheme is that the Rabi frequency Ω'_{rf} is suppressed by a factor of $\sqrt{2}$ and is also limited by the achievable Rabi frequency of the microwave fields (Ω_{mw}). The latter can be addressed by further amplifying the microwave fields before they are sent to the microwave horn which would significantly increase Ω_{mw}. Additional increases in Ω_{mw} can be achieved by reducing the distance between the microwave horn and the ion(s) by placing the horn inside the vacuum system. It is also possible to use a microwave waveguide on a microfabricated surface trap to increase Ω_{mw} [38].

5.1.2 STIRAP

Preparation of the dressed-state $|D\rangle$ can not be achieved in the same way one usually prepares a bare atomic state. In this work $|D\rangle$ is prepared using a partial Stimulated Raman Adiabatic Passage (STIRAP) process. For illustrative purposes we first consider a three-level system and a complete STIRAP pulse sequence process as shown in figure 5.5 (a) and (b) respectively. STIRAP is often used to transfer population between two

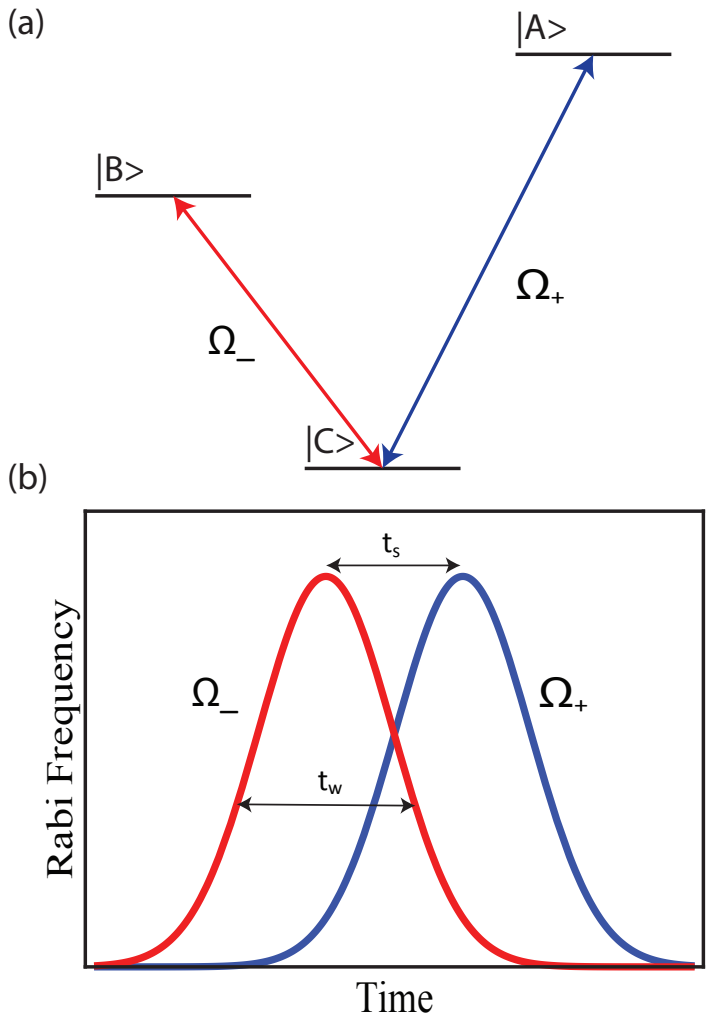

Figure 5.5: Illustration of STIRAP. (a) shows three states coupled together using two fields with Rabi frequency Ω_- and Ω_+ to transfer population from $|A\rangle$ to $|B\rangle$ via state $|C\rangle$ which, if done correct, does not get populated. (b) shows the two Gaussian Rabi frequency pulse envelopes of FWHM width t_w separated in time t_s in a counter-intuitive order where, in order to transfer population from $|A\rangle$ to $|B\rangle$, $|B\rangle$ and $|C\rangle$ are coupled first to create a coherent superposition. The second pulse then couples $|A\rangle$ to this superposition.

states, $|A\rangle$ and $|B\rangle$, via a third state, $|C\rangle$, where direct transition is forbidden. While it would seem natural to achieve this by first applying a π-pulse to transfer population from $|A\rangle$ to $|C\rangle$ followed by a second π-pulse transferring population from $|C\rangle$ to $|A\rangle$, the

intermediate state $|C\rangle$ is often one which induces significant decoherence and should be avoided. A special feature of STIRAP is that population is transferred between state $|A\rangle$ and $|B\rangle$ without populating $|C\rangle$. This is achieved using a adiabatic non-intuitive Gaussian pulse sequence shown in figure 5.5 (b) where $|B\rangle$ and $|C\rangle$ are coupled before $|A\rangle$ and $|C\rangle$. Adiabatic in this case means that the environment of the ion created by the driving fields, in this case the STIRAP pulses, changes slow enough for the instantaneous eigenstates (adiabatic states) of the system to follow so that the dark state, which only connects the initial and final state, is populated at all times [115].

We use Gaussian envelopes for the STIRAP pulses which are defined by

$$\Omega_+(t) = \Omega_\mathrm{P} \exp\left[-\frac{t^2}{2\left(t_w/2\sqrt{2\ln 2}\right)^2}\right] \tag{5.20}$$

$$\Omega_-(t) = \Omega_\mathrm{p} \exp\left[-\frac{(t-t_s)^2}{2\left(t_w/2\sqrt{2\ln 2}\right)^2}\right] \tag{5.21}$$

where Ω_P is the maximum amplitude of the Gaussian waveform which also corresponds to the peak Rabi frequency, t_s is the separation between the two pulses and t_w is the width of the waveform.

For the case of the ground state hyperfine manifold of $^{171}\mathrm{Yb}^+$ shown in figure 5.1, $|A\rangle$, $|B\rangle$ and $|C\rangle$ correspond to $|+1\rangle$, $|-1\rangle$ and $|0\rangle$ respectively. Figure 5.6 (a) shows a typical STIRAP pulse sequence used in our experiments where, for illustrative purposes, $\Omega_p = 2\pi \times 25\,\mathrm{kHz}$, $t_w = 300\,\mu\mathrm{s}$ and $t_s = 350\,\mu\mathrm{s}$. Figure 5.6 (b) shows the result of a numerical simulation of the population of the three involved bare states and the dressed-state $|D\rangle$, $|u\rangle$ and $|d\rangle$ and it shows how the population evolves after preparation in $|+1\rangle$ when subjected to the non-intuitive pulse sequence shown in figure 5.6 (a).

The steps involved in transferring population between $|+1\rangle$ and $|-1\rangle$, during which $|D\rangle$ is populated using STIRAP, are as follows (compare with figure 5.6):

1. The population is transferred to state $|+1\rangle$.

2. A resonant pulse is applied to couple the unpopulated states $|0\rangle$ and $|-1\rangle$. While this does not change the population of $|+1\rangle$ it does create a coherent superposition between states $|0\rangle$ and $|-1\rangle$.

3. After some time delay a second pulse resonant with the $|+1\rangle \leftrightarrow |0\rangle$ transition is applied which couples $|+1\rangle$ to the superposition. This leads to the dark state to

evolve from the bare state $|+1\rangle$ via the dressed state $|D\rangle = \frac{1}{\sqrt{2}}(|+1\rangle - |-1\rangle)$ to the bare state $|-1\rangle$ without populating $|0\rangle$. The population in $|D\rangle$ is maximised when $\Omega_- = \Omega_+$ i.e. when the Rabi frequencies of the two transitions are equal. Any non-adiabatic processes will lead to population in $|0\rangle$ and therefore lead to a reduced transfer efficiency and indeed a reduced preparation efficiency of $|D\rangle$.

While we can see that STIRAP is a useful way of transferring population between two states it also becomes obvious that it is a great tool for preparing $|D\rangle$. The population in $|D\rangle$ is maximised at the crossing of the two pulses where the amplitudes are equal. If we want to maintain the population in $|D\rangle$ for some time we simply hold the amplitudes constant at their crossing. During this hold the qubit is formed of $|D\rangle$ and $|0'\rangle$ and can be manipulated using a rf field as described above. Following qubit manipulation, the STIRAP pulse sequence simply carries on which transfers any population in $|D\rangle$ to $|-1\rangle$ while leaving population in $|0'\rangle$ unaffected. This allows state detection of the dressed-state qubit using the bare states.

5.2 Experimental setup

Preparing the dressed-state requires two Gaussian pulses in the microwave regime separated in time. These pulses need to be held at a constant amplitude for a certain amount of time before the pulse sequence is resumed. The experimental setup to achieve this is shown in figure 5.7. During the hold, when the population in $|D\rangle$ is maximised, a rf field is required to manipulate the dressed-state qubit. In this section the experimental setup used for generating the required microwave and rf fields is also described.

5.2.1 Microwave setup

To implement microwave dressed-states for a single ion, two microwave fields coupling $|+1\rangle \leftrightarrow |0\rangle$ and $|-1\rangle \leftrightarrow |0\rangle$ are required. We achieve these fields using the setup shown in figure 5.7 where the output from a high frequency source[1] is frequency mixed with the two outputs from a two-channel low frequency source[2]. The two low frequency signals are first combined using a power splitter/combiner[3]. The high frequency signal is then mixed with the combined low frequency signals using a high frequency mixer[4]. Here, the mixer produces first order-sidebands corresponding to the microwave frequency plus and minus

[1] HP 83712B
[2] Agilent 33522A
[3] Mini-Circuit ZMSC-2-2
[4] Mini-Circuit ZX05-153LH-S+

(*a*)

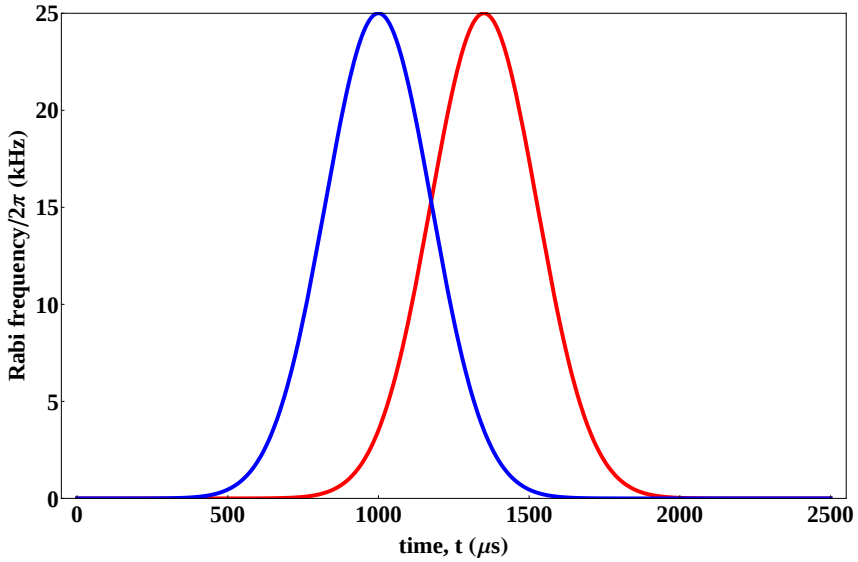

(*b*)

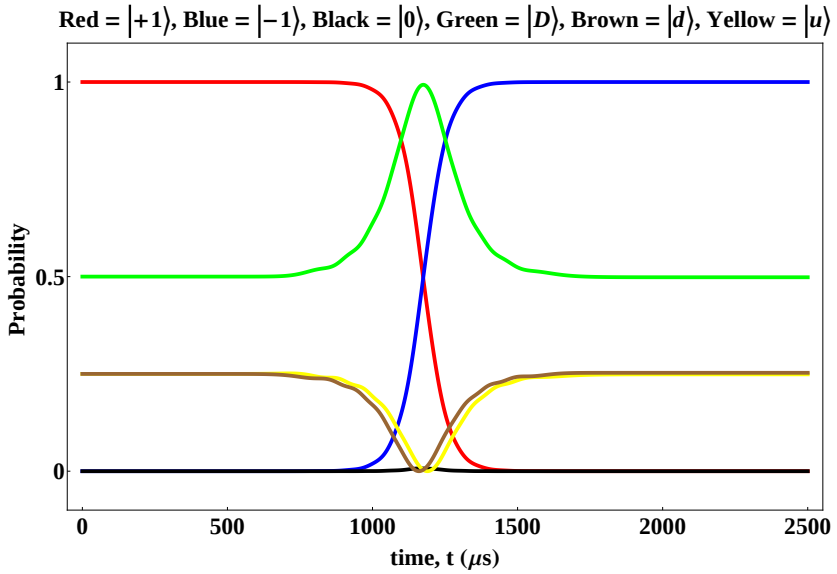

Figure 5.6: (a) typical STIRAP pulse sequence where $\Omega_p = 2\pi\times 25\,\text{kHz}$, $t_w = 300\,\mu\text{s}$ and $t_s = 350\,\mu\text{s}$. (b) numerical simulation of the population of the bare states $|+1\rangle$, $|0\rangle$ and $|-1\rangle$ as well as the dressed state $|D\rangle = \frac{1}{\sqrt{2}}(|+1\rangle - |-1\rangle)$, $|u\rangle = \frac{1}{2}|+1\rangle + \frac{1}{2}|-1\rangle + \frac{1}{\sqrt{2}}|0\rangle$ and $|d\rangle = \frac{1}{2}|+1\rangle + \frac{1}{2}|-1\rangle - \frac{1}{\sqrt{2}}|0\rangle$ when subjected to the pulse sequence shown in (a). While STIRAP is shown to transfer population from $|+1\rangle$ to $|-1\rangle$ without populating the intermediate state $|0\rangle$ it can also be seen that population in $|D\rangle$ is maximised at the crossing point of the two STIRAP pulses.

each of the two low frequency signals. It is then possible to use, for example, the positive first-order sideband corresponding to one of the low frequency signals to couple $|-1\rangle \leftrightarrow |0\rangle$ and the first order positive sideband corresponding to the other low frequency signal to couple $|+1\rangle \leftrightarrow |0\rangle$. The other two sidebands are far off-resonant and do not effect the experiment.

To produce the required complex waveforms such as Gaussian pulses with a hold at a specific point in time to prepare $|D\rangle$, the two waveforms are created using LABVIEW running on an FPGA which has its own digital-to-analog converter (DAC). The waveforms are then each mixed with one of the two low frequency signals using low frequency mixers[5]. When the waveform is mixed with the low frequency signal the mixer acts like a dynamic switch where the amplitude of the waveform determines the amplitude of the low frequency output.

Before the STIRAP pulse sequence is applied to the ion we prepare the ion in $|-1\rangle$ or $|+1\rangle$ using a microwave π-pulse and require a further π-pulse after STIRAP as part of the detection sequence. We therefore require the microwave setup to also be able to output a constant microwave signal just before and after the STIRAP pulse sequence. While in principle the same analog outputs used for the complex waveform generation could be used, in practice it is easier to switch between different analog outputs. To achieve this a fast analog switch is used between the output of the FPGA and the low frequency mixer to switch between a constant voltage (corresponding to a constant microwave output) and the waveforms required to implement the STIRAP pulse sequence.

The final microwave setup can be seen in figure 5.7 where the final switch, amplifier and microwave horn as shown in chapter 4 are not shown. Figure 5.8 shows the analog signal, as measured on a oscilloscope, sent to the low frequency mixers where the violet and blue coloured pulses correspond to the signal measured at point 3 and 4 in figure 5.7 respectively. Clearly visible is the STIRAP pulse sequence which is sandwiched in between two π-pulses as part of the state preparation and detection sequence. The green signal corresponds to a TTL pulse which turns the rf field on for single qubit manipulation via a rf switch.

Table 5.1 shows typical powers and frequencies used in the experiments shown in this chapter along with the resultant output after the final mixer [6]. The final frequencies and corresponding powers (before amplification using the setup shown in chapter 4) used to

[5] Mini Circuit ZX05-1L-S+

[6] Only first-order terms are considered as they are used in the experiment however one has to be aware of higher-order terms due to the non-linear properties of a mixer and ensure they do not couple to any unwanted transitions.

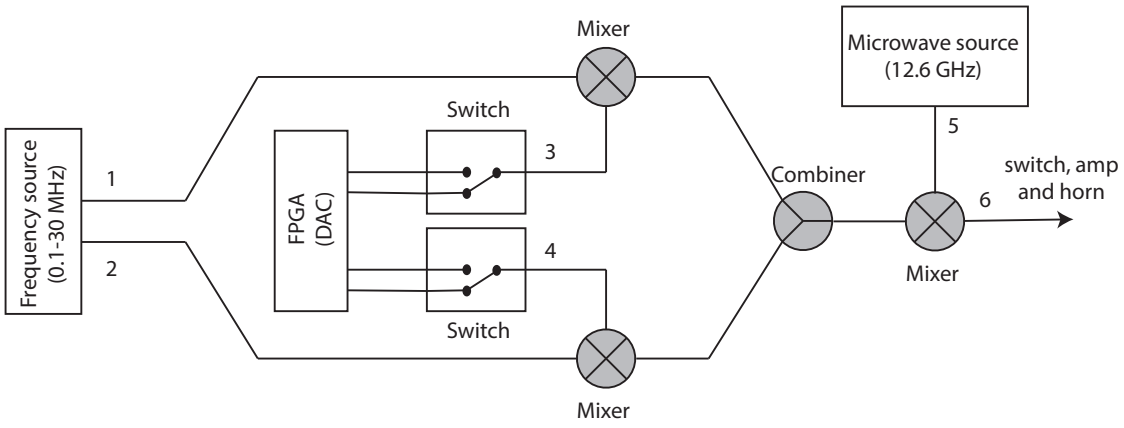

Figure 5.7: Illustration of the microwave setup used in this chapter to prepare $|D\rangle$. Two low frequency signals are individually mixed with either a constant voltage to implement single qubit gates or a pulse envelope corresponding to the required Gaussian STIRAP pulses. Two switches are used to switch between the two different voltage profiles. The two signals are then combined before being lifted into the microwave regime using a high frequency mixer which mixes the two signals with a 12.6 GHz signal. The output is then passed through a switch, amplifier and microwave horn which is not shown here however an illustration of this can be found in chapter 4. The numbering corresponds to points at which the frequency and power of the signals was measured which can be seen in table 5.1.

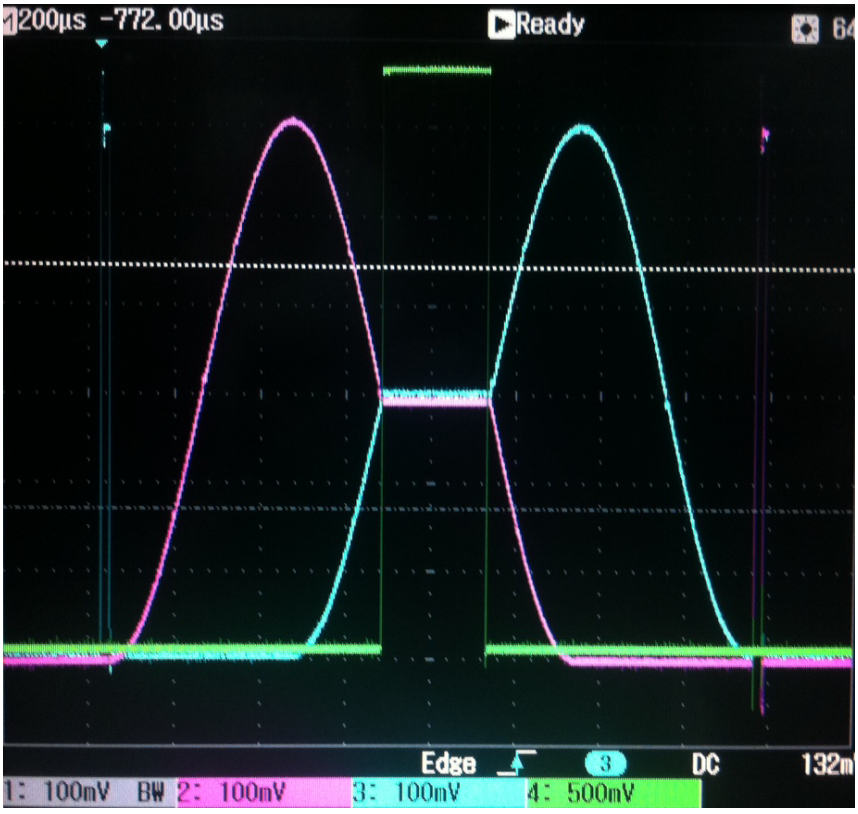

Figure 5.8: Picture of the analog pulse sequence used for STIRAP. The violet and blue signals are measured using a oscilloscope connected to points 3 and 4 in figure 5.7 respectively. The green signal corresponds to a TTL pulse sent to the rf switch for single qubit manipulation during the hold of the STIRAP.

Number	Frequency	Power	Transition
1	2.210 MHz	-1 dBm	
2	29.636 MHz	0 dBm	
3	Gaussian/dc	0.61 V	
4	Gaussian/dc	0.61 V	
5	12.626859 GHz	6 dBm	
6	12.626859 GHz	-37 dBm	
	12.629066 GHz (+2.210 MHz)	-18 dBm	$\|0\rangle \leftrightarrow \|-1\rangle$
	12.624646 GHz (-2.210 MHz)	-18 dBm	
	12.656492 GHz (+29.636 MHz)	-18 dBm	$\|0\rangle \leftrightarrow \|+1\rangle$
	12.597220 GHz (-29.636 MHz)	-18 dBm	

Table 5.1: Table showing typical frequencies and corresponding powers used in the experiments in this chapter measured at six different points of the experimental setup as illustrated by the numbering in figure 5.7. The number in the bracket illustrates which low frequency signal mixed with the 12.6 GHz signal to obtain the quoted resultant frequency. The powers given for number 3 and 4 correspond to the peak power of the Gaussian waveform. Also shown is which frequency of the resultant spectrum couples to the desired transitions. The numbers shown here correspond to a Rabi frequency of $2\pi\times25$ kHz once the signal has been amplified using the setup shown in chapter 4.

couple $|0\rangle \leftrightarrow |-1\rangle$ and $|0\rangle \leftrightarrow |+1\rangle$ are also shown. Following amplification this results in a Rabi frequency of $2\pi\times25$ kHz .

The comparably low Rabi frequency is not a fundamental limit and it should be possible to increase this by upgrading the microwave setup. The current limits of the setup are the inexpensive mixers which have a high conversion loss. Furthermore the third-order intercept point (IP3) of the mixers is comparably low. This means that in order to keep unwanted intermodulations to a minimum, the power of the signals being mixed have to be kept low which limits the achievable Rabi frequency. Using more sophisticated mixers with a higher IP3 and lower conversion losses, together with a pre-amplification stage, should then allow us to improve the achievable Rabi frequency by an order of magnitude. This would be comparable to the achieved clock state Rabi frequency shown in chapter 4 where the amplifier was directly fed by the 12.6 GHz source. Further increases of the Rabi frequency are possible using a microwave waveguide integrated into a surface trap with which Rabi frequencies on the order of megahertz have been reported [38].

5.2.2 Radio frequency (rf) setup

The dressed-state qubit formed of $|D\rangle$ and $|0'\rangle$ can be manipulated by applying an rf field resonant with either $|+1\rangle \leftrightarrow |0'\rangle$ or $|-1\rangle \leftrightarrow |0'\rangle$. In this chapter we choose the rf field to be resonant with $|+1\rangle \leftrightarrow |0'\rangle$. For typical B-field strengths used in our experiments ($\approx$ 10 G) the Zeeman splitting is on the order of 10 MHz.

To broadcast the rf to the ion a signal corresponding to the Zeeman splitting is used to drive a simple resonant LCR circuit as shown in figure 5.9. The inductance is created

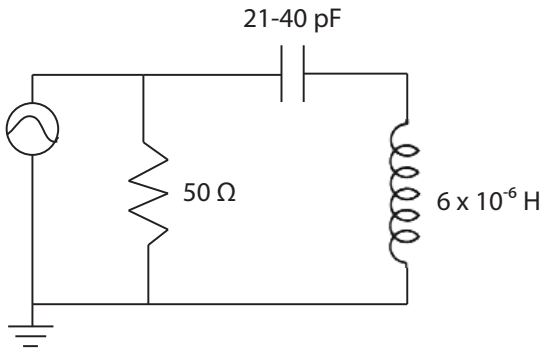

Figure 5.9: Illustration of the resonant LCR circuit used to broadcast rf to the ion.

using a coil which transmits the rf to the ion. A 50Ω resistor is used to impedance match the source[7] to the rest of the circuit and a variable capacitor is used to be able to tune the resonant frequency. The coil creating the inductance and transmitting the rf field to the ion is designed to fit inside the recessed part of the front imaging viewport, as shown in figure 5.10, which reduces the distance to the ion to ≈1 cm. The radius of the coil is ≈1 cm and consists of 3 turns which results in an inductance of 6×10^{-6}H. For a capacitance range of 21-40 pF the achievable resonant frequency range was measured to be 10-14 MHz. This was measured by using a directional coupler[8] to measure the amplitude of the rf signal reflection from the LCR circuit as a function of the applied rf frequency. Resonance then corresponds to the minimum reflection. While a larger number of turns would be advantageous to increase the magnetic field at the ion, the capacitance would have to be reduced to maintain a constant resonant frequency and was limited by the adverse effects from stray capacitances.

Characterisation

To ensure that this setup will be able to drive transitions between the Zeeman states in the ${}^2S_{1/2}|F=1\rangle$ manifold, without the need for any amplification, a simple experiment using the bare states was performed. The experiment consists of applying 10 V_{pp} of rf resonant with $|+1\rangle \leftrightarrow |0'\rangle$ to the LCR circuit for an increasing time to observe Rabi oscillations. State detection using light near 369 nm does not allow us to distinguish between population in $|0'\rangle$ and $|+1\rangle$ and therefore requires using the experimental sequence shown in figure 5.11. Following the population being optically pumped into $|0\rangle$ the population is

[7] Stanford research systems, model: DS345
[8] Mini-Circuits, Part Number: ZDC-20-3

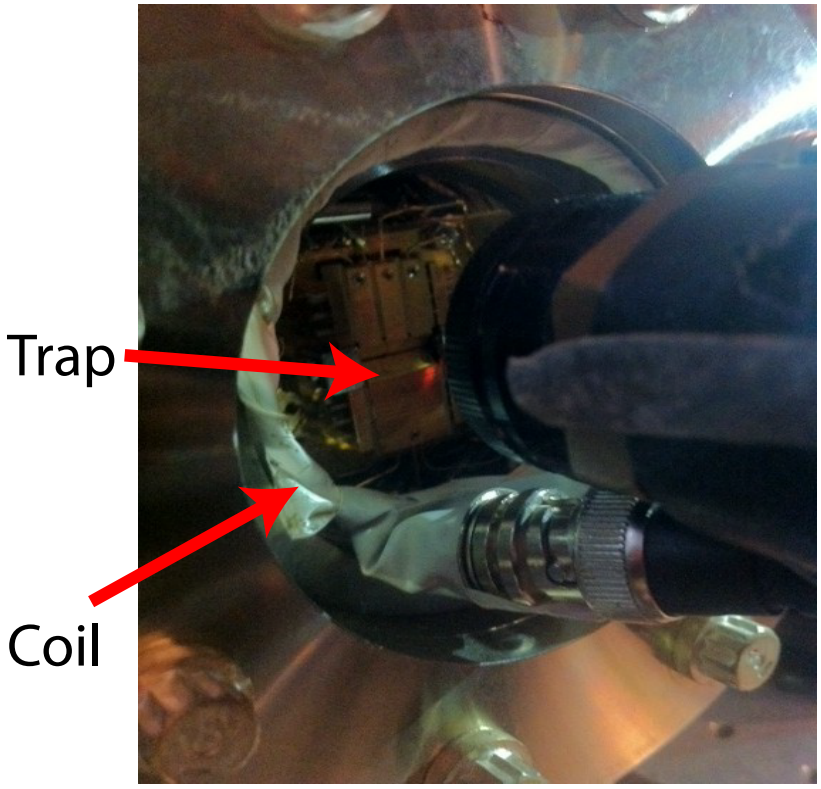

Figure 5.10: Picture showing the placement of the coil inside the recessed part of the front imaging viewport. Also shown is the ion trap which is ≈1 cm away from the centre of the coil.

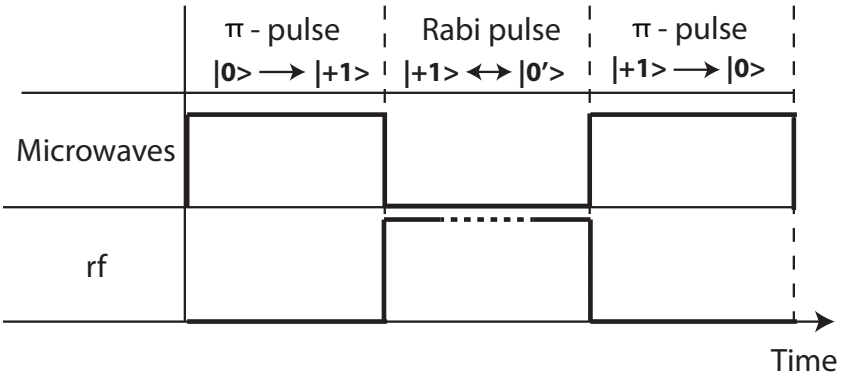

Figure 5.11: Experimental pulse sequence to drive and detect Rabi oscillations between the Zeeman states in the $^2S_{1/2}|F=1\rangle$ manifold. The laser pulses for state preparation and detection are not shown.

transferred to $|+1\rangle$ using a microwave π-pulse resonant with $|0\rangle \leftrightarrow |+1\rangle$. We then apply rf resonant with $|+1\rangle \leftrightarrow |0'\rangle$. For the state detection sequence to distinguish between $|0'\rangle$ and $|+1\rangle$ after the rf pulse has been applied, a microwave π-pulse first returns any population left in $|+1\rangle$ back to $|0\rangle$. This results in many photons being detected if the population is in $|0'\rangle$ and no photons being detected if the population is in $|0\rangle$ which corresponds to $|+1\rangle$ at the end of the rf pulse. Using this pulse sequence we can detect Rabi oscillations between $|+1\rangle$ and $|0'\rangle$ which are shown in figure 5.12. The Rabi frequency is measured to be $2\pi\times18\,\mathrm{kHz}$ which is sufficient for the experiments in this chapter.

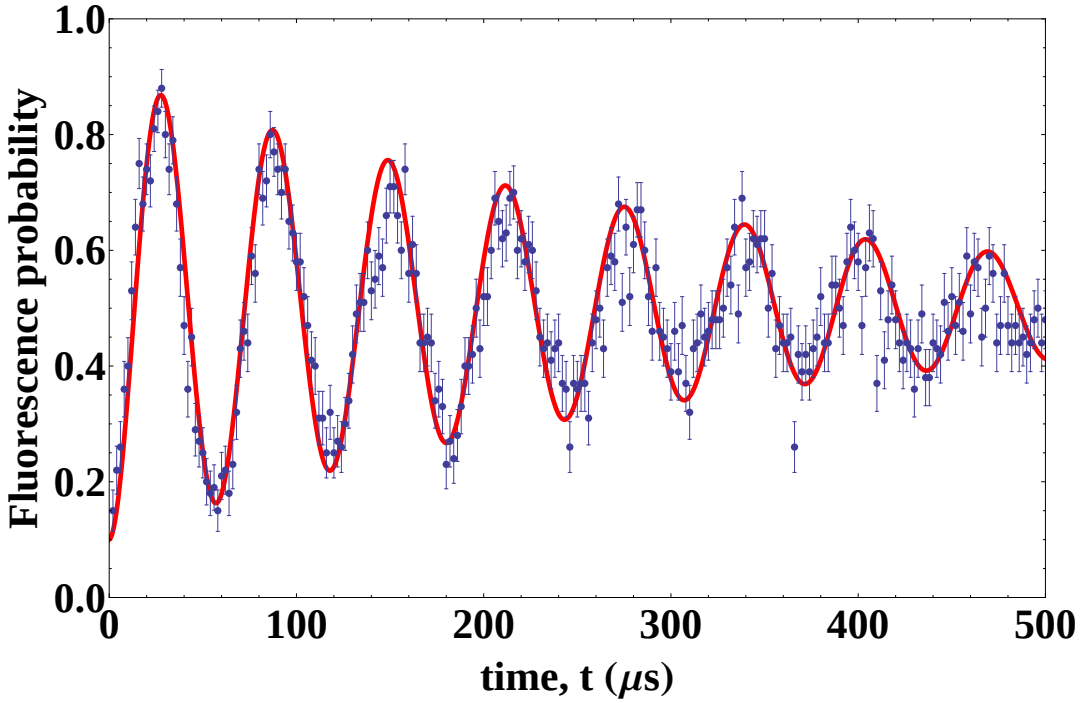

Figure 5.12: Rabi oscillations between $|0'\rangle$ and $|+1\rangle$. A resonant 10 V_{pp} rf signal applied to the LCR circuit sandwiched between two microwave π-pulses resonant with $|0\rangle \leftrightarrow |+1\rangle$ is applied for an increasing time t. The resulting Rabi oscillations have a frequency of $2\pi\times18\,\mathrm{kHz}$. Each data point corresponds to 100 measurements.

5.3 Robustness of dressed-state preparation

The robustness of STIRAP in ions has already been investigated experimentally [116] using lasers. Here the focus was on the effect of the separation between the two pulses on the transfer efficiency of STIRAP. A wide range of separations from the intuitive to the non-intuitive order of the pulses were investigated. The robustness was studied in more detail theoretically, looking at effects on the transfer efficiency of STIRAP from parameters such as pulse width, pulse separation and ion motion [117]. Furthermore, an investigation using microwaves has also been performed [40].

To determine the robustness of preparation of $|D\rangle$ for our experimental setup the transfer efficiency between $|+1\rangle$ and $|-1\rangle$ using STIRAP is considered. Since our state detection method does not allow us to distinguish between $|+1\rangle$ and $|-1\rangle$ we add a final π-pulse to swap the population between $|-1\rangle$ and $|0\rangle$. The complete experimental sequence to implement STIRAP therefore becomes:

1. After a period of Doppler cooling the ion is prepared in $|0\rangle$.

2. A π-pulse resonant with $|0\rangle \leftrightarrow |+1\rangle$ transfers the population to $|+1\rangle$.

3. The STIRAP pulse sequence described in section 5.1.2 is then used to transfer population to $|-1\rangle$ via the dark state $|D\rangle$. Any imperfections during STIRAP will cause the population in $|-1\rangle$ to be reduced.

4. A π-pulse resonant with $|-1\rangle \leftrightarrow |0\rangle$ is applied to swap the population between $|-1\rangle$ and $|0\rangle$.

5. The state detection sequence is used to detect the state of the ion. Any population in $|0\rangle$ due to imperfections in the STIRAP sequence is transferred to $|-1\rangle$ via the final π-pulse. Also, this π-pulse does not effect any population in $|0'\rangle$ or $|+1\rangle$. Therefore, any imperfections during the STIRAP process which lead to a reduction in the transfer efficiency as well as population in $|D\rangle$ will lead to a bright result (many photons being scattered) during state detection. A successful STIRAP however will lead to a dark result (no photons being scattered). We therefore have a simple method of determining the fidelity of our STIRAP pulse sequence.

With this experimental sequence we can now investigate the robustness of STIRAP with a focus being on the pulse width (t_w) and the pulse separation (t_s) for a fixed Rabi frequency (Ω_{P}).

Previous work has already demonstrated that the highest transfer efficiency is achieved for on resonant microwave fields of equal coupling strengths [40]. We therefore perform the following experimental steps before the start of an experiment involving the use of STIRAP:

1. A frequency sweep over the $|0\rangle \leftrightarrow |+1\rangle$ transition using one of the low frequency signals (recall that this will then be mixed with a microwave signal) is performed. The resonant frequency from this sweep can be determined to within $\approx 1\,\mathrm{kHz}$ without too much overhead on the time it takes to obtain these measurements[9]. This

[9] Determining a more accurate resonant frequency was found to have no measurable effect on the STIRAP transfer efficiency.

frequency is then programmed into the frequency source

2. A Rabi flopping experiment, as described in chapter 4, is then performed to determine the π-time.

3. Step 1 is performed for the $|0\rangle \leftrightarrow |-1\rangle$ transition.

4. Step 2 is performed for the $|0\rangle \leftrightarrow |-1\rangle$ transition to check if the two π-times are equal.

5. If the π-times for the two transitions are different, they are altered using the output power of the rf frequency source until they are equal.

Having calibrated the experimental setup we first consider the effects of the pulse width on the transfer efficiency. This is done for a peak Rabi frequency of $2\pi \times 25\,\text{kHz}$ and a pulse separation of $t_s = 356\,\mu\text{s}$. The dependence of the probability of being in $|F = 1\rangle$ on the pulse width is shown in figure 5.13. Each data point consists of 1000 measurements and t_w was varied in steps of $50\,\mu\text{s}$. We can see that STIRAP is extremely robust to changes in t_w and the maximum transfer efficiency of $\approx 91\%$ (excluding infidelities from state preparation and detection) is observed for t_w in the range of 150-650 μs. The transfer efficiency slowly decreases for larger pulse widths as the pulse separation, which is kept constant, becomes less optimum. In other words, for a fixed pulse separation the overlap between the two pulses increases with an increase in pulse width. The effect of varying the separation or overlap between the two pulses is shown below.

The measured transfer efficiency of our STIRAP pulse sequence is currently limited by the detection efficiency as described in chapter 4 and the achievable peak Rabi frequency. Increasing the peak Rabi frequency will allow for shorter STIRAP pulses while remaining in the adiabatic regime which will increase the transfer rate and thereby reduce the effects from noise. Both points will be addressed in future experiments and should significantly improve the achievable fidelity.

An investigation into the dependence of the pulse separation (t_s) on the transfer efficiency has also been undertaken. Here the peak Rabi frequency again is $2\pi \times 25\,\text{kHz}$ and will be kept at this level for the experiments shown in this chapter and $t_w = 450\,\mu\text{s}$. The pulse separation is varied between 0 and $720\,\mu\text{s}$ with the results shown in figure 5.14. Again, STIRAP is shown to be very robust over a large range of t_s and a maximum transfer efficiency is observed for a t_s in the range of 120-485 μs.

In this section the calibration of the experimental setup to ensure that both STIRAP pulses are on resonance with their respective transitions and the two π times are equal

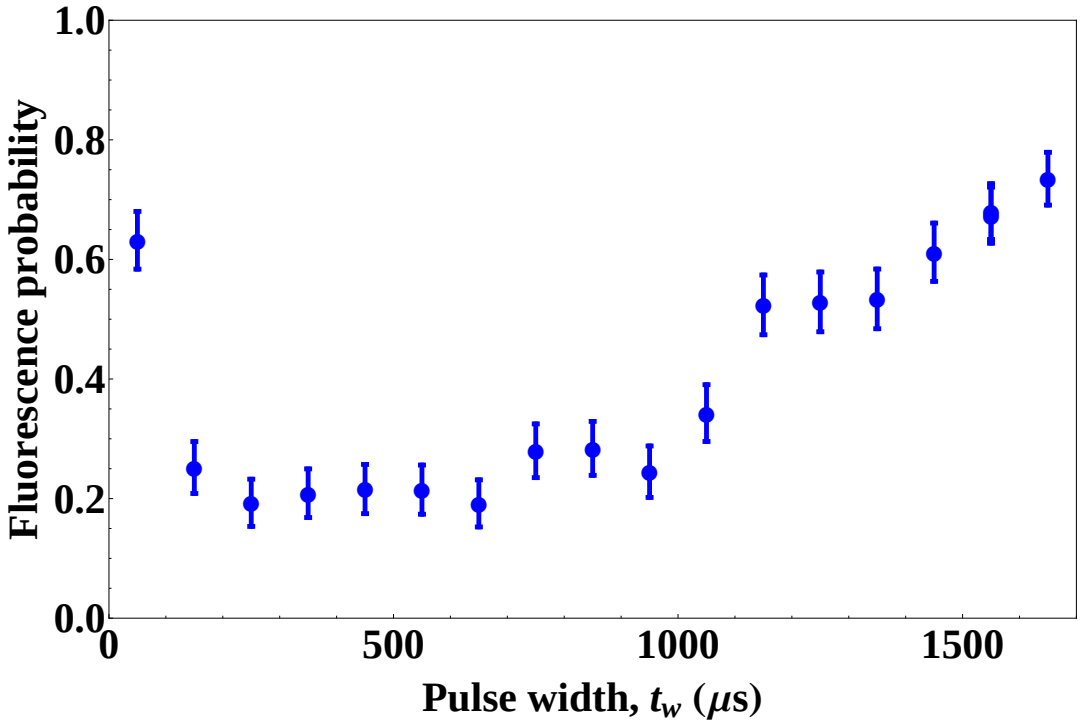

Figure 5.13: The effect of the FWHM of the two pulses on the transfer efficiency is shown. The data has been taken with a fixed pulse separation of $t_s = 356\,\mu$s and a peak Rabi frequency of $2\pi\times25$ kHz. A maximum transfer efficiency is observed for t_w in the range of 150-650 μs. Each data point corresponds to 1000 measurements.

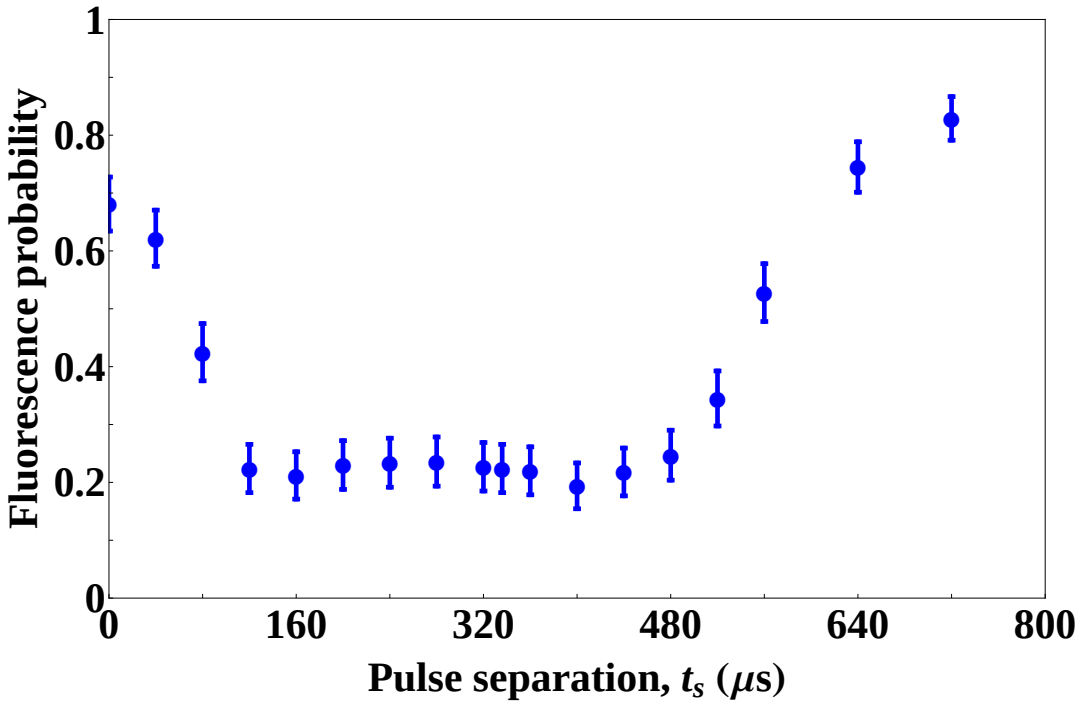

Figure 5.14: The effect of the separation between the two pulses on the transfer efficiency is shown. The data has been taken with a fixed pulse width of $t_w = 400\,\mu$s and a peak Rabi frequency of $2\pi\times25$ kHz. A maximum transfer efficiency is observed for t_s in the range of 120-485 μs. Each data point corresponds to 1000 measurements.

has been described. The dependence of t_w and t_s on the STIRAP transfer efficiency was then investigated. Following this investigation the pulse width and separation are set to $t_w = 450\,\mu$s and $t_s = 356\,\mu$s respectively for the remaining experiments shown in this chapter.

5.4 Lifetime measurement of dressed-state

We have shown that the population in $|D\rangle$ is maximised at the cross-over of the two STIRAP pulses where $\Omega_+ = \Omega_-$. At this point we can use the states $|D\rangle$ and $|0'\rangle$ as a qubit. To determine how useful this qubit is for quantum information processing it is important to determine the lifetime of $|D\rangle$.

The lifetime of $|D\rangle$ is measured by modifying the STIRAP pulse sequence as shown in figure 5.15 (a). In section 1 of figure 5.15 (a) the Gaussian pulses prepare $|D\rangle$ and the sequence is interrupted and the amplitude held constant at the point where $\Omega_+ = \Omega_-$. In the experiments shown in this chapter the microwave Rabi frequency during the hold, Ω_{mw}, is measured to be $2\pi \times 16\,$kHz. The amplitudes are then held constant for a length of time t_h in section 2. This is followed by the STIRAP pulse sequence resuming which transfers any population left in $|D\rangle$ to $|-1\rangle$ during section 3. Following a final π pulse transferring population between $|-1\rangle$ and $|0\rangle$ the population in $|0\rangle$ is measured. We can perform this experiment for an increasing t_h and measure the decay in population in $|0\rangle$ which corresponds to the population in $|D\rangle$. This is shown in figure 5.15 (b). A fully decohered state $|D\rangle$ will correspond to a measured population in $|0\rangle$ of 1/3 since there are three states involved in the STIRAP process. Using an exponential fit the lifetime of $|D\rangle$ is found to be 550 ms. Magnetic field fluctuations are most dominant in the low frequency range [111, 118]. Since $|D\rangle$ is susceptible to noise corresponding to $\Omega_{mw}/\sqrt{2}$, increasing the Rabi frequency of the dressing fields will reduce the susceptibility to low frequency magnetic field noise and is therefore expected to further increase the lifetime of $|D\rangle$.

5.5 Coherent manipulation of a dressed-state qubit

The possibility of implementing arbitrary rotations of the dressed-state qubit using a single rf field is one of the advantages of our method and will be demonstrated in this section.

(*a*)

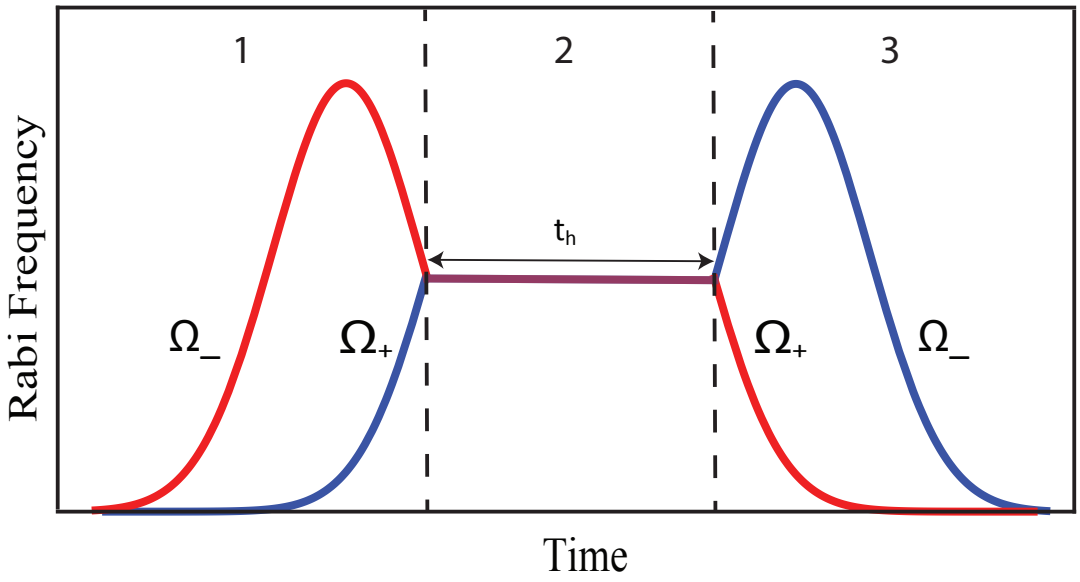

(*b*)

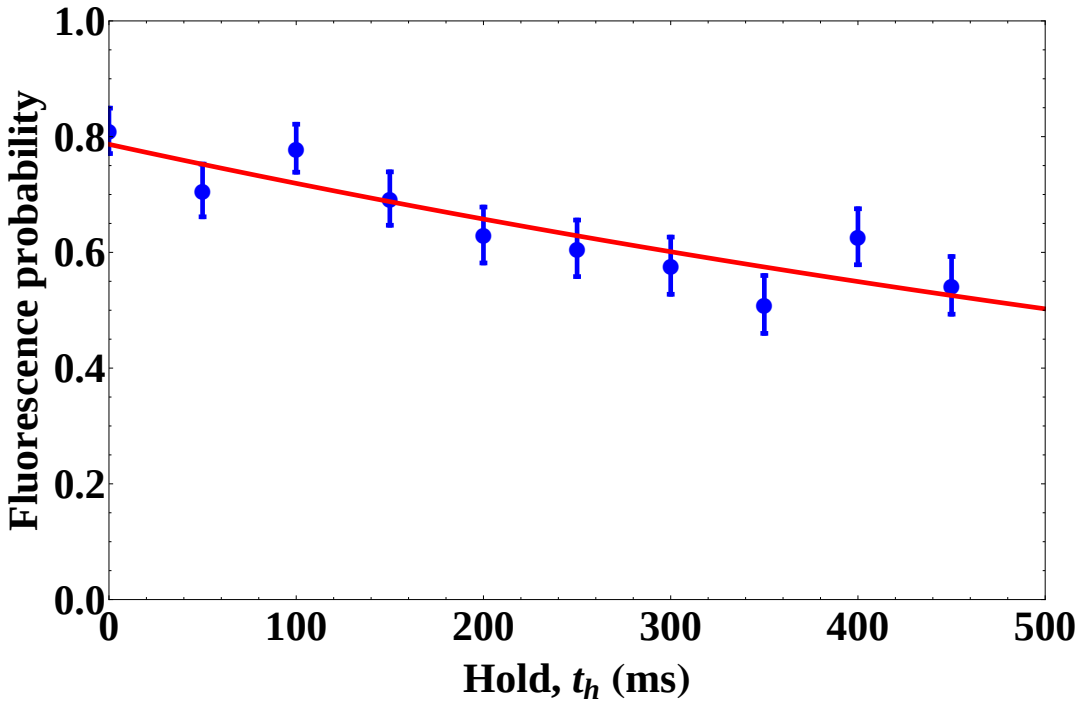

Figure 5.15: (a) shows an illustration of the STIRAP pulse sequence used to measure the lifetime of $|D\rangle$. The illustration is split into three sections. Section 1 prepares $|D\rangle$ following initial preparation in $|+1\rangle$. In section 2 the STIRAP is paused at the point where the population in $|D\rangle$ is maximum. The amplitude of the pulses are now held constant for time t_h. In section 3 the STIRAP pulse sequence is resumed and any population in $|D\rangle$ is transferred to $|-1\rangle$. (b) shows a lifetime measurements of $|D\rangle$ where the population in $|0\rangle$ has been measured following the STIRAP pulse sequence shown in (a) for various hold times t_h. The peak Rabi frequency was $2\pi\times25\,\mathrm{kHz}$ while the Rabi frequency during the hold was $2\pi\times16\,\mathrm{kHz}$ and $t_w = 450\,\mu\mathrm{s}$ and $t_s = 356\,\mu\mathrm{s}$. Using an exponential fit the lifetime of $|D\rangle$ is calculated to be 550 ms. Each data point corresponds to 1000 measurements.

5.5.1 Rabi oscillations

During the hold time of STIRAP the dressed-state qubit is formed of $|D\rangle$ and $|0'\rangle$ and can be manipulated using a single rf field resonant with $|0'\rangle \leftrightarrow |+1\rangle$. To ensure that the rf field is on resonance we first prepare $|D\rangle$ and then perform a frequency sweep of the rf field during the hold of STIRAP. The resonant frequency is then programmed into the rf source. Rabi oscillations are induced in the same way as for the bare states described in chapter 4 once the dressed-state qubit has been prepared. During the hold of STIRAP we apply 5 V_{pp} of rf resonant with $|0'\rangle \leftrightarrow |+1\rangle$ to the LCR circuit described above for an increasing amount of time. When the rf is only being applied for a very short amount of time most population will remain in $|D\rangle$ and will be transferred to $|0\rangle$ via the second half of STIRAP and a final π-pulse. This will lead to no photons being scattered during state detection. When increasing the time the rf field is being applied for, more population will be transferred to $|0'\rangle$ where it is unaffected by the second half of STIRAP and the final π-pulse. The resultant Rabi oscillations between $|D\rangle$ and $|0'\rangle$ are shown in figure 5.16.

Rabi oscillation data is shown from 0 to 2 ms in figure 5.16 (a) and from 100 to 101 ms in figure 5.16 (b). The Rabi frequency in (a) is measured to be $\Omega'_{rf} = 2\pi\times1.9\,\text{kHz}$. The decay in amplitude of the Rabi oscillations can be used to determine the minimum T_2 time of the qubit and has been measured to be 500 ms, close to the absolute limit set by the lifetime of $|D\rangle$. This is an increase of three orders of magnitude compared to the magnetic field sensitive bare states and further demonstrates the robustness of this dressed-state qubit.

The Rabi frequency in figure 5.16 (b) appears changed due to slow drifts of experimental parameters. For example, heating of the components in the LCR matching circuit can cause small effects on the amplitude of the rf signal applied to the ion. While there is little heating and a resultant small drift in amplitude for short rf pulses, the small drift in amplitude of the rf signal and Rabi frequency for every Rabi oscillation will add up and result in a measurable change in Rabi frequency when the rf has been applied for over 100 ms during which many Rabi oscillations have occurred.

5.5.2 Ramsey experiment

In chapter 4 a Ramsey experiment was performed where we used two resonant $\pi/2$-pulses, separated in time. Here the phase of the second $\pi/2$-pulse was varied. Our current rf setup does not allow for such an experiment to be performed on the dressed-state qubit. However, to demonstrate that arbitrary rotations can indeed be performed using our method we simply detune the two rf $\pi/2$-pulses from resonance. The detuning is chosen

(*a*)

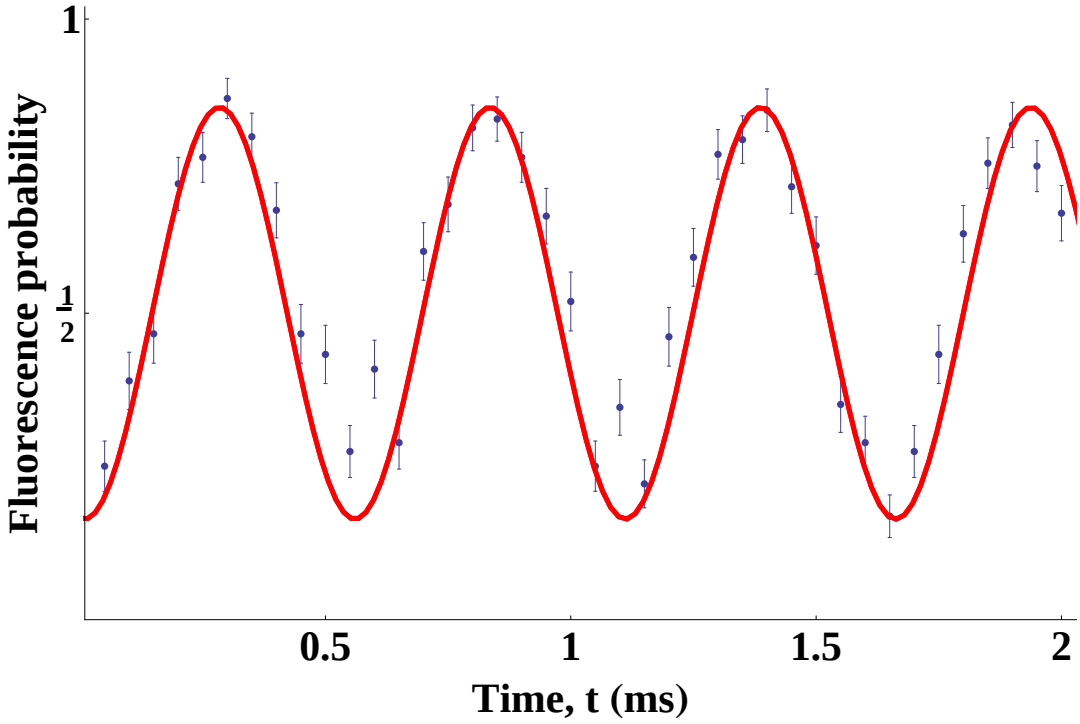

(*b*)

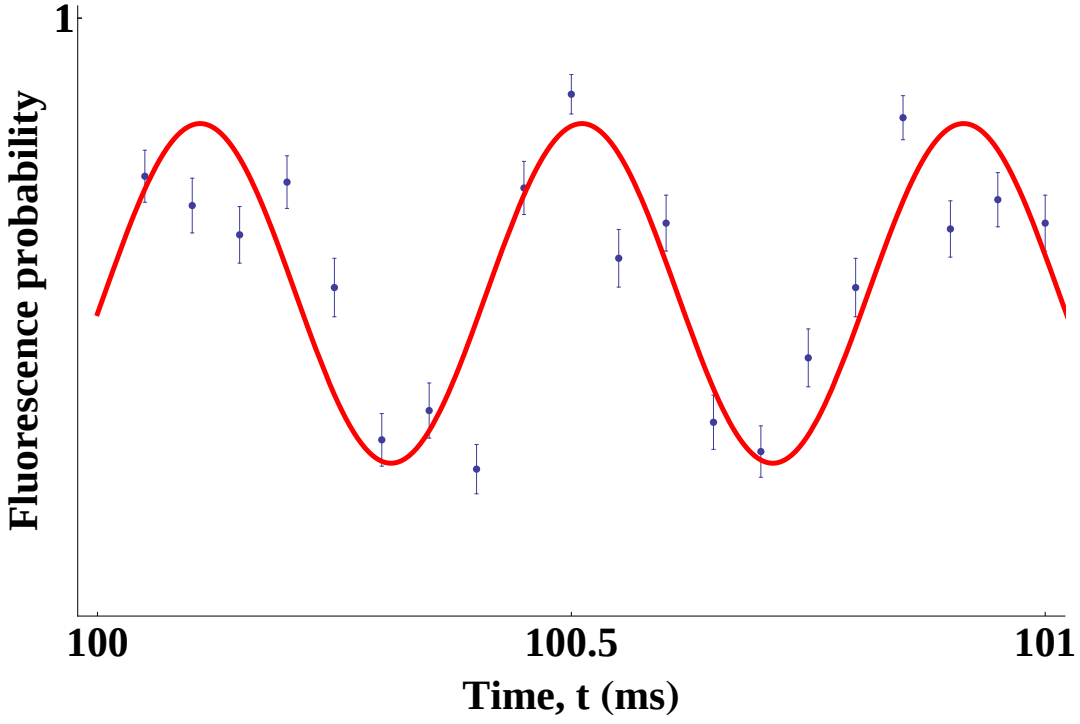

Figure 5.16: Rabi oscillations between $|0'\rangle$ and $|D\rangle$. Following preparation in $|D\rangle$ a rf pulse resonant with $|0'\rangle \leftrightarrow |+1\rangle$ is applied for an increasing amount of time t which results in Rabi oscillations. To illustrate the robustness of the dressed-state qubit (a) shows Rabi oscillations during the first 2 ms and (b) shows Rabi oscillations for a window of 1 ms after the rf has been applied for 100 ms. The Rabi frequency is measured to be $\Omega'_{rf} = 2\pi\times 1.9\,\mathrm{kHz}$ based on the data shown in (a). The Rabi frequency in (b) appears changed due to slow fluctuations of experimental parameters. Each point in (a) corresponds to 100 measurements and 50 for each point in (b).

to satisfy $\delta_{rf} \ll \Omega'_{rf}$ to not affect the nature of the $\pi/2$-pulses. The separation in time between these two pulses will cause the rf field and the qubit to obtain a relative phase with each other. This changes the axis on the Bloch sphere the second $\pi/2$-pulse operates on and therefore leads to Ramsey fringes. This is shown in figure 5.17. From the period of the fringes a detuning from resonance of 160 Hz is inferred.

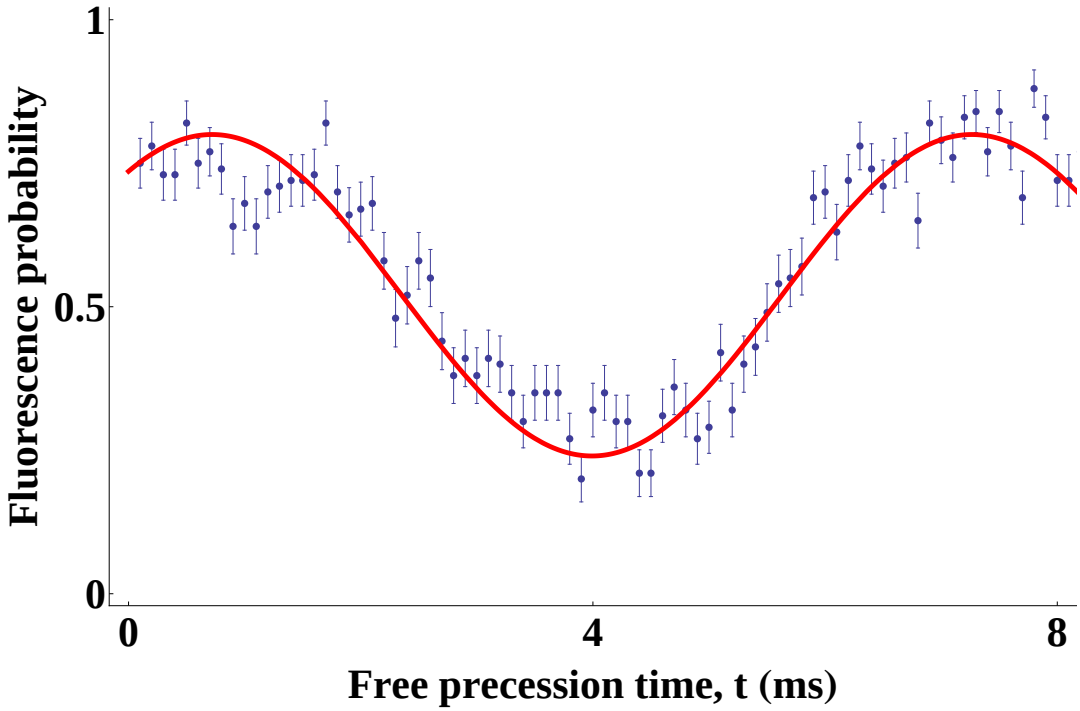

Figure 5.17: Ramsey fringe between $|0'\rangle$ and $|D\rangle$. Following preparation in $|D\rangle$ a detuned rf $\pi/2$-pulse is applied followed by a second detuned $\pi/2$-pulse after a variable precession time t which results in Ramsey fringes. The period of these fringes is measured to be $1/(160\,\text{Hz})$ indicating that the $\pi/2$-pulses were 160 Hz off-resonant. Each point corresponds to 100 measurements.

In future experiments changes to the rf setup which will involve adding a second rf source, switches and a combiner will allow for a T_2 measurement to be performed in a way as was described in chapter 4.

5.6 Summary

Quantum gates using microwave radiation in conjunction with a static magnetic field gradient require the use of at least one magnetic field sensitive state. These states are very susceptible to magnetic field fluctuations which limits the achievable coherence time and resultant gate fidelity. In this chapter a dressed-state qubit which is less sensitive to magnetic field fluctuations is presented following the work by Timoney *et al.* [40]. A

new method to manipulate the dressed-state qubit is then presented which significantly simplifies the experimental setup and allows for arbitrary qubit rotations to be performed by simply changing the phase of the rf field. A STIRAP pulse sequence is used to prepare the dressed-state qubit and an investigation into the preparation efficiency as a function of STIRAP parameters shows the robustness of this process. A lifetime measurement of the dressed-state is then presented to determine the usefulness of the qubit for quantum information processing using our experimental setup. The lifetime is found to be 550 ms. To demonstrate our new method of dressed-state qubit manipulation we use a single rf field to implement Rabi oscillations and use this measurement to determine the minimum T_2 time which is found to be 500 ms, close to the dressed-state lifetime. A single rf field is also used to implement Ramsey fringes which demonstrates that arbitrary qubit rotations can be implemented using our method by simply changing the phase of the rf field.

Future improvements to the microwave setup to increase the Rabi frequency of the dressing fields is expected to significantly improve the preparation efficiency of the dressed-state and further improve the coherence time of the qubit. With this and improvements to the rf setup, multi-qubit gate operations as suggested by Timoney *et al.* [40] should allow for high fidelities to be achieved. This has the potential to outperform laser driven gates and provides an exciting platform for the implementation of microwave based quantum technology.

Chapter 6

Two-dimensional ion trap lattice on a microchip

6.1 Introduction

The introduction of microfabrication techniques to the field of ion trapping has lead to the development of impressive microfabricated radio-frequency (rf) ion trap devices [42]. Using such devices, all the building blocks for scalable quantum computing have been demonstrated [41], including ion combination and separation and shuttling through junctions [43, 44] as well as two-qubit gate operations [38]. A drawback of current microfabricated ion traps stems from the ions at the rf nil naturally forming a 1-dimensional string, limiting their usefulness for applications that require the formation of arbitrary 2-dimensional (2D) ion lattices. Penning traps offer a platform for a 2D lattice of ions, but the rotating crystal makes individual ion addressing and readout experimentally challenging, and the lattice geometry is limited to the naturally forming Wigner crystal [20].

There are many potential applications for a 2D ion lattice including B-field and E-field sensing [119], force detection [120], interactions between neutral atoms and ions [121] and cluster state quantum computing [122]. Another application for a 2D ion lattice is in the field of analogue quantum simulation where the Hamiltonian of a complicated many-body system can be realised and its properties measured [123, 124]. Examples of many-body systems that can be simulated include quantum magnetism [125], high temperature superconductivity [126], the fractional quantum hall effect [127] and synthetic gauge fields [128].

We have already seen some very impressive small scale quantum simulations using rf ion traps [46–52] for which one-dimensional strings of ions were used. In order to simulate

more complicated systems it has been proposed to develop a 2D quantum simulator which consists of a 2D lattice of individual rf ion traps [45, 53, 54]. In their proposals single ions are trapped in individual rf ion traps and placed close enough together for the ions to interact with neighbouring ions via the Coulomb force. Such a system has the potential to reach a regime classical computers currently cannot operate in. So far, experimental progress towards a 2D lattice of ions has been limited to trapping dust particles and clouds of ions using a wire mesh [129] and above PCB boards [130].

The challenge lies in developing microfabrication techniques that allow a scalable 2D lattice of rf ion traps to be fabricated with the long term goal to reduce the ion-ion separation enough for coherent interactions to be measured. The optimum trap geometries of such a device have been well studied [92, 131] and will be discussed in detail in chapter 7.

In operating a microfabricated ion surface trap, restrictions on the rf voltage that can be applied due to low flashover voltages exist [42, 132]. The flashover voltage is the voltage at which electric discharge occurs between two conductors that are separated by an insulator. This prohibits a large trap depth and ion-electrode distance, d, which limits the achievable ion lifetime and secular frequencies. The result of a small ion-electrode distance is a large heating rate of the ion motion which scales as d^{-4} [133] limiting the fidelity of motion dependant qubit gate operations. It is therefore desirable to increase the maximum rf voltage that can be applied to microfabricated devices. Being able to apply large voltages to devices such as microelectromechanical systems (MEMS) would also be useful in the field of nanoelectrospray thruster arrays for spacecraft [134–137] as the maximum achievable electric field directly impacts the achievable thrust.

In this chapter a general microfabrication process to achieve large breakdown voltages in microfabricated devices is shown and this advance is used to fabricate a 2D lattice of rf ion traps on a microchip. This advance can also be used for other surface electrode ion trap geometries. We use this device to demonstrate, for the first time, a 2D lattice of $^{174}Yb^{+}$ ions, deterministic trapping of multiple ions at lattice sites and rudimentary ion shuttling between lattice sites. Since this is a microfabricated device it addresses the challenge of scaling 2D ion lattices to a large number of ions and brings us a step closer to reducing the ion-ion separation to a point where quantum simulations can be performed. Furthermore, this device is suitable for 2D sensing applications. The work in this chapter is based on the work we have shown in [138].

This chapter is structured as follows. First, a brief description of the fabrication of

the microchip is given. The experimental setup including a new vacuum system, and the optical setup is then described. Experimental results are then presented and discussed which includes secular frequency and ion lifetime measurements, the demonstration of a 2D lattice of singly trapped ions and rudimentary shuttling between individual lattice sites.

6.2 Microfabrication of a 2D lattice of ion traps on a microchip

As the name microfabrication suggests, it involves the fabrication of structures on the micrometer scale and has lead to many advances in the field of ion trap quantum technology. While macroscopic scale traps are still widely used and have many advantages for certain experiments, microfabricated ion traps offer a very promising route towards realizing devices with very small electrode structures which can hold and move hundreds, if not thousands, of ions.

One of the most common microfabricated ion trap is the asymmetric (surface) trap [42] which is the focus of this chapter. Here, the electrodes which provide the trapping fields are in one plane and the ion is trapped tens of micrometers above it. Laser beams for ionisation and cooling are aligned parallel to the surface.

There are some considerations that have to be taken into account when working with a surface trap. Compared to macroscopic ion traps, the microfabricated asymmetric counterpart provides a much lower trap depth. Furthermore, the ion is trapped very close to the surface, making it more susceptible to electric field noise causing heating of the motional state of the ion. A low ion height also makes aligning laser beams close to the surface, while minimising scatter off the electrodes, challenging. Furthermore, microfabricated devices make use of semi-conductors which compared to metals used in macroscopic traps have a higher resistance and capacitance which needs to be taken into account when applying the trapping fields. This causes a higher power dissipation which is given by [42]

$$P_D \approx \frac{1}{2} V^2 C^2 R \Omega^2 \tag{6.1}$$

where V is the voltage applied to the device, C is the capacitance, R is the resistance and Ω is the drive frequency. A higher power dissipation causes heating of the device and can limit the maximum voltage that can be applied. However it should be noted that flashover voltages are often the greater limitation. Being able to apply large voltages to the device

is often desirable as this increases the trap depth and allows the trap to be designed with a larger ion height. A method to substantially increase the flashover voltage of a microfabricated ion trap will be discussed in more detail below. A comprehensive overview of different microfabricated ion traps and their corresponding fabrication techniques has been written by M. Hughes *et al.* [42].

The microchip shown in this chapter was fabricated by H. Rattanasonti at the University of Southampton, to a design and fabrication process created by Dr. R. Sterling. A detailed description of the fabrication and design is found in his thesis [88], and will be briefly summarised below.

6.2.1 Fabrication process

In order to keep the fabrication as simple as possible the process steps are kept to a minimum and are made up of standard processes which can easily be performed in the clean room.

To start off with a commercially available silicon-on-insulator (SOI) wafer[1] is used. A SOI wafer has already been used by Britton *et al.* to fabricate a linear ion trap [139]. Here, a different fabrication process is shown which allows extremely large voltages to be applied to the device. This advance is then used to fabricate and operate a 2D lattice of ion traps on a microchip. The SOI wafer consists of a 600 μm thick silicon handle layer which is degenerately n-doped with arsenic, on top of which is a 10 μm thick layer of silicon dioxide (SiO_2) followed by a 30 μm thick device layer of silicon with the same doping as the handle layer. A thick oxide layer was chosen to increase the path length between the electrodes and the handle layer and to reduce the capacitance between the rf electrode and ground. A schematic of this wafer is shown in Fig. 6.1.

During fabrication of the device several micrometers of photosensitive photoresist are spun evenly on top of the device layer. Once baked, the required electrode pattern is transferred to the wafer using a pre-drawn mask which protects certain areas of the photoresist from a UV light source. The unprotected areas of the silicon device layer are then etched away using a deep reactive ion etch. This exposes the SiO_2 which is isotropically etched away by placing the structure into a hydrofluoric (HF) bath. The electrodes are then coated in an adhesion layer of chrome and 500 nm of gold. Using a gold layer as part of the electrode structure mitigates the aforementioned problem of the large resistance of semiconductor materials compared to that of metals used in macroscopic traps. The final

[1] The wafer was obtained from Ultrasil Corporation with the silicon having a resistivity of 0.001-0.005 Ω cm.

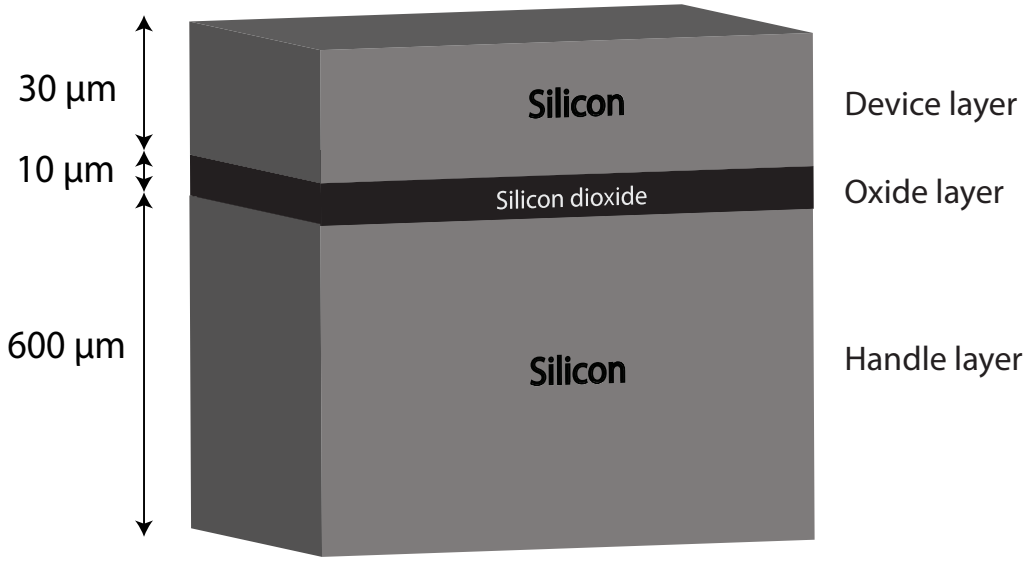

Figure 6.1: Schematic of the silicon-on-insulator (SOI) wafer used in the fabrication of the microchip consisting of a 600 μm thick silicon handle layer which is degenerately n-doped with arsenic, a 10 μm thick layer of silicon dioxide (SiO_2) and a 30 μm thick device layer of silicon with the same doping as the handle layer.

layers of the structure can be seen in figure 6.2 (a).

A common problem that has been observed in microfabricated ion traps is low flashover voltages [42, 132]. A large oxide layer which increases the path length between the electrodes and the handle layer only results in modest increases in the flashover voltage and would not be sufficient to operate the microchip shown in this chapter. To substantially increase the flashover voltage a specialised fabrication technique was developed. Since the voltage breakdown usually occurs across the SiO_2 (insulator) surface rather than through the SiO_2 bulk it would be advantageous to increase the path length between the device and handle layer. This is achieved by wafer bonding two SOI wafers with 5 μm thick oxide surfaces together which then forms the 10 μm thick SiO_2 layer. We now find that when we remove the SiO_2 layer during the buffered HF etch to expose the handle layer that there is an increased etch rate developing along the interface where the two substrates were bonded together. This leads to an anisotropic etch laterally under the electrodes. By applying the buffered HF etch for 130 - 140 minutes, a 60 μm V-shaped undercut is achieved which is illustrated in figure 6.2 (b). This increases the path length between the device and handle layer from approximately 10 μm to 120 μm and results in flashover voltages which are measured to be $V_{dc} = 1298(5)$ V and $V_{rf} = 1061(32)$ V [93]. This is a substantial increase compared to the flashover voltages of ≈ 150 V observed by Britton *et*

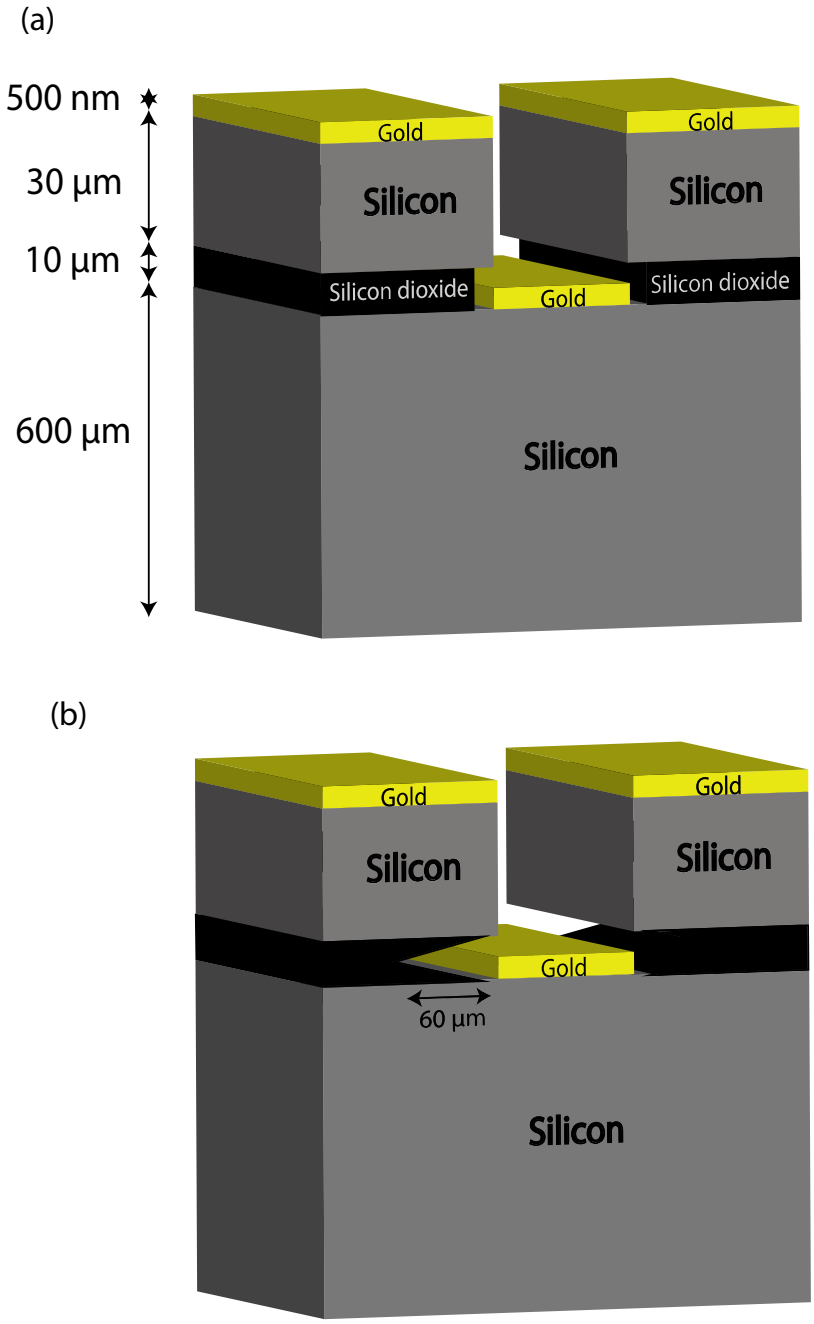

Figure 6.2: (a) Not to scale schematic of a cross section of the silicon-on-insulator wafer structure which includes a 500 nm layer of gold. By using various etches it is possible to make the required electrode patterns. The 10 μm thick SiO_2 layer prevents electrical breakdown with the silicon handle layer and ensures a low capacitance required to keep the power dissipation to a minimum. (b) Not to scale schematic of a cross section of the wafer after an optimised 60 μm anisotropic buffered HF etch laterally under the silicon device layer. This increases the path length to ground from 10 μm to 120 μm and allows much larger voltages to be applied to the device.

al. [139] and allows us to successfully operate the microchip presented in this chapter.

6.2.2 The microchip

The fabrication process described above is used to fabricate a microchip with recessed ground electrodes within a 2D electrode geometry. Here the gold coated device layer pattern provides the trapping fields with the handle layer held at ground. This was the first 2D lattice of ion traps on a microchip and the first microfabricated ion trap in our laboratory so it was decided to start off with a comparably large ion height, which is set by the electrode geometry, to reduce heating of the ions and to minimise scatter off the surface from the laser beams. Unlike in other microfabricated ion traps the trap depth will be large despite the large ion height due to the high voltages that can be applied to the microchip.

The microchip consists of 29 individual hexagonal shaped traps which are arranged in a triangular lattice and each capable of trapping an ion. This allows each ion to have up to six nearest neighbours with an ion-ion separation of 270.5 μm. The smallest separation between the polygons is 20 μm. For this geometry the ion-electrode distance is 156 μm. Due to the recessed ground electrode, the ion height from the top of the device layer is 116 μm. The lattice is surrounded by six larger electrodes which static voltages can be applied to in order to globally compensate for stray electric fields. These can shift the position of the ions and induce unwanted micromotion. In this trap, compensating each ion individually which is part of a large ion lattice is not possible. This will however be possible in future traps currently being fabricated using a different fabrication method by adding individual control electrodes for every polygon. A scanning electron microscope (SEM) is used to produce an image of the fabricated microchip which can be seen in figure 6.3 (a) with the inset showing two hexagonal traps made up of the gold coated rf electrode as well as the recessed ground electrode. The 60 μm V-shaped undercut into the SiO_2 layer ensuring large voltages can be applied to the lattice is shown in figure 6.3 (b) where a SEM has been used to take a image of the cross-section of the layered SOI structure.

To allow the microchip to be placed inside a vacuum chamber and to be electrically connected to a vacuum system feedthrough, conductive glue[2] is used to attach the handle layer of the chip to a Ceramic Pin Grid Array (CPGA) chip carrier. A wire-bonder is then used to connect the rf, ground and static voltage electrodes to gold bond pads on the chip carrier. The bond pads make a connection with 100 pins at the back of the chip carrier

[2]Epoxy Technology, Part number: EPO-TEK H21D

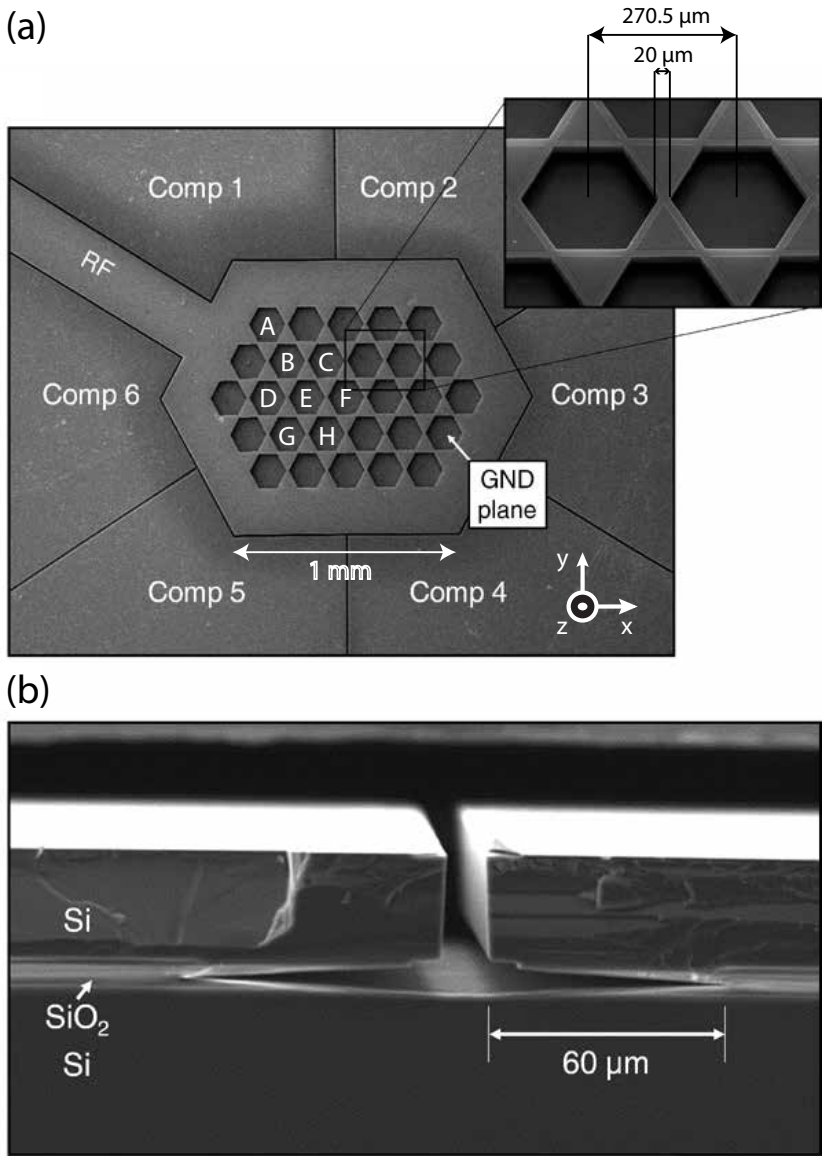

Figure 6.3: (a) A image from a SEM of the finished microchip. The inset shows a close-up of two of the hexagonal traps including the recessed ground electrode. Letters A to H represent the lattice sites that were used during the experiments presented in this chapter. (b) A image of the cross section of the layered SOI structure at the interface between two compensation electrodes taken using a SEM. The 60 μm V-shaped undercut into the SiO_2 layer is clearly visible.

which are then used to connect to a feedthrough inside the vacuum system. A picture of this can be seen in figure 6.4.

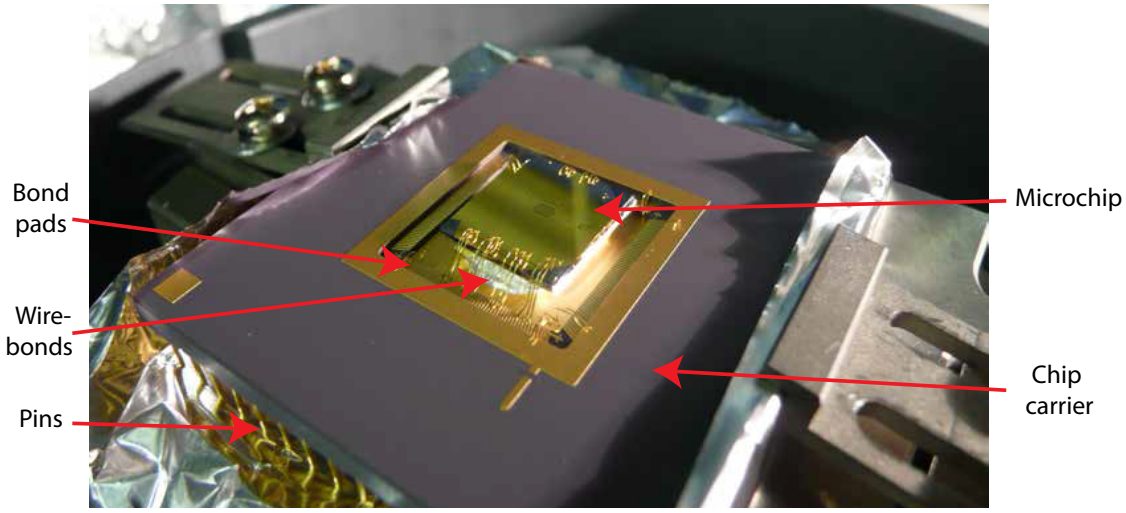

Figure 6.4: Picture of the microchip mounted onto a CPGA chip carrier. The electrodes are connected to the backside pins via wire-bonds.

6.3 Experimental setup

Due to the experimental setup described in chapter 3 being used for other experiments, a new setup which will be described in this section had to be designed and built to allow the microchip to be operated. This includes a new vacuum system which was built with the capability to house symmetric as well as asymmetric ion traps. The system also provides a number of feedthroughs allowing the application of high power microwaves and currents which will be of importance in future experiments. A new imaging system which allows a large area of the microchip to be imaged and which can share the same photon detection devices as described in chapter 3 was also required. With a new vacuum system comes a new optical setup that had to be put in place and aligned. Since the vacuum system will operate a surface trap, a way of precisely aligning the laser beams close to the surface of the microchip also had to be designed.

6.3.1 Vacuum system

The vacuum system used in the experiments described in this chapter is based on a design by James Sayers and Dr. Robin Sterling whose thesis should be referred to for a more detailed description of the design [88]. This section will focus on the important parts of the system as well as changes that were made to the design to make it more suitable for our experiments.

A picture of the fully assembled vacuum system can be seen in figure 6.5. A special

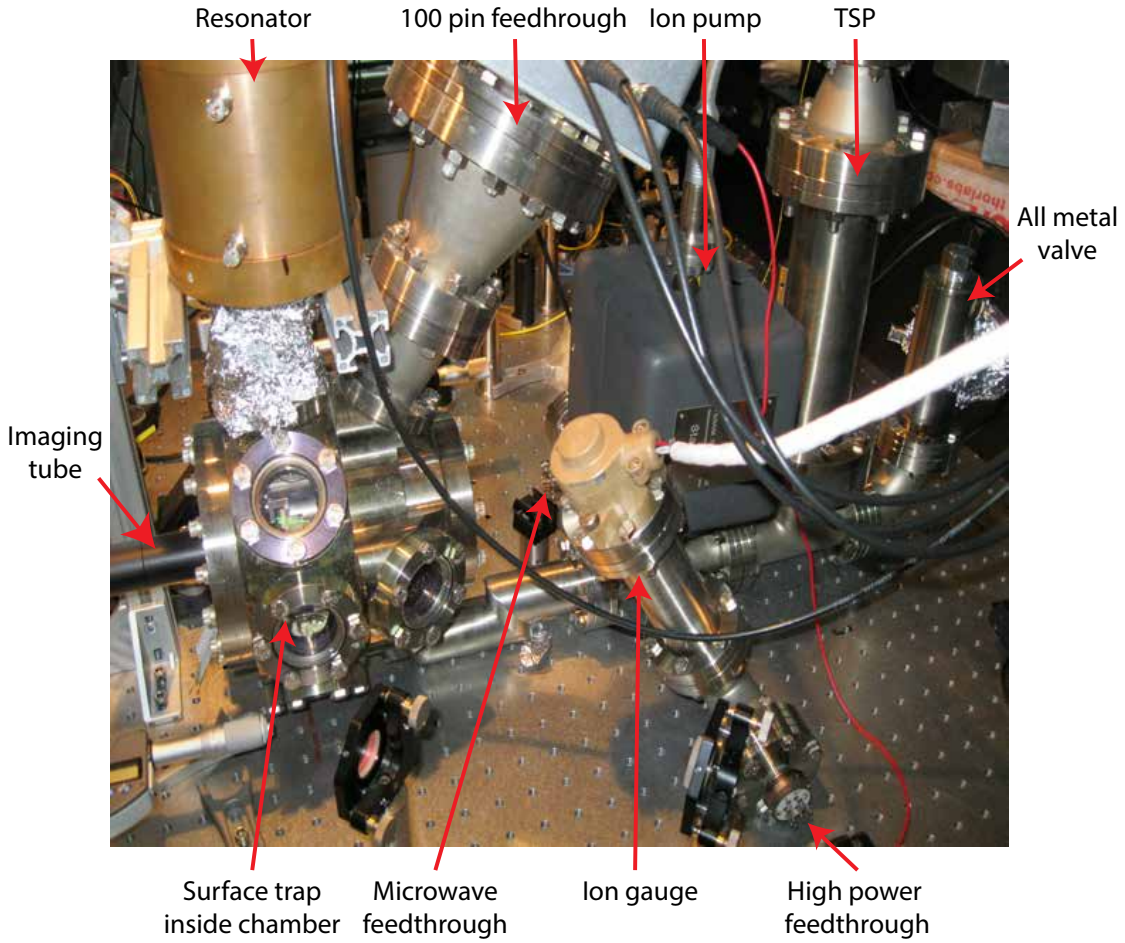

Figure 6.5: Picture of a new vacuum system designed to accommodate both symmetric and asymmetric traps and used for the experiments shown in this chapter.

feature of the system is the capability of holding symmetric as well as asymmetric ion traps in the hemisphere, into which laser beams can simply be aligned via its eight viewports. Another important feature is the ability to transmit high power microwaves and currents to future microchips. The hemisphere houses a chip bracket made up of two PEEK plates sandwiched together by two metal clamps. The chip carrier holding the microchip can be mounted inside the hemisphere using this chip bracket. Pin receptacles (male part) in the PEEK are used to connect the pins from the chip carrier with pin receptacles (female part) crimped to 100 UHV compatible Kapton ribbon wires [3]. These cables are then connected to a flange with two 50 pin sub miniature D-type feedthroughs [4]. The pins used to connect to each electrode are shown in appendix A. The chip bracket can be moved forward and backward allowing accurate alignment with the Yb ovens and the front viewport used by

[3] Allectra, Part number: 380-D50FXPR-500
[4] Allectra, Part number: 210-D50-C100-2

the imaging system for photon collection. A picture of the microchip mounted inside the vacuum system can be seen in figure 6.6.

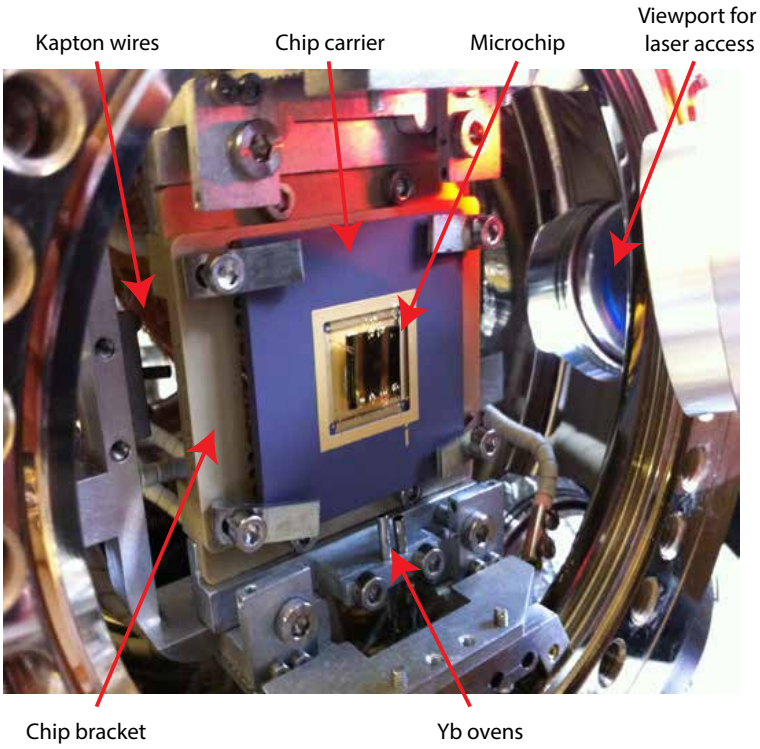

Figure 6.6: A picture of the chip carrier, holding the microchip, mounted onto the PEEK chip bracket inside the hemisphere. For this picture the front viewport through which the ions are imaged has been removed. Clearly visible is one of the viewports that can be used to align laser beams along the surface of the microchip. Two ovens which can be used to resistively heat a sample of either natural (left) or enriched (right) Yb are shown. Some of the 100 Kapton ribbon wires used to make electrical connections between two sub miniature feedthroughs and the microchip can also be seen.

Evacuation of vacuum system

In order to evacuate the system it is connected to a turbo pump until a pressure of 10^{-6} torr is reached. The system is then leak tested and appropriate components are outgassed. A large homebuilt oven is then used to bake the system at 200°C for approximately 12 days. A pressure of $\approx 10^{-9}$ torr is reached after the temperature has been reduced back down to room temperature. A titanium sublimation pump is then used to reduce the pressure to $\leq 10^{-11}$ torr. A detailed description of how we reduce the pressure inside the vacuum system is shown in appendix B.

In a previous design of the vacuum system the ion gauge was positioned close to the ion pump. During the evacuation procedure we however experienced problems with the filament of the ion gauge blowing out several times. An investigation into this problem

lead to the conclusion that when turning on the ion pump it can release titanium dust into the system and coat the ion gauge filament if close by. When turning on the ion gauge the sharp temperature rise of the tungsten filament can cause alloying between the titanium and the tungsten which will change the electrical properties of the filament and cause it to blow out. A elbow and nipple was therefore used to move the ion gauge much further away from the ion pump and we have not experienced any problems of this nature since then.

6.3.2 Imaging of ions

To detect ions trapped on the microchip the setup shown in figure 6.7 is used to collect the fluorescence resulting from the decay on the 369 nm $^2S_{1/2}$ to $^2P_{1/2}$ transition. It partly consists of a triplet with a magnification M_{tr} of -12.29 which is placed 25 mm away from the ion to initially collect the photons, reduce spherical aberration and provide a magnification. A focused image is formed 396 mm after the triplet where an iris can be used to spatially filter the image without affecting the photons from the ion. A doublet

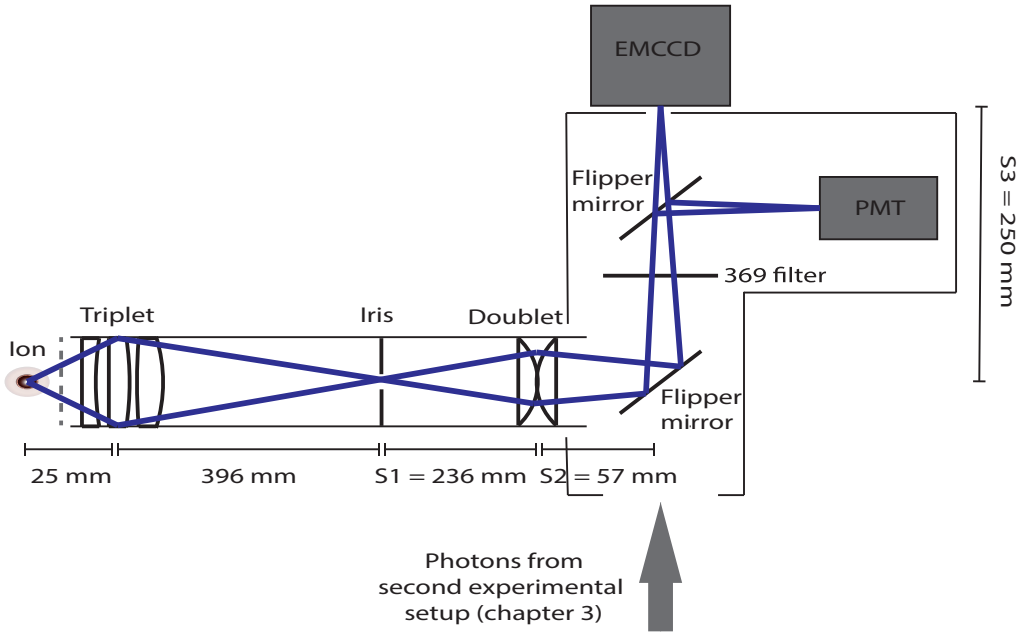

Figure 6.7: Imaging setup used to detect fluorescence at 369 nm from trapped ions. The fluorescence is collected using a triplet. The image is then focused through an iris to remove any unwanted scatter before a doublet magnifies the image onto a EMCCD or a PMT via a bandpass filter and two motorised flipper mirrors.

made up of two plano-convex lenses is then used to determine the final magnification of the image. The combined magnification of the triplet M_{tr} and the doublet M_d gives the

total magnification M_t of the imaging setup and is given by

$$M_t = M_{tr} + M_d. \tag{6.2}$$

For a 500 μm by 500 μm area of the microchip surface to be viewed on a detector with a detector size of 8000 μm by 8000 μm, the total required magnification is calculated to be 16. Using equation 6.2, the required magnification of the doublet is therefore -1.30.

The doublet magnification in terms of the object distance (distance between the iris and the doublet), $S1$, and the image distance (distance between the doublet and the detector), $S2 + S3$, is given by

$$M_d = \frac{S1}{S2 + S3}. \tag{6.3}$$

A relationship between these distances to the focal length of the two lenses in the doublet, f_1 and f_2, is given by

$$\frac{1}{S1} - \frac{1}{S2 + S3} = \frac{1}{f_1} + \frac{1}{f_2}. \tag{6.4}$$

The required magnification of the doublet can be achieved by careful choice of the lenses as well as the position of the doublet. Using focal lengths of $f_1 = 400\,\text{mm}$ and $f_2 = 200\,\text{mm}$ and setting $S1 = 236\,\text{mm}$ and $S2 + S3 = (57 + 250)\,\text{mm}$ the required doublet magnification and total magnification of -1.30 and 16 respectively can be obtained.

This setup is mounted inside a lens tube which can be moved to view different areas of the microchip via a XYZ translation stage. The lens tube directs the fluorescence into a light-tight metal box. Inside this box, a motorised flipper mirror (allowing photons to be detected from either of the two experimental setups) directs the fluorescence through a bandpass filter. This filter is used to filter out any unwanted light which is not at 369 nm. A second flipper mirror is then used to direct the fluorescence to the electron-multiplying charge-coupled device (EMCCD) or the photon multiplier tube (PMT). In the experiments presented in this chapter only the EMCCD is used. However future experiments will require the use of the PMT.

6.3.3 Optical setup

There are some important factors to take into consideration when designing the optical setup for the operation of a surface trap. The laser beams need to be very close to the surface of the microchip. To ensure scattering off the surface is minimised, a clean Gaussian beam profile is required. Furthermore, the beams are required to move in a direction perpendicular to the surface of the microchip for their alignment to coincide

with the ion height. This needs to be achieved while maintaining their parallel alignment to the surface to ensure a lattice of trapping sites can be addressed at the same time.

The optical setup used for the experiments in this chapter is shown in figure 6.8. Single mode fibres are used to send the light required for ionisation (399 nm), cooling (369 nm) and repumping (935 nm) from the laser setup described in chapter 3 to the optical setup described here. The 369 and 399 are overlapped using a bandpass filter which transmits light at 369 nm but reflects light at 399 nm. A dichroic mirror is then used to overlap these UV beams with the 935 beam. A lens mounted to the 399 translation stage allows to optimise the beam size and more importantly allows the beam to be directed to specific trapping regions within the lattice that is being laser cooled. In order to focus all beams to the trapping regions and be able to alter the beam height from the microchip while maintaining its parallel alignment with the chip a final translation stage is required. A schematic of the final translation stage is shown in figure 6.8. The final mirror labelled 2 is attached to the green platform. The position of this platform and indeed the final mirror can be adjusted using the micrometer labelled 1 and is used in the experiment to adjust the beam height from the chip. Focusing the beams to the trapping regions is achieved by mounting a lens to a platform shown in red which in turn is mounted on top of the green platform. The position of the focal point of the beams can be changed using the micrometer labelled 3 which adjusts the position of the red platform and the final lens. Since the red platform is mounted on top of the green platform, with the top part of each platform being moved with the relevant micrometer, adjusting the beam height does not affect the position of the focal point and adjusting the position of the focal point does not affect the beam height. A picture of the translation stage can be seen in figure 6.9.

Charge build up on the surface

Charge build up on the surface of any trap is an undesirable effect as it shifts the ion away from the rf nil causing micromotion. Due to its time varying nature it also makes the required level of micromotion compensation using static voltage electrodes very unpredictable and time consuming.

The atomic oven alignment in our setup is non-optimal resulting in the possibility of Yb being deposited on the gold coated surface of the microchip. Unfortunately Yb has a work function of 2.6 eV and can therefore be charged up by 369 nm light, which has an energy of 3.36 eV, if it is deposited on a dielectric. While gold is not a dielectric, it is very likely that parts of the surface contain a thin dielectric layer due to imperfect cleaning of

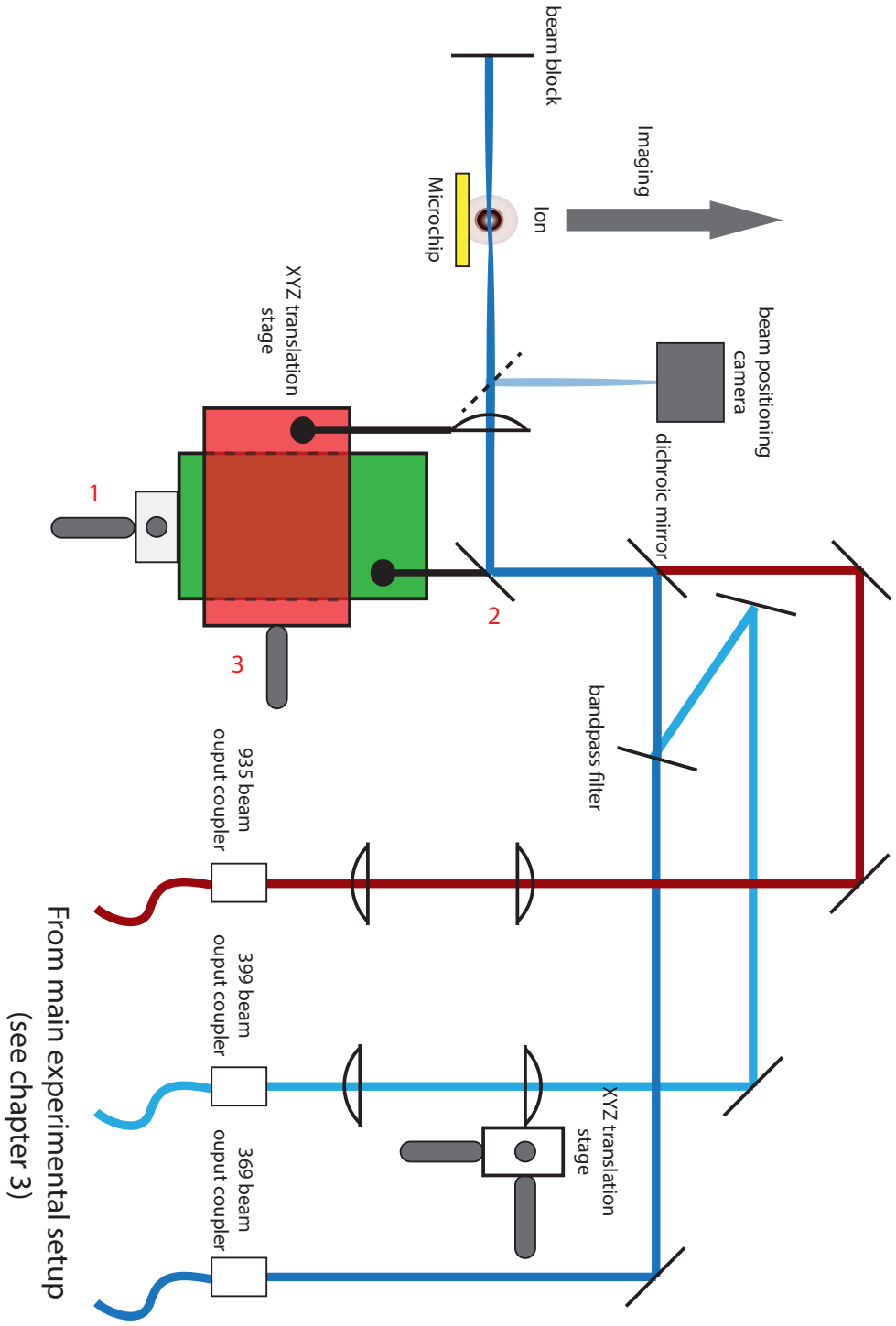

Figure 6.8: Schematic of the optical setup. Light at 369 nm, 399 nm and 935 nm is guided from the main experimental setup shown in chapter 3 to the setup shown here using single mode fibres. The beams are overlapped and focused to the trapping sites. Lenses mounted on XYZ translation stages are used for careful and reproducible beam alignment at the trapping sites. A beam positioning camera is used to monitor the position and profile of the beams and is a useful tool to ensure that all beams are overlapped. Scattered photons from the ion(s) is then collected using a imaging system. The red dashed box indicates the position of the vacuum system. The numbering refers to the beam alignment procedure discussed in section 6.3.3.

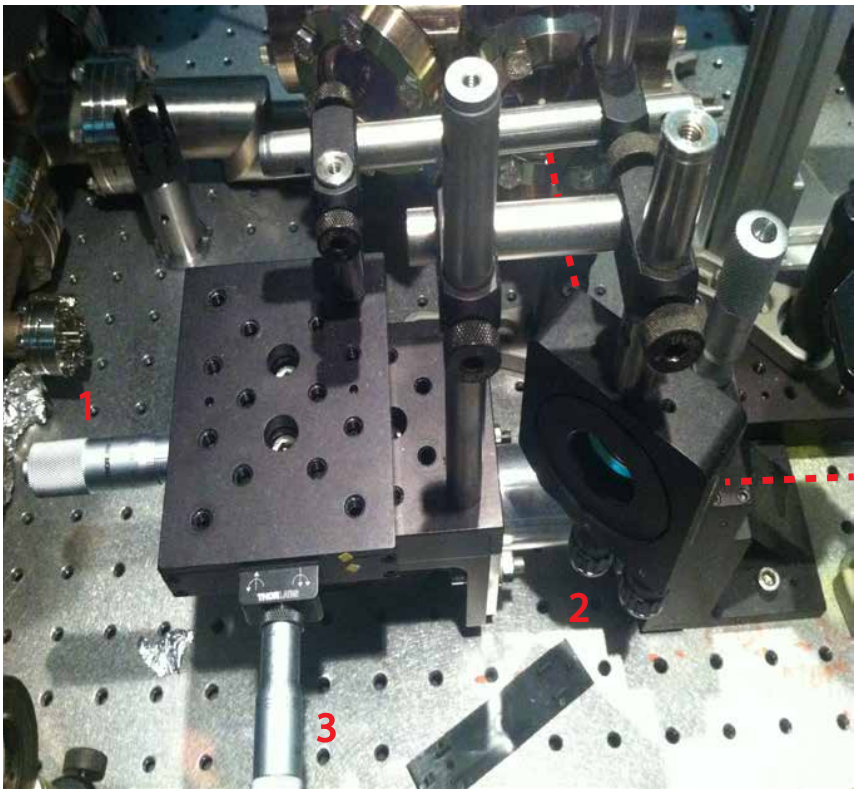

Figure 6.9: Picture of the final translation stage used to align the beams parallel to the surface of the microchip. The numbers correspond to the numbering in figure 6.8. The red dashed line illustrates the beam path.

the microchip. Any exposure of the surface to 369 light should therefore be avoided. Any required beam steering onto the surface of the microchip for alignment purposes should be done at the lowest possible laser intensity and only if absolutely necessary.

To reduce the frequency at which 369 light has to be steered onto the surface of the microchip for alignment purposes, a beam sampler is used to direct a small proportion of the laser beams after the final lens onto a CCD array[5]. This allows to continuously monitor the position of the beams as well as ensure that all beams are overlapped. To ensure that the overlap and the profile of the beams on the CCD corresponds to the case at the microchip, great care is taken to match the distance between the final lens all laser beams pass through and the CCD array to the distance between the final lens and the microchip. Since the CCD is extremely sensitive to the intensity of the beams a filter[6] is added to the beam path. A specific point on the CCD now corresponds to where ions can be trapped on the microchip (once calibrated to a trapped ion) and the beams can simply be aligned to that point whenever any misalignment has taken place instead of going through the beam alignment procedure explained below which requires beams to be

[5]Basler, Part number: acA1300-30gm
[6]Thorlabs, Part number: NE10A-A 350-700 nm

steered onto the surface of the microchip.

Aligning beams to the microchip

Before the beams are aligned along the surface of the microchip, the following steps are carried out:

- the beam intensities are reduced as much as possible. Prolonged exposure of the beams to the chip surface should be avoided whenever possible.
- the beams are coarsely aligned through the hemisphere passing in between the microchip and the large window used to image the ions.
- the distance between the final lens and the trapping region is coarsely matched to the focal length using the micrometer labelled as 3 in figure 6.8.
- the 369, 399 and 935 beams are overlapped with each other.

Once the 369, 399 and 935 beams are overlapped with each other the 399 and 935 beams are blocked using their respective iris. Using the final mirror labelled as 2 in figure 6.8, which is mounted to the green platform, the 369 beam is angled towards the surface of the microchip. The scatter visible on the EMCCD is then used to ensure the beam is addressing the correct region of polygons. The micrometer labelled as 1 which adjusts the position of the final mirror labelled 2 and the horizontal adjustment of that same mirror is then used to walk the 369 beam until it is parallel to the surface. To check if the beam is parallel to the surface the micrometer labelled as 1 is adjusted until the beam starts to clip the surface which manifests itself as scatter on the microchip which is visible on the EMCCD. If the level of scatter is approximately constant across the microchip then the beam is aligned parallel to the surface with an accuracy sufficient for the experiments presented in this chapter. The beam height is now adjusted to coincide with the ion height of 116 μm using the micrometer labelled 1.

The irises of the 399 and 935 beam are now opened. Due to chromatic aberration it is likely that the beams will not be properly overlapped any more after the 369 beam has been aligned to the trapping regions. We therefore use the CCD setup shown above to make small adjustments to the alignment of the 399 and 935 beam to ensure all beams are of similar size and are overlapped. Once ions have been trapped, the pixel numbers corresponding to the beam positions on the CCD array are noted down and used for future beam alignment purposes.

Resonator design parameters	
Shield diameter (mm)	108±2
Shield height (mm)	120±2
Coil diameter (mm)	42±2
Coil wire diameter (mm)	5.0±0.1
Winding pitch (mm)	9±3
Number of turns	6.75 ± 0.25

Table 6.1: Table showing the design parameters of the resonator used to apply a oscillating trapping field to the microchip.

6.3.4 Resonator

The oscillating trapping potential is applied to the microchip via a helical resonator, similar to the resonator described in chapter 3. The design parameters differ to account for the larger capacitance and resistance of the microchip. The parameters of the resonator for a microchip with a capacitance of $C = 26 \pm 2$ pF and a resistance of $\approx 10\ \Omega$ are shown in table 6.3.4. A picture of the resonator can be seen in figure 6.10. Once attached to the microchip the resonant frequency f_0 was found to be 32.2 ± 0.2 MHz and the Q was measured to be 160 ± 20.

Figure 6.10: Picture of the resonator used to apply a oscillating trapping potential to the microchip.

6.4 Experimental results

In this section we present measurements which characterise the microchip and demonstrate, for the first time, trapping of single ions in two dimensions using a lattice of individual microfabricated rf ion traps.

In order to trap single Yb ions on the microchip the following general steps need to be performed:

- Align the ionisation, cooling and repumping beams to the required trapping sites using the method described in section 6.3.3. Any required beam steering onto the surface of the microchip for alignment purposes should be performed with the lowest possible laser intensity to minimise charge build up.

- Block all laser beams.

- Apply the rf and static voltages to the electrodes.

- Wait approximately one hour to reduce any effects from charge build up on the surface from aligning the laser beams.

- Apply the required laser power.

- Resistively heat the atomic oven to produce a neutral Yb flux at he trapping sites until the required number of ions are trapped.

6.4.1 Secular frequency and ion lifetime measurements

To trap a single $^{174}Yb^{+}$ ion above polygon A (see figure 6.3) an rf power $P = 4\,\mathrm{W}$ at a drive frequency $\Omega_D/2\pi = 32.2\,\mathrm{MHz}$ is applied to the microchip via the helical coil resonator described above. At this stage all other electrodes are held at ground. The pseudopotential of the microchip $116\,\mu\mathrm{m}$ above the surface (corresponding to the ion height) is shown in figure 6.11. The 369, 399 and 935 laser beams with powers of approximately $200\,\mu\mathrm{W}$, $100\,\mu\mathrm{W}$ and $4\,\mathrm{mW}$ respectively are focused down to a beam waist at the trapping region of approximately $200\,\mu\mathrm{m}$. A picture of a single crystallised ion trapped above polygon A is shown in figure 6.12. To measure the secular frequencies of the ion a 3 V peak-to-peak oscillating voltage is applied to electrode Comp 1. When the oscillation frequency corresponds to the frequency of the ion motion along one of the axis of motion, a 'fuzzing out' like behaviour of the ion, or more precisely a reduction in fluorescence, can be observed on the EMCCD. The ion secular frequencies along the principal axes were measured to be $(\nu_x, \nu_y, \nu_z)/2\pi = (1.58, 1.47, 3.30) \pm 0.01\,\mathrm{MHz}$. These measurements, together with numerical simulations, predict a trap depth of 0.42(2) eV, corresponding to a voltage V applied to the microchip of 455(3) V. Using the relationship between the power applied to a resonator of a given Q and the rf voltage applied to the microchip given by [92]

$$\mathrm{V} = \kappa\sqrt{2PQ}, \tag{6.5}$$

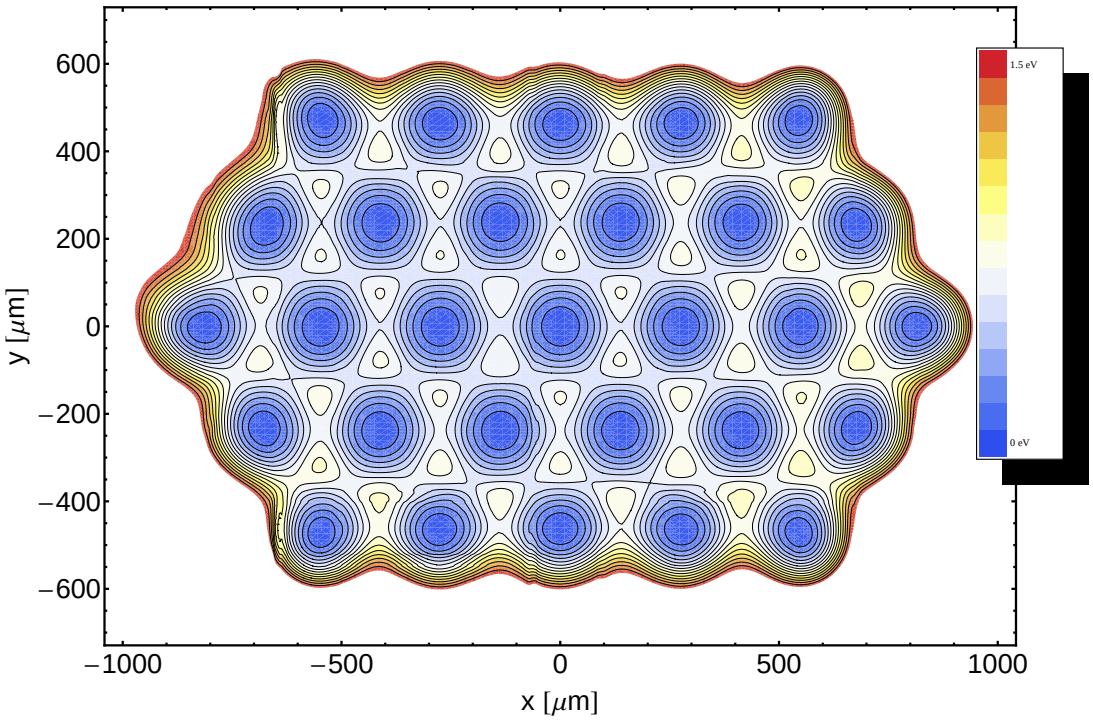

Figure 6.11: Pseudopotential of the microchip 116 μm above the surface, which corresponds to the ion height, for a $^{174}Yb^{+}$ ion, a drive frequency of $\Omega_D/2\pi = 32.2$ MHz and a voltage of 455 V.

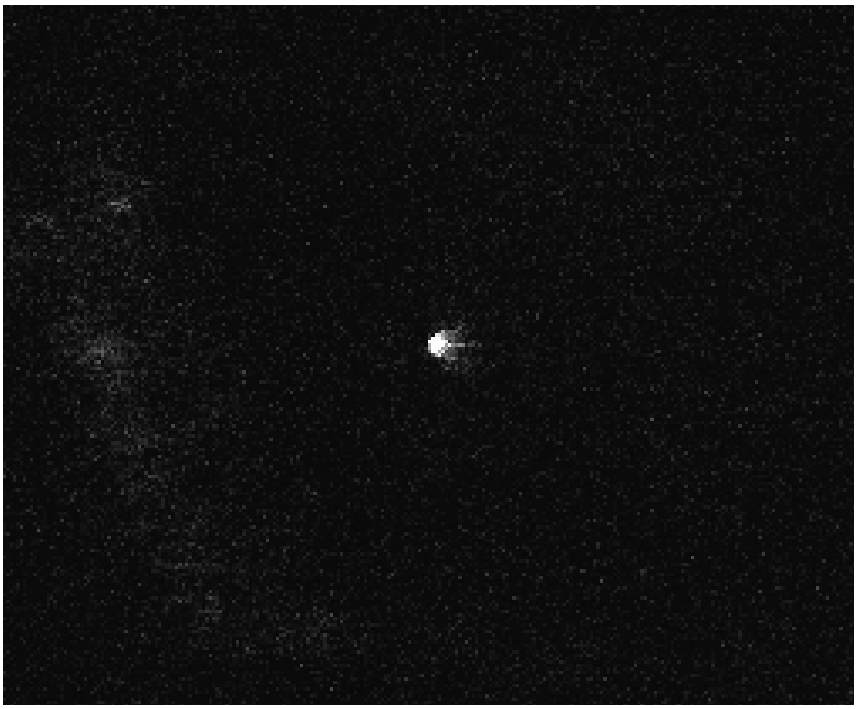

Figure 6.12: Picture of a single crystallised ion trapped above polygon A. The additional scatter stems from 369 nm light hitting the edges of the polygon.

κ is calculated to be 13.57. Determining κ allows us to calculate the voltage at the microchip for any given power applied to the resonator.

By reducing the rf voltage to 125 V the minimum achievable secular frequency the ion can easily be trapped at is measured to be $\nu_y/2\pi \approx \nu_z/2\pi \approx 0.5\,\mathrm{MHz}$.

As the number of ions in the lattice grows the ion lifetime becomes increasingly important due to the disruptive nature on remaining ions in the lattice when trying to replace a lost ion. The lifetime of an ion in our lattice with cooling light was measured to be ~ 90 minutes. This was likely limited by background collisions and can be increased by aligning light at 638 nm into the trapping region to depopulate the $^2F_{7/2}$ state which population can be transferred to from the $^2D_{3/2}$ state via background collisions (see chapter 3). By blocking the 369 laser light, which interrupts the cooling cycle of the ion, for an increasing length of time, the lifetime of the ion without cooling was measured to be ≥ 5 minutes.

6.4.2 Two-dimensional ion lattice

Using this microchip allows trapping of a 2D lattice of ions. This requires the beam profile of the laser beams to be altered to cover several rows of trapping regions. There are several ways of achieving this. One possibility would be to align a beam along one row, allow the beam to exit the vacuum system using a viewport on the opposite side from where the beam entered the vacuum system and then reflect the beam back but displaced to address the next row of trapping regions. This process could be repeated until the required number of rows are addressed with laser light. This would be particularly useful if the available beam intensity limits the beam size to only one row of trapping regions. In our case sufficient beam powers are available to shape the beam profile into a sheet of light to address three rows. The beam profiles are reshaped by replacing the final lens before the beam enters the vacuum system with a cylindrical lens which has a focal length of 150 mm. The 369, 399 and 935 beam sizes at the microchip are measured to be $\approx 900\,\mu$m by $50\,\mu$m. The beam powers of the 369, 399 and 935 are measured to be 1.5 mW, 0.9 mW and 4 mW respectively.

A 2D lattice of ions is trapped by repeating the trapping procedure multiple times until the lattice consists of the required number of ions. Due to the large trap depth this process is greatly simplified as the ion loss rate during trapping is low. A picture of a 2D ion lattice consisting of 6 crystallised ions trapped in adjacent lattice sites (sites C, D, E, F, G and H) is shown in figure 6.13. Nevertheless, due to the stochastic nature of trapping ions and due to problems with loosing ions via background collisions this was

very challenging. Furthermore, repeatedly running the atomic ovens made it increasingly difficult to trap ions which is expected to be caused by coating of the electrodes. A larger lattice of ions can in principle be trapped, however the viewable area is currently limited by our imaging system. Furthermore, obtaining a larger lattice requires the oven to be run for an even longer time or run more often making it increasingly likely to lose already trapped ions due to collisions with background gas as well as increasing the possibility of uncontrollably trapping multiple ions in one lattice site. A potential solution to this problem is discussed later on in this chapter.

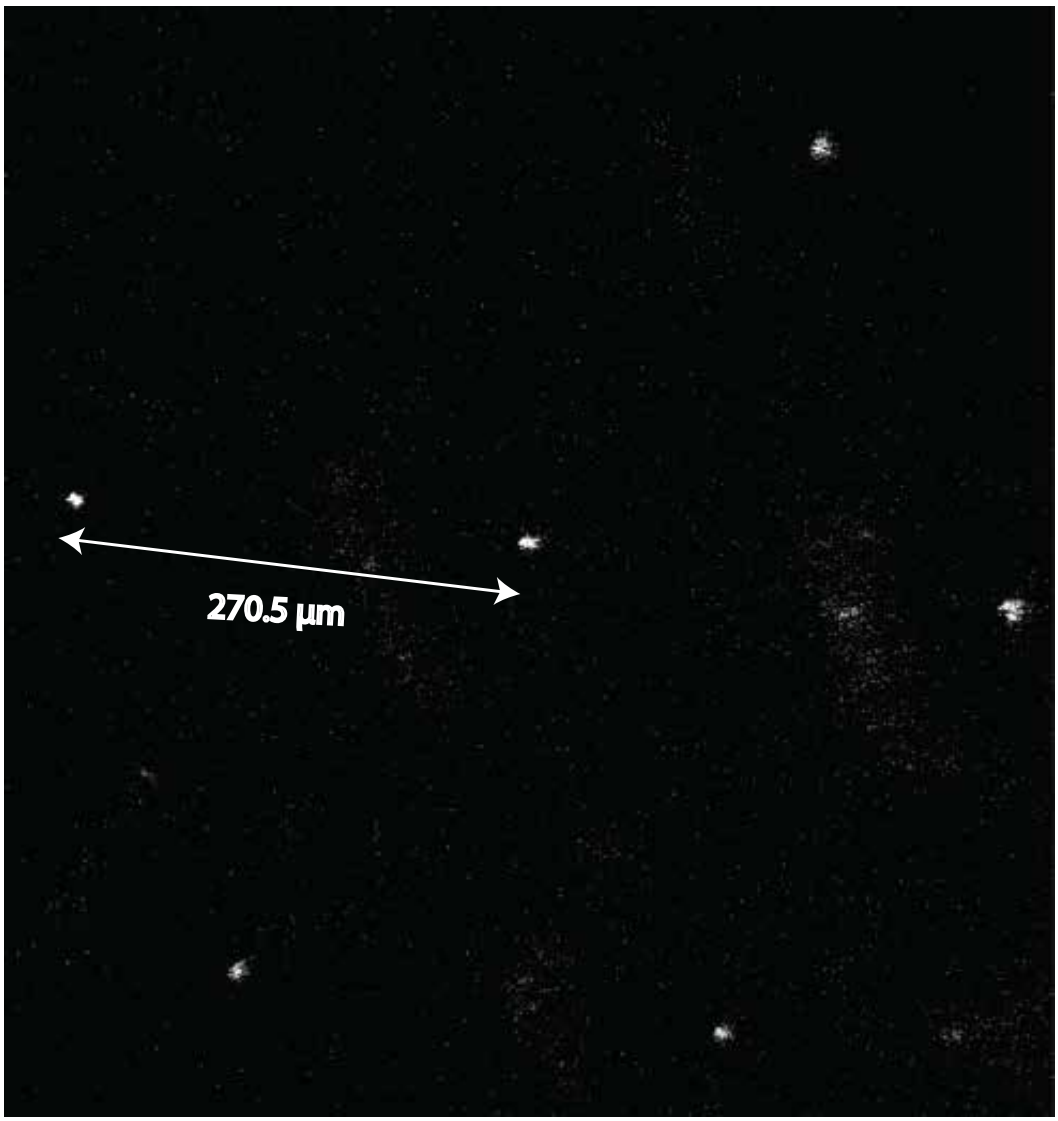

Figure 6.13: A 2D lattice of ions trapped above lattice sites C, D, E, F, G and H (see figure 6.3) with an ion-ion separation of 270.5 μm.

From a quantum simulation point of view it has been suggested that when investigating

Bose-Hubbard physics, such as superfluid-Mott insulator transitions, defects in the lattice can result in site-dependant phonon tunneling rates [126]. Such defects can consist in the form of a missing ion within the lattice of ions as shown in figure 6.13 where lattice site B does not have an ion. A defect could also be trapping multiple ions in a single lattice site which is part of a larger lattice of ions, which would allow for the simulation of spin models with spin greater than 1/2 [45].

To test if defects could be created on this microchip we first ensure that the 399 ionisation beam is aligned to the appropriate lattice site of interest. By repeating the trapping procedure multiple times it is then possible to load more than one crystalised ion into a single lattice site. A picture of three ions can be seen in figure 6.14.

Figure 6.14: A lattice defect consisting of three ions in a single lattice site.

6.4.3 Ion shuttling between lattice sites

During the work with this 2D lattice of rf ion traps, several issues related to the long term successful operation of these lattices became apparent. Over time it became more difficult to trap crystallised ions due to micromotion. While micromotion of a single ion can be compensated for using the large electrodes surrounding the lattice it was found that the voltages required to do this for a given lattice site varied over time and made trapping and compensating ions more challenging the more trapping attempts were performed with this microchip. This could be caused by the atomic beam of neutral atoms required during the loading process as this can deposit a layer of Yb on the electrodes of the microchip. Scatter from the laser beams used for trapping can then ionise these atoms due to the photoelectric effect which causes a charge to build up on the electrodes. Furthermore, due to the stochastic nature of trapping ions, it can take many trapping attempts to realise the ion lattice geometry one would want for their specific experiment. Not only does this

increase coating of the electrodes, the time required for loading the required geometry can lead to ions which had already been trapped being removed from the trapping potential via background collisions.

It is therefore advantageous to find a way to efficiently trap the required lattice geometry of ions without degrading the performance of the 2D lattice. One way to achieve this would be to trap ions in a specific zone on the microchip followed by shuttling of the ions to their desired positions.

To demonstrate the feasibility of this scheme a single ion is shuttled from lattice site E (refer to figure 6.3) to D and back to E again. This is illustrated in figure 6.15. Here, a single ion is trapped and laser cooled in lattice site E during step 1. During step 2 the rf voltage is reduced to minimise the rf barrier between the individual sites while a series of voltage profiles are then applied to the static voltage electrodes which transport the ion to lattice site D. Following another period of laser cooling of the ion in site D during step 3, similar voltage profiles are used to shuttle the ion back to site E. The only difference in the voltage profile is a reverse of the voltage on comp 3 and 6. The ion is then being laser cooled in site E during step 5.

While the microchip presented in this chapter does not allow shuttling protocols to be applied to individual lattice sites, the addition of local electrodes to each trapping site will address this in future microchip designs. This will also allow for site specific micromotion compensation which will significantly simplify trapping large lattices of ions and shuttling ions between different lattice sites.

6.5 Conclusion

The work presented in this chapter has demonstrated a fabrication process which significantly increases the voltage that can be applied to microfabricated devices. This advance was then used to fabricate a 2D lattice of rf ion traps on a microchip. We characterised the microchip by trapping a 2D lattice of ions, by measuring ion lifetimes and by measuring secular frequencies which are used to calculate the trap depth. The large trap depth that can be achieved due to the high voltages that can be applied to the microchip significantly simplified the successful demonstration of the first 2D lattice of $^{174}Yb^{+}$ ions using rf ion traps on a microchip. This result offers many potential uses in experiments involving 2D force measurements, B-field and E-field sensing and with further advances could offer a platform for cluster state generation and quantum simulation.

During the operation of the microchip the difficulty of loading and maintaining a 2D

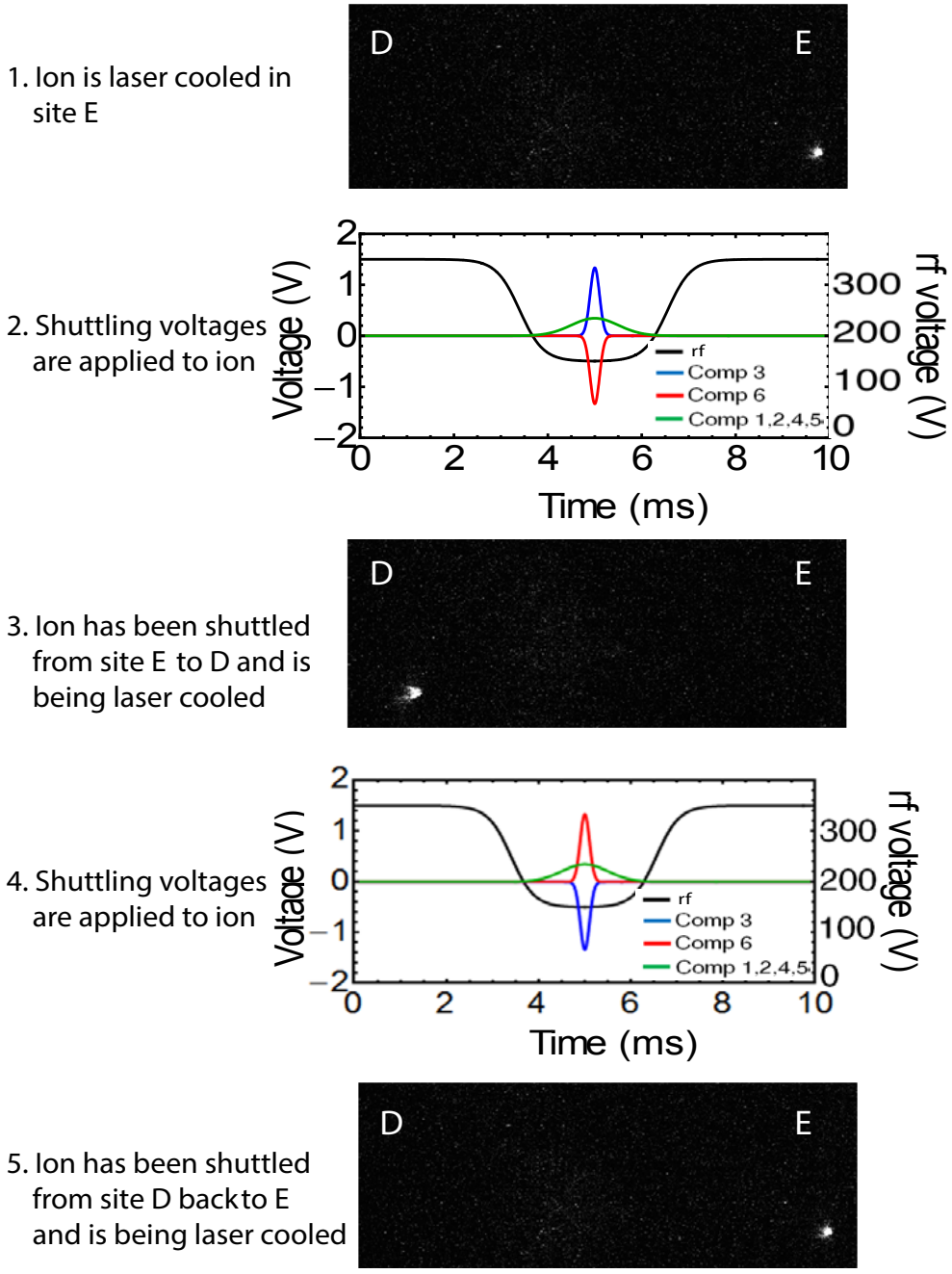

Figure 6.15: In step 1 a single ion is laser cooled in site E. A voltage profile shown in step 2 is used to shuttle the ion to site D. The ion is then being laser cooled in site D during step 3. A similar voltage profile but with the voltages on comp 3 and 6 reversed is then applied during step 4 to shuttle the ion back to site E. Finally, the ion is laser cooled in site E during step 5.

lattice of ions became apparent which stems from the disruptive effect on already trapped ions and on the surface of the microchip when trapping ions. We have therefore also shown the possibility of performing rudimentary shuttling operations between neighbouring lattice sites which could be part of a scheme to load large ion lattices.

In quantum simulations the interaction between ions located in separate potential wells is mediated via the Coulomb force. This dipole-dipole interaction between two ions separated by a distance A is given by [140, 141]

$$\hat{H}_c = -\frac{\hbar\Omega_{ex}}{2}(a_1 a_2^\dagger + a_1^\dagger a_2) \tag{6.6}$$

where a_i and $a_i^\dagger$ are the harmonic oscillator creation and annihilation operators of ion i and the coupling strength between the motional states is given by [140, 141]

$$\Omega_{ex} = \frac{q_1 q_2}{2\pi\epsilon_0\sqrt{m_1 m_2 \nu_1 \nu_2}A^3} \tag{6.7}$$

where q_i and m_i is the charge and the mass and ν_i the secular frequency of the corresponding ion. We can see from equation 6.7 that $\Omega_{ex} \propto 1/A^3$ indicating that the ions should be placed as close together as possible. For $^{171}Yb^+$ ions trapped on the microchip presented in this chapter with an ion-ion separation of $A = 270.5\,\mu$m, the coupling strength $\Omega_{ex} = 2\pi \times 4\,$Hz for a secular frequency of $\nu/2\pi = 0.5\,$MHz. This coupling strength is not sufficient for quantum simulations and is considerably lower than that achieved between individual wells on linear surface traps [140, 141]. Since we now have a scalable approach to produce 2D lattices of rf ion traps on a microchip the next major step towards the successful implementation of a 2D quantum simulation is the fabrication and operation of a microchip where the ion-ion separation is small enough to observe a coupling between the ions.

To achieve this goal it is desirable to answer the question of what would be the optimum geometry of an ion trap lattice which maximises the ratio of an effective spin-spin interaction rate between neighbouring ions to the decoherence rate from effects such as ion heating. The answer to this question along with an explanation of how an effective spin-spin coupling between ions can be achieved will be discussed in the next chapter. At the end of that chapter, in section 7.8, I will come back to the lattice presented in this chapter and illustrate how simple modifications to the microchip design shown in this chapter should allow interaction rates suitable for the implementation of 2D quantum simulations to be achieved.

Chapter 7

Optimisation of two-dimensional ion trap arrays for quantum simulation

7.1 Introduction

It was demonstrated in the previous chapter that it is indeed possible to create a two-dimensional (2D) lattice of individually trapped ions on a microchip. Since this is a microchip it can be scaled to many more ions. On the route to the successful implementation of 2D quantum simulations with ions, the challenge now lies in developing a optimal 2D lattice geometry which maximises the coupling rate between neighbouring ions while minimising decoherence detrimental to the experimental realisation of quantum simulations. We thereby ensure that the highest possible quantum simulation fidelity can be achieved using the most efficient experimental setup. Determining this optimal geometry is the main focus of our work presented in [55]. This paper is shown in this chapter however small alterations have been made where necessary.

In order to create this optimal 2D lattice of trapped ions a repeating 2D surface geometry is required which takes the coupling rate as well as sources of decoherence into account. Decoherence due to anomalous heating is a major issue for large scale quantum simulations. As this heating scales approximately as r^{-4} [91], where r is the ion height above the trap surface, it is advantageous for ions to be trapped high above the surface. However, when individual surface microtraps are placed close together (increasing the coupling rate between neighbouring ions), so that their separation is less than around twice the ion height, the individual electric fields start to overlap and distort the resulting trapping

fields [131]. In extreme cases this can lead to the traps combining to produce a singular trapping zone. To compensate for this the electrode structure has to be altered when operating within this regime [131]. Schmied *et al.* [131] have investigated surface-electrode geometries and developed an algorithm that optimises geometries to maximise the electric field curvatures of individual trapping sites for arbitrary ion heights and separations. Individual trapping sites shown in [131, 142] were optimised using this algorithm leading to non-intuitive electrode patterns which can contain many isolated radio-frequency (rf) and static voltage electrodes. Another proposal [130] which works outside this regime uses rf electrodes with controllable rf voltages to lower trap frequencies and decrease ion-ion distances and, therefore, increase coupling rates. However, this requires the use of multiple independent rf electrodes and individually controllable rf voltages posing an additional experimental complication.

In this chapter the focus will lie on the optimisation process for ion trap topologies based on a single island of rf electrode, reducing the requirement for buried rf wires and multiple rf electrodes. The development of an optimum lattice geometry where the ratio of coupling rate to the decoherence rate due to ion heating is maximised and made homogeneous across the lattice is achieved by minimising the secular frequencies of the trapping sites. This is done whilst, simultaneously, keeping the trapping depths above a minimum trap depth (for illustrative purposes 0.1 eV is used) to allow for successful operation of the proposed 2D lattice designs. The optimal lattice topologies considered in this work are for hexagonal, square and centred rectangular lattices. An investigation is also carried out on how optimal geometries depend on the overall lattice size. This is followed by a discussion of the choice of and scaling for experimental parameters such as rf voltage, drive frequency, ion mass and electric field noise density.

7.2 Ion-ion interactions and Lattice Geometry

7.2.1 Ion-ion interactions

The equilibrium position of the ions is determined by the total potential dominated by forces such as the trapping force, $F_T = -mx\nu_i^2$, and the coulomb force, $F_C = -e^2/(4\pi\epsilon_0 A^2)$, between the individual ions. Laser beams or magnetic field gradients can be used to impart an additional force to the ions which displace the ion(s) depending on its internal state. The ratio of the change in the Coulomb force to the change in the restoring force due to this displacement is given by [45]

$$\beta = \frac{e^2}{2\pi\epsilon_0 m\nu^2 A^3} = \frac{\Omega_{ex}}{\nu}, \tag{7.1}$$

where A is the ion-ion spacing, ν is the trap's secular frequency, m is the mass of the ion and Ω_{ex} is the coupling strength of the coulomb interaction defined in the previous chapter. There are two regimes to consider. When $\beta > 1$, the change in the Coulomb force, δF_C, due to the displacement of an ion is dominant over the change in the restoring force, δF_T. This results in an interaction over a large number of trapping sites. When $\beta < 1$, the opposite is true resulting in an interaction which decays rapidly across the array and generally only acts on nearest neighbour ions. Trapping ions in a 2D lattice of microtraps makes it possible to satisfy the condition that $\beta < 1$ allowing systems with short range interactions to be simulated. In the case where $\beta < 1$ the interaction strength, or state dependant coupling rate, can be given as [45]

$$J = \frac{\beta F^2}{\hbar m\nu^2} \tag{7.2}$$

where F is the magnitude of the state dependant force applied to each ion. We will consider how this force is applied later in this chapter. An illustration of this interacting system is shown in figure 7.1.

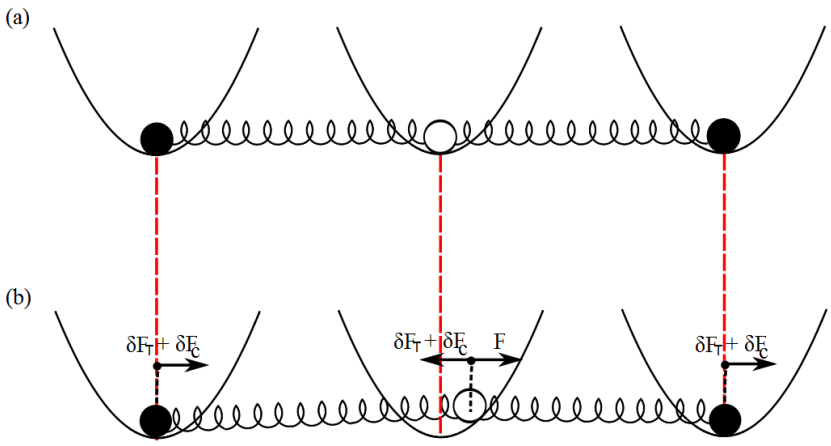

Figure 7.1: Pictorial diagram of three ions in adjacent traps. The ions feel a Coulomb force indicated by the springs between each ion and can be placed in two different states indicated by their colour. (a) Pictorial diagram showing the case with no state dependent force present. (b) Pictorial diagram showing how the system reacts to the presence of a state dependent force, F. Here the ions feel a change in the Coulomb force, δF_C, due to the displacement of the ions and a change in the restoring force, δF_T.

It is important to consider sources of decoherence when designing a 2D ion trap array. The internal state of an ion can remain coherent for 10's of seconds [143, 144]. However, motional decoherence due to anomalous heating of ions will be an important factor during

quantum operations within small scale ion traps as the implementation of spin dependant couplings involves the use of motional states of the ion. The coupling, J, will be observable if the coupling time, $T_J = 1/J$, is less than the motional decoherence time in the system and, therefore, the ratio of these two times is an important parameter and is given by

$$K_{sim} = \frac{T_{\dot{n}}}{T_J} \tag{7.3}$$

where [91],

$$T_{\dot{n}} = \frac{4m\nu\hbar}{e^2 S_E(\nu)}. \tag{7.4}$$

Here $S_E(\nu)$ is the electric field noise density [42, 91]. In order for an interaction to occur on faster time-scales than the decoherence in the system, we require $K_{sim} > 1$ and it is the aim of the optimisation process presented in this chapter to optimise the geometry in order to maximise this parameter. To acquire an understanding of how a geometry can affect K_{sim} it is necessary to determine its form with respect to the geometry variables. The form of T_J can be found by substituting equation 7.1 into 7.2 and is given by

$$T_J = \frac{2\pi\epsilon_0 m^2\nu^4 A^3\hbar}{e^2 F^2}. \tag{7.5}$$

The K_{sim} parameter can then be expressed as

$$K_{sim} = \frac{2F^2}{S_E(\nu)\pi\epsilon_0 m\nu^3 A^3}. \tag{7.6}$$

The secular frequency, ν, of a trapped ion [145] can be expressed as a function of α defined as

$$\alpha = \frac{V}{\Omega} \tag{7.7}$$

where V is the amplitude of the rf voltage applied to the trap and Ω is 2π times the drive frequency in Hz, yielding,

$$\nu = \frac{eV\eta_{geo}}{\sqrt{2}m\Omega r^2} = \frac{e\alpha\eta_{geo}}{\sqrt{2}mr^2} \tag{7.8}$$

where r is the height of an ion above the surface, e is the charge of an electron and η_{geo} is an efficiency factor which can range between zero and one depending on the form of the geometry [145].

The secular frequency given in equation 7.8 can then be used along with $S_E(\nu) =$

$\Xi r^{-4}\nu^{-1}$, where Ξ is a coefficient that can be experimentally obtained and depends on the temperature and surface of the trap electrodes (see [42] for a listing) to re-express equation 7.6 in the form

$$K_{sim} = \frac{4F^2 m r^8}{\Xi \alpha^2 \eta_{geo}^2 \pi \epsilon_0 A^3}. \tag{7.9}$$

To further understand how the geometry effects the K_{sim} value we will now introduce the parameters of a lattice geometry and relate them to equation 7.9.

7.2.2 Two-dimensional ion trap lattice geometry

A lattice is a regular tiling of a space by a primitive unit cell. In total there exist five types of cell which can be used to form a 2D lattice: centred rectangular, hexagonal and square as shown in figure 7.2, and rectangular and oblique [146]. The rectangular and oblique structures are not considered in this work due to their non-uniform ion-ion distances. Previous works [129, 130] concentrate on lattices created from square unit cells and the previous chapter presented the operation of a hexagonal lattices [138].

Figure 7.2 shows the polygon-polygon separation which is equal to the ion-ion distance, A, in equation 7.9. The polygon radius, R, along with the separation, will determine the height above the surface at which the ion is trapped, r, with larger polygon radii yielding higher ion heights. Another variable to be considered is the gap between the outer polygon in the array to the edge of the rf electrode, g. This can be used to alter the homogeneity of the individual trapping sites within the array. In general, a non-homogeneous system results in spin dependant coupling rates which are a function of the lattice site, posing a significant problem for the scalability of such an array [147].

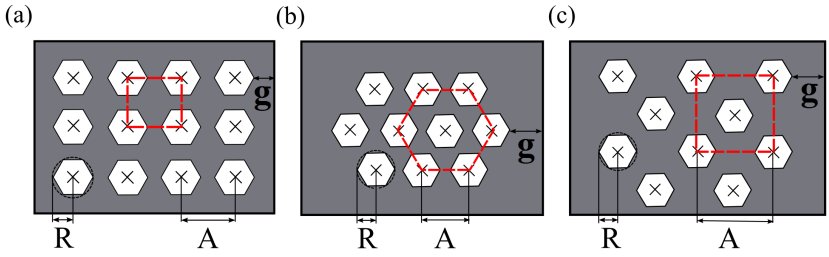

Figure 7.2: Diagrams showing the polygon radii R, the separation between the polygon centrers, A, and the distance between the last polygon and the edge of the rf electrode (shown in grey), g. (a) Diagram showing a three by four ion trap surface array consisting of six sided polygons arranged with square unit cells. (b) Diagram showing a similar surface array arranged into hexagonal unit cells. (c) Diagram showing a surface array arranged into centred rectangular unit cells. The unit cells are indicated by dashed lines.

7.3 Simulation of lattices

To determine the electric field produced by a two-dimensional array a method based on the Biot-Savart like law described by Oliveira and Miranda [5] was used. This method calculates the electric field produced by an arbitrarily shaped two-dimensional electrode which is held at a potential V whilst the rest of the plane is held at a potential of zero. The electric field observed at a given point, $\overline{X}$, in space due to such an area held at a potential and bounded by a path C is given by [5]

$$E_{(\overline{X})} = \frac{V}{2\pi} \oint_C \frac{(\overline{x} - \overline{x}') \times d\overline{s}}{|\overline{x} - \overline{x}'|^3} \tag{7.10}$$

where the curve, C, bounds the electrode and $\overline{x}'$ and $\overline{x}$ are vectors that locate the source point and field point respectively. By calculating the electric field in this manner an assumption is made that there is no gap between the areas held at the potential, V, and the areas held at zero. In microfabricated surface traps, gaps between the electrodes are required and typically range from 3 μm - 10 μm [42]. If, however, these gaps are small in comparison to the electrode structures they will not alter the trapping fields significantly [4, 43, 142]. The electric fields of individual electrodes can then be combined to determine potential nils and, therefore, trapping positions in the 2D trap lattice, using the numerical Gauss-Newton algorithm. The secular frequencies, trap depths and ion heights at these positions can then be determined.

To calculate the error of the numerical integration, Bjoern Lekitsch undertook a study in which he compared simulations of five wire symmetric surface trap geometries with different central static electrode and rf rail widths in the gapless plane approximation using the method of Oliveira and Miranda [5] to results obtained with analytical equations described by House [4]. In all the geometries simulated the two rf rails were of equal width. Similarly to House, the outer static voltage electrodes were approximated as an infinitely long ground plane although the length of the inner rails were set to 3000 μm instead of infinite. A selection of the simulation results are shown in table 7.1.

In these results a general error for the ion heights and secular frequencies of less than 2% and 3% respectively was found, which leads to a maximum error in K_{sim} of 10%. For the following simulations it is therefore assumed that the maximum K_{sim} error is 10%. Additionally, numerical simulations of the geometries were carried out using methods described in [148], which indicate similar errors and trends for the ion height and secular frequency as the results obtained with the Biot-Savart like method.

Electrode parameters				Simulations		House equations	
rf width [μm]	central static electrode width [μm]	rf Volt. [V]	rf freq. [MHz]	r [μm]	ν [MHz]	r [μm]	ν [MHz]
100	50	250	75	55.8	6.86	55.9	6.87
100	50	500	60	55.8	4.29	55.9	4.29
200	100	250	30	110.1	2.17	111.8	2.20
200	100	500	40	110.1	3.26	111.8	3.30
500	150	250	20	165.4	1.48	167.7	1.52
500	150	500	25	165.4	2.37	167.7	2.43

Table 7.1: Table showing the secular frequency, ν, and ion height, r, for different five wire surface trap geometries as calculated by the analytical method in House [4] and simulated by the method used in this work based on the Biot-Savart like law [5].

7.4 Lattice geometry optimisation

In this section we show how the parameters of the lattice geometry R, A, g and n (as discussed in section 7.2.2) can be optimised to achieve the highest possible K_{sim} value across the lattice for a given set of experimental parameters. To do this, we first show how to maximise the homogeneity of individual site properties over the lattice by varying the distance between the outer polygon in the lattice to the edge of the rf electrode, g, and show how this scales with the lattice size. These homogeneous lattices are then used to calculate the optimum number of sides, n, a polygon within the lat sticehould possess in order to maximise K_{sim}. A method for the optimisation of the polygon radii, R, and separation, A, of a lattice is then described along with a discussion on how these vary with increased lattice size and ion mass.

7.4.1 Increasing the homogeneity of K_{sim} across the lattice

A homogenous K_{sim} accross the whole lattice is achieved by ensuring that the secular frequencies, ion height and trap depth is homogenous across all the individual lattice sites. As shown in figure 7.3, K_{sim} of the trapping sites in a lattice of length L can be altered to approach a common value if the distance, g, between the edge of the outer polygon and the edge of the rf electrode containing the polygon lattice is adjusted. As the value of g is increased, the K_{sim} value of the sites towards the centre drops and the outer sites K_{sim} value rises, resulting in the properties converging towards each other. If the distance g is increased further beyond the point at which maximum homogeneity occurs the outer site properties drift away from those of the central sites and, therefore, decrease the homogeneity of the array.

In order to simplify the optimisation process in this chapter it is desirable to provide a value of g which is universal for all lattice sizes. The value of g is therefore given in units of lattice side length, L. The lattice side length is determined by the polygon separation, A, and radius, R, and can be expressed as

$$L = (M-1)A + 2R, \tag{7.11}$$

where M is the number of lattice sites along one side of an array.

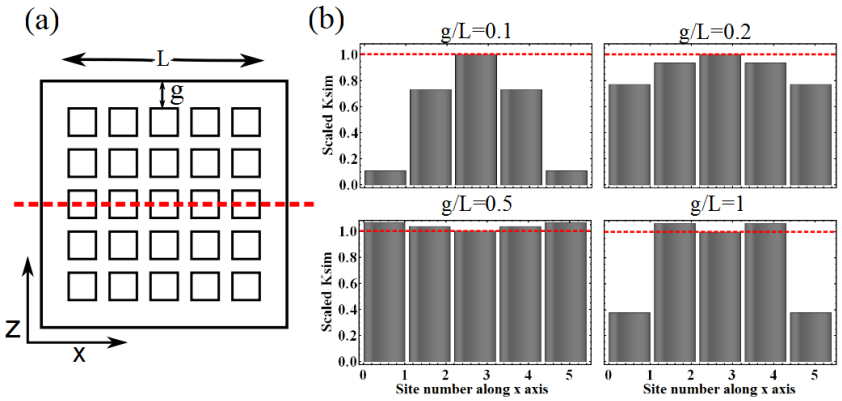

Figure 7.3: Diagram showing the effect of varying the distance g on the scaled K_{sim} value of the individual trapping sites. The K_{sim} values shown are scaled with that of the central site. (a) Representation of a 5 by 5 square type lattice array indicating the axis labelling. (b) Slice across the array (indicated by the dotted line in (a)) for g/L values of 0.1, 0.2, 0.5 and 1.

In order to quantify the arrays homogeneity, H is defined as the average deviation of K_{sim} of each lattice site from the K_{sim} of the central site and is given by

$$H = \frac{1}{N}\sum_{n=1}^{N}\left|1 - \frac{K_{sim_n}}{K_{sim_{centre}}}\right| \tag{7.12}$$

where N is the total number of trapping sites in the lattice.

Figure 7.4 shows H for a five by five square type unit cell lattice for $0 < g/L < 1.5$. The maximum homogeneity, and thus the optimum g/L, is found when H is minimised. The error associated with H is given by

$$\sigma_H = \frac{\sqrt{N(\sigma_{Ksim})^2 + N(\sigma_{Ksim_{centre}})^2}}{N} \tag{7.13}$$

where the error on all K_{sim} values is 10%, as shown in section 7.3. This yields an overall fractional error on H of $0.13/\sqrt{N}$.

Now that we have determined how to optimise g/L for a given number of lattice sites

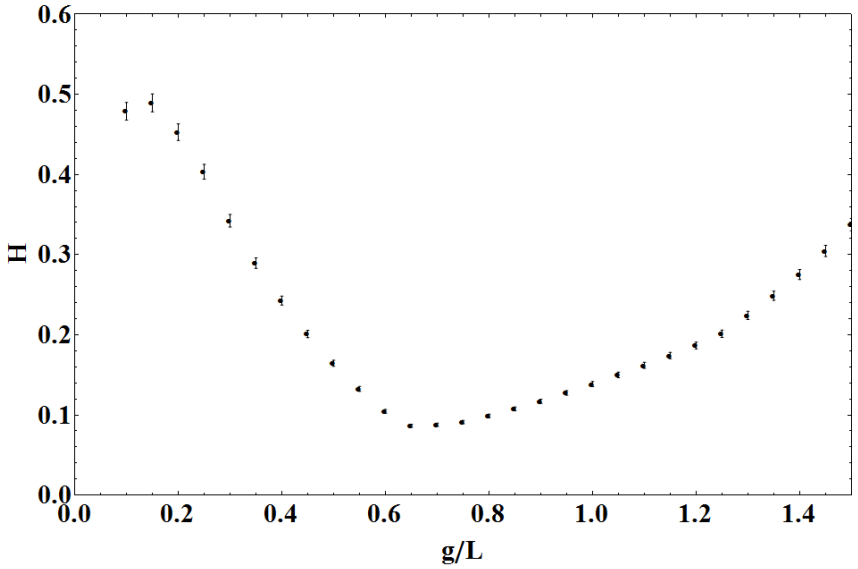

Figure 7.4: Graph showing the average deviation of the K_{sim} of each lattice site from the K_{sim} of the central site, H, for a five by five square type unit cell lattice for $0 < g/L < 1.5$. The error on H is given by $\frac{0.13}{\sqrt{N}}H$ and the error of the minimum of H is determined by observing the spread of g/L which agrees, within error, with the minimum position.

Lattice Type	a	b	B
Square	0.20±0.01	5.21±0.38	0.74±0.03
Hexagonal	0.39±0.08	3.76±1.40	0.54±0.14
Centre Rectangular	0.31±0.04	7.84±2.43	0.76±0.11

Table 7.2: Table showing a and b values for the fits which describe g/L as a function of the number of sites in the lattice.

N we can find out how the optimum g/L scales with a change in N. Figure 7.5 shows the optimum g/L for hexagonal, central rectangular and square unit cell lattices of different sizes. The curves are found to be described by an equation of the form $g/L = a + bN^{-B}$ with a, b and B values for different lattice types shown in table 7.2. For large lattices, the optimum g/L is found to become independent of N, as trapping sites close to the edge of the lattice are influenced only by the electric field created by that edge. In small lattices, however, the optimum g/L increases as the effect of the electric field from the opposite edge of the lattice increases.

7.4.2 Optimising the number of polygon sides

Let each site be a polygon of n sides. We now investigate the optimum number of polygon sides, n, providing the highest K_{sim} value on the central trapping site.

To ensure the results are universal for all lattice geometries, g/L is set to the value which maximises the homogeneity of each lattice, and all other parameters are scaled by

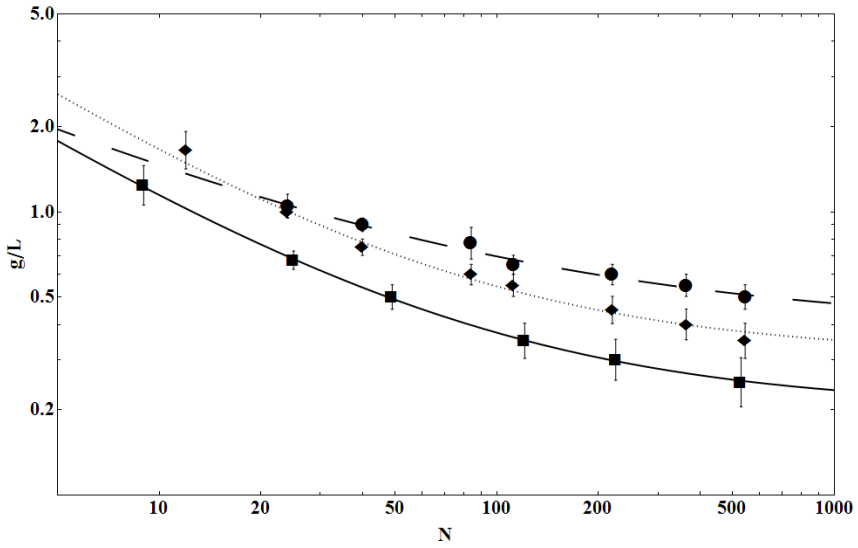

Figure 7.5: Graph showing the optimum g/L as a function of the total number of trapping sites, N, for square lattices (square markers), hexagonal lattices (circular markers) and centre rectangular lattices (diamond markers). The curves are given by $g/L = a + bN^{-B}$ with a, b and B values for different lattice types shown in table 7.2.

normalising K_{sim} to that of an identical geometry with polygons of 100 sides. This also allows comparison between the different types of lattices.

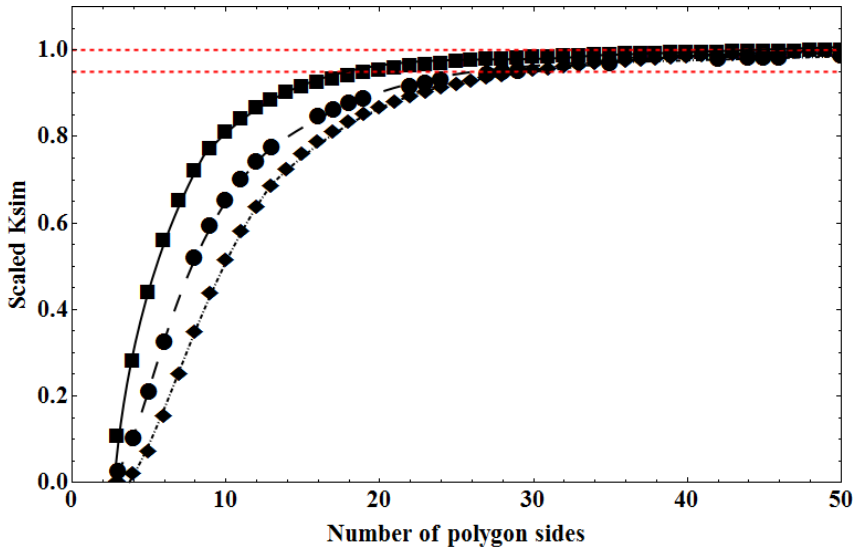

Figure 7.6: Graph showing the relationship between the number of polygon sides and K_{sim} for square (square markers), hexagonal (circular markers) and central rectangular (diamond markers) unit cell lattices. The dashed lines show the asymptotes of 1 and 0.95 of the scaled K_{sim} value.

Figure 7.6 shows the scaled K_{sim} for the central site as the number of polygon sides is varied. As the number of sides is increased the value of K_{sim} approaches an asymptote, shown by the upper dashed line. This indicates that the best geometry will be made from circular electrodes. However, simulation times grow with increasing polygon side number

and so it is advantageous to reduce this number to a minimum. It is shown that ≈95% of the maximum achievable K_{sim} (indicated by the lower dashed line) can be achieved with around ≥25-30 sides in the polygons.

7.4.3 Optimisation method for polygon separation and radius

In this section we now maximise K_{sim} of any arbitrary geometry. We can then go on to determine optimum geometries and show how they scale and, ultimately, are determined by $\alpha = V/\Omega$. The value of g which was found to give the maximum K_{sim} homogeneity across the lattice in section 7.4.1 will be used here. Furthermore, the number of sides for each polygon is set to 25 as this was found to provide a good approximation to the optimum circular geometry while keeping the simulation time at a minimum, as shown in section 7.4.2.

When considering any fixed arbitrary geometry, equation 7.9 shows that K_{sim} can be maximised by reducing the value of α. However, the minimum achievable α is limited by the lowest usable trap depth, as the trap depth is proportional to α^2 and is given by

$$T_D = \frac{\zeta e^2 \alpha^2}{\pi^2 m} \tag{7.14}$$

where e is the charge of an ion and ζ is a geometrical factor which is a function of A and R [4].

We can now focus on finding optimal geometries which we define as geometries, which yield the highest value of K_{sim} for a given value of α. This will be carried out by fixing the trap depth at a reasonable minimum value (we use 0.1 eV for illustration purposes) which, as discussed above, provides the maximum K_{sim} for a given geometry, and then investigate the dependence of α on the polygon radius, separation and ion height. To determine these dependencies a K_{sim} contour plot is made by calculating K_{sim} over a range of polygon separation, A, and radius, R, with a resolution of $1\mu m$. The range of polygon radius and separation used should not create traps with inter-well barriers of less than the minimum trap depth. To ensure this, the polygon radius was kept to less than a third of the polygon separation. For each combination of polygon separation and radius, a value of α which yields the minimum trap depth is found and, thus, maximises the K_{sim} of the particular geometry. By following this method one can obtain the α required to achieve the minimum trap depth, the ion height, r, and K_{sim} for each geometry. From the resulting data the polygon separation and radius which yields the highest K_{sim} for a given α (the optimum geometry) can then be found. A graphical example of such data is

shown in figure 7.7.

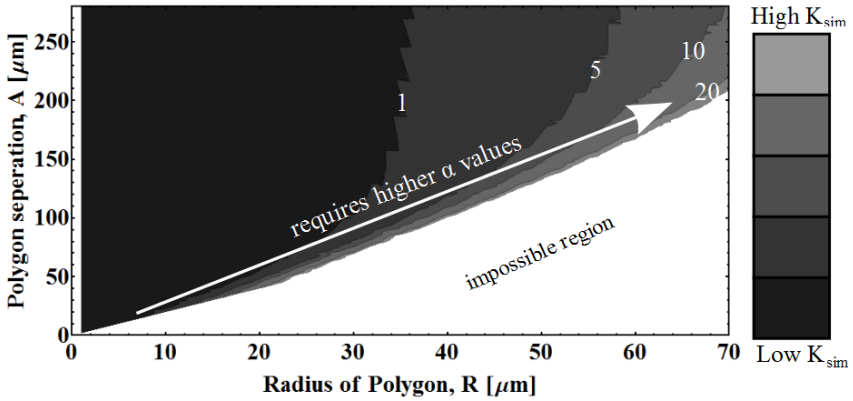

Figure 7.7: Example graph showing how the K_{sim} (absolute values indicated by numbers on contour lines) varies as a function of polygon radius and separation. The graph also indicates that the value of α increases as the radius and separation are increased. This data was obtained using the method described in section 7.4.3 with a polygon separation and radius resolution of 1 μm and a minimum trap depth of 0.1 eV. The value of α in the figure ranges from zero to ≈ 1.5 VMHz^{-1}. The impossible region describes geometries where individual trapping sites start to combine to a single one and so posses a polygon radius, R, greater than or equal to a third of the polygon separation, A.

It can be seen from this method and the example data in figure 7.7 that the highest K_{sim} will be achieved with an infinite value of α, R and A. However, other effects may limit the magnitude of α. In order to determine a limit on α it is, therefore, necessary to describe the various lattice and trapping field dependant properties (such as secular frequency, ion height and K_{sim}) in terms of α.

In order to do this we first need to plot the optimum parameters (polygon radius, separation and ion height) as a function of α, as shown in figures 7.8(a), (b) and (c) which allows us to determine linear relationships of the form

$$r = k_r \alpha \tag{7.15}$$

$$A = k_A \alpha \tag{7.16}$$

and

$$R = k_R \alpha \tag{7.17}$$

for the optimal geometries. The values of k_r, k_A and k_R are dependant on the number of trapping sites in a lattice, as shown in figures 7.9(a),(b) and (c) respectively, for lattices made from square type unit cells of polygons.

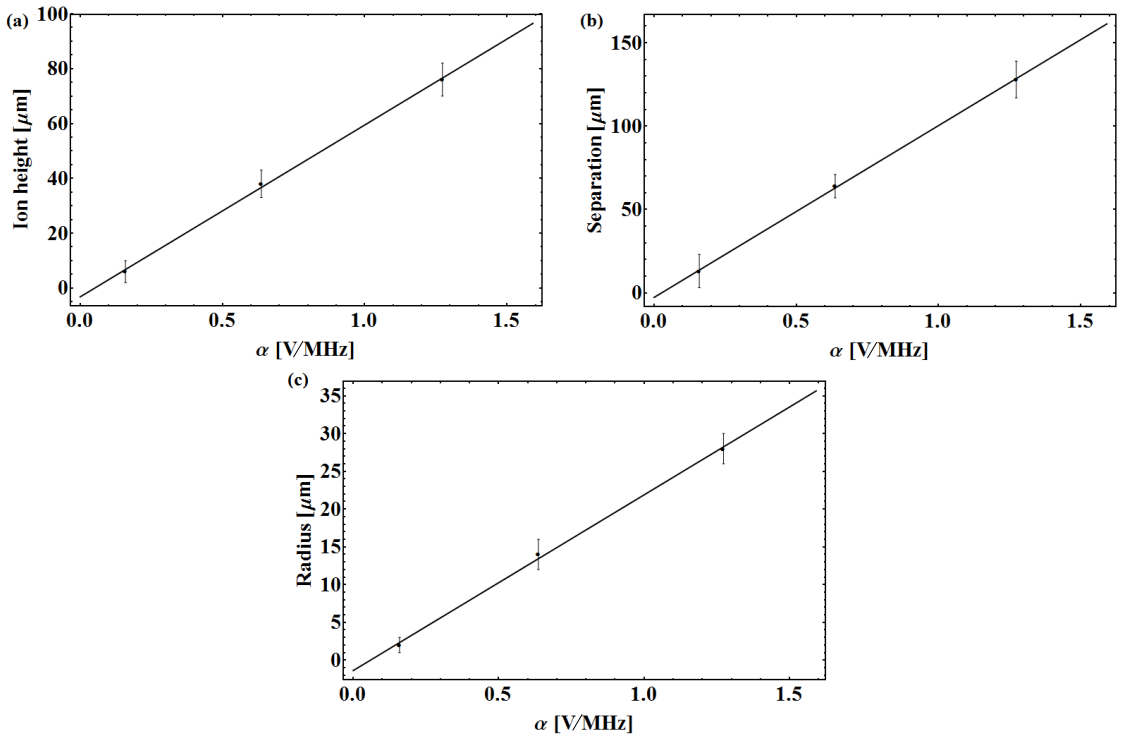

Figure 7.8: Graphs showing the ion height (a), polygon separation (b) and polygon radius (c) of an optimised lattice as a function of the ratio α. In all cases the plots are shown using $\alpha = V/\Omega$ where Ω is 2π times the drive frequency in Hz, and for lattices made from square unit cells of polygons with 81 sites and for $^{171}Yb^{+}$ ions.

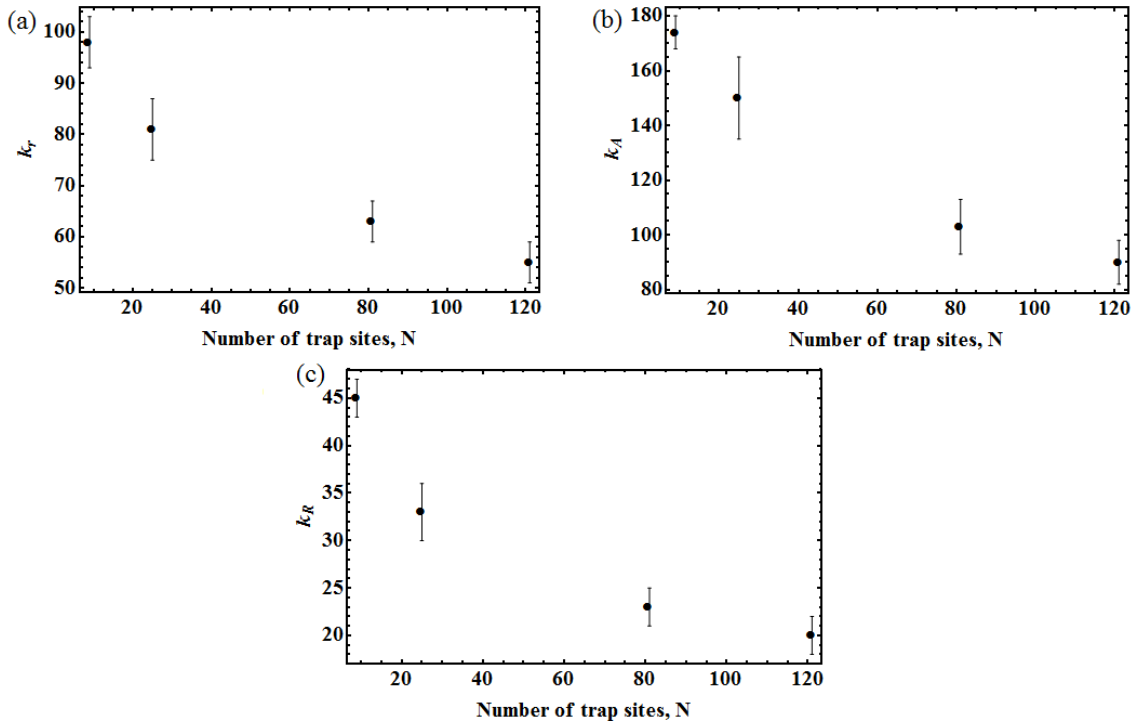

Figure 7.9: Graphs showing the value of k_r (a), k_A (b) and k_R (c) as a function of the number of trapping sites, N. In all cases the plots are shown using $\alpha = V/\Omega$ where Ω is 2π times the drive frequency in Hz and are for arrays made from square unit cells of polygons using $^{171}Yb^{+}$ ions.

It is important to stress that equations 7.15, 7.16 and 7.17 are only valid in the case of optimal geometries, which depend solely on α. With this in mind, it is now possible to re-express the secular frequency given in equation 7.8 to describe the secular frequency of an ion trapped on an optimised geometry by

$$\nu = \frac{e\eta_{geo}}{\sqrt{2}k_r^2 m\alpha}. \tag{7.18}$$

In the same manner K_{sim} given in equation 7.9 can also be re-expressed to describe that given by an optimised geometry and now reads as

$$K_{sim} = \frac{4F^2 m k_r^8 \alpha^3}{\Xi\eta_{geo}^2 \pi\epsilon_0 k_A^3}. \tag{7.19}$$

Equation 7.19 shows that, for optimal geometries, K_{sim} is proportional to α^3 (as the value of α determines the electrode dimensions to be used) and so, to produce an array with a high K_{sim} for a given number of lattice sites (as k_r and k_A are a function of the number of trapping sites), a large value for α is preferable. Equations 7.16 and 7.17 show that the optimum geometry size is proportional to α. It, therefore, follows that larger lattice geometries will produce larger values of K_{sim}. This effect is illustrated in figure 7.7 which shows K_{sim} as a function of polygon radius and separation. For optimised lattices, the optimal radius and separation will fall on a line described by $A = (k_A/k_R)\,R$, with higher values of α required for higher values of separation and radius as shown in equations 7.16 and 7.17 respectively.

The heating rate in ion traps has a strong dependency on the ion height ($\propto 1/r^4$) [91]. A large K_{sim} is achieved with large values of α, resulting in large ion heights, as shown in equation 7.15. It, therefore, can be concluded that a different scaling of the heating rate (for example in cryogenic systems) does not change the optimisation process and optimal geometries.

It has now been shown that the optimal geometry for a given minimum trap depth and ion mass is determined solely by the value of α and does not depend on the scaling of the heating rate.

Optimal geometries and their K_{sim} values (in units of $1/\alpha^3$) can now be found by creating contour plots (such as shown in figure 7.7) for different numbers of lattice sites, N, lattice unit cell type and ion mass, m. The error on the K_{sim} value, calculated from equation 7.9, was determined to be $\pm 10\%$ by comparing the secular frequency and ion heights obtained using the lattice geometry optimisation program with those predicted by

House's analytical solutions for a five wire surface trap geometry [4].

7.5 Optimisation results and analysis

In this section, optimum polygon separations, A, and radii, R, are obtained using the method outlined above for square, hexagonal and centre rectangular unit cell type lattices. These are shown as a function of lattice size and ion mass with the experimental constraint, α, scaled out. Throughout this optimisation example, $^{171}Yb^{+}$ ions will be used unless otherwise stated.

Figure 7.10 shows how the optimum scaled radius, R/α, and separation, A/α, of polygons vary as a function of lattice size for $^{171}Yb^{+}$ ions. As explained in the previous section we have assumed a minimum trap depth of 0.1 eV for illustrative purposes. It can be seen from this figure that as the size of the lattice increases, the optimum polygon radius and separation asymptotically tend towards values representative of an infinitely large lattice. This is expected as once a lattice becomes large enough, the addition of extra lattice sites will represent only a small change in the overall electrode geometry and, therefore, produce a small change in the electric field produced by the geometry. When the lattice is small however, additional lattice sites will represent a larger change in the geometry and will, therefore, cause a larger change in the electric field. Figure 7.11 shows how the scaled $\mathrm{K}_{sim}/(F^2\alpha^3)$ scales as a function of the number of lattice sites, N, using scaled optimum polygon radii, R/α, and separations, A/α. The state dependant force F will be considered in more detail in section 7.6.2. Due to the dependence of K_{sim} on the geometry, the relationship between $\mathrm{K}_{sim}/(\mathrm{F}^2\alpha^3)$ and the number of sites is expected to be of similar form to that for optimal polygon radii, R/α, and separation, A/α, with the maximum $\mathrm{K}_{sim}/(\mathrm{F}^2\alpha^3)$ asymptotically tending towards a value representative of an infinitely large lattice.

Using the data shown in figures 7.10(a), 7.10(b) and 7.11 the optimum radii and separation of the polygons were found to follow a $c + dN^{-E}$ and $f + gN^{-G}$ relationship, respectively, while the maximum $\mathrm{K}_{sim}/(\mathrm{F}^2\alpha^3)$ follows a $k + lN^{-Q}$ trend. The values of c, d, E, f, g, G k, l, and Q are shown in tables 7.3, 7.4 and 7.5.

Using the data shown in figures 7.12(a) and 7.12(b) the optimum radii and separation of the polygons as a function of the ion mass was found to follow a $o+pm^{-0.5}$ and $q+sm^{-0.5}$ relationship, respectively, with values of o, p, q and s shown in tables 7.6 and 7.7. Figure 7.13 shows how the optimum $\mathrm{K}_{sim}/(\mathrm{F}^2\alpha^3)$ varies as a function of the mass of the trapped ion, m, for 220 (square unit cells) and 225 (hexagonal and centred rectangular unit cells)

Lattice Type	c [(μm MHz)/V]	d [(μm MHz)/V]	E
Square	-5±1	101±7	0.29±0.03
Hexagonal	1±3	85±6	0.40±0.08
Centre Rectangular	-2±2	68±6	0.34±0.05

Table 7.3: Table showing c, d and E values for the fits which describe R/α as a function of the number of sites in the lattice.

Lattice Type	f [(μm MHz)/V]	g [(μm MHz)/V]	G
Square	-136±7	457±5	0.15±0.01
Hexagonal	13±24	547±288	0.48±0.21
Centre Rectangular	40±15	831±282	0.57±0.13

Table 7.4: Table showing f and g and G values for the fits which describe A/α as a function of the number of sites in the lattice.

Lattice Type	k [MHz^3/(N^2V^3)]	l [MHz^3/(N^2V^3)]	Q
Square	-(2.69±2.97)×10^{34}	(3.09±1.31)×10^{36}	(0.61±0.13)
Hexagonal	(0.52±6.00)×10^{33}	(3.51±1.54)×10^{36}	(0.86±0.12)
Centre Rectangular	-(3.09±6.12)×10^{35}	(5.23±5.11)×10^{37}	(0.65±0.26)

Table 7.5: Table showing k, l and Q values for the fits which describe $K_{sim}/(F^2\alpha^3)$ as a function of the number of sites in the lattice.

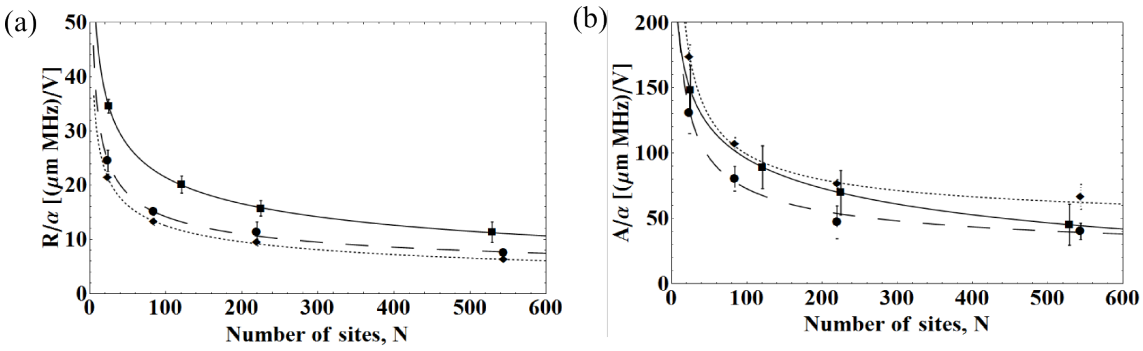

Figure 7.10: (a) Graph showing how the optimum polygon radius, R/α, varies as a function of the number of sites. (b) Graph showing how the optimum polygon separation, A/α, varies as a function of the number of sites. For both (a) and (b) the results shown are for square (square markers), hexagonal (circular markers) and centre rectangular (diamond markers) unit cell lattices with $^{171}Yb^+$ ions.

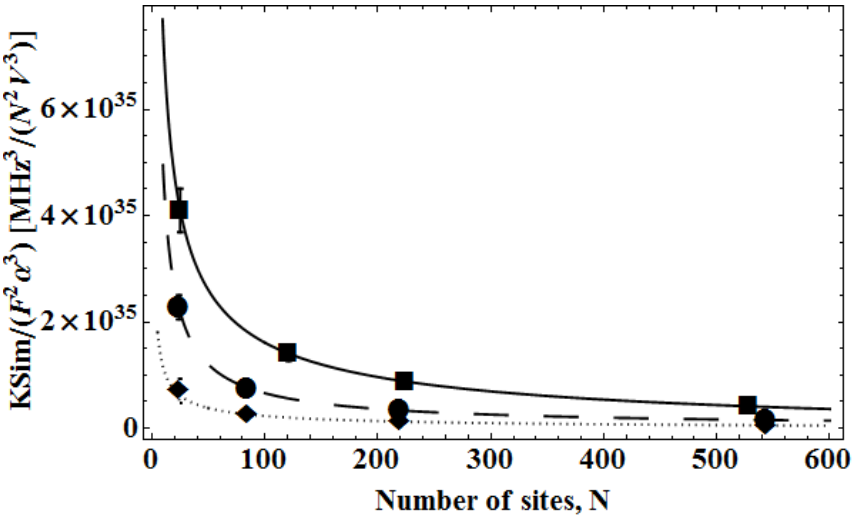

Figure 7.11: Graph showing how the optimum $K_{sim}/(F^2\alpha^3)$ varies as a function of the number of sites for optimum lattices with $^{171}Yb^+$ ions. This is shown for square (square markers), hexagonal (circular markers) and centre rectangular (diamond markers) unit cell lattices. Here F is a state dependant force applied to the ions in the lattice.

Lattice Type	o $[(\mu m\,MHz)/V]$	p $[(\mu m\,MHz)/V amu]$
Square	-56±6	138±10
Hexagonal	-34±7	88±11
Centre Rectangular	-48±3	110±6

Table 7.6: Table showing o and p values for the fits which describe R/α as a function of ion mass.

trapping sites. It is found that the optimum $K_{sim}/(F^2\alpha^3)$ scales as $u + vm^{-0.5}$, with the values of u and v shown in table 7.8.

We note, as shown in figure 7.12, that as the mass of the ion is increased, the polygon radii and separation will have to be decreased in order to provide trapping regions with a depth of above 0.1 eV for a given α for 220 (square unit cells) and 225 (hexagonal and centred rectangular unit cells) trapping sites. It is also clear to see that ions with lighter masses will provide higher $K_{sim}/(F^2\alpha^3)$ values but will require larger lattice geometries compared to heavier ions.

Lattice Type	q $[(\mu m\,MHz)/V]$	s $[(\mu m\,MHz)/V amu]$
Square	-176±47	489±65
Hexagonal	-311±15	678±22
Centre Rectangular	-402±28	911±51

Table 7.7: Table showing q and s values for the fits which describe A/α as a function of ion mass.

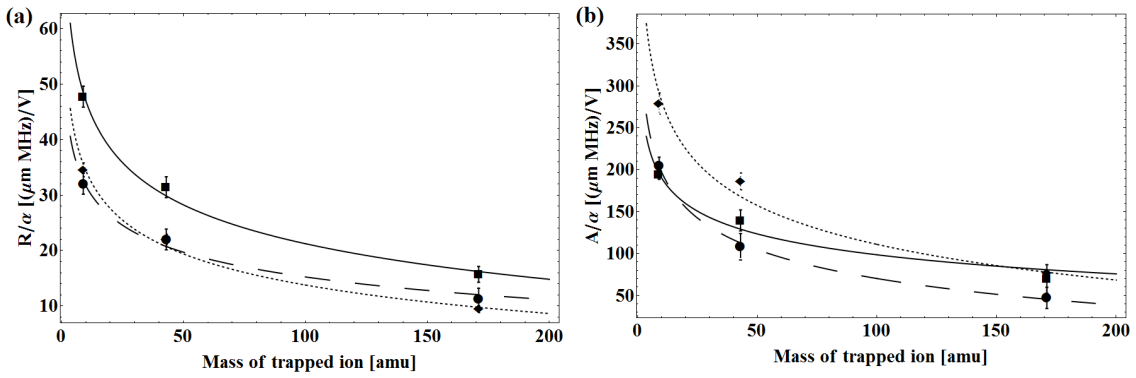

Figure 7.12: (a) Graph showing how the optimum polygon radius varies as a function of the ion mass for 220 (square type unit cells) and 225 (hexagonal and centre rectangular type unit cells) trapping sites. (b) Graph showing how the optimum polygon separation varies as a function of the ion mass. In both graphs this is shown for square (square markers), hexagonal (circular markers) and centre rectangular (diamond markers) unit cell lattices and the polygon radii and separations are scaled with α.

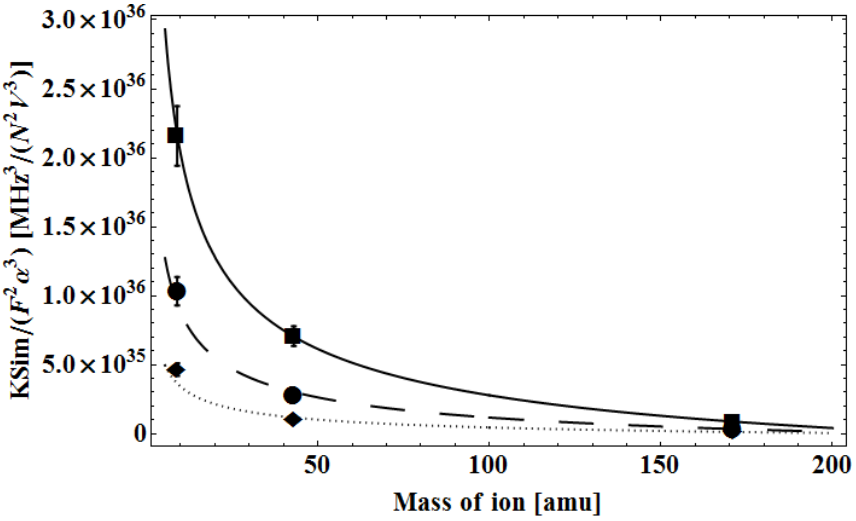

Figure 7.13: Graph showing how the optimum $K_{sim}/(F^2\alpha^3)$ varies as a function of the ion mass for 220 (square type unit cells (circular markers)) and 225 (hexagonal and centre rectangular type unit cells (square markers and diamond markers respectively)) trapping sites.

Lattice Type	u [$MHz^3/(N^2V^3)$]	v [$MHz^3/(N^2V^3amu)$]
Square	-(5.25±3.00)×10^{35}	(7.96±1.72)×10^{36}
Hexagonal	-(1.25±0.60)×10^{35}	(5.08±1.29)×10^{36}
Centre Rectangular	-(2.56±1.28)×10^{34}	(3.27±0.86)×10^{36}

Table 7.8: Table showing u and v values for the fits which describe $K_{sim}/(F^2\alpha^3)$ as a function of the ion mass.

7.6 Constraints on α

In this section the considerations which could limit the value of α are discussed. To do this it will be shown how the power dissipation in a chip trap, the quantum simulation error and the interaction time vary as a function of α. This is important as from this a value of α can be determined for a given experiment, which will be shown in section 7.7.

7.6.1 Power dissipation in optimised arrays

The power dissipation of an ion trap chip is determined by the voltage, V, frequency, Ω, as well as the capacitance and resistance of the lattice trap itself. This may, for a given capacitance and resistance, affect the value of α (the ratio between the rf voltage and drive frequency) which can be used. As the value of α is used to determine the optimum polygon radii and separation of a geometry, as shown in figure 7.10, for a given number of sites, N, and stability parameter, q, it is important to know how the power dissipation varies as a function of α.

The power dissipation of a chip is approximately given by [42]

$$P_D \approx \frac{1}{2} V^2 C^2 R \Omega^2, \tag{7.20}$$

where C and R are the capacitance and resistance of the chip. It is not possible to apply any combination of V and Ω to a geometry as they must be chosen so that the ion is stably trapped which is determined by the stability parameter [129, 145]

$$q = \frac{2e\eta_{geo}V}{mr^2\Omega^2} = \frac{2e\eta_{geo}\alpha}{mr^2\Omega} \tag{7.21}$$

and should be between zero and 0.9, where e is the charge of an electron.

The ion height, r, of ions trapped in the optimised lattices shown in this work have been found to be linearly proportional to α. This relationship is shown in figure 7.8 (a) with the constant of proportionality, k_r found to be ≈ 60.7 mV^{-1}s^{-1} for the example case of a square type lattice with 81 sites using ^{171}Yb$^+$ ions. Considering one particular ion height, r_0, substituting for $r_0 = k_r\alpha_0$ and rearranging equation 7.21 for Ω yields

$$\Omega_0 = \frac{2e\eta_{geo}}{mk_r^2\alpha_0 q}. \tag{7.22}$$

This equation can be re-expressed for V_0 by noting that $V_0 = \Omega_0\alpha_0$ and is given by

$$V_0 = \frac{2e\eta_{geo}}{mk_r^2 q}. \tag{7.23}$$

Equations 7.22 and 7.23 show that, for a given ion mass, m, ion height, r_0, stability parameter, q, and number of trapping sites in the array (as k_r is a function of the number of trapping sites), there is one unique voltage, V_0, and unique parameter α_0. This means that a given ion height (and, therefore, a chosen value of α) determines both the voltage and drive frequency to be applied to the trap.

To express the power dissipation, P_D, in terms of α equation 7.22 and 7.23 can be substituted into equation 7.21 giving

$$P_D = \frac{8e^4C^2R}{k_r^8 m^4 q^4 \alpha^2}. \tag{7.24}$$

Equation 7.24 shows that as α is increased, the power dissipated is reduced. This means that the power dissipation is low for high values of α and, as high values of α provide high values of K_{sim} (see figures 7.11 and 7.13), power dissipation will not impact on producing high values of K_{sim} in optimised geometries. However, a low value of α will result in a high power dissipation in the chip and, so, the maximum allowable power dissipation in a chip will determine the lowest α which can be applied to a geometry.

7.6.2 Quantum simulation error

An upper limit on α can be obtained from an estimation of the error of a quantum simulation one could perform using an optimised lattice. Using the method described in [149], the error for the simulation of the Ising model is given by

$$E_0 \approx \frac{1}{2}\eta^2 \sum_j (2\overline{n}+1) \left\langle \left[\left[O(t), \sigma_j^z(t) \right], \sigma_j^z(t) \right] \right\rangle. \tag{7.25}$$

Here $\overline{n}$ is the mean radial phonon number of the ions, O is the observable of the quantum simulation and η is a parameter which characterises ion displacements caused by the state dependant force and is given by [149]

$$\eta = \frac{F\sqrt{\hbar/(2m\nu)}}{\hbar\nu} \tag{7.26}$$

where m is the mass of a trapped ion and $\nu/2\pi$ is its secular frequency.

If O is an M-site observable then there exist M non-vanishing commutators (for example a two-site correlation function ($M = 2$) or a spin average ($M = 1$)) and so the error

on the simulation will not be dependant on the number of ions, N, in the array [149]. The error in equation 7.25 can now be re-written as

$$E_0 \approx \frac{F^2 M(\overline{n} + \frac{1}{2})}{2\hbar m \nu^3}. \tag{7.27}$$

Equations 7.19 and 7.27 show that both the K_{sim} and the error of the simulation, E_0, are proportional to the square of the state dependant force, F. It follows that the way in which this force is applied to the ions will determine the dependence of the simulation error on α. In what follows this state dependant force is assumed to either be applied by laser beams or magnetic field gradients. Both cases will be analysed.

To calculate the laser power required to achieve a force, F, it is assumed, for illustrative purposes, that the laser beam is focused to a sheet given by 25 μm multiplied by the width of the array. The laser intensity required to provide a state dependant force, F, can be provided by a laser beam of power, P. If the output power of the laser used is assumed to be constant, then the force applied to the ions will be dependant on α. This is because the lattice size is dependant on α and, therefore, so will the spacial area of the beam required to impart a force onto the ions. It is, therefore, required to express this force as a function of α. The intensity of a beam required to provide a state dependant force, F, is given by [29]

$$I_0 = \frac{F \Delta \lambda I_{sat}}{\pi \hbar \gamma^2} \tag{7.28}$$

where Δ is the detuning of the laser from resonance, λ is the wavelength of the laser, I_{sat} is the saturation intensity of the ion and γ is 2π times the natural transition linewidth. The power of a laser beam is given by

$$P = I_0 a \tag{7.29}$$

where a is the spacial area to which the beam is focused. The beam is assumed to be focused to form a light sheet across the array with an area given by $a = (n_s - 1)AW = (n_s - 1)k_A \alpha W$, where n_s is the number of trapping sites (or polygons) along one side of the array and W is the width of the light sheet. By using equations 7.28 and 7.29 the force applied to the ions by a laser power, P, can be expressed as

$$F = \frac{\pi \hbar P \gamma^2}{a \Delta \lambda I_{sat}}. \tag{7.30}$$

The form of E_0 for the case of lasers applying the state dependant force can now be found by using equations 7.18, 7.30 and the general error equation 7.27 yielding

$$E_{0laser} = \frac{4\sqrt{2}}{9}\frac{\pi^2\hbar^2}{e^3}\frac{Mk_r^6\gamma^4m^2P^2\alpha(\overline{n}+\frac{1}{2})}{\eta_{geo}^3(n_s-1)^2k_A^2W^2\Delta^2\lambda^2I_{sat}^2}. \tag{7.31}$$

It follows that both, the K_{sim} and simulation error E_0, will decrease with increasing laser detuning, Δ. Therefore, the optimum detuning, for a given laser power and α, corresponds to the lowest detuning which provides the required K_{sim}. The optimum detuning to achieve the lowest simulation error for $^{171}\mathrm{Yb}^+$ will be discussed in section 7.6.3.

Magnetic fields can also be used to provide the state dependant force, F, and is given by [126]

$$F_{\hat{i}} = \left(\frac{\hbar}{2}\right)\partial_i\omega\left\langle\sigma^{(\hat{i})}\right\rangle \tag{7.32}$$

where $\omega = \gamma_g bi$ is the position dependant spin resonance frequency with $\gamma_g = e/m_e$ being the gyromagnetic ratio and i is the x, y or z direction. The magnetic field gradient b is assumed to arise from a magnetic field of the form $\overline{B} = \overline{B_0} + b\hat{i}$, where B_0 is a constant magnetic field offset. From this, the state dependant force, $F_{\hat{i}}$, produced from a magnetic field gradient, $b_{\hat{i}}$, is found to be

$$F_{\hat{i}} \approx \frac{\hbar e b_{\hat{i}}}{2m_e} \tag{7.33}$$

where m_e and e is the mass and charge of an electron respectively. If one assumes the magnetic field is created by a current carrying wire located on the surface of a polygon, at a distance a from the centre of the polygon and making an angle of 45° with respect to the x-axis then the magnetic field gradient will be of the form

$$b_{r'} = \frac{\mu_0 I}{2\pi r'^2}. \tag{7.34}$$

Here μ_0 is the permeability of free space, I is the current flowing through the wire and r'^2 is the distance squared of the ion from the current carrying wire and is equal to $r^2 + a^2$ where r is the ion height. We assume, for simplicity, that the distance a scales linearly with α with a constant of proportionality of k_a in order to keep the angle of r' to the x-z plane, θ, independent of α. As the ion height is known to scale linearly with α, from equation 7.15, it is possible to express the magnetic field gradient along r' as

$$b_{r'} = \frac{\mu_0 I}{2\pi\alpha^2 \left(k_r^2 + k_a^2\right)}. \tag{7.35}$$

The component of this magnetic field gradient in the x-z plane can now be shown to be

$$b_{x,z} = \frac{\mu_0 I \cos\theta}{4\pi\alpha^2 \left(k_r^2 + k_a^2\right)}. \tag{7.36}$$

The form of K_{sim} for the case of magnetic field gradients applying the state dependant force can be found by using equations 7.18, 7.33, 7.36 and the general error equation 7.27 yielding

$$E_{0mag} = \frac{\sqrt{2}}{64} \frac{\hbar\mu_0}{\pi^2 m_e^2 e} \frac{k_r^6 m^2 I^2 \cos^2\theta M \left(\overline{n} + \frac{1}{2}\right)}{\eta_{geo}^3 \left(k_r^2 + k_a^2\right)^2 \alpha}. \tag{7.37}$$

Equations 7.31 and 7.37 show that the quantum simulation error is proportional to α for a state dependant force created by a laser beam and proportional to α^{-1} for a magnetic field gradient created by current carrying wires. For the case of laser beams the α scaling implies that as α is increased (yielding larger K_{sim} values and geometries as shown in section 7.4.3) the quantum simulation error will rise and, therefore, provide an upper limit on the value of α. For the magnetic field gradient case the upper limit on α comes from the current creating the gradient. While the α scaling for the quantum simulation error using magnetic field gradients implies that a larger α is advantageous, the current required to achieve a given magnetic field gradient scales as α^2 as can be deduced from equation 7.35. The maximum current that one can apply to the lattice therefore provides an upper limit for α.

It is also interesting at this point to note the different scaling of the laser and magnetic field gradient forces with α given in equations 7.30 and 7.32 respectively. The laser force can be seen to be $\propto \alpha^{-1}$ as it is a function of the inverse of the laser sheet cross section, a, which is $\propto \alpha^1$. The magnetic gradient force, on the other hand, is $\propto \alpha^{-2}$ as it is a function of the magnetic field gradient $b_{r'}$ which is $\propto \alpha^{-2}$ due to r' having a linear relationship with α in the geometry considered.

7.6.3 Spontaneous emission

When applying the state dependant force to the ions using a laser beam, additional decoherence will occur via spontaneous emission. The spontaneous emission rate is given by [33, 150]

$$S = \frac{\gamma g^2}{6}\left(\frac{1}{\Delta^2} + \frac{2}{(\Delta_{fs} - \Delta)^2}\right) \tag{7.38}$$

where γ is 2π times the linewidth in Hz, Δ is the laser detuning from resonance, Δ_{fs} is the fine structure splitting of the ion ($\approx$ 100 THz for $^{171}Yb^{+}$) and g is the single photon Rabi frequency given by

$$g = \gamma\sqrt{\frac{I_0}{2I_{sat}}}. \tag{7.39}$$

Here, I_0 is the laser intensity and I_{sat} is the saturation intensity of the ion. It is possible to express the single photon Rabi frequency in terms of the laser power, P, by using equation 7.29 giving

$$g = \gamma\sqrt{\frac{P}{2(n_s - 1)k_A\alpha W I_{sat}}}. \tag{7.40}$$

It is now possible to describe an additional parameter, L_{sim}, which describes the ratio of interaction rate to the spontaneous emission rate as

$$L_{sim} = \frac{T_S}{T_J} \tag{7.41}$$

where

$$T_S = \frac{1}{S}. \tag{7.42}$$

It has been shown that the detuning which minimises the effect of spontaneous emission is $\approx$ 33 THz for $^{171}Yb^{+}$ [151]. It, therefore, follows that the value of L_{sim} will be maximised with this detuning. This additional parameter is analogous to the parameter K_{sim} in equation 7.3 and is also required to be greater than unity, just like the original K_{sim}, when considering a state dependent force created using laser light. If magnetic field gradients are to be used to apply the state dependent force then L_{sim} is not relevant.

7.6.4 Other considerations

It is important to note here that an increase in α will increase the time taken for ion-ion interactions to take place in optimised lattice structures, as we will show in equation 7.44. Equation 7.5 gives an expression for the time taken for an ion-ion interaction to occur in any given fixed lattice structure. This can be expressed for optimised lattice structures by including the expressions for the ion-ion separation (polygon separation, A) and secular

frequency, ν, from equations 7.16 and 7.18 respectively, to yield

$$T_J = \frac{e^2\pi\epsilon_0\hbar}{2}\frac{\eta_{geo}^4 k_A^3}{k_r^8 F^2 m^2 \alpha}. \tag{7.43}$$

An expression to give the interaction time in optimised lattices as a function of α can now be arrived at by using equations 7.43 and 7.30,

$$T_J = \frac{9}{8}\frac{e^2\epsilon_0}{\pi\hbar}\frac{\eta_{geo}^4 k_A^3((n_s-1)k_A w)^2\Delta^2\lambda^2 I_{sat}^2\alpha}{k_r^8\gamma^4 P^2 m^2}. \tag{7.44}$$

Equation 7.44 clearly shows that as α is increased, the time taken for an ion-ion interaction will increase and, so, it may be preferable to limit the magnitude of α after taking into account the effects on K_{sim}. A similar equation can also be derived for the use with magnetic field gradients. It is also important to note here that increasing the laser power, P, will increase the value of L_{sim} as the spontaneous emission rate is proportional to P whereas the coupling rate is proportional to P^2 as shown in equations 7.38 and 7.44 respectively.

With the use of the equations derived in this section, optimal geometries can be calculated given certain experimental parameters. A example case study will be described in the following section.

7.7 Example case study

In this section, an example case will be presented to show how a 2D lattice for the use in quantum simulations can be designed using the work in this chapter, whose successful operation is within reach of current technology when using lasers. The magnetic field gradient case is then considered to create a state dependant force and it is found that this may be more challenging to realise.

From equation 7.23 we can see that there is a unique voltage for a given mass, m, lattice type and stability parameter, q. For this example case, a lattice comprised of square type unit cells with 9 trapping sites for $^{171}\mathrm{Yb}^+$ ions with a stability parameter $q = 0.5$ is chosen. Using these parameters the voltage can now be determined by calculating k_r. k_r can be found by plotting the ion height of an optimised lattice against α, as shown in figure 7.8 (a), and finding the gradient of this linear relationship. For this example case $k_r \approx 98$ $\mathrm{mV}^{-1}\mathrm{s}^{-1}$. Using this result and equation 7.23 the unique voltage is found to be ≈ 34 V where η_{geo} has been calculated to be ≈ 0.145.

The α dependant polygon radius and separation can be calculated by producing the

corresponding graphs in figure 7.10, using the method described in section 7.4.3, for the lattice type and ion to be used. For this example case the optimum radius and separation of the polygons in terms of α is $\approx 45\alpha$ μm and $\approx 174\alpha$ μm respectively.

The next step is to choose a laser detuning from resonance and a maximum acceptable error, E_0, to be tolerated. For $^{171}Yb^+$, as explained in section 7.6.3, the optimum detuning is ≈ 33 THz giving a wavelength of ≈ 355 nm which is therefore used in this example case together with a maximum acceptable error of 0.25. Note that in this example case the array is assumed to be at cryogenic temperatures which corresponds to an electric field noise density three orders of magnitude less than at room temperature. We can see from equation 7.31 that α needs to be minimised in order to keep the quantum simulation error low. The minimum α is determined by the lowest ion height one can easily achieve which for this example case we choose to be equal to 30 μm. For this case we find $\alpha \approx 0.3$ $V\,\mathrm{MHz}^{-1}$. Having determined α we find the optimum radius and separation to be equal to ≈ 14 μm and ≈ 52 μm respectively which results in $\Omega_{ex}/2\pi = 92$ Hz for a secular frequency of $\nu/2\pi = 3.2$ MHz. To calculate the required laser power, equation 7.31 should be set to the maximum acceptable error and solved for the laser power, which is found to be $\approx$ 7.3 W assuming the ions to be cooled to $\overline{n} \ll 1$ and M = 1 (one side average observable). These conditions provide a coupling rate $J/2\pi = 90$ Hz with a $\beta \approx 2.8\times10^{-5}$. This laser power can, for example, be achieved using a commercially available diode pumped solid state (Coherent Paladin range) or fibre (Coherent Talisker range) laser system. Table 7.9 summarises all parameters for this example case study.

Figure 7.14 shows the effect a change of α and laser power, P, has on the quantum simulation error (solid curves), K_{sim} (dashed curves) and L_{sim} (dotted lines). The cross corresponds to the 2D lattice designed in this example case which represents the optimum case in terms of achieving the highest K_{sim} and L_{sim} for a maximum quantum simulation error of 0.25. One should note that the main limitations in achieving lower quantum simulation errors stem from the lowest achievable ion height (lowest α) and magnitude of electric field noise density. Figure 7.14 also shows that higher values of K_{sim} and L_{sim} can be achieved with any given geometry (given by the value of α) by simply increasing the power of the laser. However, this can only be achieved at the expense of higher quantum simulation errors.

State dependant forces can also be created using magnetic field gradients as described in section 7.6.2. Figure 7.15 shows the K_{sim} (solid curves) and the quantum simulation error (dashed curves) as a function of the magnetic field gradient, b, and α for traps

α	R [μm]	A [μm]	Δ [THz]	P [W]	M	K_{sim}	L_{sim}	E_0
0.3	14	52	33	7.3	1	35.6	14.4	0.25

Table 7.9: Table summarising the parameters for a 3 by 3 square type unit cell lattice at cryogenic temperature as shown in the example case study.

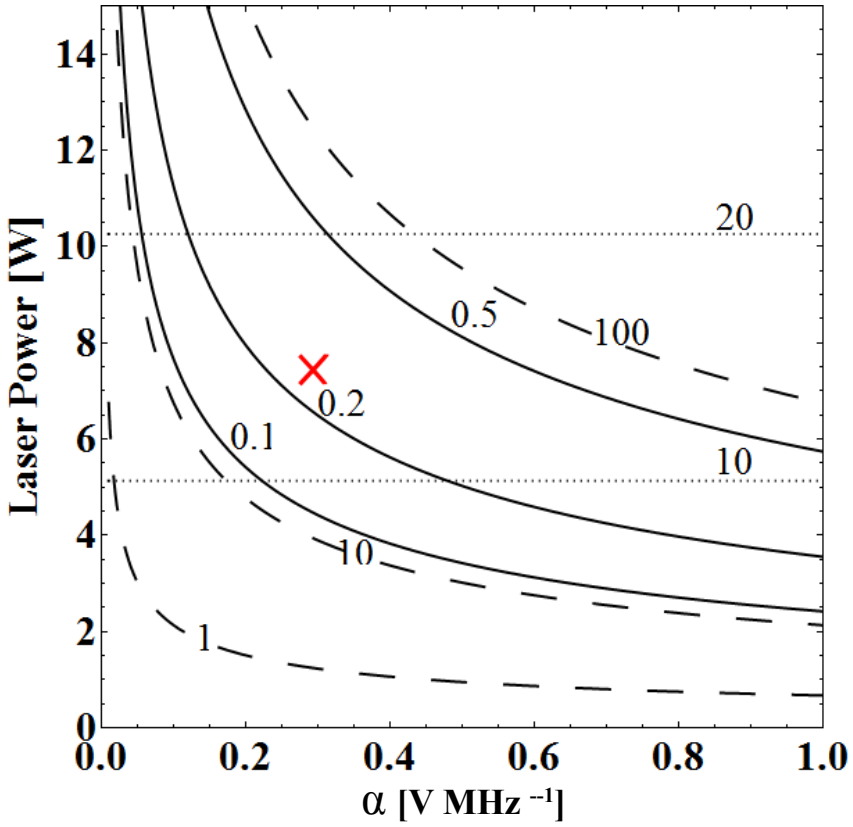

Figure 7.14: Graph showing the quantum simulation error (solid curves), K_{sim} (dashed curves) and L_{sim} (dotted lines) for a three by three square type unit cell lattice with $^{171}Yb^{+}$ ions as a function of α and laser power. Here traps are operated at cryogenic temperature. The cross indicates the example case.

operated at cryogenic temperature. Here we use $^{171}Yb^{+}$ ions in a three by three square unit cell array. As described in section 7.6.2, $E_0 \propto \alpha^{-1}$ indicating that a large α is advantageous. The limit on the maximum α is dependant on the maximum current one can apply to the geometry. Using equation 7.35 it is possible to calculate the current required to create a desired magnetic field gradient. In order to illustrate the magnitude of currents required we assume $k_a = k_r$, which will result in an angle $\theta = 45°$ (as shown in section 7.6.2). We also set α to ≈ 0.3, determined by the lowest achievable ion height which, for illustration purposes, we have set to 30 μm. The reason for choosing the minimum α value can be seen when considering equation 7.35 which clearly shows that, for a given magnetic field gradient, $I \propto \alpha^2$. In the magnetic field gradient case, the chosen α sets K_{sim} and E_0. For this case, again, we choose M = 1, $\overline{n} \ll 1$, $K_{sim} = 2$ and $E_0 \approx 0.01$ which requires a magnetic field gradient of $\approx$ 33,000 Tm^{-1} and is indicated by the cross on figure 7.15. This is achievable with a current of $\approx$ 1,200 A yielding a coupling rate $J/2\pi = 38$ Hz and a $\beta \approx 2.8{\times}10^{-8}$. From this simple example case one can conclude that using magnetic field gradients to provide state dependant forces for the use in quantum simulations using the methods and trap designs shown in this chapter is quite challenging. However, geometries trapping ions in chains allow for sizeable magnetic gradient induced couplings [152] and, so, a detailed investigation into optimising the wires used for producing magnetic field gradients in the geometries discussed in this chapter could improve results.

7.8 Modification of the 2D ion trap lattice on a microchip

In chapter 6 we presented the successful operation of a 2D ion trap lattice on a microchip. While the microchip has many applications, the ion-ion separation of 270.5 μm results in a coulomb coupling strength $\Omega_{ex}/2\pi = 4$ Hz for a secular frequency of $\nu/2\pi = 0.5$ MHz which is insufficient for the implementation of quantum simulations. As has been shown in this chapter it should however be possible to produce a lattice with a significantly reduced ion-ion separation, to achieve coupling strengths suitable for quantum simulations. Due to the simple fabrication technique of the microchip presented in chapter 6 a lattice, based on the optimisation process shown in this chapter, with a much smaller ion-ion separation can be fabricated simply by using a different wafer thickness and a modified fabrication mask.

The modified microchip would consist of an SOI wafer with a 2.5 μm thick device layer and two 1.25 μm thick oxide layers wafer bonded together. The width of the handle

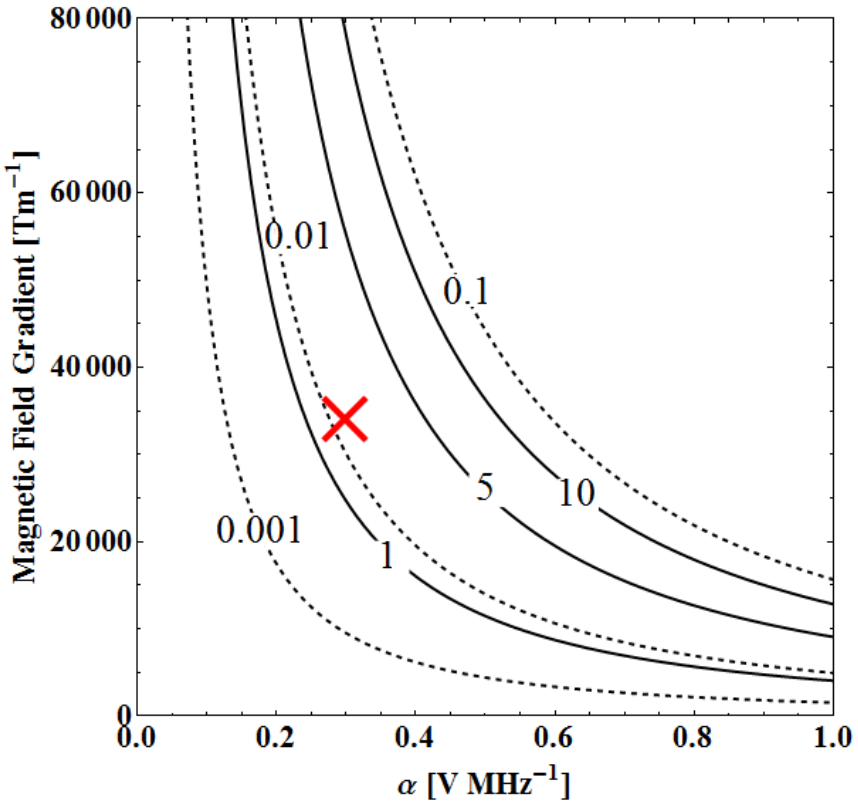

Figure 7.15: Graph showing the quantum simulation error (dashed curves) and the K_{sim} (solid curves) of a three by three square type unit cell lattice with $^{171}Yb^{+}$ ions as a function of α and magnetic field gradient. Here traps are operated at cryogenic temperatures.

layer remains the same to ensure that the wafer does not break. The hexagon radius and separation would be 13 μm and 32 μm respectively which would result in an ion-ion separation of 32 μm and an ion height of 15 μm. For a secular frequency of $\nu/2\pi = 1$ MHz the coulomb coupling strength would be $\Omega_{ex}/2\pi = 1.3$ kHz. Using a 355 nm laser with a power of 2.4 W focused to a light sheet of width 160 μm and depth 30 μm an effective spin-spin coupling rate of $J/2\pi = 1.2$ kHz could be achievable which would result in a quantum simulation error $E_0 = 0.25$ (as in the example case, M = 1). At this ion height the electric-field noise density at a cryogenic temperature of 6 K is estimated to be $S_E(\nu) \approx 1.6 \times 10^{-11} V^2 m^{-2} Hz^{-1}$ using figure 20 in reference [42] which, for the above secular frequency, results in a heating rate of $\dot{n} = 540 s^{-1}$. We therefore find that $K_{sim} = 14.2$ and $L_{sim} = 29.1$. We can see that by making simple modifications to the microchip successfully operated in chapter 6, the coupling strength can be increased significantly and offers a exciting platform for the implementation of 2D quantum simulations.

7.9 Conclusion

Two-dimensional arrays of surface ion traps have the potential to provide a technology with which quantum simulations can be performed. In order for ion traps to be used successfully for this purpose a greater understanding is required of how the various geometry parameters affect the ions trapped above them. Throughout this chapter square, hexagonal and centre rectangular unit cell arrays of microtraps have been modelled in the gap-less plane approximation using the Biot-Savart like law in electrostatics [5]. Decoherence due to motional heating [91] was then compared to the ion-ion interaction [45] to provide a ratio used to describe how much faster an ion-ion interaction occurs in comparison to the motional decoherence, K_{sim}. This chapter investigated how various parameters in the array can be adjusted in order to optimise the device's ability to perform quantum simulations and shows how the interactions can be made as homogeneous as possible over the device. It has been shown how the homogeneity of the K_{sim} across an array can be altered by varying the distance from the outer polygon to the edge of the rf electrode. The distance required to maximise the K_{sim} homogeneity is also shown to vary as a function of the total size of the lattice. The number of polygon sides, n, required to maximise K_{sim} has also been found.

It has also been shown that the K_{sim} of a given lattice geometry can be maximised by reducing the value of α. However, as α reduces so does the trap depth. This results in the conclusion that the maximum K_{sim} of a geometry can be achieved by reducing the value

of α until the trap depth reaches a reasonable minimum value.

Using this information, optimal geometries as a function of α have been presented. This has been achieved by finding the relationships of polygon separation and radius with α for optimal geometries. It was found that, for these optimal geometries, K_{sim} scales as α^3. The individual polygon separation and radius were found to posses a linear relationship with α and, therefore, larger geometries have been found to produce larger values of K_{sim}. Therefore, the optimal lattice geometry is dependent solely on the value of α for a given ion mass and number of trapping sites in the array.

A case study for determining an optimum geometry consisting of 9 trapping sites arranged into square type unit cells for $^{171}Yb^{+}$ ions has also been presented. It was shown how the value of α can be chosen (and, therefore, the geometry dimensions) by taking into account the laser power (or static magnetic field gradient) required to produce a state dependant force acting on the ions, the K_{sim} and the error on the simulation. From this it has been found that to carry out quantum simulations with reasonable K_{sim} and error values it is preferable to use traps held at cryogenic temperatures as this reduces decoherence due to heating effects on the ions. Other methods known to significantly decrease the anomalous heating rate include pulsed laser electrode cleaning [153] and Argon-ion beam electrode cleaning [154].

Finally, it was shown how making changes to the lattice geometry of the successfully operated microchip presented in chapter 6 has the potential to offer an exciting platform for the implementation of 2D quantum simulations.

Chapter 8

Conclusion

The work presented in this thesis is part of a large effort in the Ion Quantum Technology (IQT) group at the University of Sussex to develop scalable quantum technology. The first part of the thesis covered the first coherent manipulation experiments using $^{171}Yb^{+}$ in our laboratory and led to the implementation and novel manipulation of a dressed-state qubit which is resilient to magnetic field fluctuations. This qubit will now be used for the implementation of high fidelity multi-qubit gates based on microwave and radio-frequency (rf) fields in conjunction with a static magnetic field gradient. The second part of the thesis focused on developing a scalable architecture for the implementation of two-dimensional (2D) quantum simulations using a lattice of ions on a microchip.

In more detail, a magnetic field sensitive as well as a magnetic field insensitive qubit in the $^{2}S_{1/2}$ ground state of a $^{171}Yb^{+}$ ion has been characterised. It was found that the magnetic field insensitive qubit has a coherence time of 1.5 s demonstrating its usefulness for storing quantum information. A promising scheme for implementing multi-qubit gate operations is based on using microwaves in conjunction with a static magnetic field gradient [34]. Since this scheme requires the qubit states to have different magnetic moments, a magnetic field sensitive qubit has been characterised and the coherence time was found to be $\approx 500\,\mu$s which is limited by magnetic field fluctuations. Such fluctuations are known to limit the achievable gate fidelity [36]. To circumvent this problem we have used microwave dressed-states to create a new qubit which is robust against magnetic field fluctuations but still remains sensitive to a magnetic field gradient [40]. We have characterised this qubit by measuring the lifetime of the dressed-state which was found to be 550 ms. A new method to manipulate the dressed-state qubit has also been presented which allows arbitrary qubit rotations on the Bloch sphere to be implemented using only a single rf field [113]. This method was used to measure a coherence time of 500 ms, close

to the lifetime of the dressed-state. Furthermore, our method significantly simplifies the experimental setup required for multi-qubit gate operations.

Towards the realisation of scalable 2D quantum simulations a novel fabrication technique has been presented that allows very large voltages to be applied to microfabricated devices. This is of particular interest in the field of microfabricated ion traps as the maximum achievable ion height and trap depth are limited by the voltage that can be applied to the trap. We have used this advance to demonstrate the first successful operation of a 2D lattice of ion traps on a microchip [138]. The microchip was characterised by measuring the secular frequencies of an ion and the ion lifetime with and without Doppler cooling. Ion shuttling between lattice sites has also been demonstrated which could be part of a scheme to load large ion lattices and refill a lattice site when an ion has been lost. An important question to answer is what would be the optimum geometry of an ion trap lattice to maximise the ratio of the ion-ion coupling strength to the sources of decoherence such as motional heating of the ions and off-resonant excitation to unwanted states. It was shown how to arrive at an answer to this question for a given set of experimental constraints and an example for a 3 by 3 lattice of $^{171}Yb^{+}$ ions [55] was given. While the ion-ion spacing on our particular microchip is too large for quantum simulations we follow our optimisation method and illustrate how simple modifications to the microchip design would allow for 2D spin lattices to be simulated.

8.0.1 Discussion and future work

The successful implementation of a microwave dressed-state qubit with a coherence time of 500 ms together with a simple method to perform arbitrary qubit rotations offers a exciting platform for the implementation of scalable high fidelity multi-qubit gate operations. Currently the limiting factor in achieving a longer coherence time and a higher dressed-state preparation fidelity is the achievable Rabi frequency of the dressing fields. The achievable Rabi frequency is limited by the amplifier we currently use before sending the signal to the microwave horn and by the frequency mixer we use to mix the low frequency signals with the 12.6 GHz signal. We plan to increase the Rabi frequency by adding a pre-amplification stage to the microwave generation setup. We also plan to use more sophisticated mixers which can be driven with a higher local oscillator power and thereby allow a higher output power for a given intermodulation strength to be achieved. More long term, the Rabi frequency could also be increased by using a waveguide integrated into a microfabricated surface trap [38].

To implement a microwave-dressed two-qubit Mølmer and Sørensen gate using a similar method to that described by Timoney *et al.* [40], we require our rf generation setup to be updated to produce four individually controlled rf fields. We also require a static magnetic field gradient which can be created using permanent magnets or by using current carrying wires embedded in a microfabricated surface trap. Recently, we have added four in-vacuum rare earth nickel coated samarium cobalt magnets to our setup and a preliminary magnetic field gradient of ≈ 24 T/m has been measured. We have so far used this to individually address two ions in frequency space and to resolve motional sidebands. The next step is to use this magnetic field gradient in conjunction with microwave dressed-states to implement a high fidelity two-qubit gate. The successful implementation of such a gate would immediately be scalable to more ions by making simple modifications to the microwave and rf generation setup.

The microchip used to successfully trap a 2D lattice of ions which was presented in this thesis was the first microfabricated surface trap in the group [138] and its operation revealed a number of challenges that need to be overcome on the route to implementing 2D quantum simulations. A challenge in operating the microchip was micromotion which changed every time the atomic ovens were used to trap ions and continuously degraded the performance of the chip. This is expected to be caused by charge build up due to Yb coating on the surface of the microchip and can only be compensated for globally using the static voltage electrodes surrounding the lattice. Micromotion, together with ion losses during loading due to background collisions, made trapping of large lattices of ions very challenging. It also made shuttling of ions difficult as the voltage profiles required to successfully move an ion between neighbouring lattice sites changed every time a new ion was loaded. To address this issue future microchip designs will incorporate a lip to block part of the atomic flux and thereby minimise Yb coating. Furthermore, static voltage electrodes will be added to each lattice site to allow micromotion to be compensated separately at every site. This will also allow for site dependant secular frequencies to be achieved. Finally, the rudimentary shuttling of ions between lattice sites presented in this thesis could be used as part of a loading scheme based on trapping in an area of the lattice which will not be used for the experiment and on shuttling operations to fill the required lattice sites. As already discussed in chapter 7 the ion-ion spacing of the lattice can be reduced significantly by modifying the microchip design and together with the modifications illustrated above this has the potential to provide a very exciting architecture for the implementation of 2D quantum simulations.

Bibliography

[1] J. H. Wesenberg, R. J. Epstein, D. Leibfried, R. B. Blakestad, J. Britton, J. P. Home, W. M. Itano, J. D. Jost, E. Knill, C. Langer, R. Ozeri, S. Seidelin, and D. J. Wineland. Fluorescence during Doppler cooling of a single trapped atom. *Phys. Rev. A*, 76:053416, Nov 2007. viii, 42, 43, 44

[2] W. A. Bell and J. G. Tracy. Stable isotope inventory requirements and enrichment capabilities. *Oak Ridge National Laboratory*, 1985. xiv, 19

[3] Altaf H. Nizamani, James J. McLoughlin, and Winfried K. Hensinger. Doppler-free Yb spectroscopy with the fluorescence spot technique. *Phys. Rev. A*, 82:043408, Oct 2010. xiv, 20, 40

[4] M. G. House. Analytic model for electrostatic fields in surface-electrode ion traps. *Phys. Rev. A*, 78(3):033402, Sep 2008. xv, 124, 125, 129, 133

[5] Mário H Oliveira and Josá A Miranda. Biot-Savart-like law in electrostatics. *Eur. J. Phys.*, 22:31–38, 2001. xv, 124, 125, 148

[6] S. Olmschenk. Quantum teleportation between distant matter qubits. *Ph.D. thesis, University of Michigan*, 2009. xvii, 14, 22, 50, 60

[7] James J. McLoughlin, Altaf H. Nizamani, James D. Siverns, Robin C. Sterling, Marcus D. Hughes, Bjoern Lekitsch, Björn Stein, Seb Weidt, and Winfried K. Hensinger. Versatile ytterbium ion trap experiment for operation of scalable ion-trap chips with motional heating and transition-frequency measurements. *Phys. Rev. A*, 83:013406, Jan 2011. xix, 40, 43, 44

[8] A. M. Turing. On computable numbers, with an application to the entscheidungsproblem. *Proc. London Math. Soc.*, 42:230–265, 1936. 2

[9] R. P. Feynman. Simulating physics with computers. *International Journal of Theoretical Physics*, 21:467–488, 1982. 2, 7

[10] D. Deutsch. Quantum theory, the church-turing principle and the universal quantum computer. *Proc. R. Soc. Lond. A*, 400. 3

[11] P. W. Shor. Algorithms for quantum computation: discrete logarithms and factoring. In *Proceedings of the 35th Annual Symposium on Foundations of Computer Science*, SFCS '94, pages 124–134. IEEE Computer Society, 1994. 3

[12] Lov K. Grover. A fast quantum mechanical algorithm for database search. In *STOC '96 Proceedings of the twenty-eighth annual ACM symposium on Theory of computing*, pages 212–219, 1996. 3

[13] A. M. Steane. Error correcting codes in quantum theory. *Phys. Rev. Lett.*, 77:793–797, Jul 1996. 3

[14] P. W. Shor. Fault-tolerant quantum computation. *Proc. 37th Annual Symposium on Foundations of Computer Science, IEEE Computer Society Press*, pages 56–65, 1996. 3

[15] David P. DiVincenzo. The physical implementation of quantum computation. *Fortschritte der Physik*, 48(9-11):771–783, 2000. 3

[16] E. Knill, R. Laflamme, and G. J. Milburn. A scheme for efficient quantum computation with linear optics. *Nature*, 409:46–52, 2001. 4

[17] Daniel Loss and David P. DiVincenzo. Quantum computation with quantum dots. *Phys. Rev. A*, 57:120–126, Jan 1998. 4

[18] Ivan H. Deutsch, Gavin K. Brennen, and Poul S. Jessen. Quantum computing with neutral atoms in an optical lattice. *Fortschritte der Physik*, 48(9-11):925–943, 2000. 4

[19] J. I. Cirac and P. Zoller. Quantum computations with cold trapped ions. *Phys. Rev. Lett.*, 74:4091–4094, May 1995. 4, 5, 54

[20] Joseph W Britton, Brian C. Sawyer, Adam C. Keith, C. C. Joseph Wang, James K. Freericks, Hermann Uys, Michael J. Biercuk, and John J. Bollinger. Engineered two-dimensional ising interactions in a trapped-ion quantum simulator with hundreds of spins. *Nature*, 484:489–492, 2012. 5, 93

[21] C. Monroe, D. M. Meekhof, B. E. King, W. M. Itano, and D. J. Wineland. Demonstration of a fundamental quantum logic gate. *Phys. Rev. Lett.*, 75:4714–4717, Dec 1995. 5, 10

[22] Ferdinand Schmidt-Kaler, Hartmut Häffner, Mark Riebe, Stephan Gulde, Gavin P. T. Lancaster, Thomas Deutschle, Christoph Becher, Christian F. Roos, Jürgen Eschner, and Rainer Blatt. Realization of the Cirac-Zoller controlled-NOT quantum gate. *Nature*, 422:408–411, 2003. 5

[23] Anders Sørensen and Klaus Mølmer. Quantum computation with ions in thermal motion. *Phys. Rev. Lett.*, 82:1971–1974, Mar 1999. 5, 54

[24] Klaus Mølmer and Anders Sørensen. Multiparticle entanglement of hot trapped ions. *Phys. Rev. Lett.*, 82:1835–1838, Mar 1999. 5

[25] Anders Sørensen and Klaus Mølmer. Entanglement and quantum computation with ions in thermal motion. *Phys. Rev. A*, 62(2):022311, Jul 2000. 5

[26] S. Schneider G. J. Milburn and D. F. V. James. Ion trap quantum computing with warm ions. *Fortschr. Phys.*, 48:801–810, 2000. 5, 54

[27] E. Solano, R. L. de Matos Filho, and N. Zagury. Deterministic bell states and measurement of the motional state of two trapped ions. *Phys. Rev. A*, 59:R2539–R2543, Apr 1999. 5

[28] D. Leibfried, B. DeMarco, V. Meyer, D. Lucas, M. Barrett, J. Britton, W. M. Itano, B. Jelenkovic, C. Langer, T. Rosenband, and D. J. Wineland. Experimental demonstration of a robust, high-fidelity geometric two ion-qubit phase gate. *Nature*, 422:412–415, 2003. 5, 54

[29] P. C. Haljan, K.-A. Brickman, L. Deslauriers, P. J. Lee, and C. Monroe. Spin-dependent forces on trapped ions for phase-stable quantum gates and entangled states of spin and motion. *Phys. Rev. Lett.*, 94(15):153602, Apr 2005. 5, 139

[30] C. A. Sacket, D. Kielpinski, B. E. King, C. Langer, V. Meyer, C. J. Myatt, M. Rowe, Q. A. Turchette, W. M. Itano, D. J. Wineland, and C. Monroe. Experimental entanglement of four particles. *Nature*, 404:256–259, 2000. 5

[31] Thomas Monz, Philipp Schindler, Julio T. Barreiro, Michael Chwalla, Daniel Nigg, William A. Coish, Maximilian Harlander, Wolfgang Hänsel, Markus Hennrich, and Rainer Blatt. 14-qubit entanglement: Creation and coherence. *Phys. Rev. Lett.*, 106:130506, Mar 2011. 5, 16

[32] Jan Benhelm, Gerhard Kirchmair, Christian F. Roos, and Rainer Blatt. Towards fault-tolerant quantum computing with trapped ions. *Nat. Phys*, 4:463–466, 2008. 5

[33] R. Ozeri, W. M. Itano, R. B. Blakestad, J. Britton, J. Chiaverini, J. D. Jost, C. Langer, D. Leibfried, R. Reichle, S. Seidelin, J. H. Wesenberg, and D. J. Wineland. Errors in trapped-ion quantum gates due to spontaneous photon scattering. *Phys. Rev. A*, 75:042329, Apr 2007. 6, 141

[34] Florian Mintert and Christof Wunderlich. Ion-trap quantum logic using long-wavelength radiation. *Phys. Rev. Lett.*, 87(25):257904, Nov 2001. 6, 56, 57, 58, 59, 150

[35] M. Johanning, A. Braun, N. Timoney, V. Elman, W. Neuhauser, and Chr. Wunderlich. Individual addressing of trapped ions and coupling of motional and spin states using rf radiation. *Phys. Rev. Lett.*, 102:073004, Feb 2009. 6, 57

[36] A. Khromova, Ch. Piltz, B. Scharfenberger, T. F. Gloger, M. Johanning, A. F. Varón, and Ch. Wunderlich. Designer spin pseudomolecule implemented with trapped ions in a magnetic gradient. *Phys. Rev. Lett.*, 108:220502, Jun 2012. 6, 7, 19, 150

[37] C. Ospelkaus, C. E. Langer, J. M. Amini, K. R. Brown, D. Leibfried, and D. J. Wineland. Trapped-ion quantum logic gates based on oscillating magnetic fields. *Phys. Rev. Lett.*, 101(9):090502, Aug 2008. 6

[38] C. Ospelkaus, U. Warring, Y. Colombe, K. R. Brown, J. M. Amini, D. Leibfried, and D. J. Wineland. Microwave quantum logic gates for trapped ions. *Nature*, 476(7359):181–184, 2011. 6, 7, 18, 73, 80, 93, 151

[39] U. Warring, C. Ospelkaus, Y. Colombe, R. Jördens, D. Leibfried, and D. J. Wineland. Individual-ion addressing with microwave field gradients. *Phys. Rev. Lett.*, 110:173002, Apr 2013. 6, 14

[40] N. Timoney, I. Baumgart, M. Johanning, A. F. Varon, M. B. Plenio, A. Retzker, and Ch. Wunderlich. Quantum gates and memory using microwave-dressed states. *Nature*, 476:185–188, 2011. 7, 59, 67, 68, 83, 84, 91, 92, 150, 152

[41] D. Kielpinski, C.R. Monroe, and D.J. Wineland. Architecture for a large-scale ion-trap quantum computer. *Nature*, 417:709–711, 2002. 7, 10, 93

[42] Marcus D. Hughes, Bjoern Lekitsch, Jiddu A. Broersma, and Winfried K. Hensinger. Microfabricated ion traps. *Contemporary Physics*, 52(6):505–529, 2011. 7, 12, 46, 93, 94, 95, 96, 97, 122, 123, 124, 137, 148

[43] J M Amini, H Uys, J H Wesenberg, S Seidelin, J Britton, J J Bollinger, D Leibfried, C Ospelkaus, A P VanDevender, and D J Wineland. Toward scalable ion traps for quantum information processing. *New Journal of Physics*, 12(3):033031, 2010. 7, 93, 124

[44] D L Moehring, C Highstrete, D Stick, K M Fortier, R Haltli, C Tigges, and M G Blain. Design, fabrication and experimental demonstration of junction surface ion traps. *New J. Phys.*, 13, 2011. 7, 93

[45] D.Porras and J.I.Cirac. Effective quantum spin systems with trapped ions. *Phys. Rev. Lett.*, 92(20):207901, May 2004. 7, 94, 115, 120, 121, 148

[46] R. Islam, E. E. Edwards, K. Kim, S. Korenblit, C. Noh, H. Carmichael, G. D. Lin, L. M. Duan, C. C. Joseph Wang, J. K. Freericks, and C. Monroe. Onset of a quantum phase transtion with a trapped ion quantum simulator. *Nature Communications*, 2:377, 2011. 7, 93

[47] A. Friedenauer, H. Schmitz, J. T. Glueckert, D. Porras, and T. Schaetz. Simulating a quantum magnet with trapped ions. *Nature Phys.*, 4:757–761, 2008. 7, 93

[48] R. Gerritsma, B. P. Lanyon, G. Kirchmair, F. Zähringer, C. Hempel, J. Casanova, J. J. García-Ripoll, E. Solano, R. Blatt, and C. F. Roos. Quantum simulation of the klein paradox with trapped ions. *Phys. Rev. Lett.*, 106:060503, Feb 2011. 7, 93

[49] R. Gerritsma, G. Kirchmair, F. Zähringer, E. Solano, R. Blatt, and C. F. Roos. Quantum simulation of the dirac equation. *Nature*, 463:68–71, 2010. 7, 93

[50] Lanyon BP, Hempel C, Nigg D, Müller M, Gerritsma R, Zähringer F, Schindler P, Barreiro JT, Rambach M, Kirchmair G, Hennrich M, Zoller P, Blatt R, and Roos CF. Universal digital quantum simulation with trapped ions. *Science*, 334:57–61, 2011. 7, 93

[51] K Kim, S Korenblit, R Islam, E E Edwards, M-S Chang, C Noh, H Carmichael, G-D Lin, L-M Duan, C C Joseph Wang, J K Freericks, and C f. Quantum simulation of the transverse ising model with trapped ions. *New Journal of Physics*, 13(10):105003, 2011. 7, 93

[52] R. Islam, C. Senko, W. C. Campbell, S. Korenblit, J. Smith, A. Lee, E. E. Edwards, C.-C. J. Wang, J. K. Freericks, and C. Monroe. Emergence and frustration

of magnetism with variable-range interactions in a quantum simulator. *Science*, 340(6132):583–587, 2013. 7, 16, 93

[53] J. I. Cirac and P. Zoller. A scalable quantum computer with ions in an array of microtraps. *Nature*, 404:579–581, 2000. 7, 10, 94

[54] J. Chiaverini and W. E. Lybarger. Laserless trapped-ion quantum simulations without spontaneous scattering using microtrap arrays. *Phys. Rev. A*, 77(2):022324, Feb 2008. 7, 94

[55] James D Siverns, Seb Weidt, Kim Lake, Bjoern Lekitsch, Marcus D Hughes, and Winfried K Hensinger. Optimization of two-dimensional ion trap arrays for quantum simulation. *New J. Phys*, 14:085009, 2012. 7, 119, 151

[56] D. J. Wineland, R. E. Drullinger, and F. L. Walls. Radiation-pressure cooling of bound resonant absorbers. *Phys. Rev. Lett.*, 40, 1978. 10

[57] W. Neuhauser, M. Hohenstatt, P. Toschek, and H. Dehmelt. Optical-sideband cooling of visible atom cloud confined in parabolic well. *Phys. Rev. Lett.*, 41:233–236, Jul 1978. 10

[58] M. Keller, B. Lange, K. Hayasaka, W. Lange, and H. Walther. Deterministic cavity quantum electrodynamics with trapped ions. *J. Phys. B: At. Mol. Opt. Phys.*, 36:2099–2105, 2003. 10

[59] Th. Udem, S. A. Diddams, K. R. Vogel, C. W. Oates, E. A. Curtis, W. D. Lee, W. M. Itano, R. E. Drullinger, J. C. Bergquist, and L. Hollberg. Absolute frequency measurements of the Hg^+ and ca optical clock transitions with a femtosecond laser. *Phys. Rev. Lett.*, 86:4996–4999, May 2001. 10

[60] S. A. Webster, P. Taylor, M. Roberts, G. P. Barwood, and P. Gill. Kilohertz-resolution spectroscopy of the $^2S_{1/2}$–$^2F_{7/2}$ electric octupole transition in a single $^{171}Yb^+$ ion. *Phys. Rev. A*, 65:052501, Apr 2002. 10

[61] M. Chwalla, J. Benhelm, K. Kim, G. Kirchmair, T. Monz, M. Riebe, P. Schindler, A. S. Villar, W. Hänsel, C. F. Roos, R. Blatt, M. Abgrall, G. Santarelli, G. D. Rovera, and Ph. Laurent. Absolute frequency measurement of the $^{40}Ca^+4s^2S_{1/2}$-$3d^2D_{5/2}$ clock transition. *Phys. Rev. Lett.*, 102:023002, Jan 2009. 10

[62] Rainer Blatt and David Wineland. Entangled states of trapped atomic ions. *Nature*, 453:1008–1015, June 2008. 10

[63] H. Häffner, C. F. Roos, and R. Blatt. Quantum computing with trapped ions. *Physical Reports*, 469:155–203, 2008. 10

[64] Wolfgang Paul. Electromagnetic traps for charged and neutral particles. *Rev. Mod. Phys.*, 62:531–540, Jul 1990. 10, 16

[65] M. D. Barrett, B. DeMarco, T. Schaetz, V. Meyer, D. Leibfried, J. Britton, J. Chiaverini, W. M. Itano, B. Jelenković, J. D. Jost, C. Langer, T. Rosenband, and D. J. Wineland. Sympathetic cooling of $^{9}Be^{+}$ and $^{24}Mg^{+}$ for quantum logic. *Phys. Rev. A*, 68(4):042302, Oct 2003. 10

[66] J. Benhelm, G. Kirchmair, C. F. Roos, and R. Blatt. Experimental quantum-information processing with $^{43}Ca^{+}$ ions. *Phys. Rev. A*, 77:062306, 2008. 10

[67] B. B. Blinov, L. Deslauriers, P. Lee, M. J. Madsen, R. Miller, and C. Monroe. Sympathetic cooling of trapped Cd^{+} isotopes. *Phys. Rev. A*, 65(4):040304, Apr 2002. 10

[68] Ralph G. DeVoe and Christian Kurtsiefer. Experimental study of anomalous heating and trap instabilities in a microscopic ^{137}Ba ion trap. *Phys. Rev. A*, 65:063407, Jun 2002. 10

[69] V. Letchumanan, G. Wilpers, M. Brownnutt, P. Gill, and A. G. Sinclair. Zero-point cooling and heating-rate measurements of a single $^{88}Sr^{+}$ ion. *Phys. Rev. A*, 75(6):063425, Jun 2007. 10

[70] Chr. Balzer, A. Braun, T. Hannemann, Chr. Paape, M. Ettler, W. Neuhauser, and Chr. Wunderlich. Electrodynamically trapped Yb^{+} ions for quantum information processing. *Phys. Rev. A*, 73:041407, Apr 2006. 10

[71] S. Olmschenk, K. C. Younge, D. L. Moehring, D. N. Matsukevich, P. Maunz, and C. Monroe. Manipulation and detection of a trapped Yb^{+} hyperfine qubit. *Phys. Rev. A*, 76:052314, Nov 2007. 10, 62

[72] P.K. Ghosh. *Ion Traps*. Oxford science publications. Oxford University Press, Incorporated, 1995. 11, 13

[73] H. G. Dehmelt. Radiofrequency spectroscopy of stored ions. *Adv. At. Mol. Phys.*, 3:53, 1967. 12

[74] W. K. Hensinger, S. Olmschenk, D. Stick, D. Hucul, M. Yeo, M. Acton, L. Deslauriers, C. Monroe, and J. Rabchuk. T-junction ion trap array for two-dimensional ion shuttling, storage, and manipulation. *Appl. Phys. Lett.*, 88, 2006. 12, 16

[75] M. Abramowitz and I. A. Stegun. Handbook of mathematical functions. *Dover Publications*, 1965. 13

[76] Nir Navon, Shlomi Kotler, Nitzan Akerman, Yinnon Glickman, Ido Almog, and Roee Ozeri. Addressing two-level systems variably coupled to an oscillating field. *Phys. Rev. Lett.*, 111:073001, Aug 2013. 14

[77] J. McLoughlin. Development and implementation of an Yb^+ ion trap experiment towards coherent manipulation and entanglement. *Ph.D. thesis, University of Sussex*, 2011. 17, 26, 52

[78] H. Metcalf and P. Van Der Straten. Laser cooling and trapping. *Springer*, ISBN 9780387987268, 1999. 17, 53

[79] C. J. Foot. Atomic physics. *Oxford University Press, New York*, 2005. 18

[80] B. E. King, C .S. Wood, C .J. Myatt, Q. A. Turchette, D. Leibfried, W. M. Itano, C. Monroe, and D. J. Wineland. Cooling the collective motion of trapped ions to initialize a quantum register. *Phys. Rev. Lett.*, 81:1525–1528, 1998. 18

[81] C. Monroe, D. M. Meekhof, B. E. King, S. R. Jefferts, W. M. Itano, D. J. Wineland, and P. Gould. Resolved-sideband raman cooling of a bound atom to the 3D zero-point energy. *Phys. Rev. Lett.*, 75:4011–4014, 1995. 18

[82] S. Olmschenk, D. N. Matsukevich, P. Maunz, D. Hayes, L.-M. Duan, and C. Monroe. Quantum teleportation between distant matter qubits. *Science*, 323, 2009. 19

[83] D. Hayes, D. N. Matsukevich, P. Maunz, D. Hucul, Q. Quraishi, S. Olmschenk, W. Campbell, J. Mizrahi, C. Senko, and C. Monroe. Entanglement of atomic qubits using an optical frequency comb. *Phys. Rev. Lett.*, 104, 2010. 19

[84] C. Wunderlich and C. Balzer. Quantum measurements and new concepts for experiments with trapped ions. *Advances in Atomic Molecular and Optical Physics*, 49:293–372, 2003. 19, 58

[85] A. S. Arnold, J. S. Wilson, and M. G. Boshier. A simple extended-cavity diode laser. *Rev. Sci. Instrum.*, 69, 1998. 26, 28

[86] L Ricci, M Weidemüller, T Esslinger, A Hemmerich, C Zimmermann, V Vuletic, W König, and W Hänsch, T. A compact grating-stabilized diode laser system for atomic physics. *Optics Communications*, 117:541–549, 1995. 26

[87] K. C. Harvey and C. J. Myatt. External-cavity diode laser using a grazing-incidence diffraction grating. *Optics Letters*, 16:910–912, 1991. 26

[88] R. Sterling. Ytterbium ion trapping and microfabrication of ion trap arrays. *Ph.D. thesis, University of Sussex*, 2011. 29, 35, 96, 101

[89] J. Siverns. Yb ion trap experimental set-up and two-dimensional ion trap surface array design towards analogue quantum simulations. *Ph.D. thesis, University of Sussex*, 2011. 29, 31

[90] A. Nizamani. Yb^+ ion trapping and optimum planar trap geometries for scalable quantum technology. *Ph.D. thesis, University of Sussex*, 2011. 32

[91] Q. A. Turchette, Kielpinski, B. E. King, D. Leibfried, D. M. Meekhof, C. J. Myatt, M. A. Rowe, C. A. Sackett, C. S. Wood, W. M. Itano, C. Monroe, and D. J. Wineland. Heating of trapped ions from the quantum ground state. *Phys. Rev. A*, 61(6):063418, May 2000. 38, 46, 119, 122, 132, 148

[92] J. D. Siverns, L. R. Simkins, S. Weidt, and W. K. Hensinger. On the application of radio frequency voltages to ion traps via helical resonators. *Applied Physics B*, 106, 2012. 39, 94, 111

[93] R.C. Sterling, M.D. Hughes, C. J. Mellor, and W.K. Hensinger. Increased surface flashover voltage in microfabricated devices. *arXiv:1208.5672v1*, 2012. 39, 97

[94] D. J. Berkeland and M. G. Boshier. Destabilization of dark states and optical spectroscopy in zeeman-degenerate atomic systems. *Phys. Rev. A*, 65:033413, Feb 2002. 41

[95] F. Diedrich, J. C. Bergquist, Wayne M. Itano, and D. J. Wineland. Laser cooling to the zero-point energy of motion. *Phys. Rev. Lett.*, 62:403–406, Jan 1989. 42

[96] S. Lloyd. Universal quantum simulators. *Science*, 273:1073, 1996. 47

[97] M. Acton, K. A. Brickman, P. C. Haljan, P. J. Lee, L. Deslauriers, and C. Monroe. Near-perfect simultaneous measurement of a qubit register. *Quantum Information and Computation*, 6(6):465–482, 2006. 50

[98] A. H. Myerson, D. J. Szwer, S. C. Webster, D. T. C. Allcock, M. J. Curtis, G. Imreh, J. A. Sherman, D. N. Stacey, A. M. Steane, and D. M. Lucas. High-fidelity readout of trapped-ion qubits. *Phys. Rev. Lett.*, 100:200502, May 2008. 51

[99] P. J. Lee. Quantum information processing with two trapped cadmium ions. *Ph.D. thesis, University of Michigan*, 2006. 52, 53, 55

[100] J. Randall. Quantum logic in trapped ions. *MRes project report, Imperial College*, 2012. 52, 57, 58

[101] E. Jaynes and F. Cummings. *Proceedings of the IEEE*, 51:89, 1963. 54

[102] D. J. Wineland, C. Monroe, W. M. Itano, D. Leibfried, B. E. King, and D. M. Meekhof. Experimental issues in coherent quantum-state manipulation of trapped atomic ions. *J. Res. Natl. Inst. Stand. Technol.*, 103(3), 1998. 55

[103] A. Khromova. Quantum gates with trapped ions using magnetic gradient induced coupling. *Ph.D. thesis, University of Siegen*, 2012. 57, 66

[104] Christof Wunderlich. Conditional spin resonance with trapped ions. *Laser Physics at the Limit*, page 261, 2001. 59

[105] Advanced Research and Development Activity (ARDA). A quantum information science and technology roadmap. 2004. 59

[106] N. F. Ramsey. Molecular beams. *Oxford University Press, New York*, 1985. 61

[107] Ch. Piltz, B. Scharfenberger, A. Khromova, A. F. Varón, and Ch. Wunderlich. Protecting conditional quantum gates by robust dynamical decoupling. *Phys. Rev. Lett.*, 110:200501, May 2013. 66

[108] Lorenza Viola and Seth Lloyd. Dynamical suppression of decoherence in two-state quantum systems. *Phys. Rev. A*, 58:2733–2744, Oct 1998. 67

[109] P. Rabl, P. Cappellaro, M. V. Gurudev Dutt, L. Jiang, J. R. Maze, and M. D. Lukin. Strong magnetic coupling between an electronic spin qubit and a mechanical resonator. *Phys. Rev. B*, 79:041302, Jan 2009. 67

[110] Götz S. Uhrig. Keeping a quantum bit alive by optimized π-pulse sequences. *Phys. Rev. Lett.*, 98:100504, Mar 2007. 67

[111] Michael J. Biercuk, Hermann Uys, Aaron P. VanDevender, Nobuyasu Shiga, Wayne M. Itano, and John J. Bollinger. Optimized dynamical decoupling in a model quantum memory. *Nature*, 458:996–1000, 2009. 67, 87

[112] Hendrik Bluhm, Sandra Foletti, Izhar Neder, Mark Rudner, Diana Mahalu, Vladimir Umansky, and Amir Yacoby. Dephasing time of gaas electron-spin qubits coupled to a nuclear bath exceeding 200 us. *Nature Physics*, 7:109–113, 2011. 67

[113] S. C. Webster, S. Weidt, K. Lake, J. J. McLoughlin, and W. K. Hensinger. Simple manipulation of a microwave dressed-state ion qubit. *Phys. Rev. Lett.*, 111:140501, Oct 2013. 67, 150

[114] G. K. Woodgate. Elementary atomic structure. *Second Edition*, 2002. 72

[115] M. P. Fewell, B. W. Shore, and K. Bergmann. Coherent population transfer among three states: Full algebraic solutions and the relevance of non adiabatic proceses to transfer by delayed pulses. *Aust. J. Phys.*, 50:281–308, 1997. 75

[116] Jens L Sørensen, Ditte Møller, Theis Iversen, Jakob B Thomsen, Frank Jensen, Peter Staanum, Dirk Voigt, and Michael Drewsen. Efficient coherent internal state transfer in trapped ions using stimulated raman adiabatic passage. *New Journal of Physics*, 8:261, 2006. 83

[117] Ditte Møller, Jens L. Sørensen, Jakob B. Thomsen, and Michael Drewsen. Efficient qubit detection using alkaline-earth-metal ions and a double stimulated raman adiabatic process. *Phys. Rev. A*, 76:062321, Dec 2007. 83

[118] D J Szwer, S C Webster, A M Steane, and D M Lucas. Keeping a single qubit alive by experimental dynamic decoupling. *J. Phys. B: At. Mol. Opt. Phys.*, 44:025501, 2011. 87

[119] S. Narayanan, N. Daniilidis, S. A. Möller, R. Clark, F. Ziesel, K. Singer, F. Schmidt-Kaler, and H. Häffner. Electric field compensation and sensing with a single ion in a planar trap. *J. Appl. Phys.*, 110:114909, 2011. 93

[120] Michael J. Biercuk, Hermann Uys, Joe W. Britton, Aaron P. VanDevender, and John J. Bollinger. Ultrasensitive detection of force and displacement using trapped ions. *Nat Nano*, 5:646–650, 2010. 93

[121] Christoph Zipkes, Stefan Palzer, Carlo Sias, and Michael Köhl. A trapped single ion inside a bose-einstein condensate. *Nature*, 464. 93

[122] Robert Raussendorf and Hans J. Briegel. A one-way quantum computer. *Phys. Rev. Lett.*, 86:5188–5191, May 2001. 93

[123] Ch Schneider, Diego Porras, and Tobias Schaetz. Experimental quantum simulations of many-body physics with trapped ions. *Reports on Progress in Physics*, 75(2):024401, 2012. 93

[124] R. Blatt and C. F. Roos. Quantum simulations with trapped ions. *Nat Phys*, 8:277–284, 2012. 93

[125] R Schmied, T Roscilde, V Murg, D Porras, and J I Cirac. Quantum phases of trapped ions in an optical lattice. *New Journal of Physics*, 10:045017, 2008. 93

[126] Michael Johanning, Andrés F Varón, and Christof Wunderlich. Quantum simulations with cold trapped ions. *Journal of Physics B: Atomic, Molecular and Optical Physics*, 42(15):154009, 2009. 93, 115, 140

[127] T. Shi and J. I. Cirac. Topological phenomena in trapped-ion systems. *Phys. Rev. A*, 87:013606, Jan 2013. 93

[128] Alejandro Bermudez, Tobias Schaetz, and Diego Porras. Photon-assisted-tunneling toolbox for quantum simulations in ion traps. *New Journal of Physics*, 14:053049, 2012. 93

[129] Robert J. Clark, Tongyan Lin, Kenneth R., and Isaac L. Chuang. A two-dimensional lattice ion trap for quantum simulation. *J. Appl. Phys*, 105(1):013114, 2009. 94, 123, 137

[130] Muir Kumph, Michael Brownnutt, and Rainer Blatt. Two-dimensional arrays of radio-frequency ion traps with addressable interactions. *New Journal of Physics*, 13(7):073043, 2011. 94, 120, 123

[131] Roman Schmied, Janus H. Wesenberg, and Dietrich Leibfried. Optimal surface-electrode trap lattices for quantum simulation with trapped ions. *Phys. Rev. Lett.*, 102(23):233002, Jun 2009. 94, 120

[132] D. Stick, W. K. Hensigner, S. Olmschenk, M. J. Madsen, K. Schwab, and C. Monroe. Ion trap in a semiconductor chip. *Nature Physics*, 2:36–39, 2006. 94, 97

[133] L. Deslauriers, S. Olmschenk, D. Stick, W. K. Hensinger, J. Sterk, and C. Monroe. Scaling and suppression of anomalous heating in ion traps. *Phys. Rev. Lett.*, 97(10):103007, Sep 2006. 94

[134] B. Gassend, L.F. Velasquez-Garcia, A.I. Akinwande, and M. Martinez-Sanchez. A microfabricated planar electrospray array ionic liquid ion source with integrated extractor. *J. Microelectromech. S.*, 18:679, 2009. 94

[135] R. Krpoun and H. R. Shea. Integrated out-of-plane nanoelectroscpray thruster arrays for spacecraft propulsion. *J. Micromech. Microeng.*, 19(4):045019, 2009. 94

[136] R. Krpoun, M. Rdber, and H.R. Shea. Microfabrication and test of an integrated colloid thruster. In *Micro Electro Mechanical Systems, 2008. MEMS 2008. IEEE 21st International Conference on*, page 964, 2008. 94

[137] M. D. Paine, S. Gabriel, C. G. J. Schabmueller, and A. G. R. Evans. Realisation of very high voltage electrode-nozzle systems for MEMS. *Sensors and Actuators A: Physical*, 114:112, 2004. 94

[138] R. C. Sterling, H. Rattanasonti, S. Weidt, K. Lake, P. Srinivasan, S. C. Webster, M. Kraft, and W. K. Hensinger. Two-dimensional ion trap lattice on a microchip for quantum simulation. *Nat. Commun.*, 5:3637, 2014. 94, 123, 151, 152

[139] J. Britton, D. Laibfried, J. A. Beall, R. B. Blakestad, J. H. Wesenberg, and D. J. Wineland. Scalable arrays of rf Paul traps in degenerate Si. *Appl. Phys. Lett.*, 95:173102, 2009. 96, 99

[140] K. R. Brown, C. Ospelkaus, Y. Colombe, A. C. Wilson, D. Leibfried, and D. J. Wineland. Coupled quantized mechanical oscillators. 118

[141] M. Harlander, R. Lechner, M. Brownnutt, R. Blatt, and W. Hänsel. Trapped-ion antennae for the transmission of quantum information. *Nature*, 471:200–203, 2011. 118

[142] Roman Schmied, Janus H Wesenberg, and Dietrich Leibfried. Quantum simulation of the hexagonal Kitaev model with trapped ions. *New Journal of Physics*, 13(11):115011, 2011. 120, 124

[143] C. Langer, R. Ozeri, J. D. Jost, J. Chiaverini, B. DeMarco, A. Ben-Kish, R. B. Blakestad, J. Britton, D. B. Hume, W. M. Itano, D. Leibfried, R. Reichle, T. Rosenband, T. Schaetz, P. O. Schmidt, and D. J. Wineland. Long-lived qubit memory using atomic ions. *Phys. Rev. Lett.*, 95(6):060502, Aug 2005. 121

[144] H. Häffner, F. Schmidt-Kaler, W. Hänsel, C. F. Roos, T. Körber, M. Chwalla, M. Riebe, J. Benhelm, U. D. Rapol, C. Becher, and R. Blatt. Robust entanglement. *Applied Physics B: Lasers and Optics*, 81:151–153, 2005. 121

[145] M.J.Madsen, W.K.Hensinger, D.Stick, J.A.Rabchuk, and C.Monroe. Planar ion trap geometery for microfabrication. *Applied Physics B*, 78:639, 2004. 122, 137

[146] Charles Kittel. New York: John Wiley and Sons, 1996. 123

[147] D. Mc Hugh and J. Twamley. Quantum computer using a trapped-ion spin molecule and microwave radiation. *Phys. Rev. A*, 71(1):012315, Jan 2005. 123

[148] Kilian Singer, Ulrich Poschinger, Michael Murphy, Peter Ivanov, Frank Ziesel, Tommaso Calarco, and Ferdinand Schmidt-Kaler. Colloquium: Trapped ions as quantum bits: Essential numerical tools. *Rev. Mod. Phys.*, 82(3):2609–2632, Sep 2010. 124

[149] X.-L. Deng, D. Porras, and J. I. Cirac. Effective spin quantum phases in systems of trapped ions. *Phys. Rev. A*, 72:063407, Dec 2005. 138, 139

[150] D. J. Wineland, M. Barrett, J. Britton, J. Chiaverini, B. DeMarco, W. M. Itano, B. Jelenkovic, C. Langer, D. Leibfried, V. Meyer, T. Rosenband, and T. Schatz. Quantum information processing with trapped ions. *Phil. Trans. R. Soc.*, 361:1349, May 2003. 141

[151] W. C. Campbell, J. Mizrahi, Q. Quraishi, C. Senko, D. Hayes, D. Hucul, D. N. Matsukevich, P. Maunz, and C. Monroe. Ultrafast gates for single atomic qubits. *Phys. Rev. Lett.*, 105:090502, Aug 2010. 142

[152] J. Welzel, A. Bautista-Salvador, C. Abarbanel, V. Wineman-Fisher, C. Wunderlich, R. Folman, and F. Schmidt-Kaler. Designing spin-spin interactions with one and two dimensional ion crystals in planar micro traps. *Eur. Phys. J. D*, 2011. 146

[153] D T C Allcock, L Guidoni, T P Harty, C J Ballance, M G Blain, A M Steane, and D M Lucas. Reduction of heating rate in a microfabricated ion trap by pulsed-laser cleaning. *New Journal of Physics*, 13(12):123023, 2011. 149

[154] D. A. Hite, Y. Colombe, A. C. Wilson, K. R. Brown, U. Warring, R. Jördens, J. D. Jost, K. S. McKay, D. P. Pappas, D. Leibfried, and D. J. Wineland. 100-fold reduction of electric-field noise in an ion trap cleaned with *In Situ* argon-ion-beam bombardment. *Phys. Rev. Lett.*, 109:103001, Sep 2012. 149

Appendix A

Electrical connections

This appendix shows the appropriate connections between the two 50 pin feedthroughs, the chip bracket and the electrodes of the microchip. Figure A.1 (a) shows a schematic of the chip bracket to illustrate which pin receptacle on the chip bracket is connected to which pin on the two 50 pin feedthroughs. The corresponding numbering of the two 50 pin feedthroughs is shown in figure A.1 (b).

The pins on the two 50 pin feedthroughs used for the electrodes on the microchip are shown in table A.1.

Electrode	Pin number
Comp 1	99, 40
Comp 2	86, 76, 83
Comp 3	77, 97, 95
Comp 4	8, 35
Comp 5	41, 10, 26
Comp 6	19, 27, 44
GND plane	13, 15, 29, 31, 49, 73

Table A.1: Table showing the electrodes on the microchip and the pin numbers they are connected to on the two 50 pin feedthroughs. The numbering corresponds to that shown in figure A.1 (b).

(a)

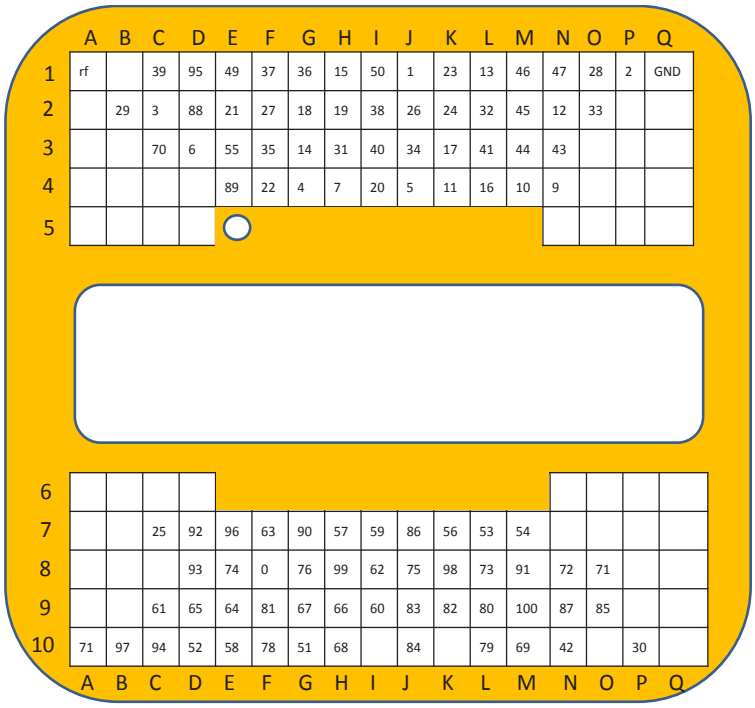

	A	B	C	D	E	F	G	H	I	J	K	L	M	N	O	P	Q
1	rf		39	95	49	37	36	15	50	1	23	13	46	47	28	2	GND
2		29	3	88	21	27	18	19	38	26	24	32	45	12	33		
3			70	6	55	35	14	31	40	34	17	41	44	43			
4					89	22	4	7	20	5	11	16	10	9			
5																	
6																	
7			25	92	96	63	90	57	59	86	56	53	54				
8				93	74	0	76	99	62	75	98	73	91	72	71		
9			61	65	64	81	67	66	60	83	82	80	100	87	85		
10	71	97	94	52	58	78	51	68		84		79	69	42		30	

(b)

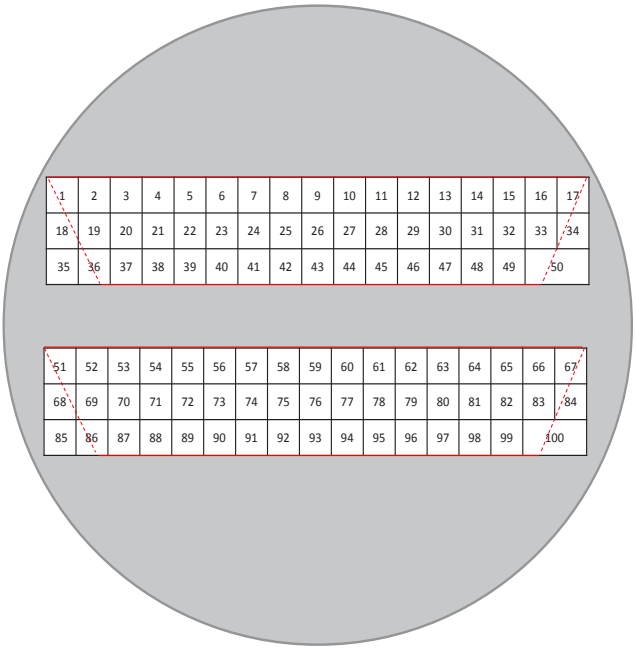

Figure A.1: (a) shows which pin receptacle on the chip bracket is connected to which pin on the two 50 pin feedthroughs. The rf and ground pins are connected to a separate feedthrough to connect to the helical resonator. (b) shows a schematic of the two 50 pin feedthroughs on a flange where the numbering corresponds to the numbers given in (a). The red lines indicate the actual shape of the feedthroughs.

Appendix B

Baking procedure

This appendix aims to describe the procedure of reaching pressures of $\approx 10^{-11}$ Torr in the vacuum system used to operate the two-dimensional lattice of ion traps on a microchip. The temperature and pressure of the vacuum system over the course of the evacuation process is shown in figure B.1. After the vacuum system has been assembled and the

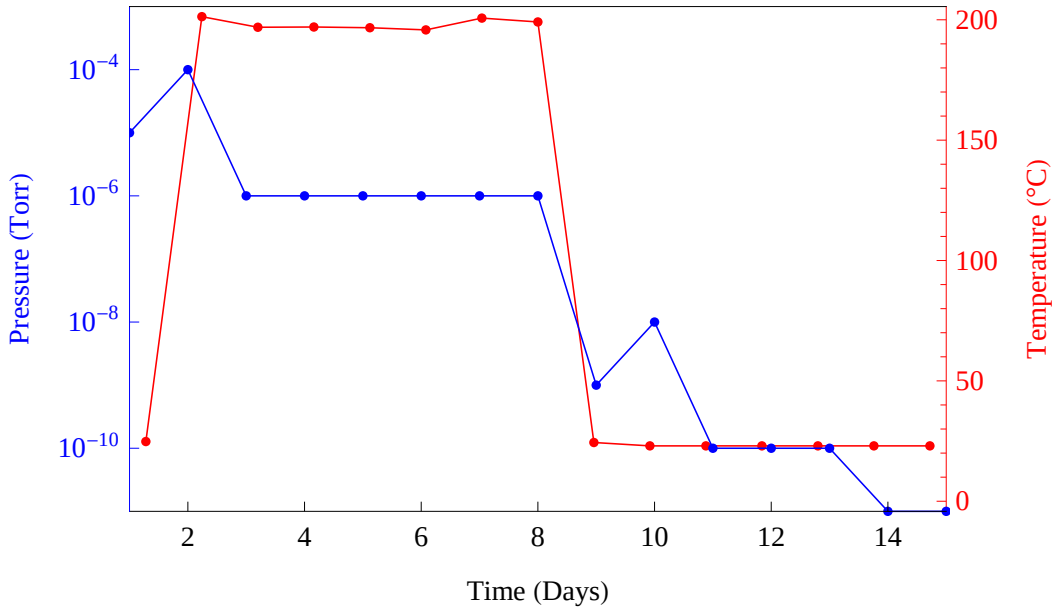

Figure B.1: Picture of a new vacuum system designed to accommodate both symmetric and asymmetric traps and used for the experiments shown in this chapter.

microchip put in place the system is moved into a homebuilt oven after which the following steps were performed:

- A turbo pump is connected to the all metal valve of the vacuum system via a 1.5 meter long metal hose. The turbo pump reduces the pressure of the system to $\approx 10^{-5}$ Torr within 3 hours.
- The microchip, atomic ovens and titanium sublimation pump (TSP) are outgassed. The microchip is outgassed by applying the voltage required to trap via a helical resonator for one hour. The atomic ovens are outgassed by applying 6 A to each oven for 15 minutes. Care must be taken that the current used to outgass the ovens is below the current required to produce a flux of Yb atoms. The TSP is outgassed by applying 30 A to each filament for 30 minutes.
- A temperature sensor is attached to the 100 pin feedthrough flange and to the large viewport used for collecting fluorescence from the ions. These are the most temperature sensitive parts of the vacuum system and therefore need to be carefully monitored during baking.
- The vacuum system is wrapped in tin foil. The viewports and feedthroughs are wrapped in at least 5 layers of foil to minimise the effects of heat spots.
- Another temperature sensor is attached at the top of the hemisphere.
- All heating elements are electrically tested.
- The oven is closed and the main fan speed is turned to maximum to ensure good circulation of air. It is important to remember to turn the small fan on as this ensures that the main fan does not overheat.
- The oven temperature is gradually increased at a rate of no more than 15°C per hour until a temperature of 200°C is reached (measured using the temperature sensor which is connected to the control unit of the heating elements. This typically takes one day which can be seen in figure B.1. One should ensure that the temperature difference between the sensor readings from under the foil and outside of the foil does not exceed 10°C.
- When the pressure has settled the 'external' ion pump which is part of the turbo pump setup is turned on.
- After approximately three hours the 'internal' ion pump which is part of the vacuum system is turned on.
- The ion gauge of the vacuum system is turned on.

- After a further two hours the oven door is opened and the all metal valve is closed (hand tight) as quickly as possible to minimise the drop in temperature inside the oven. The turbo pump is then turned off. The external ion pump remains running to maintain a low pressure inside the metal hose. This ensures that a low pressure can be reached inside the vacuum system despite the all metal valve not being closed properly.

- On days 9 and 10, after the pressure has levelled off at $\approx 10^{-9}$ Torr, the temperature of the vacuum system is reduced at a rate of 15°C following which the all metal valve is closed properly, the metal hose is disconnected and the system is moved to the optical table.

- Over the following 4 to 5 days the TSP is fired for one minute every two hours after which a pressure of $\approx 10^{-11}$ Torr is reached.